TECHNISCHE UNIVERSITÄT MÜNCHEN

Physik-Department
Lehrstuhl für Funktionelle Materialien

Nanostructured zinc oxide films for application in photovoltaics

Kuhu Sarkar, M.Sc.

Vollständiger Abdruck der von der Fakultät für Physik der Technischen Universität München zur Erlangung des akademischen Grades eines

Doktors der Naturwissenschaften (Dr. rer. nat.)

genehmigten Dissertation.

Vorsitzender:	Univ.-Prof. Dr. Martin Zacharias
Prüfer der Dissertation:	1. Univ.-Prof. Dr. Peter Müller-Buschbaum
	2. Univ.-Prof. Dr. Friedrich Simmel

Die Dissertation wurde am 24.06.2014 bei der Technischen Universität München eingereicht und durch die Fakultät für Physik am 22.07.2014 angenommen.

Abstract

Custom-tailored nanostructured morphologies of zinc oxide and zinc titanate are investigated in the present thesis. The aim is to utilize these structures for photovoltaic applications. Solution-based routines, such as pure precursor solutions and diblock copolymer-assisted sol-gel approaches, are used for synthesis of these nanostructures. The nanostructures are deposited as thin films using different techniques. Routes to impart improved tuneability to the length scales of the nanostructures are explored. These routes involve use of copolymer templates with different molecular weights and post-treatment of the films with a suitable solvent vapor. The dominant thin film morphologies obtained are classified into worm-like aggregates, spherical granules, circular vesicles, foam-like structures and nano grid-like morphology. The presented work also investigates the functionality of the thin films based on their morphology and thickness with regard to dye-sensitized solar cells. Both electrolyte-based and solid-state dye-sensitized solar cells are studied in the thesis.

Zusammenfassung

In der vorliegenden Arbeit werden die Morphologien von maßgeschneidertem, nanostrukturiertem Zinkoxid und Zinktitanat untersucht. Ziel ist es, diese Strukturen für photovoltaische Anwendungen zu nutzen. Zur Herstellung werden lösungsbasierte Verfahren, wie Sol-Gel Synthesen aus reinen Precursorlösungen oder unterstützt durch Diblockcopolymere angewendet. Die Nanostrukturen werden mit verschiedenen Methoden zu dünnen Filmen verarbeitet. Verfahren zur verbesserten Abstimmbarkeit der Längenskalen der Nanostrukturen werden sondiert. Diese beinhalten die Verwendung von Copolymertemplaten mit verschiedenen Molekulargewichten und Nachbehandlungen der Filme durch angepasste Lösungsmitteldämpfe. Die überwiegend resultierenden Morphologien dieser dünnen Filme werden in wurmartige Morphologien, sphärische Körnchen, kreisförmige Bläschen, schaumartige Strukturen und nanogitterartige Morphologien eingeteilt. Ebenso untersucht die vorliegende Arbeit die Funktionalität der dünnen Filme in Abhängigkeit der Morphologie und Dicke im Hinblick auf die Anwendung in Farbstoffsolarzellen. Sowohl elektrolytbasierte als auch feststoffbasierte Farbstoffsolarzellen werden dabei näher betrachtet.

Contents

List of abbreviations

1DDL	One-dimensional paracrystalline lattice
AFM	Atomic force microscopy
BMII	1-Butyl-3-methylimidazolium iodide
CB	Conduction band
CCD	Charge coupled device
CDW	Charge density wave
CIGS	Copper indium gallium diselenide
CIS	Copper indium diselenide
CTR	Crystal truncation rods
D149	5-[[4-[4-(2,2-Diphenylethe nyl)phenyl]-1,2,3-3a,4,8b-hexahydro-cyclopent[*b*]indol-7-yl]methylene]-2-(3-ethyl-4-oxo -2-thioxo-5-thiazolidinylidene) -4-oxo-3-thiazolidineacetic acid, an indoline dye
DI water	Deionized water
DMF	N,N-dimethylformamide, C_3H_7NO
DNA	Deoxyribonucleic acid
DSSC	Dye-sensitized solar cell
DWBA	Distorted wave Born approximation
EDX	Energy-dispersive x-ray spectroscopy
EGMT	Ethylene glycol modified titanate, $C_4H_8O_4Ti$
FF	Fill factor

FFT	Fast Fourier transformation
FTIR	Fourier transform infrared spectroscopy
FTO	Fluorine doped tin oxide, SnO_2:F
FWHM	Full width at half maximum
GIS	Grazing incidence scattering
GISAXS	Grazing incidence small angle x-ray scattering
GIUSAXS	Grazing incidence ultra small angle x-ray scattering
HABA	2-(4'-Hydroxybenzeneazo)benzoic acid
HCl	Hydrochloric acid
HOMO	Highest occupied molecular orbital
I/V	Current-voltage characteristics
ICSD	Inorganic Crystal Structure Database
IR	Infrared
ITO	Indium doped tin oxide
IUPAC	International Union of Pure and Applied Chemistry
JCPDS	Joint Committee on Powder Diffraction Standards
LED	Light emitting diode
LMA	Local monodisperse approximation
LUMO	Lowest unoccupied molecular orbital
LVDT	Linear variable differential transformer
MEMS	Microelectromechanical systems
MPP	Maximum power point
N719	Di-tetrabutylammonium cis-bis(isothiocyanato) bis(2,2'-bipyridyl-4,4'-dicarboxylato)-ruthenium(II), a ruthenium dye
ODT	Order disorder transition

P(S-*b*-4VP) ..... Poly(styrene-*block*-4-vinylpyridine)

P(S-*b*-EO) ..... Poly(styrene-*block*-ethylene oxide)

P3HT ..... Poly(3-hexyl-thiophene), $(C_{10}H_{14}S)_n$

PA ..... Polyacetylene, $(C_2H_2)_n$

PCE ..... Power conversion efficiency

PDP 3-pentadecylphenol

PEO ..... Poly(ethylene oxide), $(C_2H_4O)_n$

PL ..... Photoluminescence

PTFE ..... Polytetrafluoroethylene, $(C_2F_4)_n$

rr-P3HT ..... Regioregular poly(3-hexyl-thiophene)

SDD ..... Sample-detector distance

SEM ..... Scanning electron microscopy

SLD ..... Scattering length density

SMA ..... Supramolecular assemblies

ss-DSSC ..... Solid-state dye-sensitized solar cell

SSH ..... Su-Schrieffer-Heeger

SSL ..... Strong segregation limit

TCO ..... Transparent conductive oxide

TEM ..... Transmission electron microscopy

THF ..... Tetrahydrofuran, C_4H_8O

UV ..... Ultraviolet

UV/Vis ..... UV/Vis spectroscopy

WSL ..... Weak segregation limit

XRD ..... X-ray diffraction

ZAD ..... Zinc acetate dihydrate, $Zn(CH_3COO)_2 \cdot 2H_2O$

1. Introduction

"If I had to choose a religion, the sun as the universal giver of life would be my god."
- Napoleon Bonaparte

With an ever-increasing consumption of different forms of energy in order to sustain life, the search for inexhaustible sources becomes imperative. The radiant heat and light from the sun is a universal source of energy. Moreover, most of the other renewable sources derive their energy from the sun. Hence, harnessing the indigenous source of solar energy via active or passive technologies requires major attention from all over the world. Among all the different forms in which the solar energy can be harvested, electrical energy has the highest demand and is the primary amenity not only to support life, but also to maintain the living standards of the modern societies worldwide. The advent of exploiting solar energy for production of electricity began with the discovery of the photovoltaic effect in 1839 by M. E. Bequerel [1]. Followed by this, the first solar cell with an efficiency of around 1 % had been demonstrated by Charles Fritts in 1883 [2]. The breakthrough in the field came with the development of the first practical photovoltaic cell in the Bell Laboratories in 1953, with a power conversion efficiency of 4.5 % [3]. Since then, a rapid progress has been made by the photovoltaic industry with the launch of inorganic silicon-based solar cells and more recently with the fabrication of fully organic solar cells [4–8].

About 80-90 % of the present market share for solar cells is occupied by crystalline silicon (c-Si) solar cells and the rest 10-20 % by thin film solar cells. Although, c-Si solar cells are the most successful, they suffer from expensive production cost. They are relatively poor absorber of light, due to which a significant thick film of the order of hundreds of microns is required for sufficient absorption of light. This renders inflexibility to c-Si solar cells. Contrarily, the thin film solar cells mainly consist of materials which are good absorbers, such as amorphous silicon (a-Si), cadmium telluride (CdTe) and copper indium (gallium) diselenide (CIS or CIGS). The use of thin layers promotes the stability of electric field strength in the device, but on the other hand, the absorption is lowered due to less material (in the range of a micron thick layer). Even though less material is

needed for these cells, the problems of high cost and mechanical inflexibility of the device architecture persist [3].

The accidental discovery of conducting polymers in 1970s [9] has triggered the research on novel organic materials for implementation as active layers in solar cells. The strong absorption behavior shown by these materials, requires only thin films of the order of a few hundreds of nanometers for the functioning of the solar cells. Additionally, easy synthesis and solution-processibility of these materials have provoked their deposition on flexible substrates as well. This cheaper alternative as compared to the silicon-based solar cells have become even more promising with the use of dyes as the absorbing materials. Not only restricted to organic materials, but the use of suitable dyes as photosensitizers in combination with inorganic materials has been first co-invented in 1988 by Brian O'Regan and Michael Grätzel [10]. These solar cells are termed as dye-sensitized solar cells (DSSCs) or simply Grätzel cells. Although the power conversion efficiencies of these devices are less than the best inorganic thin film cells, DSSCs provide vast opportunities to manufacture cheap devices, with high mechanical flexibility, good transparency and significant stability via cost-effective production routines. Since the invention of DSSCs, titanium dioxide, commonly known as titania (TiO_2) as the electron-accepting medium in combination with ruthenium-based complexes as sensitizers and iodide-based electrolytes as the redox mediators have been used for a long time, providing power conversion efficiencies of around 10 % [11]. The performance of these cells have boosted to over 12 % with the use of porphyrin-based sensitizers in combination with cobalt (II/III)-based redox electrolytes [12]. More recently, DSSCs have reached a power conversion efficiency as high as 15 % with the use of perovskite with mesostructured TiO_2 [13]. These developments have instigated the quest for new materials with advanced functionality.

The working principle of a DSSC is based on three major processes: absorption of light, generation of charge carriers and their extraction at the respective electrodes. The above-mentioned processes are largely dependent on the structure of the inorganic scaffold which hosts the photosensitizer and the electrolyte/conducting polymer. A high surface area and film thickness in the range of few tens of micrometers are the prerequisites to adsorb sufficient dye molecules to harvest solar radiation. Hence, production of nanostructured inorganic metal oxide morphology plays a key role in the final device efficiency. Modeling of such nanostructures, in turn relies on the synthesis and deposition routes applied. Synthesis and depositions techniques serve as the spots contributing towards the final cost of the device in addition to the raw materials involved. Moreover, the presence of correct length scales in the developed morphology decides the efficient transport and extraction of charges in the final device. In order to address the above mentioned challenges, which all go hand in hand, the present thesis is oriented towards synthesis, deposition and

characterization of novel inorganic metal oxide nanostructures with enhanced structural tuneability.

As such, zinc oxide (ZnO) is chosen in order to investigate its performance as the electron-conducting part in the active layers of DSSCs in the present work. Similar opto-electronic properties of ZnO with even higher electron mobility and thermal stability as compared to TiO_2, make ZnO an attractive alternative to conventionally used TiO_2. In addition, the large abundance of the material reduces the cost of ZnO massively. Implementation of ZnO as the electron-conducting material in electrolyte-based DSSCs has been already proven successful, showing a maximum power conversion efficiency of around 7 %, reported so far [14]. Furthermore, a unique compound of ZnO and TiO_2, namely zinc orthotitanate (Zn_2TiO_4) is investigated as an additional alternative to ZnO. For the present thesis, a metal-free organic dye is used as the sensitizer, commercially named as D149, which has a higher molar extinction coefficient and is more environmentally friendly as compared to the ruthenium-based complexes. The liquid electrolyte-based DSSCs are often associated with certain inherent challenges, such as the corrosive nature of the iodine-based electrolytes and sealing problems encountered by the final device. Hence, DSSCs using organic hole conductors are also fabricated in the presented research using ZnO as the electron-conducting material, D149 as the photosensitizer and P3HT as the hole-conducting polymer. All the synthesis procedures followed in the present thesis are solution-based and provide a high degree of control over the morphologies produced along with their length scales. Although, such wet chemical processes are established for other inorganic metal oxide semiconductors such as TiO_2 [15], synthesis of ZnO and Zn_2TiO_4 nanostructures using these processes have been successfully reported in the present dissertation for the first time. The questions tackled along with the structure of the thesis are outlined in the following.

To start with, the theoretical aspects regarding the functioning of DSSCs, properties of the inorganic metal oxide semiconductors and polymers used in developing the system as well as the basics of the scattering methods employed to probe the structures are presented in chapter 2. A short description of all the characterization tools used in the thesis is given in chapter 3 followed by the sample preparation procedures in chapter 4. Figure 1.1 summarizes the different research topics featured in the present thesis.

The primary concern of the fundamental aspects of the present research is their influence on the performance of DSSCs. In chapter 5 (represented as figure 1.1(a)) a simple solution-based approach is demonstrated to obtain crystalline ZnO nanostructures from a commercial ZnO precursor. In order to deposit the nanostructures in the form of thin films, spray deposition is used, which is a versatile method to coat large areas as well as to upscale the film thickness. The fast kinetics of the process raises questions regarding the

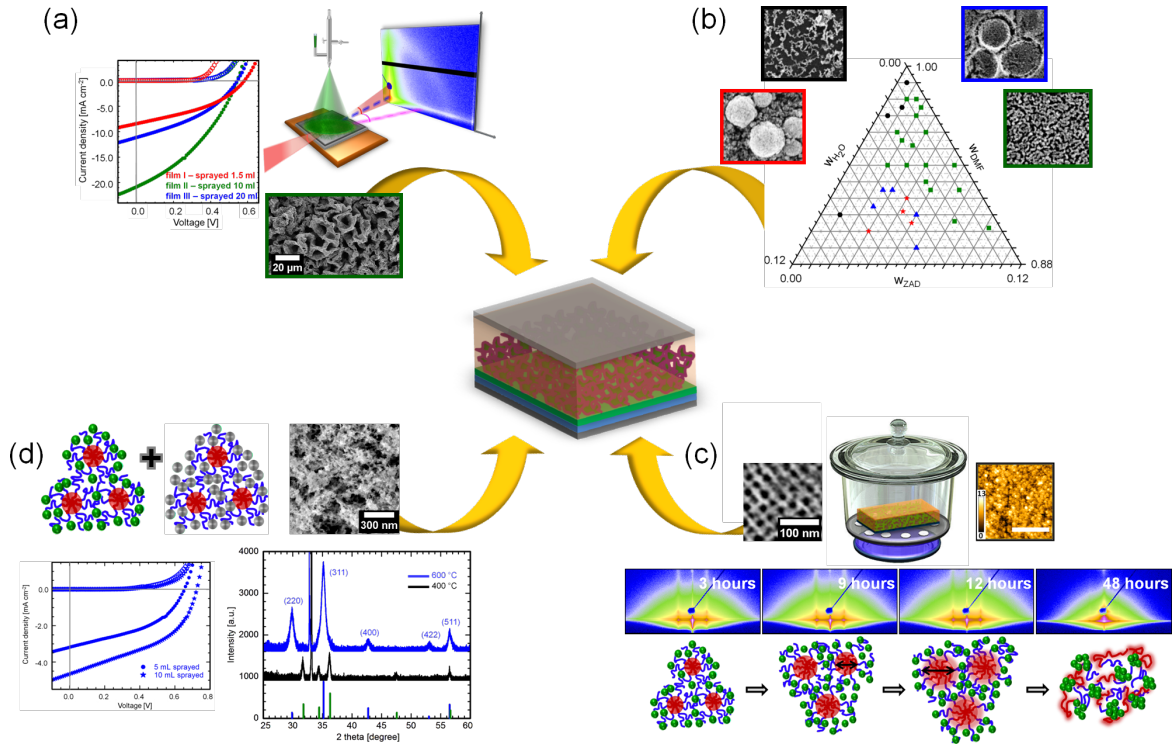

Figure 1.1.: A schematic representation of the different issues addressed in the present thesis with regard to the functioning of ZnO and Zn_2TiO_4-based dye-sensitized solar cells, which is depicted in the center. (a) Synthesis of ZnO nanostructures via a pristine solution of ZnO precursor. The aspect deals with monitoring the structure evolution during and after the spray deposition and finally to investigate the efficiency of the DSSCs obtained from the spray-deposited films. (b) Exploring the possibility to obtain varied ZnO nanostructured thin film morphologies via sol-gel synthesis assisted with a diblock copolymer template. (c) Further tuneability to the length scales is provided by treating the films deposited from sol-gel solutions, using a suitable solvent vapor stimulus. (d) Synthesis of zinc orthotitanate films via spray deposition of mixed sol-gel solutions (mixture of ZnO and TiO_2 sol-gels) as a suitable alternative to ZnO for an electron-conducting layer in DSSCs.

evolution of the structures during the spray process and the final structures obtained in the film. In order to gain this in-depth information, comprehensive scattering experiments are performed, thereby probing the length scale evolution during and after the spray process. Finally, the influence of the synthesis and deposition route for ZnO nanostructured films on the final device performance is tested.

To provide optimum functionality to the nanostructures, it is beneficial to develop routes to tune the morphology and length scales to suit a specific need. Chapter 6 (represented as figure 1.1(b)) deals with the novel routines to accomplish this, encompassing the use of a diblock copolymer template in association with the sol-gel chemistry. P(S-*b*-EO)

is used as the structure-directing template for the present case. This is followed by the question related to the influence of different block lengths of the same diblock copolymer template on the length scales of the nanostructures. Also, it is interesting to investigate the impact on film morphology when different molecular weights of the same diblock copolymer template is employed. The effect of different deposition methods on the film morphology is also an attractive option, which is deciphered in this chapter. As a supplementary study, custom-made ZnO nanocrystalline powders and terpineol-based pastes from those powders are produced. This raises the natural question whether these pastes are tangible to be transferred as thin films on substrates and used as electron-conducting layers for DSSCs.

Another aspect that stays open is the influence of different diblock copolymer templates on the ordering of the nanostructures synthesized. In chapter 7 (represented as figure 1.1(c)), P(S-*b*-4VP) is used as an alternative template to synthesize ZnO nanostructures for comparison with the structures obtained via the P(S-*b*-EO) template. The use of different templates is not always feasible for tuning the length scales of the nanostructures. Hence, additional pathways to further fine-tune the structure sizes, such as solvent vapor annealing is investigated. In order to obtain valuable insights to the structural arrangements and tuneability of the pore sizes under the influence of a suitable solvent vapor stimulus for different time scales, x-ray scattering measurements are employed. A detailed study of the structural arrangement in the films is carried out on the basis of selectivity of the solvents used for annealing towards a specific block of the diblock copolymer template. Furthermore, the performance of ZnO nanostructured films obtained by spray deposition of sol-gel solutions as active layers in DSSCs, is investigated.

Chapter 8 (shown as figure 1.1(d)) describes the final aspect inspected in this thesis. The major concern highlighted in this chapter is the challenge to synthesize a novel compound of ZnO and TiO_2, namely Zn_2TiO_4, via the wet chemical sol-gel process. Different kinds of materials which can be obtained depending on the mixing ratio of the ZnO and TiO_2 sol-gel solutions are also characterized in this chapter. Zn_2TiO_4 is the most abundantly used compound of ZnO and TiO_2, but also the one which is sparsely investigated in terms of morphology, optical and electronic properties. The precise conditions under which this compound can be synthesized, such as the mixing ratio of the ZnO and TiO_2 sol-gel solutions and the temperature applied are discussed in this chapter. Promising opportunities of using Zn_2TiO_4 in the active layers of electrolyte-based DSSCs are also explored.

The thesis is concluded in chapter 9, where answers to all the questions posed in the present section, are summarized based on the investigations carried out throughout the thesis. A short outlook into future projects is also provided in the end of chapter 9.

2. Theoretical aspects

The materials and the systems studied in this thesis are directed towards applications in dye-sensitized solar cells (DSSCs). In this chapter, the theoretical background of the materials and processes related to the fabrication and functioning of the final devices is introduced. General theoretical background of polymers in general is discussed in section 2.1, with a special emphasis on block copolymers, which are used as structure-directing templates for the inorganic metal oxides. These inorganic metal oxides in turn constitute the main part of the active layers in DSSCs and are backfilled by organic polymers in case of solid-state DSSCs. This special class of polymers is termed as conducting polymers. The band structure and charge transport in conducting polymers are also reported in this section. The fundamental principles of copolymer template-assisted novel structuring routine to obtain metal oxide (zinc oxide and zinc orthotitanate) nanomorphologies are presented in section 2.2. The working mechanism and the kinetics of the processes occurring in electrolyte-based as well as solid-state DSSCs are introduced in section 2.3. Lastly, theoretical background about the x-ray scattering methods used to probe the films is discussed in section 2.4, along with an overview about the interpretation of the data obtained.

2.1. Polymer basics

The fundamental aspects of polymer physics are introduced in this chapter. General properties of the polymers along with basic definitions are presented, which are then followed by crystallization behavior of polymers. Section 2.1.1 details the theoretical aspects for diblock copolymers. Remarks on the micro-phase separation of diblock copolymers are also given in the same section. Electrically conducting polymers are described in section 2.1.2 on the basis of the type of charge carriers and hopping transport of the charges in such a system.

General properties and definitions

The term 'polymer' refers to a large molecule or a macromolecule constituted of repeating units, known as monomers, covalently bound to each other. The number of monomeric units building the polymer is referred to as the degree of polymerization, n or N. Molecules in general are classified on the basis of their molecular weights M. Molecules with $M < 1000$ g mol^{-1} are known as macromolecules, whereas, those with M between 1000 and 10000 g mol^{-1} are known as oligomers. The large molecules are only considered as polymers when they have a $M > 10000$ g mol^{-1}. For example, if a monomer A is repeatedly linked with covalent bonds, a polymer A-A-A-$\cdots$-A-A-A is produced and is called polyA or PA on the monomer-based nomenclature. For instance, the monomer styrene can link with one another repeatedly to produce polystyrene, abbreviated as PS with a structural formula $(C_8H_8)_n$, where n is the degree of polymerization. The different ways to name and represent polymeric molecules can be found in the glossary of the International Union for Pure and Applied Chemistry (IUPAC) [16].

Several polymers occur in nature and are known as biopolymers such as DNA and proteins like cellulose, which are the fundamental building-blocks for different biological systems. Only some of these polymers are completely monodisperse, meaning all the molecules have the same length and possess the exact same degree of polymerization. However, most of the polymers used in daily-life are man-made and are termed as synthetic polymers. Different chemical reactions are used for the synthesis of polymers, which are commonly known as polymerization reactions. All these routes yield polymer molecules with different sizes and hence varied chain lengths. As a result of this, statistical mean values are obtained in order to describe the polymers. The so-called number average molecular weight M_n is the arithmetic mean of the individual polymeric molecules

$$M_n = \frac{\sum_i n_i M_i}{\sum_i n_i}, \tag{2.1}$$

also known as the first moment of the statistical distribution of the molar masses, where M_i is the molar mass of component i and n_i is the number of chains of component i. The so-called weight average molar mass M_ω is defined as the ratio of the second central moment to the first central moment of the statistical distribution as

$$M_\omega = \frac{\sum_i \omega_i M_i}{\sum_i \omega_i}, \tag{2.2}$$

where ω_i is the total mass of the macromolecules of component i, ($\omega_i = n_i M_i$). The width of the distribution of the molar masses is described by the polydispersity index P as

$$P = \frac{M_\omega}{M_n} = U + 1, \tag{2.3}$$

where U is the so-called inconsistency. For the case of $P = 1$, a polymer is monodisperse without any inconsistency. For all the synthetic polymers $P > 1$. The polydispersity strongly depends on the synthesis procedure used. Since the properties of the polymers depend strongly on the distribution of their molecular weights, the choice of polymerization route is defined by the end use of the polymer. For cost-effective production in industries, step-growth polymerization or polycondensation are the commonly used routes where random fragments of polymers and monomers can react with each other, giving rise to a wide distribution of molecular weights, known as the Schulz-Zimm distribution function. On the other hand, for scientific applications, a polydispersity index close to 1 is preferred due to which the commonly used synthesis routes is chain (anionic) polymerization where a step-by-step growth of the polymer chains occurs giving rise to a narrow Poisson distribution function.

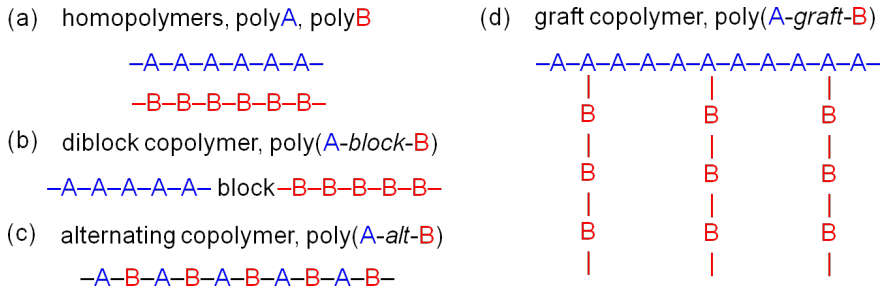

Figure 2.1.: Commonly observed constitutions of two different polymers A & B as (a) homopolymers, (b) diblock copolymer, (c) alternating copolymer and (g) graft copolymer.

Different monomer units can link with each other in different manner giving rise to different architectures of the polymer chains, depending on the synthesis route. From a simple chain-like architecture, branches of monomer units can form or several other complicated branching lead to the formation of ring-like polymers, brush-like structures or star-shaped geometries. Also more than one kind of monomer can be linked together to obtain a polymer. These special polymers are named as block copolymers and have derived different nomenclature depending on the pattern that the monomer units follow to be linked together. Some different constitutions from two different monomer units are shown in figure 2.1. The simplest polymer chains obtained are the homopolymers consisting of identical monomer units (figure 2.1(a)). When two blocks of identical monomer units are covalently linked together, diblock copolymers are formed (figure 2.1(b)), which are detailed in section 2.1.1. If the monomer units are linked to each other in an alternating manner, the polymer is known as an alternating copolymer (figure 2.1(c)). On the other hand, if no such order is present, the polymer is known as random copolymer. When structurally distinct monomer units form the side chains which are attached to a backbone

of different monomer units, the polymer is known as a graft copolymer as shown in figure 2.1(d).

Polymer crystallization

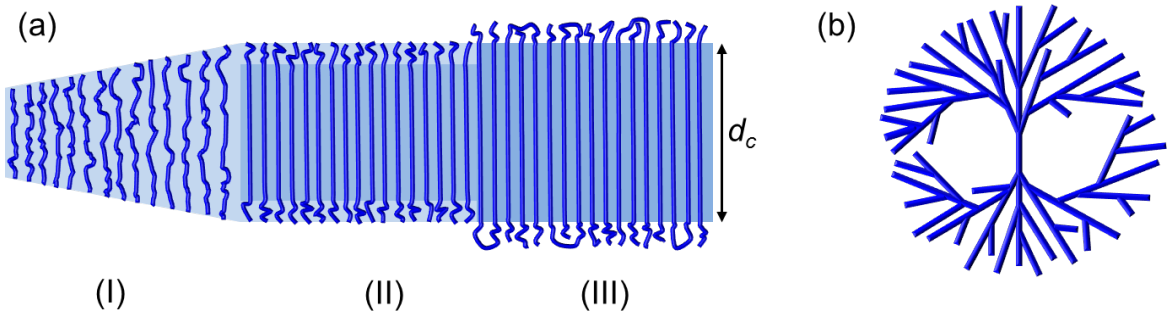

Figure 2.2.: (a) Polymer crystallization is shown as a multi-stage growth model as described in [17], with (I) growth of a mesomorphic layer, (II) solidification of the core and (III) stabilization of the crystal via surface ordering. The thickness of the crystal is represented by d_c. (b) Schematic representation of a spherulite crystal structure.

The physical properties of polymers depend strongly on the temperature. Several important temperatures signify the transitions from one state to another. Since all polymers are fully or partially amorphous, glass transition temperature T_g is a characteristic temperature. This describes the transition of the solid, glassy state of the polymer to a more soft, rubber-like state. Some of the polymers are also able to partially crystallize and hence are also characterized by two additional temperatures, namely, the crystallization and the melting temperature, represented by T_c and T_m, respectively, where $T_g < T_c < T_m$. In contrast to organic molecules and oligomers, the crystallizable polymers do not form complete crystals and are typically separated by amorphous regions in the same polymer. This state does not attend thermal equilibrium but is kinetically driven and often known as the semi-crystalline state. A full crystallization of the polymer is hindered by their polydispersity, meaning different chain lengths possess varied degree of entanglements of the coiled polymer chains, which have a high entropic activation barrier. The full crystallization of the polymer would require a complete disentanglement of all the chains. The aspect of crystallinity plays a crucial role in charge transport in conducting polymers such as poly(3-hexylthiophene) (abbreviated as P3HT) as detailed in section 2.1.2. It has been reported that in regioregular P3HT (rr-P3HT), a high crystallinity and hence, a better charge transport is observed [18]. Generally, polymer crystals have a layered structure with the thickness of the crystal represented by d_c, which depends on T_c and is independent of the molecular weight of the polymer [19]. Laterally (perpendicular to

the direction of the polymer chains), the crystals can grow up to several micrometers. The crystallization of the polymer chains is described by a multi-stage growth model, as schematically represented in figure 2.2(a). Crystallization of the polymer starts with the formation of nuclei, which are regions within the amorphous polymer melt with an enhanced inner order. These nuclei are often reported to be formed due to thermal fluctuations or even impurities [17]. Followed by this, an intermediate phase, known as the "mesophase" is formed representing a virtual transition from the amorphous phase to the crystalline phase. In the mesomorphic phase, the single polymer chains as well as neighboring chains fold themselves in order to obtain an ordered arrangement as seen in figure 2.2(a). At a certain thickness, the core of the mesomorphic phase solidifies and forms a block, which is followed by the ordering of the chains on the surface, thereby stabilizing the crystal. The crystalline lamellae with thickness d_c can macroscopically rearrange to form so-called spherulites as shown in figure 2.2(b). Such crystallites mainly result from branching and splaying of chains during the crystal growth. Such spherulite structures are often observed in the poly(ethylene oxide) (PEO) homopolymer as well as in the diblock copolymer of poly(styrene-*b*-ethylene oxide) (P(S-*b*-EO)), which is one of the most investigated templates for structuring zinc oxide and zinc orthotitanate in the present thesis [20].

2.1.1. Block copolymers

Depending on the monomer blocks, two homopolymers in a blend either form a homogeneous mixture or phase separate on the basis of Gibb's free energy. In case of the blend shows the later behavior, the two homopolymers separate macroscopically into two pure phases. In case of diblock copolymers, the two blocks, each constituted of identical monomer units are covalently bound to each other and hence, do not show macro-phase separation. Instead separation in the length scale of the chain occurs, commonly termed as micro-phase separation. In a diblock copolymer, the different blocks A and B have different degrees of polymerization N_A and N_B. The phase behavior is described by the total degree of polymerization $N = N_A + N_B$ along with the block ratio f_A and f_B calculated as

$$f_A = \frac{N_A}{N_A + N_B} \tag{2.4}$$

$$f_B = \frac{N_B}{N_A + N_B} = 1 - f_A. \tag{2.5}$$

N describes the chain length of the diblock copolymer and therefore, decides the size of the micro-phase-separated domains. The block length on the other hand governs the domain structure. In addition, the interaction parameter χ describes the interaction between two

homopolymers and is also known as the Flory-Huggins parameter [21,22] and represented as

$$\chi = \chi_S + \frac{\chi_H}{k_B T}, \tag{2.6}$$

where k_B and T are the Boltzmann constant and the temperature, whereas χ_S and χ_H are the entropic and the enthalpic term of the Flory-Huggins interaction parameter. The entropic part includes contributions from the chain ends and the conformations of the chains. For diblock copolymers, the contribution from the entropic part is more enhanced due to the longer end-to-end distance in the chains as compared to the homopolymer chains. This is due to the fact that for diblock copolymers, the chains obtain a stretched conformations rather than Gaussian coils as mainly observed for the homopolymers. Hence, the Flory-Huggins interaction parameter for a diblock copolymer χ_{A-b-B} is always equal or greater than the Flory-Huggins interaction parameter of the blend of the corresponding homopolymers, χ_{A+B}. In general, a small value of χ represents higher miscibility of the polymers. The relation between the domain structures and the block lengths for diblock copolymers is generally expressed in terms of phase diagrams. An exemplary phase diagram for diblock copolymers is shown in figure 2.3.

The degree of phase separation in a diblock copolymer is decided by the factor χN. In other words, χN describes the sharpness of the domain borders which leads to different morphologies as depicted in figure 2.3. For $\chi N \approx 10.5$, a weak segregation limit (WSL) is observed in case of symmetric blocks ($f = 0.5$), whereas, upon increasing χN, the incompatibility between the two blocks increase and a strong segregation limit (SSL) is observed for $\chi N \gg 10.5$ [23].

In general, an asymmetric phase diagram is more frequently observed resulting from the presence of conformationally different polymer blocks or different behavior shown by the blocks, such as crystallization. Additionally, when the diblock copolymer is confined to a substrate in the form of a thin film, different morphologies can be obtained due to interfacial interactions, than those reported in the phase diagram shown in figure 2.3.

2.1.2. Conducting polymers

Traditionally, polymers have been used in our daily lives mostly because of their mechanical properties and easy processibility. All polymers had been known to be electrically insulating and hence, mostly used in housing for electrical appliances, until the discovery of conducting polymers by Shirakawa, MacDiarmid and Heeger, for which they jointly received the Nobel Prize in Chemistry in the year 2000 [9]. Polyacetylene is the polymer in which the conducting behavior has been discovered for the first time in 1997. Today, with continuous research in this field, the conductivity of the polymers have been raised

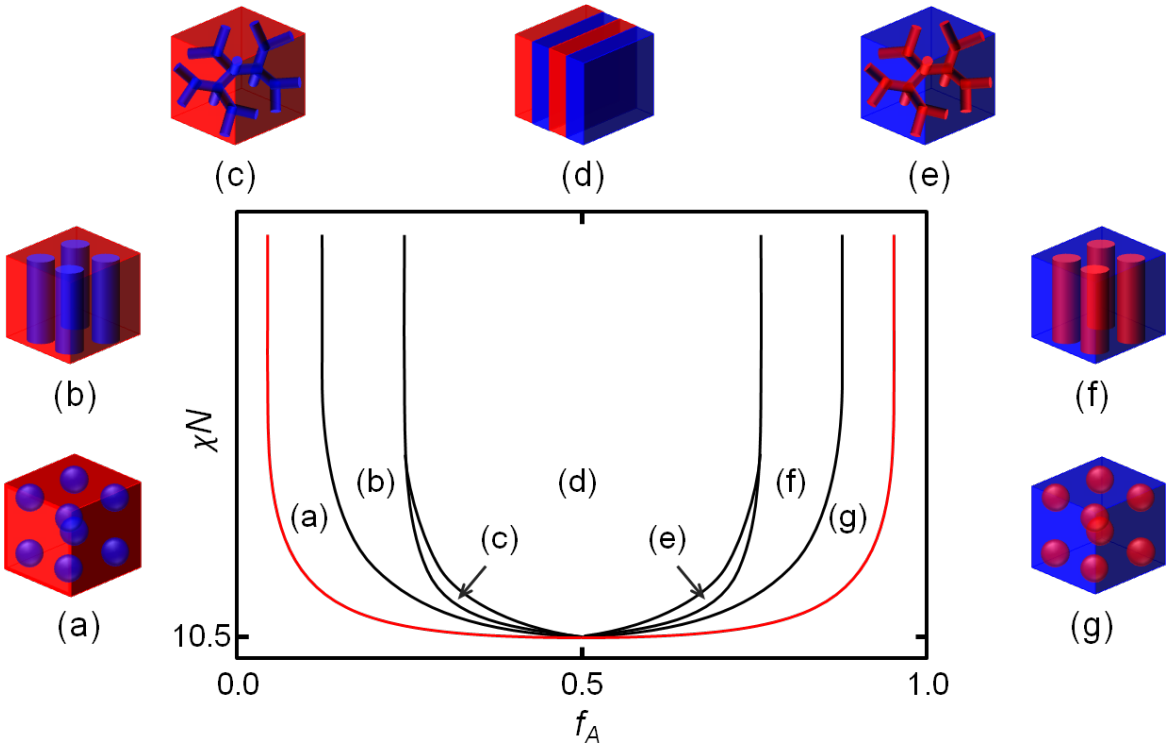

Figure 2.3.: Sketch of exemplary phase diagram of a conformationally symmetric diblock copolymer melt, P(A-*b*-B). With increasing block ratio f_A of block A (shown in blue), the structure of the A-domains inside the matrix of block B (shown in red) is changing from (a) spheres via (b) hexagonally packed cylinders to (c) a bicontinuous gyroid network. For approximately equal fractions of the two blocks, (d) a lamellar structure is formed. With further increase of f_A, the structure inverts to structures of the B-block embedded in a matrix of A changing from (e) a bicontinuous gyroid network via (f) hexagonally packed cylinders to (g) spheres. The red line indicates the order-disorder transition (ODT) below which the polymeric system is in a mixed phase without ordered structures.

to cover 10^{15} orders of magnitude. For all the conducting polymers, the presence of alternating single and double bonds, also termed as conjugated double bonds in the polymer chains is required. The reason behind this is explained from the spatial point of view, i.e., the presence of alternating double bonds refers to the presence of π-orbitals. The electrons are known to be delocalized in π-orbitals, thereby having an enhanced mobility along the chain. From an energetic point of view, overlap of the adjacent π-orbitals leads to formation of π- and π^*-bands. These π- and π^*-bands are known as valence (E_V) and conduction bands (E_C). While referring to the energy levels in conducting polymers, E_V and E_C are often known as the highest occupied molecular orbital (HOMO) and lowest unoccupied molecular orbital (LUMO), respectively.

The origin of band structures in conducting polymers is discussed in the following along with the different types of charge carriers present in the system and the charge transport mechanism.

Band structure and charge carriers

Peierl's theorem is typically used to explain the band structure of conjugated polymers. For conducting polymers, this theorem also demonstrates the origin of band gaps and thereby, explaining their insulating behavior. According to this theorem, in an one-dimensional metallic lattice of N atoms, the presence of one electron per atom with a periodic distance of a gives rise to a half-filled energy band up to the Fermi level E_F. However, in case of simple conjugated polymers such as polyacetylene, linear polymeric chains are more flexible as compared to the metallic materials. As a consequence, a distortion changes the one-dimensional chain of atoms, thereby changing the period of atoms. For example, doubling the period of the atoms will cause a modulation in the electron density, termed as a charge density wave (CDW). Due to the formation of a new lattice, the Brillouin zone is reduced to half, which will insert an energy gap $\triangle E_g$ right at the Fermi energy. The energy of this band gap reduces the total energy of the system and hence, the distorted system is energetically more favorable. The size of the band gap largely depends on the degree of polymerization, doping and the structure. Typically, the band gap for most of the practically used conducting polymers lies in the range of 1.5 to 3 eV [17]. P3HT is used as the conducting polymer in the present study, which has a band gap of 2.4 eV [24].

In polymers, the charges are transported by quasiparticles, which combine the charges in the system with the lattice distortions. Three primary quasiparticles are known namely, solitons, polarons and bipolarons, for systems having degenerate ground state. The energy levels of these quasiparticles are schematically represented in figures 2.4(a), (b) and (c) for polyacetylene (PA) chains. The interaction of two quasiparticles either leads to their annihilation or formation of new particles. The Su-Schrieffer-Heeger (SSH) model describes the charge and spin of the quasiparticles. According to this model, a reversed charge-spin relation of the solitons is observed which are considered as the primary quasiparticles, whereas, the polarons and bipolarons are produced by the interaction between the solitons and that between solitons and polarons, respectively. When two degenerate ground states of PA meet, a neutral soliton (S^0) is produced, with no charge and a spin of ½. A positive soliton (S^+) is produced when the charge at the boundary is extracted, leaving behind a positive charge. Since, no unpaired spin is present for this case, the spin is 0. Similarly negative solitons (S^-) are produced via doping or excitation by light. The polarons are the quasiparticles formed from the interaction between a charged and a

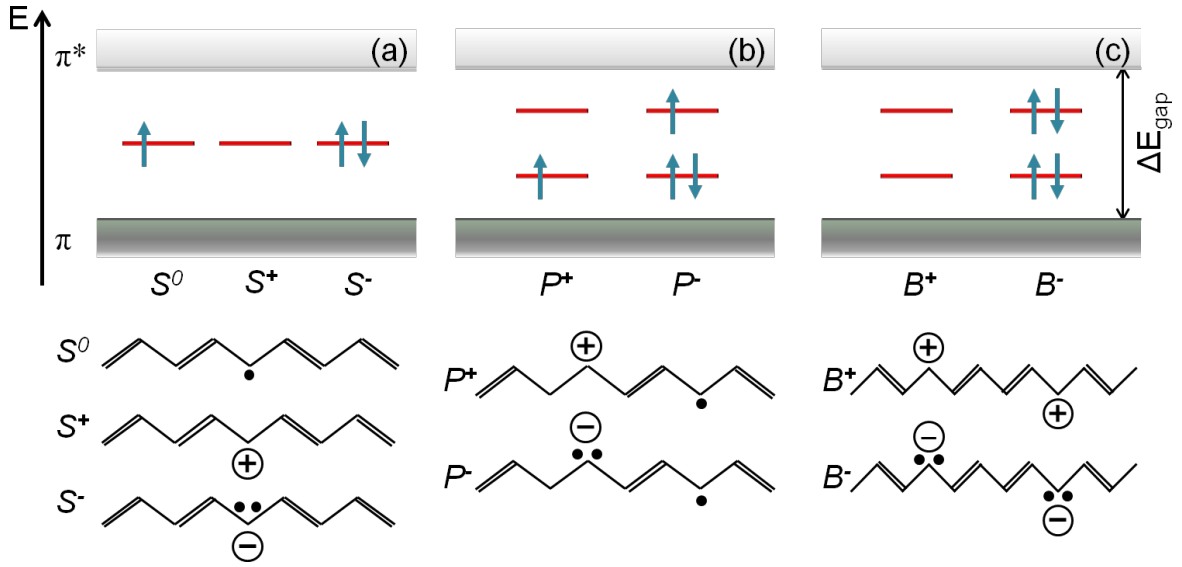

Figure 2.4.: Schematic representation of the energy states of charge carriers (quasiparticles) in a conducting polymer, exemplarily shown for PA chains. In the illustration, the dots represent the electrons which do not belong to the π-bond, whereas $\oplus$ and $\ominus$ show the net charge on the quasiparticles. (a) Neutral, positive and negative solitons are represented for PA as S^0, S^+ and S^-. (b) Polarons are shown with always a positive (P^+) or a negative (P^-) charge. (c) Bipolarons are shown having two positive B^+ or two negative charges, B^-.

neutral soliton, thereby possessing both a charge and a spin (figure 2.4(b)). A bipolaron is a bound state of two charged solitons of the same charge or two polarons whose neutral solitons annihilate each other. As a result, the bipolarons have no spin but a net charge (figure 2.4(c)). Although in the symbolic representation of the quasiparticles in figure 2.4, the charges are marked in certain positions, but these charges are delocalized on the polymer chains. As an example, experiments and calculations have shown that a soliton shows a structural relaxation over 14 carbon atoms in a PA chain. This soliton exerts an effective mass of six times larger than that of an electron. For bipolarons, the presence of identical charges on the same polymer chain gives rise to Coulomb repulsion, which is neutralized by the polarization capabilities of the polymeric system.

Charge transport

Propagation of charges in conducting polymer signifies transport of polarons rather than electrons in case of band transport in inorganic materials. The transport of charges along the polymer chains is possible without any hindrance due to the presence of the delocalized π-orbitals as mentioned before. However, for the transport from one chain to another, a hopping mechanism is established for conducting polymers. The hopping of the polarons

is assumed to take place between localized states in the polymer, which are shown in red in figure 2.5.

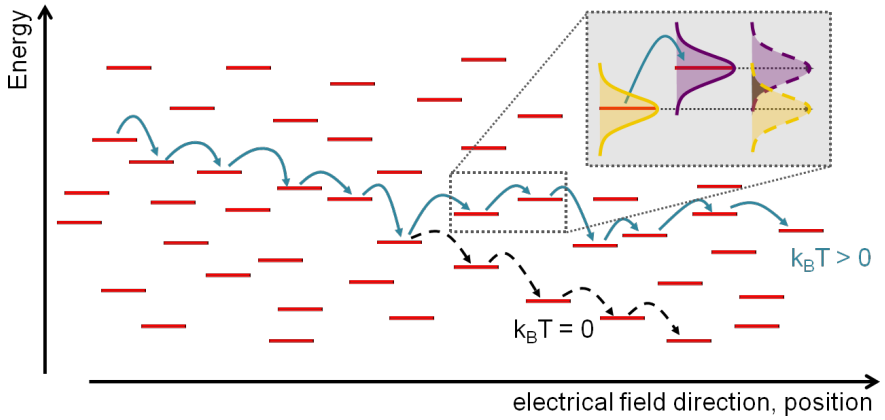

Figure 2.5.: Representation of hopping transport of charge carriers in a conducting polymer. The red lines indicate localized energy states within which the charges hop, as indicated by the blue arrows, following an external electric field $\vec{E}$. In the presence of external energy ($k_BT > 0$), the charges may even hop to higher energy states. In the absence of any external energy ($k_BT = 0$), the charge carriers relax to energetically low states (trap states) as represented by the black dashed arrows. Hopping is supported only if there is an overlap of the energy states which are supposed to have a Gaussian distribution. This is shown as an inset for the projection of two neighboring energy states, where a weak overlap is present.

The presence of these localized states in the polymer is caused by spatial or energetic disorders in the polymer. Each localized state is configured to have a Gaussian distribution. For the hopping of charges from one site to the other the states should show at least a weak overlap in energies as schematically illustrated in the inset of figure 2.5. This model of charge transport is often referred to as the Gaussian disorder model which considers the presence of a regular array of hopping sites as shown in figure 2.5. The charge transport mechanism is driven by the Boltzmann activation energy k_BT. The charges need to overcome this activation energy barrier in order to hop from one localized state to another via absorbing or emitting of a phonon. Therefore, the conductivity of the polymers increase at higher temperatures due to an increased availability of phonons. In the absence of any external energy, the charges hop towards low energy states until they get trapped finally. The trapped charge carriers can then again escape a trap with a Boltzmann activation of the traps. In addition to external energy, the crystallinity of the polymer significantly enhances the mobility of the charge carriers. Hence, for applications in photovoltaics, crystallinity of the conducting polymers involved is ensured by an annealing step before evaluating the device. Also, the operation of solar cells usually above

the room temperature is beneficial for hopping transport of the charge carriers within the conducting polymer.

2.2. Block copolymer-assisted sol-gel synthesis

Nanostructuring of inorganic metal oxide thin films is particularly interesting in the present work in order to implement them in solar cells. A high performance of these devices demands suitable length scales in the thin films of the order of tens of nanometers, which has been extensively concocted using various methods. A sol-gel route assisted with block copolymer templates for structure directing, to obtain the nanostructures of ZnO, TiO_2 and Zn_2TiO_4 is followed in the present thesis. The process is described in detail in section 2.2.1. The fundamental properties of the metal oxides, which are the main focus of the present study are then discussed in the subsequent subsections: Section 2.2.2 describes the basic properties of ZnO, Section 2.2.3 gives an overview of the fundamental properties related to the ternary compound Zn_2TiO_4.

2.2.1. Basic principles

Sol-gel synthesis is a solution-based wet chemical synthesis route, which has been classically introduced for the synthesis of inorganic metal oxides such as silica network and carbon based materials in a solution medium [25]. But lately, this technique has been extended for the development of nanostructures using functional inorganic metal oxide semiconductors such as TiO_2 and ZnO [15,26]. The sol-gel process is essentially a bottom-up method where a network of the given material is obtained from initial small molecules, which are generally the precursors for the desired material. Usually, metal alkoxides are used as precursors containing an organic group 'R'. These precursors react with the solvent and subsequently undergo chemical reaction, known as hydrolysis as depicted exemplarily for a ZnO precursor in equation 2.7:

$$(\mathrm{RCOO})\mathrm{Zn\text{-}OOCR} + \mathrm{H_2O} \overset{\text{hydrol.}}{\rightleftharpoons} (\mathrm{RCOO})\mathrm{Zn\text{-}OH} + \mathrm{RCOOH} \tag{2.7}$$

From the reaction, it should be noted that for the case of ZnO, a precursor containing an acetate group is used as described later in section 4.1. Similar reactions for other metal alkoxide precursors, for instance TiO_2, can be found in [27]. Via the hydrolysis reaction, nanoparticles are formed in the solution, thereby producing the so-called "sol". These hydrolyzed nanoparticles then cross-link with one another to form a three dimensional network in the solution, with tuneable pore size in the sub-micrometer range. The remaining solvent gets trapped in these pores, and a "gel" is thus obtained. The cross-linking of

the hydrolyzed nanoparticles is defined again by some chemical reactions, namely water and alcohol (acid in case of a precursors containing an acetate group) condensation as shown exemplarily for the ZnO system in equations 2.8 and 2.9.

$$\text{(RCOO)Zn-OH} + \text{HO-Zn(RCOO)} \overset{\text{cond. 1}}{\rightleftharpoons} \text{(RCOO)Zn-O-Zn(OOCR)} + \text{H}_2\text{O} \quad (2.8)$$

$$\text{(RCOO)Zn-OH} + \text{(RCOO)-Zn(RCOO)} \overset{\text{cond. 2}}{\rightleftharpoons} \text{(RCOO)Zn-O-Zn(OOCR)} + \text{RCOOH} \quad (2.9)$$

The hydrolysis and the condensation reactions 1 and 2 take place in equilibrium in the sol-gel solution. However, the rate of these reactions mostly depends on the size of the precursor molecules. Large molecules are shown to have slower reaction kinetics than the smaller molecules [28]. The pore size of the synthesized nanostructured network can be tuned by varying the concentration of the solution and the reaction temperature. It has been shown in literature that the presence of an acidic or a basic environment along with temperature and humidity also influence the reaction kinetics leading to formation of varied length scales in the nanostructured network [29].

However, the opportunities available by adapting the reaction environment to tune the length scales of the nanostructures are limited and the nanostructures obtained are often ill-defined. In order to produce more ordered nanostructures providing enhanced surface area in the final device, a copolymer is used as a template in combination with the sol-gel process. The simplest of the copolymers is a diblock copolymer, which is used for the present investigations. The specific class of diblock copolymers selected for the templates are amphiphilic in nature, which have a hydrophobic block covalently linked to a hydrophilic block. It has been shown that such copolymers undergo micro-phase separation if the product of degree of polymerization N and the interaction parameters χ of the two blocks $(\chi N) > 10.5$ (section 2.1.1). Due to the micro-phase separation, different morphologies are obtained such as spherical, cylinders, lamellas and gyroids structures (section 2.1.1). One of the most important requirements that the chosen diblock copolymer template needs to fulfill is the selectivity of one of the blocks towards the metal oxide precursor nanoparticles.

In order to access the above-mentioned morphologies in solution, a suitable pair of solvents is used. A non-selective solvent, commonly known as the “good” solvent, is used to dissolve both the blocks of the copolymer, whereas, a selective solvent, commonly termed as “poor” solvent, is used to dissolve only one of the blocks (the hydrophilic block for the present cases). The addition of the polymer in the “good-poor” solvent pair results in the onset of a series of complex thermodynamic processes. As a result of these processes, micelles are formed in the solution. This happens because one of the blocks (the hydrophobic block for the presented investigations) tends to minimize its interface with

the surrounding solvent environment due to the presence of the selective solvent in the solution. Thus, it forms the micellar core. The other block still remains hydrophilic and thereby, extends from the core to the solvent environment, forming the micellar corona. This phase separation at a nanoscale is used in the present study for nanostructuring metal oxides in the present study. Depending on the weight fractions of the solvent systems, micelles of different sizes are obtained, which can also undergo fusion and separation with one another. In order to synthesize varied morphologies of zinc oxide and zinc orthotitanate using the phase-separated polymeric solution, the precursor sol is added to the system. For the copolymer templates used in the present thesis, the hydrophilic blocks preferentially host the precursor nanoparticles via hydrogen bonds in combination with electrostatic and van-der-Waals interactions. The presence of the precursor nanoparticles in one of the polymer blocks in turn, results in its selective swelling. Additional processes such as formation of the metal oxide colloids begins and the nanoparticles incorporated in different micelles also tend to cross-link with one another. The selective swelling of one of the blocks of the micelles also influences the mechanism of interaction of the micelles forming different equilibrium conditions in the system. This leads to formation of various metastable structures in the solution, which on deposition on a substrate get arrested resulting in unique morphologies. Hence, a high degree of control of the length scales can be achieved by selecting certain block lengths of the polymer as well as the weight fraction of the solvents and the precursor used in the process. Additionally, pH and reaction environment provide enhanced flexibility to manipulate the length scales derived in the system.

In addition to all the thermodynamic and kinetic processes occurring in the solution, the structural rearrangements during and after deposition of the solution on substrates via different depositions methods (section 4.2.2) can also contribute in deciding the final morphology of the film. This is based on the equilibration of the rearrangement processes on the film after deposition with respect to the drying time provided by a particular method. Mainly two opposing processes play major role in modifying the final film morphology, one being the cross-linking tendency among the colloidal nanoparticles and the other being the interaction among the polymer molecules. In case, the former process is more favored, a less ordered morphology is obtained. Contrarily, for the later case, the morphology is mainly driven by the polymeric rearrangements, resulting in more ordered architectures. These interactions also depend on the size of the nanoparticles as well as their concentration. A very high concentration of the nanoparticles results in even distribution of the material in the polymeric matrix, whereas, for smaller amounts, the mobility is enhanced, which finally results in the formation of large aggregates in the final films [27].

After the deposition of the sol-gel solution, the ZnO-polymer hybrid film can be further treated with solvent vapor or other external stimuli depending on the copolymer template used. If the template is sensitive towards external perturbations, further structural arrangements can be promoted in the morphologies obtained. Additionally, a high temperature treatment can be applied to the films in order to combust the polymeric scaffold, leaving behind the pure metal oxide nanostructure. Typical temperatures used for calcination is 400 °C. The polymer template and the unreacted residues are known to be eliminated from the system at even a lower temperature, however, this high temperature treatment is required in order to impart crystallinity to the metal oxides. This largely depends on the precursor used, the size of the precursor molecules and the polymer system used. For certain precursor of titania, such as ethylene glycol-modified titanate (EGMT), room temperature is enough to attain crystallinity. Hence, in such cases, different routes to remove the polymer template are used such as extraction via UV light or by solvent extraction [30]. Any of these methods for removal of the template from the system might also result in modification of surface properties of the films or a change in the overall morphology due to the shrinkage of the material left after removal of the polymer matrix, usually known as pattern collapse [31].

A high degree of control over the length scales and the morphology of the metal oxide thin films is established by using the template-assisted sol-gel route. Variation of block lengths of a certain polymer and the surrounding solvent environment along with the precursor concentration can be employed to design a specific morphology or to maneuver the length scales of a desired morphology. Being a solution-based approach, this technique also has the additional flexibility to be deposited via a large number of methods such as via spin-coating, solution-casting, blade-coating and spray deposition, as explored in the present thesis. Furthermore, this synthesis route can be extended to other systems and also to achieve hierarchical structuring routes by multiple coating of one or different metal oxide layers on the same substrate [32, 33].

2.2.2. Zinc oxide properties

Zinc oxide (ZnO) is a II-VI compound which exists in different modifications. Along with amorphous ZnO, two commonly known crystalline phases exist: Wurtzite and zincblende. Wurtzite is thermodynamically the most stable phase occurring under ambient conditions. In addition to this, zincblende structures can be stabilized by growing them on substrates with cubic lattice, whereas, under high pressures (about 10 GPa), ZnO is converted to rocksalt motif. Since wurtzite is the most commonly obtained phase, this particular crystalline phase is considered for further discussion in the following. The crystalline

structure of wurtzite phase is shown in figure 2.6. The hexagonal wurtzite phase is composed of Zn^{2+} and O^{2-} ions with tetrahedral arrangements with each anion being surrounded by four cations and vice versa. Although the Zn-O bond is sometimes referred to as the covalent bond, a considerable degree of polarity is present due to the high electronegativity of the oxygen atom. This high polarity of the bond is reported to be favorable for the formation of wurtzite phase over zincblende [34]. Additionally, the strong binding energy results in high thermal stability of the material. In the wurtzite crystalline matrix, the neighboring tetrahedrons form bilayers of Zn and O atoms as shown in the figure 2.6. Table 2.2 lists the corresponding Bragg reflexes in section 2.4.1.

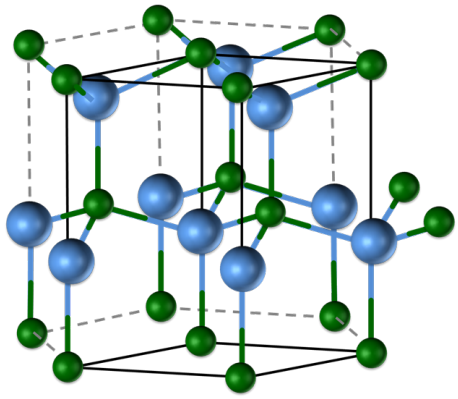

Figure 2.6: Crystal structure of wurtzite ZnO. The spheres in blue and green represent oxygen and zinc atoms, respectively. The structure is adapted from [34].

The wurtzite phase exhibits a direct and wide band gap of 3.37 eV at room temperature, due to which, ZnO shows good absorption in the UV spectral region [34]. This property of ZnO is very useful in using it as UV filters in nano electronic devices such as hybrid solar cells, where the ZnO film protects the sensitive polymer from degradation via UV irradiation. ZnO is also incorporated in several sun protection creams to protect human skin from UV. The absorption increases for wavelengths less than 368 nm. ZnO is thus transparent to the visible light and shows a high refractive index of 2.0041 [35]. Some of the important properties of bulk ZnO is listed in table 2.1.

band gap energy	3.2-3.5 eV
exciton binding energy	59-63 meV
density	5.606 g cm^{-3}
bond length	1.99 Å

Table 2.1.: Fundamental properties of wurtzite ZnO taken from reference [36].

The crystallinity of ZnO is a crucial aspect in terms of conductivity of the charges. Even in the absence of any dopants, wurtzite ZnO almost always shows n-type behavior. In spite of this fact, the use of ZnO as a semiconductor in electronic devices is limited by the lack

of control over its electrical conductivity. Although lot of speculations have been made regarding the origin of conductivity in ZnO, the recent state-of-the-art density functional theory (DFT) calculations have attributed the origin of n-type conductivity in ZnO to the presence of point defects in the crystalline structure. Various native defects are identified in crystalline ZnO phase such as oxygen and zinc vacancies, zinc and oxygen interstitials as well as zinc and oxygen antisites. In short, oxygen vacancies are deep donors and cannot explain the n-type conductivity. Zinc interstitials and zinc antisites are shallow donors, but have high formation energies under n-type conditions. Also, they are fast diffusers which make them relatively unstable to sustain in the system as point defects. Oxygen interstitials also exist in significant concentration and act as deep acceptors, but have high formation energies. Oxygen antisites have the highest formation energies among acceptor-type native point defects and are present in very small concentration. The presence of all the above-mentioned point defects however, cannot satisfactorily explain the native n-type conductivity of ZnO. But there are additional defects present having a low formation energy such as the zinc vacancies, which can contribute towards n-type conductivity and are often observed to be the source of green luminescence in ZnO. Unintentional incorporation of impurities in the crystalline structure of ZnO also acts as shallow donors. For certain cases, DFT calculations have shown the presence of interstitial hydrogen (H) atoms, which can be incorporated during most of the growth processes for the crystalline phase. However, interstitial H is highly mobile which fails to explain the stability of n-type conductivity in ZnO at elevated temperatures. With more extensive research, it is shown that substitutional H atoms are also present in the crystalline matrix, which explains the high temperature stability of electrical conductivity of the material. Further details about the point defects and tuning of conductivity of ZnO is provided in reference [37].

The electron mobility in the compound involves transport in the conduction band and strongly varies with temperature and has its maximum at 80 K with a maximum reported value of 2100 $cm^2\ V^{-1}\ s^{-1}$ [38], which reduces to 200 $cm^2\ V^{-1}\ s^{-1}$ at room temperature. For temperatures below 40 K, hopping conduction involving mixed bands is reported [38]. It has been shown that ZnO nanoparticles of size in the range of 60 nm show electrical conductivity in the range of 2×10^{-6} to 2×10^{-4} S cm^{-1} at 400 to 600 °C [39]. For nanostructured thin films, the grain boundaries play an important role in deciding the electrical conductivity. An accumulation of the charge carriers at the grain boundaries results in the trapping of these charges, thereby decreasing their mobility. However, a multiple-trapping-and-release model has also been proposed facilitating inter-grain charge transport in ZnO nanostructures [40].

2.2.3. Zinc titanate properties

Zinc titanate exists in five different crystalline forms, namely zinc orthotitanate (Zn_2TiO_4), zinc metatitanate ($ZnTiO_3$), $Zn_3Ti_2O_7$, $ZnTi_3O_7$ and $Zn_4Ti_5O_{14}$ [41]. Out of these, only three modifications are widely reported based on their relative thermodynamic stability: Zn_2TiO_4, $ZnTiO_3$ and $Zn_2Ti_3O_8$. For the present thesis, Zn_2TiO_4 is the material of choice due to the wide range of applications provided by the material. Zn_2TiO_4 is studied as a complementary system to zinc oxide in the present work. They have been largely used in white color pigments, as photocatalysts and majorly as sorbents for the desulfurization of hot coal gases [42]. The corresponding Bragg reflexes of Zn_2TiO_4 is given in table 2.2 in section 2.4.1.

Zn_2TiO_4 has an inverse spinel structure with a lattice constant of 8.48 Å. Such a structure is described by 56 atoms in the unit cell. This complex crystal structure can be found in reference [43]. In this unit cell, 32 oxygen atoms comprise an face-centered cubic (fcc) lattice. This lattice is then associated with interstitial tetrahedral and octahedral sites. One oxygen atom is bonded to four cations: One Zn atom in terahedral condition and three Ti atoms in octahedral conditions. It is a direct band gap semiconductor showing n-type conductivity [43, 44]. For the synthesis of Zn_2TiO_4, a typical high temperature of 600 °C is required as reported in [45]. For lower temperatures, often some metastable phases of zinc titanate are obtained along with Zn_2TiO_4. A series of band gaps have been calculated for the material for different synthesis methods and different amounts of ZnO and TiO_2 used as the starting materials. The variation in the band gap energy also results from the different calculation methods used and the range reported extends between 3.18 and 5.0 eV [46–48]. On the basis of density of states calculations, the same has been derived as 4.0 eV [46]. Zn_2TiO_4 is transparent in the visible to infrared region (360 to 1000 nm) and absorbs highly in the UV region ($<$ 360 nm). Zn_2TiO_4 has a refractive index of 1.8, which is lower than both ZnO and TiO_2 [46]. The typical bond lengths calculated from density of states calculations for Zn-O, Ti-O and Zn-Ti bonds are 2.12, 1.83 and 3.51 Å, respectively [46]. Although the electrical conductivity of the material is not reported, a decreases in the resistivity is observed with increasing ZnO content in the system [49].

2.3. Solar cells

The photovoltaic devices have derived their name from the photovoltaic effect which describes the conversion of light (photon) to electrical energy (voltage) [50]. Photovoltaic cells, commonly known as solar cells, function on the basis of certain fundamental pro-

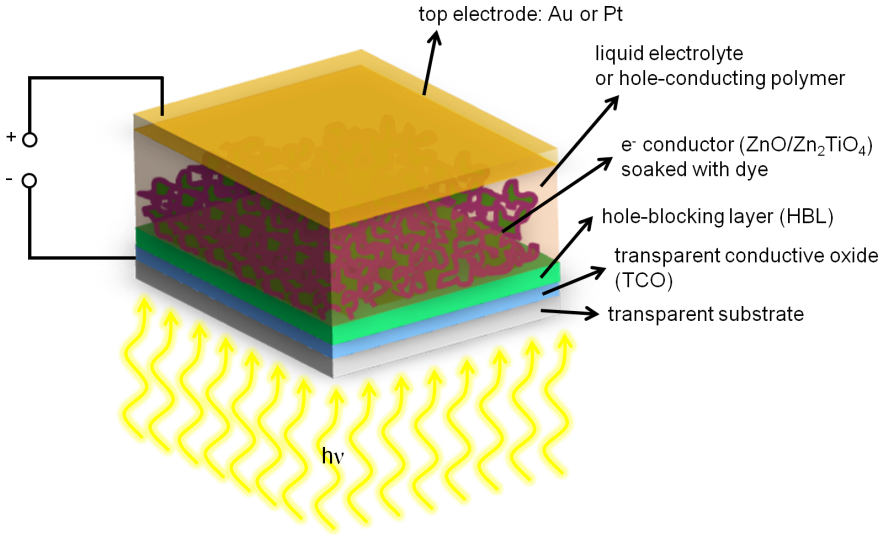

Figure 2.7.: Schematic representation of the basic set up of a dye-sensitized solar cell. Light enters through the glass substrate coated with a transparent conductive oxide and gets absorbed in the dye. The charges generated are transported to the bottom and the top electrodes where they are extracted.

cesses namely, light (from sun consisting of UV, IR and visible wavelengths) absorption, generation of free charge carriers and transport of the charge carriers to the two electrodes, defining the top and bottom contacts of a typical sandwich architecture of the solar cells discussed in this work. The solar cells fabricated for the presented investigations are classified in the category of dye-sensitized solar cells (DSSCs). In general, a common difference of the DSSCs, hybrid and the organic solar cells from the conventional silicon solar cells lies in the fact that the above-mentioned processes occur in different materials comprising the active layer of the cell rather than in one single layer as in the silicon solar cells. A basic set up of a DSSC is shown in figure 2.7.

DSSCs studied in the present work are based on ZnO as the electron-conducting part of the active layer as shown in figure 2.7. ZnO is soaked with a sensitizing dye which is responsible for the absorption of visible spectrum of light. The ZnO film is nanostructured in order to increase the effective surface area for dye adsorption as well as to provide suitable length scales for diffusion of charges. Different materials are then incorporated into the nanostructured ZnO network soaked with dye. For the conventional DSSCs, a liquid electrolyte is used and the resulting solar cells are referred to as liquid electrolyte-based dye-sensitized solar cells (section 2.3.1). The second type of DSSC that are studied are the so-called solid-state dye-sensitized solar cells, abbreviated as ss-DSSCs (section 2.3.2). A conducting polymer is used for the transport of holes in ss-DSSCs. The main processes involved for the functioning of DSSCs follow different mechanisms for the

two classes and are therefore described separately. Thus, ZnO, dye and the conducting polymer/electrolyte compose the active layer of a DSSC. For both types of DSSCs, a transparent conductive oxide such as fluorine-doped tin oxide layer (FTO) coated on glass is used as the cathode. At this electrode, the extraction of the electron takes place due to which a low work function of the material is required. A metal electrode is used as the top contact (see figure 2.7) which is beneficial for the extraction of holes and hence, a higher work function of the electrode material is necessary. This is also important to ensure the blocking of electrons at the top electrode. The charges extracted are combined via an external circuit (figure 2.7).

2.3.1. Liquid electrolyte-based dye-sensitized solar cells

The functioning of a liquid electrolyte-based DSSC fundamentally lies on conversion of solar energy to electrical energy via the photo-induced injection of electrons from the excited dye molecules to the metal oxide semiconductor [50]. A redox mediator ensures continuous regeneration of the dye molecules in a cyclic process. The catalytically active platinum particles used as the top electrode efficiently reduce oxidized redox species in the electrolyte. Initially Tsubomura et al. have sensitized porous ZnO, attaining a power conversion efficiency of 1.5 % [51]. With the advent of different dyes and electrolytes along with improvement in the surface area and film thickness of the inorganic metal oxide, the degree of dye adsorption is improved, thereby lifting the power conversion efficiency for a TiO_2-based DSSC as high as 12 % till the present day [12]. Liquid electrolyte-based DSSCs are primarily investigated in the present thesis and hence, the functioning of the device is discussed in detail in the following paragraphs.

Absorption, electron injection and regeneration of the oxidized dye

In DSSCs, the absorption of the incoming light occurs in the dye monolayer covering the nanostructured ZnO surface. However, for the light to get absorbed, the energy of the incident photons must be equal or more to the energy gap between the ground state (D) and excited state of the dye (D^*). This can be represented as

$$E = \frac{hc}{\lambda} \geqslant \triangle E_{gap}. \tag{2.10}$$

The working mechanism and the on-going kinetics in an electrolyte-based DSSC, depending on the time scales of their occurrence, is represented in figure 2.8. All the reactions taking place for an efficient functioning of the device are listed as follows:

$$D + h\nu \longrightarrow D^* \qquad \text{photoexcitation} \qquad (2.11)$$

$$D^* \longrightarrow D^+ + e^-_{ZnO} \qquad \text{charge injection} \qquad (2.12)$$

$$D^+ + I^- \longrightarrow (D \cdots I) \qquad \text{complex formation} \qquad (2.13)$$

$$(D \cdots I) + I^- \longrightarrow D + I_2^{\bullet -} \qquad \text{dye regeneration} \qquad (2.14)$$

$$2I_2^{\bullet -} \longrightarrow I_3^- + I^- \qquad \text{disproportionation} \qquad (2.15)$$

$$I_3^- + 2e^- \longrightarrow 3I^- \qquad \text{electrolyte regeneration} \qquad (2.16)$$

$$D^* \longrightarrow D \qquad \text{dye relaxation} \qquad (2.17)$$

$$D^+ + e^-_{ZnO} \longrightarrow D \qquad \text{recombination via dye} \qquad (2.18)$$

$$2e^-_{ZnO} + I_3^- \longrightarrow 3I^- \qquad \text{recombination via electrolyte} \qquad (2.19)$$

The absorption of sunlight by the dye molecules follow the Franck Condon principle, stated in [52,53]. After absorbing a photon, the dye evolves to a singlet excited state from the singlet ground state within a time scale of 10^{-15} s (reaction 2.11). Internal conversion in the singlet excited state may occur with a typical time of 10^{-14} to 10^{-13} s. Relaxation of the dye molecule from a singlet excited state to the ground state can occur via radiative fluorescence with a time range of 10^{-9} to 10^{-5} s (reaction 2.17). Additionally, intersystem crossing of the excited singlet state to a triplet state also occurs which happens in 10^{-6} s. Relaxation of the excited triplet state to the ground state is a slow process and can occur with radiative phosphorescence in 10^{-5} to 10^{-3} s (figure 2.8). Apart from the radiative decays, several internal radiationless conversions are also possible [54]. D^* injects an electron to the conduction band (E_C) of the inorganic semiconductor (ZnO in the present case) within 10^{-15} to 10^{-12} s time scale (reaction 2.12). The transport of the charges should be a quicker process as compared to the radiative and non-radiative recombinations in the dye molecules in order to ensure maximum charge generation and injection. After charge injection, the oxidized dye (D^+) is reduced via formation of a $(D \cdots I)$ complex by iodide present in the liquid electrolyte (reaction 2.13). Quantum chemical calculations have shown that formation of such complexes is energetically stable and depends on the electrolyte used. Also, formation of such complexes has been reported for ruthenium-based sensitizers. The complex dissociates upon interaction with a second iodide ion to the ground state of the dye and a diiodide ion (reaction 2.14) in the range of a few microseconds. The regeneration of the dye is mostly a faster process as compared to the electron injection to ZnO. Two diiodide ions on the other hand can interact to produce a triiodide and an iodide ion as shown by the disproportionation reaction 2.15.

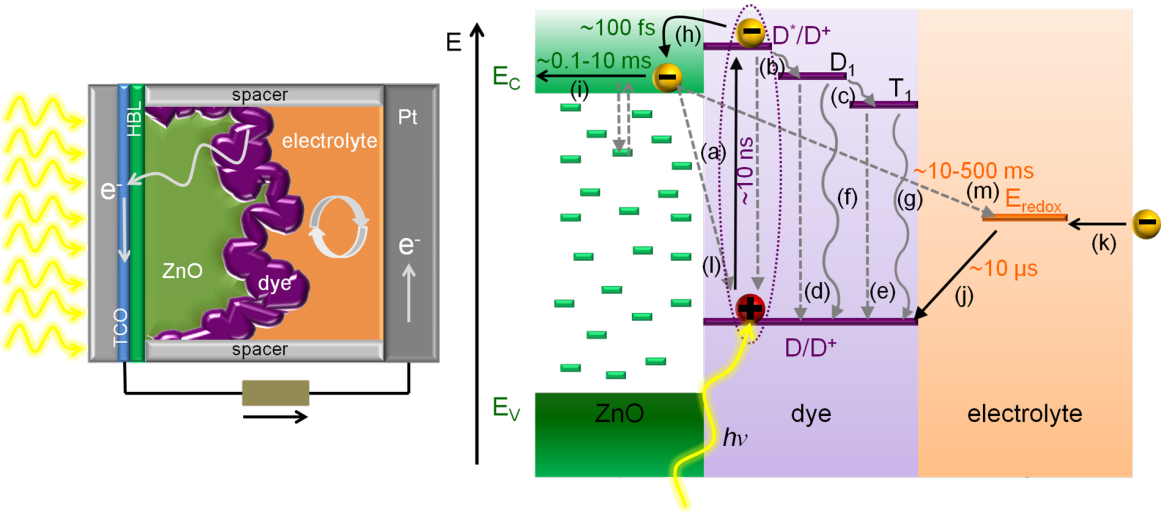

Figure 2.8.: The left image represents the cross-section of a typical electrolyte-based DSSC as shown in figure 2.7. The active layer (ZnO + dye) along with the the electrolyte is sandwiched between the TCO substrate and the platinum (Pt) electrode. The image on the right is a detailed energy diagram of the electrolyte-based DSSC showing different kinetic processes occurring in the cell with different time scales. The major processes are indicated by black solid arrows, the recombination processes by dashed gray arrows and the wavy gray arrows represent radiationless decay. Absorption of $h\nu$ by the dye (a) leads to formation of excited singlet (D^*/D^+ and D_1) and excited triplet (T_1) states in the dye. Internal conversions (b) or inter-system crossing (c) are possible leading to fluorescence (d) and phosphorescence (e). Internal or external radiationless conversions are indicated by (f & g). The injection of the electron to the conduction band (E_C) of ZnO (h) is followed by diffusion of the charges (i). The energy states between the valence band (E_V) and conduction band (E_C) of ZnO is populated by trap states. The dye regeneration and electrolyte regeneration are shown by (j) & (k), respectively. The recombination processes via dye and electrolyte are marked as (l) & (m), respectively.

The triiodide formed then gets reduced at the platinum electrode and the electrolyte is regenerated as shown by the reaction 2.16.

Electron transport and recombination reactions

Unlike in the organic or the hybrid solar cells, the excited charges in the dye are generated in the vicinity of ZnO (since there is ideally only a monolayer of dye adsorbed on ZnO). Hence, the separated charges are injected to ZnO via electron transfer. This electron transfer from dye to ZnO is basically visualized as a tunneling process described by Gerischer [55]. The sharp Franck Condon energy levels in the dye molecules are assumed

to have a Gaussian distribution in Gerischer's model. A schematic representation of the model is provided in figure 2.9.

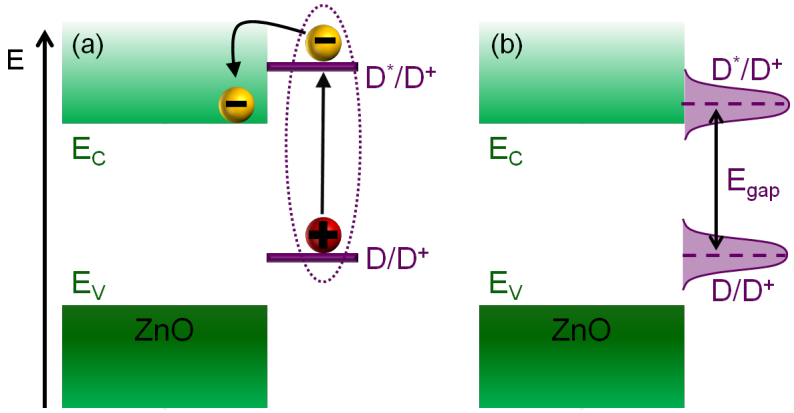

Figure 2.9.: Electron transfer and Gerischer's model in a DSSC. (a) The conduction (E_C) and valence (E_V) band of ZnO as well as the ground (D/D^+) and the excited (D^*/D^+) state of the dye are shown. Upon absorption of photon, the dye molecules are excited and the bound electron-hole pair is formed as outlined by the dashed ellipse, which in turn is dissociated when the electron is transferred from the excited state of dye to the E_C of ZnO. (b) According to Gerischer's model, the ground and the excited states of the dye have a Gaussian distribution and an electron transfer to E_C of ZnO only occurs due to the presence of an overlap as shown. The transfer of charge from E_V to the ground state of dye is not possible due to the missing overlap.

According to this model, the charge transfer from the occupied donor level to the empty acceptor level only occurs when there is an overlap of the donor and acceptor energy levels. The distribution of the energy levels $W_{don}(E)$ for the dye molecules can be written as

$$W_{don}(E) = \frac{1}{\sqrt{4\pi k_B T L_{don}}} \exp\left(-\frac{(E - E_{don})^2}{4k_B T L_{don}}\right), \tag{2.20}$$

with the reorganization energy L_{don} and the most probable electron transfer energy E_{don}. T and k_B are the temperature and the Boltzmann constant, respectively, describing the thermal energy fluctuations. Since light is absorbed by the dye molecules, charge transfer from the occupied excited state of the dye to the vacant conduction band (E_C) of ZnO is fulfilled according to Gerischer's model. In case of a successful overlap of the energy states of the excited dye and ZnO, as shown in figure 2.9(b), the rate of charge transfer can be written as

$$j_{don} = B_{don} c_{don} \int_{-\infty}^{\infty} \chi_{don}(E) W_{don}(E) D_{vac}(E) dE, \tag{2.21}$$

where B_{don} are all energy independent factors, c_{don} is the electron concentration, χ_{don} the transfer probability, and D_{vac} the vacant electron states in zinc oxide. To some extent, the overlap of the energy states is governed by the interaction of the dye molecules with the semiconductor. In the present case, the polar surface of ZnO helps the dye to adhere in an efficient way.

For efficient charge extraction, it is extremely necessary to prevent the electron back transfer from the valence band E_V of ZnO to the ground state of the dye. This is beneficial while using wide band gap semiconductors such as ZnO, TiO_2 or Zn_2TiO_4 as the electron conductor, which have a valence band at a considerably lower energy compared to that of the ground state of the dye. Among various factors limiting the performance of DSSCs, the principle contribution is by the overpotential at the ZnO/dye interface, lowering the open-circuit voltage of a DSSC. This inherent overpotential comes from the difference in the mean energy level E_{don} of the dye with the conduction band of ZnO. The former is required to be higher than the latter, in order to ensure an overlap of the energy states for the charge transfer. This inherently results in an overpotential, which cannot be avoided for the functioning of a DSSC. However, this can be reduced and theoretically it has been predicted to boost up the efficiency of a DSSC to as high as 20 % with a reduction in overpotential by 0.4 eV [56]. A particular feature of charge transfer in ZnO involves the trapping and detrapping events within the band gap of the material. Various defects contributing to the trap states (see section 2.2.2) are observed via several time-dependent methods. This might result in heterogeneity of the films, thereby affecting the final performance. These trap states are schematically shown in figure 2.8 between the E_V and E_C of ZnO. Additionally, another common problem hindering the lifetime of the devices is the bleaching of the dye with time and the corrosive nature of the liquid electrolyte used. Search for more stable and environment-friendly materials in these directions is still on-going. The thickness of the ZnO film as well as the dye loading have also shown remarkable influence on the performance of the device. On one hand, an excessive loading of dye for thinner films leads to aggregation of dye molecules hindering electron transfer to the conduction band of ZnO, whereas on the other, an optimum film thickness (in the range of 16 to 20 µm) is required to adsorb sufficient dye for efficient light harvesting. However, an increase in the film thickness also contributes towards more recombination pathways [57].

The undesired recombination reactions are the main sources for the loss mechanisms in DSSCs. Among many recombination pathways, two routes, as represented by reactions 2.18 and 2.19, are particularly harmful for the device performance. The relaxation of the excited state of the dye before charge injection is also observed in some cases. However, for the present investigations, a dye with a high molar extinction coefficient is used as

detailed in section 4.1. Recombination of the injected electrons in the conduction band of ZnO with the triiodide ions depends on the I_3^- concentration in the electrolyte, which hampers the open-circuit voltage [58]. Finally, for long exposure times of the DSSC to light enhances the absorption of UV light by ZnO, thereby forming electron-hole pairs. The reaction of the hole with I_3^- has been reported to deplete the concentration of I_3^-. This scenario can be prevented by installing UV filters during measurements and final functioning of the devices. It should be noted that the working principle and the kinetics discussed for an electrolyte-based DSSC with ZnO as the acceptor material, are also valid when ZnO is replaced by Zn_2TiO_4 (as discussed in results chapter 8).

2.3.2. Solid-state dye-sensitized solar cells

Mainly due to leakage and corrosion problems produced by the electrolyte-based DSSCs, several attempts have been made in order to replace the liquid electrolyte with polymer electrolytes, ionic liquids with high viscosity, p-type semiconductors such as CuI and CuSCN and organic hole conductors [59]. In the present thesis a conducting polymer, namely P3HT is used to investigate the performance of solid-state DSSCs (ss-DSSCs) with ZnO as the electron conductor. The highest power conversion efficiency of around 10 % is reported recently for ss-DSSCs [60]. The fundamental processes occurring in the device such as light absorption, charge injection and dye regeneration are similar to the electrolyte-based DSSCs. Only the transport of the charges in P3HT follows a different mechanism, which is exclusively detailed in section 2.1.2.

Working mechanism and challenges

A schematic representation of the basic processes taking place during the functioning of an ss-DSSC is shown in figure 2.10. The hole is directly injected from the dye to the conducting polymer and transported to the electrode via hopping transport mechanism (refer to section 2.1.2). The most crucial parameter in designing an efficient ss-DSSC is proper filling of the hole conductor into the nanostructured film of ZnO to form an inter-percolating network. Since, the conducting polymers consist of large molecules, the length scales present in the ZnO film is even more critical as compared to the electrolyte-based DSSCs and hence, requires a careful tailoring. The main problem faced by the porous morphology of ZnO is the trapped air within the structures, which prevents the hole-conducting material to be incorporated into the scaffold of ZnO. This area of research is still under heavy investigations in order to establish proper filling of the pores. Some of the promising methods reported so far include pre-soaking of the nanostructures in a solvent bath in order to get rid of the air inclusions, before filling the conducting polymer,

direct polymerization of the monomers within the structures, vacuum backfilling of the conducting polymer or attaching similar functional groups to the dye molecules as in the conducting-polymer in order to improve connections at the dye/hole conductor interface. The first strategy has been proven to be an effective way to incorporate P3HT in titania nanostructures resulting in a degree of backfilling as high as 84 % [61]. Hence, the pre-soaking route is also tested in the present thesis for ZnO nanostructures.

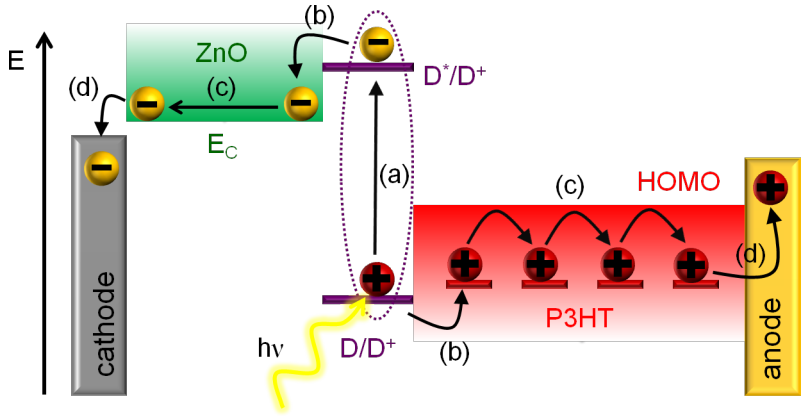

Figure 2.10.: Schematic representation of the electron transfer processes in an ss-DSSC (band bending is omitted). Absorption of $h\nu$ leads to the formation of the electron-hole pair in the excited dye (a) which gets dissociated and the charges are transferred to the E_C of ZnO and HOMO of P3HT (b). The transport of free charge carriers to the electrodes is shown by (c). The charges are finally extracted at the respective electrodes (d).

Photoexcitation of the charges occurs in the dye monolayer leading to the formation of the electron-hole pair, commonly known as an exciton. ss-DSSCS are very prone to recombination reactions from the separated charges because of close proximity of electrons and holes throughout the network. This provides negligible potential barriers at the ZnO/dye and dye/P3HT interfaces. Therefore, the open-circuit voltage and the fill factor are typically reduced for ss-DSSCs. To prevent this reaction, often co-adsorbents are added to the dye to create an insulating layer [62]. In order to further suppress the recombination reactions, blocking layers are used at both electrodes. The recombination of the injected electrons from ZnO with the holes in the dye is almost negligible due to subsequent injection of the holes into P3HT within nanosecond time scale. An optimum active layer thickness of 2 µm is reported for ss-DSSCs [63]. The theoretical maximum power conversion efficiency, as decided by the overpotential from the overlap of the energy states, is estimated to be 23 % [64].

2.4. Scattering basics

In contrast to real-space imaging techniques, x-ray scattering methods are used to probe a larger area of the samples and to obtain statistically relevant information about the crystallinity and structural length scales present in the volume of the thin films. In order to serve the purpose, diffraction and grazing incidence small angle scattering measurements are performed using elastic x-ray scattering methods, where the energies of the incoming (E_i) and the final (E_f) x-ray beam are the same. General aspects of x-ray scattering methods are discussed in the present section followed by the detailed description of x-ray diffraction in section 2.4.1 and grazing incidence small angle x-ray scattering in section 2.4.2.

Scattering contrast and general definitions

The principle necessity for a scattering event to occur is a change in the refractive index (n) of the medium of propagation of the electromagnetic wave. For x-rays, the refractive index is slightly less than unity and is represented as

$$n = 1 - \delta + i\beta, \tag{2.22}$$

where δ is the dispersive part and β denotes the absorbing part. Both δ and β depend on the wavelength λ and can be written as

$$\delta = \frac{\lambda^2}{2\pi}\rho, \tag{2.23}$$

$$\beta = \frac{\lambda}{4\pi}\mu, \tag{2.24}$$

for the case of a homogeneous medium and far away from absorption edges. $\rho = r_e\rho_e$ represents the scattering length density (SLD) of the medium and μ denotes the absorption coefficient. The SLD depends on the electron density (ρ_e) of the material under investigation, the classical electron radius $r_e = 2.814 \cdot 10^{-5}$ Å, being a constant [65]. Typically, for x-rays δ is of the order of 10^{-6} and $\beta \approx 10^{-7}$. Scattering experiments with x-rays depend on the difference in scattering length density (electron density) of the investigated materials. This difference is commonly termed as scattering contrast.

After interaction of the x-rays with the samples, specular and diffuse scattering are observed. These two scenarios are presented in figures 2.11(a) and (b). Under specular conditions, the incident x-ray beam $\vec{k_i}$ impinges the sample under an angle α_i[1] and the

[1] In x-ray scattering literature, the angles are generally measured towards the surface and not with respect to the surface normal, as it is known from optics literature.

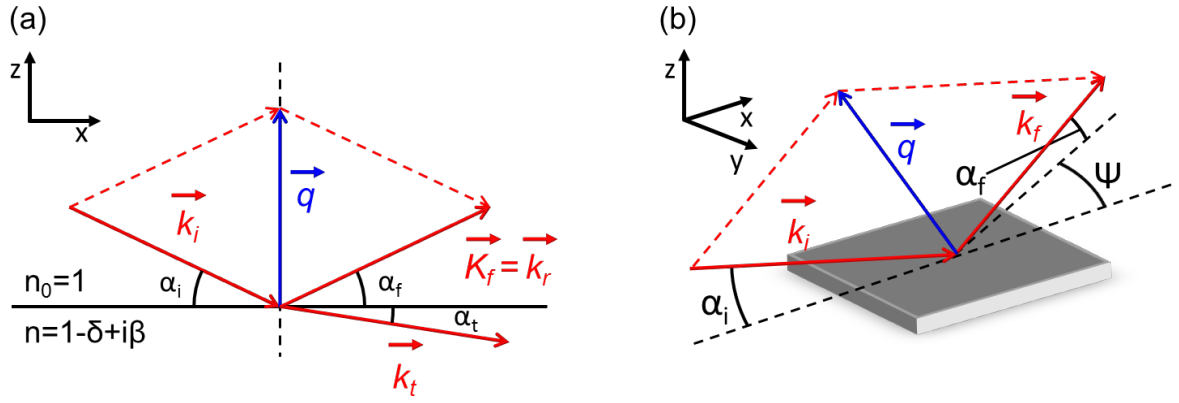

Figure 2.11.: Basic definitions of directions and angles for (a) specular scattering and (b) diffuse scattering geometries.

reflected beam $\vec{k_i}$ exits the sample under a final angle of α_f which is equal to α_i. The reflected beam stays in the xz-plane as shown in figure 2.11(a). The momentum transfer of the scattered beam is given by the scattering vector $\vec{q}$ as

$$\vec{q} = \vec{k_f} - \vec{k_i}. \tag{2.25}$$

For the x-rays with wavelength λ, the modulus of the wavevector is $k = 2\pi/\lambda$. For diffuse scattering, the scattered beam is not restricted to the xz-plane, but also extends in the xy-plane with the additional scattering angle of ψ. Snell's law of refraction is applied to the x-rays as

$$\cos(\alpha_i) = n\cos(\alpha_t), \tag{2.26}$$

with the transmitted wave $\vec{k_t}$ at the exit angle α_t. As dispersion $\delta > 1$, the refractive index of x-rays $n < 1$. As a result, air comprises the material of higher refractive index. With $\alpha_t = 0$, there is an angle of total external reflection when the beam travels from air to the material. Under small angle approximations, this determines the critical angle of the material α_c

$$\alpha_c = \alpha_i \approx \sqrt{2\delta} = \lambda\sqrt{\frac{\rho}{\pi}}, \tag{2.27}$$

where ρ is the scattering length density of the material for x-rays. Due to total external reflection, α_i has a significant impact on the penetration depth of the x-ray beam into the material. For $\alpha_i \leqslant \alpha_c$, the evanescent waves of the x-rays only partly penetrates the sample. The penetration depth of the x-rays denotes the depth at which the intensity of the x-ray beam is damped to 1/e of the original intensity. The scattering depth Λ of the beam on the other hand is approximated to be half of the penetration depth [66] as the scattered beam experiences damping again on its way from the scattering event to the surface. For $\alpha_i < \alpha_c$, the scattering depth is of the order of 50 Å, which increases to the order of several hundreds of nanometers for $\alpha_i > \alpha_c$.

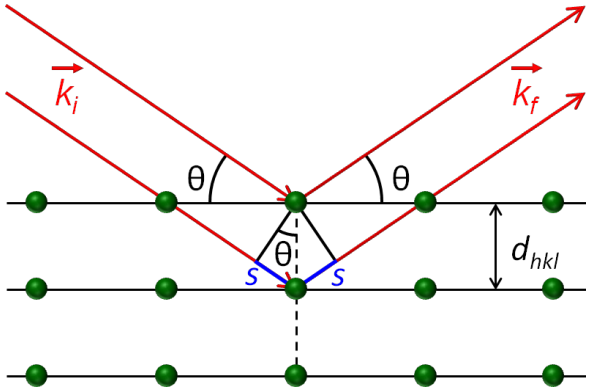

Figure 2.12: Graphical illustration of the Bragg equation. The incoming x-ray beam $\vec{k_i}$ is scattered at the electron clouds (green) of the atoms, placed on the lattice planes of the crystal structure with a characteristic spacing of d_{hkl}. X-rays which are scattered on lower lattice planes have to travel increased path lengths, as indicated by the blue lines S, which depends on the angle θ.

2.4.1. X-ray diffraction

In order to investigate the crystal structure of the samples, x-ray diffraction is used. The ordered crystalline structure of the material under investigation on atomic length scales is revealed via this method. Different lattice planes in a crystal act as a periodic grating, which is used to scatter a monochromatic x-ray beam since the lattice dimension is similar to the wavelength of the x-rays. In principle, the scattered intensity depends on the interaction of the x-ray beam with the electrons present around the atoms of the crystal as well as the position of those atoms in the lattice. Therefore, every sample provides a unique scattering data which is representative of the crystalline phases of the material present in the sample.

Figure 2.12 shows the diffraction of parallel x-ray beams at different lattice planes in a crystal. The scattered x-rays interfere and produce maximum in intensity when the Bragg condition is fulfilled. The nature of the interference, i.e., constructive or destructive, depends on the path difference S of the two beams based on the incident angle θ. The maximum in the scattered intensity obtained for constructive interference is defined by the Bragg's equation [67]

$$2d_{hkl}\sin(\theta) = n\lambda, \tag{2.28}$$

where d_{hkl} is the lattice spacing of the crystal structure and λ the x-ray wavelength. Bragg reflexes along with the relative intensities of the peaks of wurtzite zinc oxide (ZnO), zinc orthotitanate (Zn_2TiO_4) and anatase titania (TiO_2) are listed in table 2.2. Polycrystalline samples show an isotropic scattering signal, often referred to as powder diffraction, where the crystals are oriented randomly in all directions. The nanostructured films of ZnO, TiO_2 and Zn_2TiO_4 studied in this thesis, also show random orientation of crystals in thin films thereby giving rise to rings of scattered intensity known as the Debye-Scherrer rings,

	crystal order	2θ (λ_{Cu})	q [nm^{-1}]	rel. intensity
wurtzite	(100)	31.8°	22.34	57
	(002)	34.45°	24.15	44
	(101)	36.28°	25.39	100
	(102)	47.58°	32.89	23
	(110)	56.65°	36.69	32
zinc orthotitanate	(220)	29.86°	21.01	15
	(311)	35.18°	24.64	100
	(400)	42.74°	29.71	28
	(422)	53.0°	36.38	57
	(511)	56.5°	38.60	38
anatase	(101)	25.28°	17.85	100
	(103)	36.95°	25.85	10
	(004)	37.80°	26.42	20
	(112)	38.58°	26.94	10
	(200)	48.05°	33.21	35
	(105)	53.89°	36.96	20
	(211)	55.06°	37.70	20

Table 2.2.: Bragg reflexes of zinc oxide, zinc titanate and titania, which are observed for the wurtzite, zinc orthotitanate and anatase phases, respectively, along with the corresponding relative intensities (obtained from JCPDS database).

for each Bragg reflex. The crystallite size (D_{hkl}) of the polycrystalline material can be calculated from the width of the Bragg reflex using the Scherrer equation

$$D_{hkl} = \frac{K\lambda}{\Delta(2\theta)\cos(\theta)}, \tag{2.29}$$

where $K \approx 0.9$ is the Scherrer form factor, λ the wavelength, and $\Delta(2\theta)$ the full width half maximum (FWHM) of the Bragg peak found at angle 2θ [68]. With a decrease in the crystallite size along with the resolution of the scattering set up, the Bragg peaks tend to broaden. The equation is valid for sizes ranging from 5 nm to up to 200 nm [69]. The position of the Bragg reflexes can also be converted from angles to q-space using the Bragg relation as

$$q = \frac{4\pi sin(\theta)}{\lambda}. \tag{2.30}$$

2.4.2. Grazing incidence scattering

In addition to the specular scattering, the diffuse scattering of the thin films is probed using grazing incidence small angle x-ray scattering (GISAXS). For the measurements, a shallow incidence angle of $\alpha_i < 1^\circ$ is used. This accounts for illumination of a considerable large area resulting in a large scattering volume. The scattering geometry is shown in figure 2.11(b). In the set up, α_i is kept fixed and the scattered intensity is recorded by a 2d detector. Every pixel of the detector is assigned to two diffuse scattering angles, the one in the xz-plane is the exit angle and is denoted by α_f and the other in out-of-plane angle in xy-plane, represented as ψ. The scattering vector $\vec{q}$ is thus given by [70]

$$\vec{q} = \frac{2\pi}{\lambda} \begin{pmatrix} \cos(\alpha_f)\cos(\psi_f) - \cos(\alpha_i)\cos(\psi_i) \\ \cos(\alpha_f)\sin(\psi_f) - \cos(\alpha_i)\sin(\psi_i) \\ \sin(\alpha_f) + \sin(\alpha_i) \end{pmatrix}. \tag{2.31}$$

For GISAXS measurements, the contribution from the q_x component is neglected due to typically very small angles. More details about the method can be found in references [70–74].

As already mentioned in equation 2.27, the critical angle depends on the scattering length density (SLD) of the material and hence, the intensity of this peak is directly sensitive to the material investigated. This material characteristic peak is termed as the Yoneda peak which also relates to the mass density of the material which is directly proportional to the SLD [75]. Using this correlation, the porosity Φ of the material can be determined by

$$\Phi = 1 - \frac{\rho_m}{\rho_t}, \tag{2.32}$$

where ρ_m and ρ_t are the measured and the theoretical (for bulk) SLDs of the investigated material. The diffuse scattering from the material is most sensitive at the Yoneda peak position, which leads to maximum scattering intensity in the out-of-plane angles at $\alpha_i = \alpha_f = \alpha_c$.

The diffuse scattering signal obtained in a GISAXS experiment is modeled using objects of a certain size, termed as their form factor, which is described by the Fourier transform of the electron density distribution of the object. In addition to the size, a spatial distribution of the objects is also considered, which is described by the structure factor. This spatial arrangement of the objects is introduced by an interference function. Assuming N identical objects with a given size, spatial distribution and random orientation, the diffuse scattering factor as a direct measure of the recorded intensity is approximated by

$$P_{diff}(\vec{q}) \propto NS(\vec{q})F(\vec{q}), \tag{2.33}$$

where $S(\vec{q})$ is the structure factor and $F(\vec{q})$ is the form factor. In the present thesis, this approximation is used only in order to extract information in the lateral (q_y) direction. This simplification is known as effective surface approximation [72]. More precisely, the diffuse scattering is described under the framework of Distorted Wave Born Approximation (DWBA), which allows four terms to account for different modes of reflection and scattering. These scattering events are: (1) only scattering, (2) reflection on the substrate followed by scattering, (3) scattering followed by a reflection on the substrate, and (4) first a reflection on the substrate, then scattering, followed by another reflection on the substrate. On the basis of the scattering events, the waves interfere coherently producing the effective form factor. For investigations in the present thesis, the form factor is considered to have a cylindrical geometry. For the structure factor, a paracrystalline lattice is assumed where the cylinders are arranged periodically, thereby providing a short-range order. A loss of long-range order is introduced in the fitting model, which increases with growing distance of the position from the origin of this lattice. A one-dimensional paracrystalline lattice (1DDL) is used to describe the spatial distribution (the interference function $S(\vec{q})$) of the form factors in the presented model. In a 1DDL, the arrangement is independent towards the orientation of the system.

In the model used, a size distribution of the objects is also taken into account. The local monodisperse approximation (LMA) is introduced to include objects with different sizes. Under this approximation, the scattering is assumed to occur from only one specific area, which allows for the decoupling of the height and radii of the scattering objects. As a result, the total scattered intensity can be calculated as a sum of individual intensities scattered by single domains of monodisperse objects. For the analysis of the GISAXS data, up to three form factors with three individual 1DDL distributions, all following a Gaussian distribution are used.

3. Characterization methods

In the present chapter, different techniques to characterize nanostructured ZnO, ZnO-polymer hybrid and ZnO-TiO_2 nanocomposite films in order to study their surface and volume structures are presented. The structural characterization of the above-mentioned films are performed via different real- and reciprocal-space imaging methods described in section 3.1. The spectroscopic and electronic characterization of the films are performed by the techniques described in section 3.2. The applied characterization tools with the instrument specifications and working principle are described in the following sections. Also a detailed insight to the sample preparation and measurement protocol is provided, whenever necessary. Additionally, the principles of analysis of the corresponding data are given in the respective subsections.

In detail, the structure and film thickness are analyzed by the real-space techniques, such as scanning electron microscopy (section 3.1.1), atomic force microscopy (section 3.1.2) and height profilometry (section 3.1.3). The crystallinity and the in-depth length scales in the films are probed by x-ray diffraction (section 3.1.4) and grazing incidence small angle x-ray scattering (section 3.1.5), respectively. Furthermore, the optical properties of the films are studied by UV/Vis spectroscopy (section 3.2.1), photoluminescence spectroscopy (section 3.2.2) and Fourier transform infrared spectroscopy (section 3.2.3). The surface composition of the films is analyzed with the aid of energy-dispersive x-ray spectroscopy (section 3.2.4) and finally, the functioning of the solar cells is determined using current/voltage measurements (section 3.2.5).

3.1. Structural characterization

For efficient functioning of the solar cells, morphology, crystallinity and the film thickness are the major factors which play an important role. The morphology of the surface and cross-sections along with the thickness and surface roughness of the films are probed via the real-space imaging tools, whereas, the reciprocal-space techniques provide average information over large area about the length scales in the volume of the films, as well as their porosity and crystallinity. All the graphs of 1d data are plotted with the software Genplot version v.2.11 by Computer Graphic Service Ltd.

3.1.1. Scanning electron microscopy

Scanning Electron Microscopy (SEM) is an imaging technique designed for directly studying the surfaces of solid samples. Images are obtained by using electrons instead of light waves. Because of the shorter wavelength of the electrons as compared to the wavelength of photons normally used for optical microscopy, SEM has a very high resolution which allows a large area of the sample to be in focus at one time. For this reason, SEM can produce an image of great clarity which is a good representation of the sample surface. SEM is used in the present work to probe the surface of ZnO-polymer hybrid films as well as pure ZnO nanostructured films in order to obtain a preliminary qualitative information about the morphology of the thin films. All SEM measurements presented in this thesis are performed on a FESEM Gemini NVision 40[1] instrument controlled by the software SmartSEM, both provided by Carl Zeiss.

The electrons generated either by a strong electrostatic field (field emission) or from a hot filament (thermionic emission) are accelerated with a voltage of several kV and focused on the sample surface via electrostatic and magnetic lenses. The sample surface is then scanned in a line-wise manner with the electron beam. The secondary electrons generated during this process are then detected. Other processes such as backscattering of electrons and cathodoluminescence also occur upon interaction of the electron beam with the sample surface, which are not detected for the presented investigations. The signal is converted to gray-scale images with regions having different brightness. A resolution in the range of 1 to 10 nm can be achieved depending on the sample topography and the material [76]. The acquired signal also depends on the distance between the material and the detector. Different degree of brightness in the sample indicates different height of the structures present in the film or different conductivity. Higher structures appear brighter than ones which have a low height due to the higher intensity of the secondary electrons detected for the former case.

For all the measurements shown in the present work, a well-defined electron beam is ensured via a gun vacuum of $2 \cdot 10^{-9}$ mbar and a system vacuum of $2 \cdot 10^{-6}$ mbar. An aperture size of the primary electron gun between 7.5 and 10 µm is used with a working distance between the gun and the sample surface in the range of 3.5 to 4 mm. The acceleration voltage of the electron beam is adjusted to 3 to 5 kV. The secondary electrons are detected by an InLens detector system which is positioned in a ring-like manner around the electron gun. All the obtained SEM images are processed by the ImageJ v1.42q[2]

[1]FESEM NVision 40 by Carl Zeiss at the chair of Prof. A. Holleitner, Zentrum für Nanotechnologie und Nanomaterialien, TUM.

[2]ImageJ 1.42q from Wayne Rasband, National Institutes of Health, USA

software, which also enables to obtain Fourier transformation of the patterns in order to estimate the length scales on the sample surface.

Samples with less conductivity, such as films containing polymers, tend to accumulate charges as they are not conducted away. This renders the focusing of the images difficult, as a result of which darker images and poor contrast is obtained. Using a conductive substrate is often beneficial to prevent over charging of the films. Silicon substrates are used for most of the films measured via SEM. The measurement parameters are optimized for films on glass and/or with non-conductive polymers. A strip of conducting carbon tape is attached on the film to conduct away the charges, close to where the measurement is performed. Low acceleration voltage and sample-detector distance in such cases of less than 0.5 kV and 1 mm, respectively, are employed.

For measurement of cross-sectional images, the samples on silicon and glass substrates are broken over a metal edge after being scratched with a diamond cutter at the back in order to obtain a clear cross-section of the film. For the measurement of the cross-section of the solar cells prepared on FTO-coated glass substrates or of films containing the soft polymer, the sample is frozen in liquid nitrogen prior to breaking in order to avoid peeling off of the soft material from the substrate surface. Apart from these, no additional sample preparation step is required. All the cross-sectional SEM images presented in the thesis are measured after tilting the sample stage to 60° (maximum tilt limit is 63°) with respect to the horizon. A tilt correction of 90° - 60° = 30° is applied for the correct presentation of the cross-section and also to have a correct value for the film thickness.

3.1.2. Atomic force microscopy

Atomic force microscopy (AFM) is a powerful tool which allows a variety of surfaces to be imaged and characterized at the atomic level. With AFM it is possible to probe the plane parallel to the samples along with the height of the structures. Thus information about surface topography as well as height profile of the samples are achieved. The instrument used for measuring ZnO nanostructured films in the present work is supplied by Autoprobe CP Research (Veeco Metrology Group). A schematic sketch of the instrument set up is shown in figure 3.1.

The working principle of the device is based on the interatomic forces between the surface of the sample and a sharp tip with a diameter of a few tens of nanometers. A simple Lennard-Jones potential with a short-range repulsive and a long-range interactive part is assumed. The tips used for the present investigations are provided by Thermomicroscopes with a curvature radius of 10 nm. The tips are mounted onto triangle-shaped cantilevers (Ultralever OLNC-B) as shown in figure 3.1, having a resonance frequency between 70

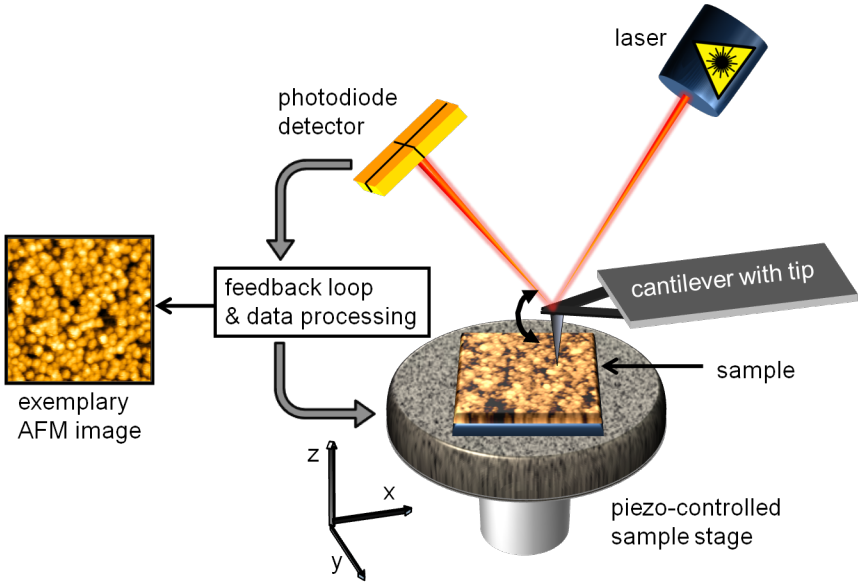

Figure 3.1.: Schematic representation of the AFM set up. The sample is mounted on a movable stage controlled by piezo elements. The cantilever with the tip is positioned on top of the sample. Deflection of the cantilever is detected by a laser beam, which is reflected from the cantilever to a multi-segmented photodiode detector. The signal is directed to a feedback system, which controls the position of the sample n z direction and processes the data.

and 80 kHz and a spring constant of 2.1 N m^{-1}. The sample is moved laterally in the xy-plane with very close proximity to the tip, the sample-tip distance being less than 100 nm. This small distance is kept fixed throughout the measurement and is necessary to detect the interatomic forces between the sample surface and the tip. Three common modes of operation are contact, non-contact and tapping mode. All the measurements performed in the present thesis are conducted under tapping mode, where the tip repeatedly touches the sample surface. This ensures minimum damage to soft samples such as polymer films. The cantilever is excited to its resonance frequency for the measurements. Depending on the surface of the film, the interatomic forces between the surface of the sample and the tip changes, which results in a change in the amplitude of the cantilever. This change is then detected by the deflection of a laser beam which is focused on the front part of the cantilever as shown in figure 3.1. This deflection of the laser is detected by a segmented photodiode, which transfers the signal to the feedback electronics which is responsible for the movement of the piezoelectic translator, which in turn moves the sample along z-direction to restore the initial sample-tip distance. The sample surface is scanned line-wise and the final data consists of 256 $\times$ 256 data points. The changes in the vertical

positioning of the tip due to the changes on the surface of the film, as recorded via the deflection of the laser, thus generates the complete height map of the film.

The samples measured need no specific treatment and are simply mounted on the sample stage using double sided adhesive tape (tesa). The area of the films scanned for the presented investigations lies within $(4 \times 4)\,\mu m^2$. All the topographic images are analyzed using Gwyddion v2.20 [77] software, mainly to extract the height of the film and to correct the polynomial background for the drift of the piezo motors. It should be noted that care must be taken regarding the ambient conditions while measuring. It has been observed that cold and dry conditions are more suitable for the measurement as compared to hot and humid surroundings. This is mainly due to the fact that a high humidity in the atmosphere results in the formation of a thin film of water around the tip due to which its interaction with the surface of the sample is altered [78].

3.1.3. Height profilometry

Profilometry is a commonly used technique to determine the thickness and roughness of thin films. For the films investigated in the present thesis, a DEKTAK 150 surface profiler by Veeco Instruments Inc.[3] is used. The instrument basically consists of three major parts: a high precision sample stage, a diamond-tipped stylus and a linear variable differential transformer (LVDT). A schematic sketch of the set up is shown in figure 3.2. The working principle of the profilometer is rather simple: The sample is mounted on the high precision stage which moves it under a stylus applying a constant force over the sample. Depending on the variation of the film thickness and roughness, the stylus experiences mechanical deflections while scanning the film surface. These lateral deflections are then converted to digital signal by the LVDT.

This method is particularly significant in determining the thickness of the spray-deposited ZnO films, which have a high surface roughness. The samples are prepared for the measurement by scratching off the ZnO film from both sides of the substrate as shown in figure 3.2. The measurements are performed by scanning over both the scratched areas in the film. The thickness of the film is then calculated from the vertical drop experienced by the stylus at the edges of the two scratched areas. Multiple scans are performed over the same film in order to obtain an average film thickness and topographical roughness. During all measurements the scan speed of 0.1 mm s^{-1}, the contact force of 1 mN, the stylus radius of 12.5 µm, a vertical scan range of 65.5 µm and a lateral scanning length of 2 cm are kept constant. The set up yields a maximum vertical resolution of 0.1 nm.

[3] located at the cleanroom of Zentrum für Nanotechnologie und Nanomaterialien (ZNN)

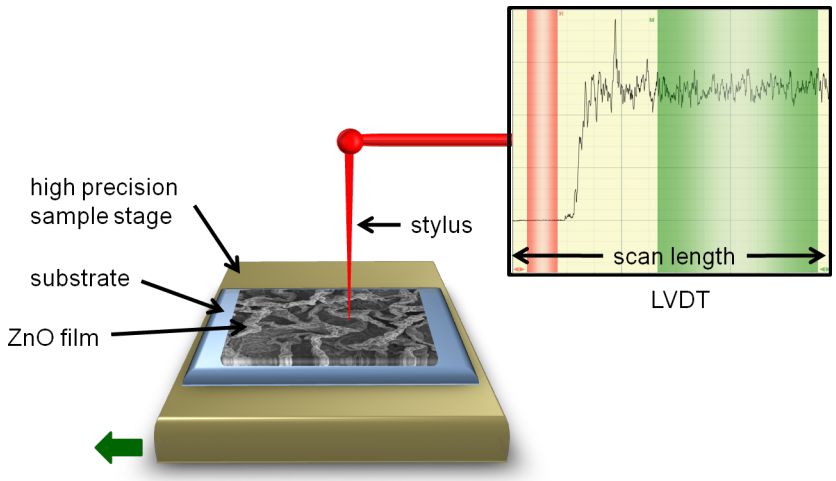

Figure 3.2.: Schematic set up of the height profilometer consisting of a movable stage on which the sample is mounted. The diamond-tipped stylus is used to scan the sample surface. The deflections of the stylus due to height differences and roughness of the film, are converted into digital signal by LVDT and a scan length vs film thickness plot is obtained. The green arrow indicates the direction of movement of the sample stage.

3.1.4. X-ray diffraction

X-ray diffraction (XRD) is a commonly used technique to determine the crystal phases, the degree of crystallinity and the crystallite size of a polycrystalline materials. In the present thesis, XRD measurements are performed on pure ZnO as well as ZnO-TiO_2 nanocomposite films. In addition, nanocrystalline ZnO powder films are also characterized via this method. Details about the theoretical background of this technique is provided in section 2.4.1. For the various measurements performed, two XRD instruments are used. The first one is an XRD 2003 TT system from GE sensing and inspection technologies[4] (cited as **XRD instrument I**) and the second one is a Bruker D8 ADVANCE powder diffractometer (abbreviated as **XRD instrument II**). All programs used for measurement protocol and data processing using XRD instrument II are included in the DIFFRAC.SUITE also provided by Bruker. The principle set up for XRD measurements is schematically shown in figure 3.3.

As a source for the x-ray beam, the copper K_α emission line is used, having a wavelength of $\lambda_{Cu} = 0.1541$ nm. The x-ray beam impinges the sample at an angle θ. The diffracted beam is detected by a point detector at the same angle θ with respect to the sample.

[4]assisted by Prof. Dr. Wolfgang Schmahl, Sektion Kristallographie, Theresienstr. 41, Ludwig-Maximilians-Universität

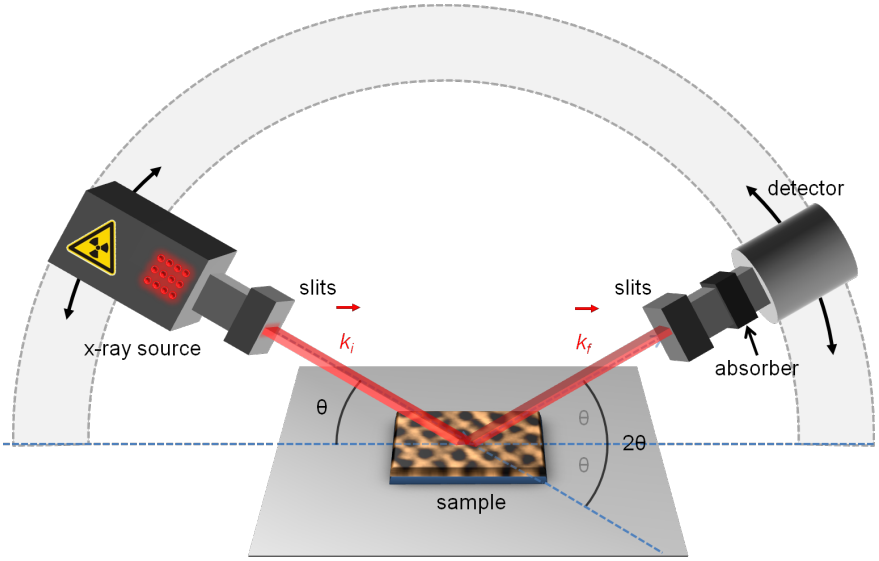

Figure 3.3.: Schematic set up of the XRD measurement. The x-ray tube and the point detector are shown. The x-ray beam impinges the sample (placed on a sample stage) under an angle θ and is detected under an angle of 2θ with respect to the incoming beam. Slits before and behind the sample are present for a collimated beam and to reduce diffuse scattering. The direction and plane of movement of the x-ray tube and the detector are indicated. The image is adapted from [32].

Since the incident and the diffracted beam have an angle of 2θ relative to each other, the measurement mode is known as coupled $\theta/2\theta$ mode.

The samples (either on glass or silicon substrates) are prepared of at least (2.5 × 2.5) cm^2 in size. For both instruments, the copper anode is operated at a voltage of 40 kV, however, a current of 100 mA is used for XRD instrument I, whereas, the same for XRD instrument II is kept constant at 40 mA. A typical 2θ range of 25° to 60° is scanned for all the samples. In XRD instrument I, each sample is measured for 9.26 h with a step size of 0.04°. In this instrument, the spin-coated samples are rotated at a speed of one rotation per second throughout the measurement to account for the polycrystallinity of the sample. For measurements using XRD instrument II, each data point is measured for 20 s with a step size of 0.028°. For samples prepared on silicon substrates, prior to every measurement, the silicon (100) peak at $2\theta = 33°$ (for λ_{Cu}) is measured for alignment, by scanning from $2\theta = 30$ to 40° with a step size of 0.01° and a counting time of 0.1 s per step. The width of the silicon (100) peak is also a measure for the resolution of the instrument. Slits of 0.6 mm are used in the set up before and after the sample position as shown in figure 3.3 for all the measurements using XRD instrument II. An automatic absorber system is installed behind the sample (figure 3.3) during the measurements to

protect the detector from over saturation depending on the angle. A long measurement time for the samples is necessary on both instruments due to the small scattering volume of the thin films.

The XRD data is evaluated with the software PeakFit Version 4.12 by SeaSolve Software Inc. The crystallite size is calculated from the fit results via the Scherrer equation, as described in chapter 2.4.1. The reference peaks for wurtzite ZnO and anatase TiO_2 are taken from the Joint Committee on Powder Diffraction Standards (JCPDS), while the theoretical peak positions and their relative intensities for crystalline zinc titanate are taken from Inorganic Crystal Structure Database (ICSD).

3.1.5. Grazing incidence small angle x-ray scattering

Grazing incidence small angle x-ray scattering (GISAXS) is performed in order to probe the structural length scales present in the volume of the film. Static as well as kinetic measurements are performed to monitor structure evolution in the film. The theoretical background about the technique is given in section 2.4.2. A schematic representation of the set up is provided in figure 3.4. All the measurements reported in the present thesis are performed at the BW4 beamline[5] of the DORIS III storage ring, P03 beamline[6] of the PETRA III storage ring in DESY and I07 beamline[7] at the Diamond Light Source.

As seen from figure 3.4, the x-ray beam impinges the sample at a shallow angle and then the scattered signal is recorded by a 2d detector. As the size of the detector is limited, the angles recorded are determined by the sample-detector distance (SDD). Hence, the length scales accessible in the film volume for commonly used photon energies on the order of around 10 keV, depends on SDD. Typical SDDs in the range of 2 to 4 m allow to probe angles less than 5° and structures in the length scale of 1 nm to 1 µm. For the measurements performed at BW4, an SDD in the range of 2 to 2.5 m is used, whereas for P03 and I07, a typical SDD of roughly 3 m is chosen. Due to the large distance between the detector and the sample, an evacuated flight tube is installed in the pathway in order to minimize scattering from air. In the I07 beamline, the flight tube is connected to a supply of helium flow to further enhance the effectiveness of the scattered signal recorded by the detector. Furthermore, a compressible flight tube geometry at P03 beamline provides fast adjustments for variable SDDs between 1 and 4 m for GISAXS measurements. For probing structures larger than 1 µm, the SDD can be further increased to up to 10 m to access length scales of the order of a few tens of micrometers. This technique is then referred to grazing incidence ultra small angle x-ray scattering (GIUSAXS) [79].

[5]beamline BW4 at the synchrotron ring DORIS III, DESY, Hamburg
[6]beamline P03 at the synchrotron ring PETRA III, DESY, Hamburg
[7]beamline I07 at the synchrotron ring of Diamond Light Source, Oxfordshire

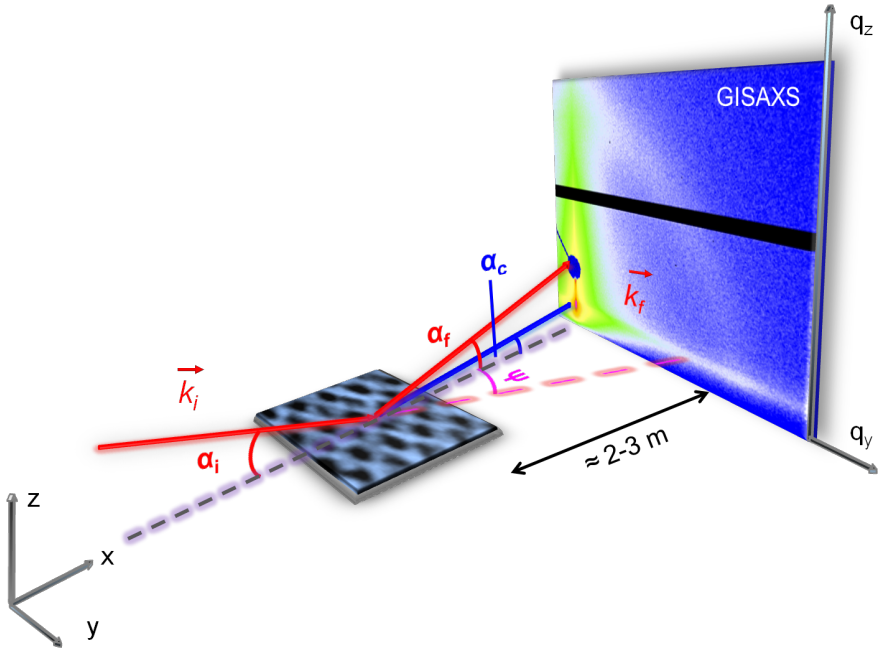

Figure 3.4.: Schematic set up for grazing incidence small angle x-ray scattering. The incident beam $\overrightarrow{k_i}$ impinges the sample under an angle α_i. The scattered beam $\overrightarrow{k_f}$ is detected by a 2d detector placed at a distance as indicated by the double-headed arrow. The scattered beam is mainly defined by two components relative to the incident beam, the one along xz-plane, also known as the exit angle α_f and the other along xy-plane known as ψ. The specularly reflected beam and the direct beam are shielded by beamstops to prevent over saturation of the detector. The exit angle at the critical angle of the material of the film is denoted as α_c and is commonly known as the Yoneda peak.

Another important parameter which needs to be taken into account for a fruitful measurement is the angle of incidence of the x-ray beam. It is carefully chosen above the critical angles of all the materials present in the films, for all the measurements. This allows the x-ray beam to penetrate the film as discussed in section 2.4.2. However, care must be taken not to choose a very high angle, which leads to loss of sensitivity towards the structures present in a thin film. The grazing incidence conditions also ensures large footprints of the beam in the millimeter range, which ensures information obtained over large sample areas. A typical beamsize of $(22 \times 12)\,\mu m^2$ [horizontal $\times$ vertical] is chosen for the measurements at the P03 beamline. A similar beamsize of $(36 \times 18)\,\mu m^2$ is chosen for the measurements at BW4 beamline. For the I07 beamline, the beamsize is provided as $(115 \times 210)\,\mu m^2$. The measurements are undertaken at similar wavelength of the x-ray beam for I07 and P03 beamlines, whereas, for the BW4 beamline, the wavelength of the x-rays is longer. For all the measurements presented in the thesis, a wavelength λ_{I07} of 0.099 nm, corresponding to an x-ray energy of 12.5 keV is used for the measurements at

I07. For P03, three slightly different wavelengths of $\lambda_{P03,1}$ 0.0984 nm, $\lambda_{P03,2}$ 0.0957 nm and $\lambda_{P03,3}$ 0.0941 nm are used corresponding to x-ray energies of 12.6, 12.9 and 13.2 keV, respectively. For all the measurements performed at BW4, the wavelength λ_{BW4} is kept constant at 0.1381 nm yielding an x-ray energy of 8.9 keV. Due to lower x-ray wavelengths chosen at I07 and P03 beamlines as compared to BW4, lower specific critical angles of the materials for the former cases are expected, as a result of which, lower incident angles are chosen for measurements at P03 and I07. For instance, an incident angle (α_i) of roughly 0.4° is chosen for the measurements at BW4, at the same time α_i of approximately 0.3° is chosen for the measurements at P03 and I07 in order to obtain similar sensitivity to the structures inside the thin films.

Depending on the beamline and the type of measurement performed, three different 2d detectors are used in the present thesis. For all the measurements performed at BW4, a MarCCD 165 area detector (Marresearch GmbH) with 2048 × 2048 pixels of an individual pixel size of $(79.1 \times 79.1)\,\mu m^2$ is used. The detector has a round active area of 165 mm diameter. The MarCCD detector has a read-out noise of roughly 10 counts/pixel [80]. As a consequence only static measurements with a counting time of roughly 30 min are performed using this detector. Such long counting times are necessary to sufficiently differentiate between the desired signal and the background noise. For all the measurements performed at I07, a Pilatus 1M (Dectris) detector is used. This is a noise free detector consisting of 10 modules with blind areas at the inter-module gaps. In total, the detector consists of 981 × 1043 = 1,023,183 pixels, each with a size of $(172 \times 172)\,\mu m^2$. The detector provides a total area of (169×179) mm^2 and a signal readout time of 2.3 ms. Finally, for all the measurements performed at P03 beamline a Pilatus 300K detector is used consisting of three segments with a total active area of (83.8×106.5) mm^2 resulting in 2d scattering data over (487×619) pixels, with the same pixel size as for Pilatus 1M detector. The detector has a readout time of roughly 5 ms. Thus, the detectors provided by Dectris allows for kinetic measurements with fast readout time, thereby providing a high time resolution. This is also supported by the absence of noise from the detector, which facilitates recording a discrete signal from the sample. The recorded intensity is then presented using a false color code with logarithmic scaling.

To avoid the oversaturation of the detector from the high intensity of the direct beam and the specular reflected beam at $\alpha_f = \alpha_i$, circular beamstops are installed in the beamline set ups. In case of using MarCCD as the detector, an additional rod-shaped beamstop is occasionally used to shield all the signal along $q_y = 0$ nm^{-1} and, thereby enhancing the scattering statistics along $q_y \neq 0$ nm^{-1} for long exposure times. Figure 3.5 shows an exemplary 2d GISAXS data obtained for a pure ZnO calcined film from a MarCCD detector. The scattering signal along $q_y = 0$ nm^{-1} provides information about the film

in the plane perpendicular to the substrate, whereas, the signal along the horizontal direction provides information about the lateral structures in the film. In order to extract quantitative information from the scattering data, line integrals are performed in the horizontal (typically at the Yoneda peak position) and vertical directions as indicated by the red and the black dashed arrows (figure 3.5), respectively. These cuts are then analyzed via the Fit2D[8] software or the DPDAK[9] program. The later is essentially used for batch processing of series of data containing large number of files, specially obtained during in-situ measurements.

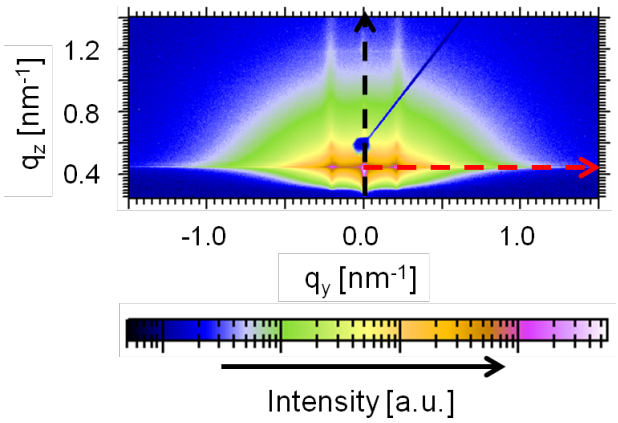

Figure 3.5: Exemplary 2d GISAXS data with dashed arrows indicating the position of the line integrals, typically performed in the horizontal (red) and vertical (black) directions for the analysis of the data.

Custom-made macros are used to fit the horizontal line cuts to the data in order to extract structural length scales in the volume of the film. The fitting model is based on a 1d paracrystal model, considering the form factor of a cylindrical geometry of the objects using the framework of the local monodisperse approximation (LMA), as detailed in section 2.4.2. Depending on the sample probed, one, two or three form and structure factors are used to fit the data. Two important sets of length scales are obtained from these fits. The first corresponds to the mean radii of the cylinders following a Gaussian distribution and the second length scale determines the mean distance between the cylinders. The used model calculates the intensity at the cut position only and the contribution from the structures along the q_z direction is neglected. For very low q_y values, the experimental resolution function of the instrument is taken into account. It is modeled with a Lorentzian-shaped resolution function.

[8]software Fit2d by Andy Hammersley, 1987-2005, ESRF, Grenoble
[9]Directly Programmable Data Analysis Kit (DPDAK) by Gunthard Benecke, DESY Hamburg & MPIKG Potsdam

3.2. Spectroscopic and electronic characterization

The pure ZnO and ZnO-TiO_2 nanocomposite films are studied for their optical absorption, electronic transitions, band gap energies, charge carrier recombination and surface composition in this section. In addition, the complete solar cells are subjected to electronic characterization in order to determine their performance.

3.2.1. UV/Vis spectroscopy

Due to the relatively large amount of energy associated with the UV radiation, it is capable of electronic excitations thereby inducing transitions within the electronic energy levels in a crystal. UV/Vis measurements are performed on the pure ZnO and ZnO-TiO_2 nanocomposite films in the present contribution using two different spectrometers: The first is the Lambda 35 (referred to as **UV/Vis instrument I** throughout the study) and the second is a Lambda 650 S (abbreviated as **UV/Vis instrument II**), both supplied by PerkinElmer.

The major components of both the devices consist of two lamps, a halogen lamp for providing light in the near infrared and the visible range and a deuterium lamp contributing for the UV region. The available wavelengths span the range between 190 and 1100 nm in case of UV/Vis instrument I, with a switch between the light sources at 326 nm. For UV/Vis instrument II, the available wavelength range stretches from 190 to 900 nm with a switch of the lamp occurring at 320 nm. Photodiodes are used as detectors for both the instruments. In addition, UV/Vis instrument II is equipped with an integrating sphere (Spectralon R, highly reflective, 150 mm).

During the UV/Vis measurements in transmission mode, the incoming beam is split into two single beams, each passing through the sample (the sample beam) and the reference (the reference beam). The intensity ratio of the beams going through the sample and the reference is saved for each measurement. The absorbance $A(\lambda)$ from the ultraviolet to the near infrared region for the present samples is calculated using this ratio by applying Beer-Lambert's law

$$A(\lambda) = -\log_{10}\left(\frac{I_t(\lambda)}{I_0(\lambda)}\right) = \alpha(\lambda) d \log_{10} \mathrm{e}, \tag{3.1}$$

with the initial and the transmitted intensities $I_0(\lambda)$ and $I_t(\lambda)$, the material specific absorption coefficient $\alpha(\lambda)$, the film thickness d, and Euler's number e. The band gap energy E_{gap} of the material is determined from the absorbance measurements by plotting $(\alpha E)^n$ versus the energy of light $E = hc/\lambda$, with Planck's constant h and the speed of light c. The band gap energy can then be obtained using the Tauc equation

$$(\alpha E)^n = B(E - E_{gap}) \tag{3.2}$$

by a linear extrapolation of the data, which intersects with the energy axis [81]. B is a constant. The exponent n depends on the type of band gap of the investigated material. In the case of a direct band gap, $n = 2$ and in the case of an indirect band gap, $n = 1/2$ [82]. Hence, a prior knowledge about the type of band gap is necessary in order to adapt the equation accordingly. For both ZnO and zinc titanate, crystalline phases exhibit a direct band gap [46,83]. Therefore, the exponent is fixed to $n = 2$ which provides a quick insight to the crystalline phase via the resulting band gap energy.

All the measurements are performed in transmission mode for the present thesis, due to which the samples are prepared on glass substrates. The glass shows strong absorption below 290 nm, as a result of which the transmission measurements for a wavelength lower than 260 nm are not undertaken. For both spectrometers, bare glass substrates are used as the reference and a so-called autozero calibration is performed before the actual measurement in order to register the signal only from the actual film. A scanning speed of 120 nm min^{-1} and 267 nm min^{-1} is used for UV/Vis instrument I and II respectively. The spectral slit size of 1 nm is chosen for both the instruments.

3.2.2. Photoluminescence spectroscopy

In the present thesis photoluminescence spectroscopy (PL) is used for measuring the radiative electon recombination across the band gap of ZnO nanostructured films. Additionally, electron transmissions from sub-bands to the top of the valence band is also probed, which indicates the presence of certain defects or trap states within the sample [84]. All the PL measurements are performed using a LS55 fluorescence spectrometer from PerkinElmer, which is controlled by the software FLWinlab, also by PerkinElmer.

A Xenon discharge lamp is used as the light source for wavelengths ranging from 200 to 800 nm generating short pulses with a half-life of $< 10\,\mu\text{s}$. For the measurements, the excitation wavelength is chosen to be well above the band gap energy of the investigated material. The emitted signal is detected under an angle of 90° with a red-sensitive Hamamatsu R928 photomultiplier. The radiative response of the sample is detected as the wavelength of the emitted light is always larger than that of the excitation wavelength. A cut-off filter is used to block all the signals below the excitation wavelength and thereby prevents them from superimposing upon the signal. For the present investigations, a reduction in a typical PL signal indicates less recombination of the generated charge carriers in the system. This phenomenon is commonly known as PL quenching and occurs when the charge carriers are spatially separated that far from one another that they fail to recombine. This marks an improvement in the crystallinity of the material and absence of defects in the sample, which improves the conductivity of the charges.

An excitation wavelength of 335 nm is kept fixed for all measurements. This wavelength corresponds to an energy of 3.37 eV which is higher than the band gap of wurtzite ZnO (section 2.2.2). The scanning speed for the emitted signal is typically chosen as 200 nm min^{-1} and in total the data obtained is averaged over six measurements for a given sample for better statistics. All the samples are prepared on silicon substrates as the boron content in the glass substrates is known to produce a strong PL response. The slit settings are kept constant for all the measurements and no calibration is performed for the measurements. The emitted signal is scanned in the range of 350 to 600 nm. The obtained data is fitted using Gaussian peaks by the software PeakFit Version 4.12 by SeaSolve Software Inc.

3.2.3. FTIR spectroscopy

Fourier transform infrared spectroscopy (FTIR) is an analytical technique to probe the chemical functional groups present in a sample. The ZnO nanocrystalline powder synthesized via solution-casting approach is investigated using FTIR in the present work. The mid infrared spectrum, i.e., approximately from 4000 to 300 cm^{-1} is used for the present measurements to detect the associated vibrational state of the molecules present in the sample under consideration. The measurements are performed using a BioRad FTS 570 C spectrometer, with a MIRacle ATR unit from PIKE Technologies[10].

The FTIR spectroscopy uses a Michelson interferometer through which the IR light is guided to the sample. The incident light is split into two parts of equal intensity using a beam splitter. One part is reflected at a stationary mirror, whereas, the second part is directed towards a moving mirror changing the optical path. The light from the two mirrors are reflected back to the beam splitter, after which, the light passes through the sample and gets focused afterwards on the detector. An interferogram is obtained which is the light output as a function of the mirror position. This interferogram is then Fourier transformed to be translated to the spatial frequency domain. The intensity of the light absorbed or transmitted at the sample is plotted as a function of wavenumber, which is the reciprocal of the wavelength. In addition, an attenuated total reflection accessory can be used to determine the changes in a totally internally reflected infrared beam when it comes in contact with the sample surface. For this purpose, the IR beam is passed through an optically dense crystal with a higher refractive index than the specimen. The sample needs to be in close contact with the crystal. Due to the total internal reflection, an evanescent wave is created on the surface of the crystal, which then penetrates the

[10] conducted by Jian Zheng, group of Prof. Klaus Köhler, Chemistry-Department, Technische Universität München, Lichtenbergstr. 4, 85748 Garching, Germany

sample up to a few microns. The attenuations in the evanescent wave, occurring due to interaction of the beam with the sample is passed to the detector in the spectrometer. The IR absorption spectra are then compared to computerized database in order to identify the signals from various chemical groups present in the sample [85].

ZnO powder probed by FTIR in the present case is transformed into a pellet which is then inserted into the measurement chamber via a sample holder. The sample preparation involves grinding of 1 to 3 mg of ZnO powder, which is then thoroughly dispersed in a matrix of 300 mg of potassium bromide (KBr) powder. The fine powder mixture is then transferred to a die and placed in a press where a high pressure is applied for nearly 2 minutes. Re-crystallization of KBr matrix results in the formation of a disc which has a thickness of close to 1 mm. For the presented investigation, the sample is scanned over a wavenumber range of 349 to 4000 cm^{-1} with a resolution of 0.5 cm^{-1}. It should be noted that the quality and handling of the pellets adversely affect the IR absorption spectra. Presence of macroscopic cracks or inhomogeneous distribution of the material in the matrix result in a low signal-to-noise ratio. Also, the pellets are often hygroscopic, which makes it difficult to eliminate the signal from O-H bonds of the water molecules.

3.2.4. EDX spectroscopy

Energy-dispersive x-ray (EDX) spectroscopy is an analytical method used for fast and non-destructive elemental analysis or chemical characterization of the samples. In the present work, EDX spectroscopy is explicitly used for the zinc titanate films. An ISI-SR-50 spectrometer from Advanced Instrumentation Laboratory is used for all the measurements presented[11].

The measurement technique is based on the spatial detection of the x-rays emitted by the atomic species present in the sample upon irradiation using a focused electron beam. The emitted characteristic x-ray spectrum is then detected by an energy-dispersive detector. The success of the this measurement tool lies in the fundamental principle that every element has its characteristic atomic structure and hence emits a unique x-ray spectrum. The incident beam of electrons excites the electrons of the sample from the ground state and cause their ejection in form of secondary electrons or backscattered electrons, thereby creating holes within the electronic structure of the atoms. Hence, electrons from higher energy levels fill the holes and the excess of energy of those electrons are emitted in the form of x-ray photons. The release of the x-rays create spectral lines which are highly specific for each element. By raster-scanning of the sample surface with the incident beam, the intensity distribution of these spectral lines can be plotted in a

[11]conducted by Karen Helm-Knapp and Dr. Stephan Geprägs, Walther-Meissner-Institut, TUM

mapping representation, thereby characterizing the different constituent elements. The relative intensities of an x-ray line is proportional to the mass concentration of the element under consideration. This is proportional to the atomic weight of the material and hence, the atom % of a certain element present on the sample surface is extracted from the EDX maps [86].

For the presented measurements, the samples are prepared on silicon substrates of (2.5 × 2.5) cm^2. Similar to the SEM measurements, presence of conductive material and substrates is beneficial. The energy of the incident beam used for all the experiments is kept constant at 25 keV. A Si-Li detector is used with an energy resolution of about 150 eV at 5 mm working distance. The x-ray spectrum for all the samples is recorded in the range of 2 to 20 keV. The most prominent spectral lines are however obtained within 10 keV.

3.2.5. I/V Characterization

In order to determine the photovoltaic performance of the solid-state and liquid electrolyte-based dye-sensitized solar cells, the current-voltage characteristics (I/V) are probed. In order to do that, the current from the solar cell is measured for an applied voltage with a Keithley 2400 sourcemeter, which is controlled using a custom-made software based on Testpoint V6. The solar cells are measured in the dark and under illumination with the solar simulator SolarConstant by K. H. Steuernagel Lichttechnik GmbH, which provides simulated solar spectrum radiation of AM1.5 corresponding to a light intensity of 1000 W m^{-2}. The light spectrum, which is close to the solar spectrum is provided by a halide lamp with rare earth metals. For homogeneous sample illumination, a reflector system is used in combination with a borosilicate filter with an integrated diffusor. Exemplary I/V-curve for a liquid electrolyte-based DSSC is shown in figure 3.6 with the basic definitions.

The typical parameters used to characterize the solar cells include the short-circuit current density (I_{SC}) at $V = 0$, the open-circuit voltage (V_{OC}) at $I = 0$ and the maximum power point (MPP), where the power density of $P = I \cdot V$ is maximum as indicated in figure 3.6. The fill factor (FF) of a solar cell is defined as the ratio between the power at the MPP and the theoretical maximum possible power $P_{\max}$ set by the product of V_{OC} and I_{SC}:

$$FF = \frac{P_{MPP}}{P_{\max}} = \frac{I_{MPP}V_{MPP}}{I_{SC}V_{OC}}. \tag{3.3}$$

An illustration of the FF is given in figure 3.6, where the FF constitutes the ratio of the areas of the blue rectangle to the gray rectangle. In the case of an ideal solar cell, the I/V-curve should have an almost rectangular shape. In addition, the series (R_S)

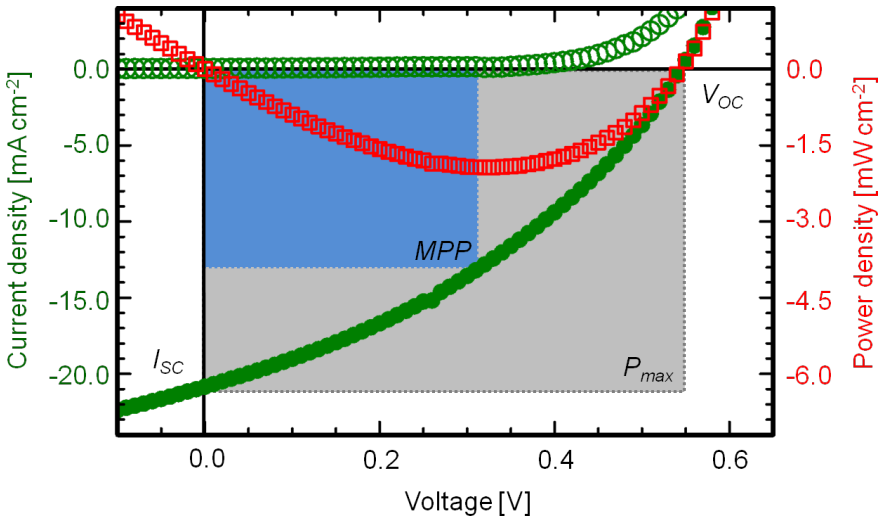

Figure 3.6.: Exemplary I/V-curve of a liquid electrolyte-based DSSC along with the basic features. The curve measured in dark (open green circles) and under illumination (green closed circles) along with the power-voltage curve (red open squares) are shown. The short-circuit current I_{SC}, the open-circuit voltage V_{OC}, and the maximum power point MPP are indicated at the corresponding positions. The fill factor FF is calculated by the ratio of the areas of blue and gray rectangles at the MPP and at P_{max}, respectively. In the example, $I_{SC} = -20.8\,\text{mA cm}^{-2}$, $V_{OC} = 0.54\,\text{V}$, $FF = 36.2\,\%$, resulting in a power conversion efficiency of $\eta = 4.1\,\%$.

and the shunt (R_{SH}) resistances are also used to describe the properties of a solar cell. The former is determined by the slope of the I/V-curve at V_{OC} and should be as low as possible. This mainly originates from the sheet resistance of the different layers present in the solar cell. The latter is determined by the slope of the I/V-curve at I_{SC}. It is a measure for leakage currents within the solar cells and consequently should be as high as possible. The shunt resistance mainly originates from recombination of electrons with the electrolyte or the polymeric hole conductor at the ZnO/dye/electrolyte or polymer interface. The power conversion efficiency (PCE) η of the solar cell is defined by the ratio of extracted power density $P_{\text{out}} = P_{\text{MPP}}$ to the incident power density P_{in} from illumination ($P_{\text{in}}(\text{AM1.5}) = 1000\,\text{W m}^{-2}$). Using the extracted parameters, the PCE of the solar cell can be calculated by

$$\eta = \frac{P_{\text{out}}}{P_{\text{in}}} = \frac{I_{SC} V_{OC} FF}{P_{\text{in}}}. \tag{3.4}$$

Before applying voltage to a set of solar cells, the light intensity of the solar simulator is set to 1000 W m^{-2} by calibration with a silicon-based solar cell (WPVS Reference Solar Cell Typ RS-ID-3 by Fraunhofer ISE). The voltage is applied from -1 V to 0.8 V in steps of 0.01 V with a delay time of 0.01 s. For the ss-DSSCs, each pixel is illuminated separately

via a shadow mask for measurements under illumination. Each pixel is measured at least six times in a loop in order to monitor the performance of the solar cell upon time-dependent illumination. After measuring, the current is normalized to the active area of the solar cell pixels, which are probed individually with optical microscopy and the resulting current density is plotted versus the voltage applied.

4. Sample preparation

The materials and the processing routes used to prepare different sample series for the entire study are described in the present chapter. The specific steps and parameters involved in the processing of a particular sample series is mentioned in the beginning from chapters 5 to 8.

Section 4.1 gives details about general specifications and characteristics of different materials used for the preparation of samples. Section 4.2 describes the processing of the samples. The sol-gel synthesis of the ZnO and TiO_2 nanostructures is introduced (section 4.2.1). Different deposition methods for the sol-gel solution onto solid substrates, in order to obtain thin films for practical applications are elaborated in section 4.2.2. These methods include spin-coating, solution-casting, spray deposition and blade-coating. Lastly, section 4.2.3 illustrates the various steps to assemble two different kinds of dye-sensitized solar cells (DSSCs) - liquid electrolyte-based DSSCs and solid-state DSSCs.

4.1. Materials

The materials used for the present thesis are classified into four categories: the inorganic metal oxide precursors, the structure-directing diblock copolymer templates, the dye and the charge-conducting component of the dye-sensitized solar cells (DSSCs). For the liquid electrolyte-based DSSCs, two different electrolytes are prepared, whereas, for the solid state DSSCs (ss-DSSCs), a hole-conducting polymer is used.

Inorganic metal oxide precursors

Two different precursors, each for zinc oxide (ZnO) and titania (TiO_2) are used in the present study. The chemical structures are depicted in figures 4.1(a) and (b), respectively.

Zinc acetate dihydrate, abbreviated as ZAD is purchased from Sigma-Aldrich (99.999% trace metals basis) and is used as the precursor for ZnO. It has a physical appearance of a white free-flowing powder with a relative density of 1.84 g cm^{-3}. Its chemical formula is quoted as $Zn(CH_3COO)_2{\cdot}2H_2O$. It crystallizes in a monoclinic unit cell [87]. Figure 4.1(a) indicates that the coordination geometry around Zn atom is octahedral as the Zn

atom is bound to two oxygen atoms from two water molecules and four oxygen atoms of the acetate ligands (two O atoms per acetate group) as shown in figure 4.1(a). ZnO derived from ZAD typically crystallizes as the wurtzite polymorph and requires a high temperature treatment of above 300 °C.

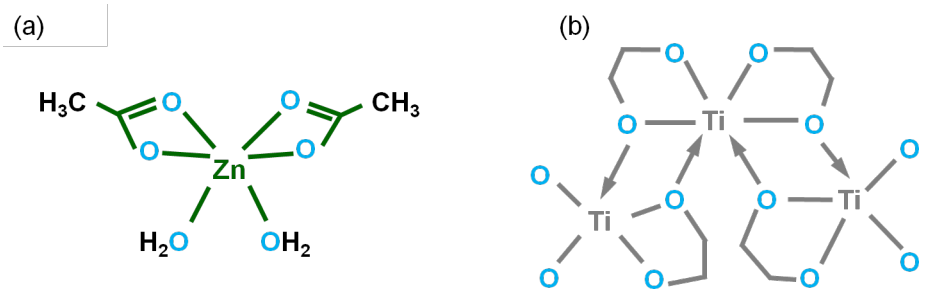

Figure 4.1.: Chemical structure of the precursors for the inorganic metal oxide semiconductors: (a) Zinc oxide (ZnO) precursor called zinc acetate dihydrate (ZAD). (b) Titania (TiO_2) precursor, known as ethylene glycol-modified titanate (EGMT). The arrows represent the coordination bonds. The zinc atom is shown in green, the oxygen atoms in light blue and the titanium atoms in gray. Carbon atoms saturated with hydrogen are at each crossover point.

Ethylene glycol-modified titanate (EGMT), also known as ethylene glycolate is used as the precursor for TiO_2 nanostructures. The chemical formula of EGMT is given as $C_4H_8O_4Ti$ and it is synthesized by Thomas Fröschl[1], using the synthesis route described in [88]. The precursor is obtained as crystalline powder, which requires a strong acidic environment to get dissolved. The unit cell of EGMT consists of TiO_6 octahedrons as seen in the sketch presented in figure 4.1(b). One oxygen atom of the ethylene glycol ($C_2H_2O_2$) ligands bridges two titanium atoms and the second oxygen atom is bound terminally to the titanium center. The powder crystalline reflexes of EGMT can be found in reference [89]. Crystallization of titania derived from EGMT can already be achieved at room temperature. Moreover, the crystalline phase of the resulting titania can be tuned from anatase to rutile by changing the pH value from above 2 to below 0 [90].

Structure-directing diblock copolymer templates

Two classes of amphiphilic diblock copolymer are used for structuring ZnO and TiO_2 films: poly(styrene-*block*-ethylene oxide), coded as P(S-*b*-EO) and poly(styrene-*block*-4-vinylpyridine), abbreviated as P(S-*b*-4VP). These diblock copolymers act as the structure-directing templates in the sol-gel synthesis route and govern the length scales of the

[1]Thomas Fröschl, group of Prof. Nicola Hüsing, Paris-Lodron University Salzburg, Hellbrunnerstr. 34, 5020 Salzburg, Austria

polymer	M_n [kg/mol]	PI	polymer block	M_n [kg/mol]	T_g [°C]
P(S-*b*-EO)	21.0	1.04	PS	16.0	75
			PEO	5.0	-63
P(S-*b*-EO)	30.0	1.07	PS	23.0	95
			PEO	7.0	-47
P(S-*b*-4VP)	23.3	1.04	PS	11.8	100
			P4VP	11.5	144
P(S-*b*-4VP)	75.0	1.10	PS	24.0	100
			P4VP	51.0	144

Table 4.1.: Properties of the structure-directing polymers: number average molecular mass M_n, polydispersity index PI, and glass transition temperatures T_g of the different polymer blocks are given.

resulting ZnO and TiO_2 nanostructures. Two different molecular weights of each of these two amphiphilic diblock copolymers are used throughout the entire study. For both families, the polystyrene (PS) block acts as the hydrophobic block. All the polymers are obtained from Polymer Source Inc., Canada and used as received. The chemical structure of both the classes of the template are drawn in figure 4.2. The specific temperatures and the polydispersity indices of the different polymers are given in table 4.1.

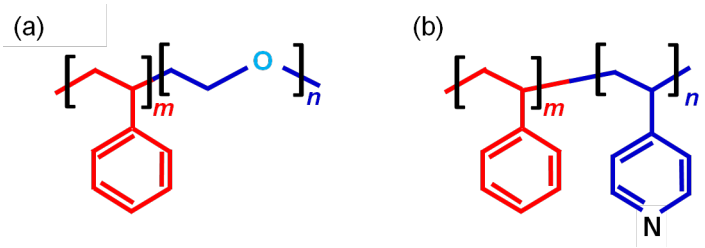

Figure 4.2.: Chemical structures of the two families of diblock copolymers used in the study. (a) P(S-*b*-EO) and (b) P(S-*b*-4VP) are shown as sketches where the oxygen atom of the PEO block is shown in light blue, the nitrogen atom of the P4VP block is shown in black, the hydrophobic block of each polymer is depicted in red and the hydrophilic blocks in blue color. The degree of polymerization for the individual monomer unit is depicted by *m* and *n*. The carbon atoms with terminal hydrogen atoms are present at each junction and at the empty line endings.

As shown in table 4.1, in the present study, a low and a high molecular weight derivative

of each of the two classes of the diblock copolymer templates is used. Hence, in total four diblock copolymer templates are used in this work.

For the low molecular weight P(S-*b*-EO), with $m = 154$ and $n = 114$ (see figure 4.2(a)), the fraction of PS is $f_{PS,low1} = 0.57$. Similarly for the high molecular weight derivative of the same polymer, $m = 221$ and $n = 159$, giving the fraction of PS, $f_{PS,high1} = 0.58$.

For the low molecular weight P(S-*b*-4VP), with $m = 113$ and $n = 112$ (see figure 4.2(b)), the fraction of PS is $f_{PS,low2} = 0.50$. For the high molecular weight P(S-*b*-4VP), with $m = 230$ and $n = 485$, the PS fraction is given as $f_{PS,high2} = 0.32$.

Dye

An indoline dye is used as the photosensitizer to absorb the incoming light in the DSSCs for the present study. It is a violet dye with the IUPAC name 5-[[4-[4-(2,2-Diphenylethenyl)phenyl]-1,2,3-3a,4,8b-hexahydrocyclopent[*b*]indol-7-yl]methylene]-2-(3-ethyl-4-oxo -2-thioxo-5-thiazolidinylidene)-4-oxo-3-thiazolidineacetic acid, abbreviated as D149 (Sigma-Aldrich). The chemical structure of the dye is shown in figure 4.3(a), the molecular formula for which can be written as $C_{42}H_{35}N_3O_4S_3$. The specialty of D149 is that it is free of any metal, as opposed to the commonly used ruthenium dyes and has shown power conversion efficiencies of more than 9 % in DSSCs with volatile liquid electrolytes [91]. D149 is reported to be highly suitable for the ZnO systems as the agglomeration of the Zn^{2+} ions at the interface upon dye adsorption is less. Additionally, it is more environmentally friendly and cheaper than the metal containing dyes. These factors play an important role in the mass production of DSSCs. Moreover, this dye has a high molar extinction coefficient of 68,700 M^{-1} cm^{-1} at 526 nm. This value is almost five times larger than that of the most commonly used ruthenium dye N719 (13,900 M^{-1} cm^{-1} at 541 nm) [92]. This allows for achieving promising efficiencies from thinner films of ZnO while using D149 as compared to N719.

The central indoline group acts as the electron-donating group, stabilized by additional phenyl rings (figure 4.3(a)). The indoline group is conjugated to an electron-accepting group, which acts as the binding group, thereby anchoring to the surface of the semiconductor [93]. The absorption spectra measurements have confirmed that the anchoring of the dye molecule on the ZnO surface is mainly caused by the formation of a bidentate complex between the carboxylate group and the polar ZnO surface. For the presented devices, the dye is dissolved in 1:1 volume ratio of acetonitrile, C_2H_3N and tert-butanol, $C_4H_{10}O$ with a 0:5 mM concentration. The solvents are purchased from Sigma-Aldrich. The dye solution is stirred overnight before being used and stored afterwards to be reused at room temperature, shielded from light.

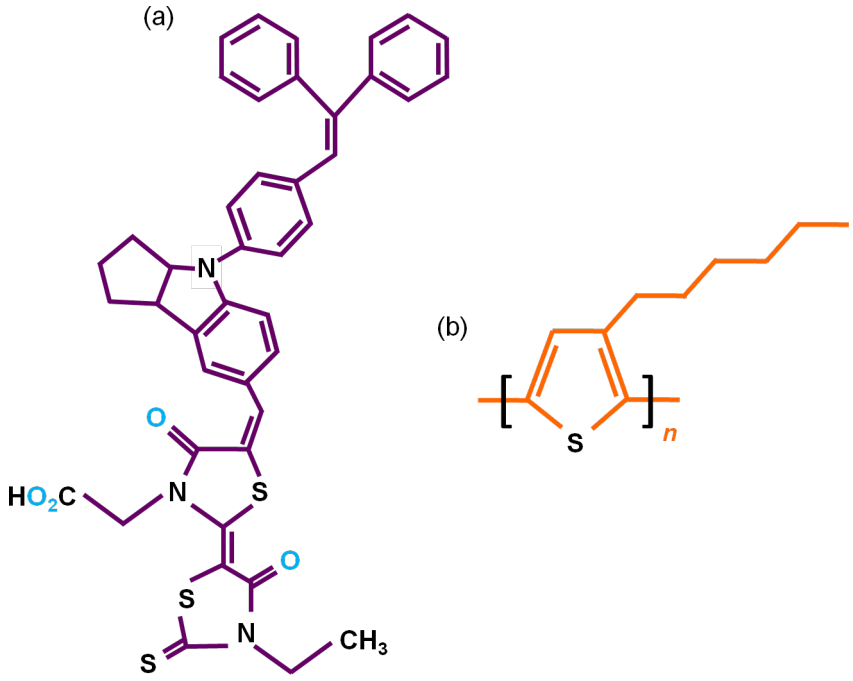

Figure 4.3.: (a) Chemical structure of the dye - D149. (b) Chemical structure of P3HT with the degree of polymerization represented by *n*. For both the sketches, the oxygen atoms are shown in light blue, the nitrogen, sulfur, carbon and hydrogen atoms in black. The carbon atoms with terminal hydrogen atoms are present at the junctions and the empty line endings.

Electrolytes and hole conductors

For the conventional DSSCs, ionic liquids or acetonitrile-based electrolytes are commonly used. It has been reported that the ionic liquids show a detriment in the performance above a certain thickness of the inorganic metal oxide active layer. This is majorly attributed to their high viscosity, which restricts the mass extraction of photocurrent. Hence, the acetonitrile-based electrolytes are favored for the present study. These electrolytes containing iodide-triiodide (I^-/I_3^-) ions are also reported to be suitable for outdoor applications due to their thermal stability, non-flammability, low volatility and low toxicity [94]. Two different acetonitrile-based electrolytes are used for the present investigations, one for the ZnO active layer and a second one for the zinc titanate active layer. For the ZnO system, an electrolyte solution consisting of 0.03 mol/L iodine (I_2), 0.3 mol/L lithium iodide (LiI) and 0.5 mol/L 4-tert-butylpyridine in acetonitrile (Sigma-Aldrich) is used (electrolyte system I). For the zinc titanate-based DSSCs, the liquid electrolyte solution consisting of 0.05 mol/L I_2, 0.1 mol/L LiI, 0.6 mol/L 1-butyl-3-methylimidazolium iodide (BMII) and 0.05 mol/L 4-tert-butylpyridine in acetonitrile : valeronitrile (Sigma-

Aldrich) volume ratio of 85 : 15 is prepared (electrolyte system II). Both the electrolytes (when they are freshly produced) are put on a mechanical shaker overnight before use.

For ss-DSSCs, the conventional conducting polymer, poly(3-hexyl-thiophene), (chemical formula: $(C_{10}H_{14}S)_n$) is used as the hole conductor [95–97]. The chemical structure of the polymer (P3HT) is demonstrated in figure 4.3(b). The backbone of the polymer chain consists of thiophene rings with alkyl chains having six carbon atoms. This makes the polymer soluble in organic solvents. The P3HT is obtained from BASF in a collaboration with Rieke Metals, with a purity of above 99 %. The weight average molecular weight is given as $M_w = 50$ kg mol^{-1} and a regioregularity of 95 %. A conductivity of $(1.3 \pm 0.3) \cdot 10^{-5}$ S cm^{-1} of the pure film annealed at 140 °C is measured, while the conductivity is determined to be (95 ± 20) S cm^{-1} after doping in iodine vapor [98].

4.2. Processing

For the synthesis of the ZnO as well as TiO_2 nanostructures, various steps are involved. The nanostructures for both the systems are obtained via sol-gel synthesis using a sacrificial diblock copolymer template. The various processes carried out in order to achieve the final nanostructured films consist of preparation of the solution or paste, deposition of the same on suitable substrates using different deposition methods, annealing of the as-deposited films wherever required and a final calcination step to remove the polymer and impart crystallinity to the nanostructures. An overview of all these different stages of synthesis and the methods is provided in this section.

4.2.1. Synthesis of nanostructures

For ZnO nanostructures, both low and high molecular weight derivatives of P(S-*b*-EO) and P(S-*b*-4VP) are used, whereas, for the synthesis of TiO_2 nanostructures, only the high molecular weight P(S-*b*-EO) is used (see table 4.1 for details about the diblock copolymers). As mentioned in section 4.1, ZAD is used as the precursor for ZnO, while EGMT is used as the precursor for TiO_2. Not only pure ZnO and TiO_2 nanostructures, but also the ZnO-TiO_2 nanocomposite structures are synthesized via the sol-gel approach. To crystallize the nanostructures, a high temperature treatment of 400 °C and 600 °C are given to the ZnO and ZnO-TiO_2 nanocomposite films, respectively.

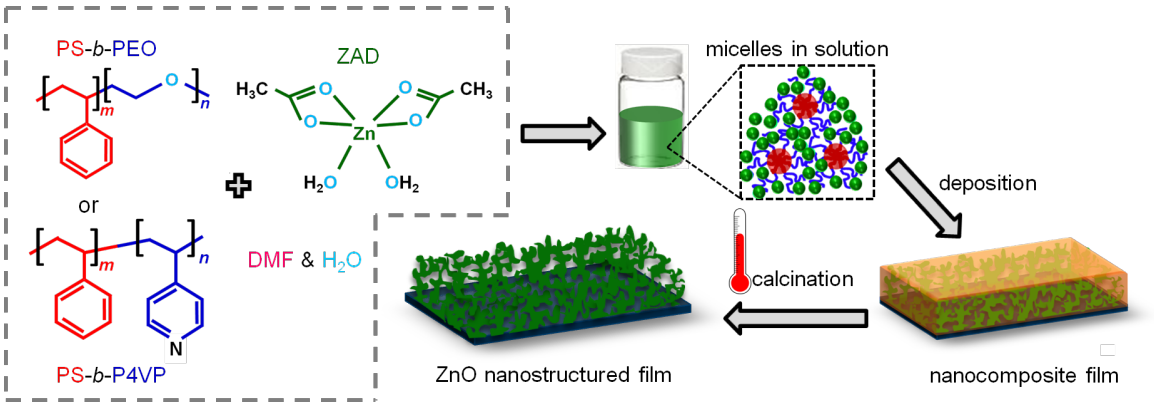

Figure 4.4.: Schematic overview of the sol-gel synthesis route using ZAD as the precursor. This is a solution-based route where the diblock copolymer is mixed with DMF and H_2O, acting as the good and the poor solvent respectively along with the addition of ZAD (shown in the glass vial with green solution). The micro-phase separation in the polymer leads to formation of micelles, as shown in the inset. The nanostructures synthesized in the solution are then deposited on a substrate to obtain a ZnO-polymer nanocomposite film, which is subjected to a high temperature calcination step to obtain the final crystalline ZnO nanostructured films.

Sol-gel synthesis with ZAD

The preparation of the ZnO sol-gel solution using both the P(S-*b*-EO) and P(S-*b*-4VP) copolymers is the same and uses the same solvents. A schematic illustration of the various steps involved in the synthesis route is shown in figure 4.4. The concentration of P(S-*b*-EO) (both low and high molecular weights) in the final sol-gel solution is maintained at 25 mg mL^{-1}, whereas, the same for low and high molecular weight P(S-*b*-4VP) is 15 mg mL^{-1}. Preparation of the sol-gel solution starts with dissolving the copolymer template in a so-called good solvent which dissolves both the blocks of the polymer equally well, which in present case is N,N-dimethylformamide (C_3H_7NO from Carl Roth GmbH; abbreviated as DMF). For this, the required amount of polymer is weighed into a pre-cleaned glass vial, where the solvent is added using a pipette. It should be noted that only half of the total volume volume of DMF required is added to the polymer. It needs to be ensured at this point that the polymer is still soluble in this reduced volume of DMF. The remaining DMF is added to the required volume of ZAD, pre-weighed in another glass vial. Both the mixtures are kept stirring on a magnetic stirrer for at least 30 min at room temperature to obtain clear solutions. These are then filtered with a 0.45 µm polytetrafluoroethylene (PTFE, $(C_2F_4)_n$, Carl Roth GmbH) filter. The next step is addition of the required amount of water (selective solvent) to the glass vial containing the polymer/DMF solution. The solutions are again subjected to stirring for another 30 min before they are mixed

drop-wise into a final vial with a motorized syringe (PHD 2000 Infuse/Withdraw, by Harvard Apparatus) using PTFE tubes. The tubes have a diameter of 1 mm and a length of about 20 cm. The injection speed is kept constant at 1 mL min^{-1}. The final sol-gel solution is stirred for not more than 60 min and is deposited on the desired substrate within this time using the methods described in section 4.2.2. The films obtained are stable under ambient conditions, but a high temperature calcination is required to obtain the final ZnO nanostructures as described below.

Sol-gel synthesis with EGMT

Synthesis of TiO_2 nanostructures using EGMT as the precursor and high molecular weight P(S-*b*-EO) as the structure-directing template is essentially a one-pot synthesis. The polymer is first weighed in a pre-cleaned glass vial and the required amount of DMF is added to it, keeping the polymer concentration at 15 mg mL^{-1}. The solution is stirred at least for 30 min after which it is filtered with a 0.45 µm PTFE filter. 37 % HCl and EGMT are then added to the solution successively. The solution is then allowed to stir on a magnetic stirrer for 30 min at room temperature, before it is heated up to 90 °C. The solution is stirred at this temperature for 15 min. Afterwards, a clear pale yellow solution is obtained which is then allowed to cool to room temperature, either before mixing it with the sol-gel solution obtained with ZAD, or coating it directly on a substrate. The films obtained from this sol-gel solution or from a solution containing mixture of ZnO and TiO_2 sol-gel solutions, need an annealing step to prevent the PEO block to form crystallites. This along with the final calcination step is described below.

Fabrication of ZnO paste

From the sol-gel solution for ZnO nanostructures, as obtained by the synthesis procedure described above, pastes are also prepared besides thin films. Custom-made nanocrystalline ZnO powder is obtained with different particle sizes via solution-casting (procedure described in section 4.2.2) of sol-gel solutions with desired compositions. The process including the synthesis of the powder as well as the paste requires four days in total. The steps involved for the fabrication of the paste (starting from the nanocrystalline ZnO powder) are represented in the form of a flow chart in figure 4.5. The routine is developed by following the synthesis protocol developed for screen-printing pastes for TiO_2 nanostructures by Ito et al. [99]. All the grounding steps mentioned in figure 4.5, are performed with the aid of a pair of marble mortar and pistil (Carl Roth GmbH). Details about the choice of the solvents for the preparation of the paste can be found in reference [99].

The final paste is deposited on the substrate (silicon, glass or FTO) via blade-coating

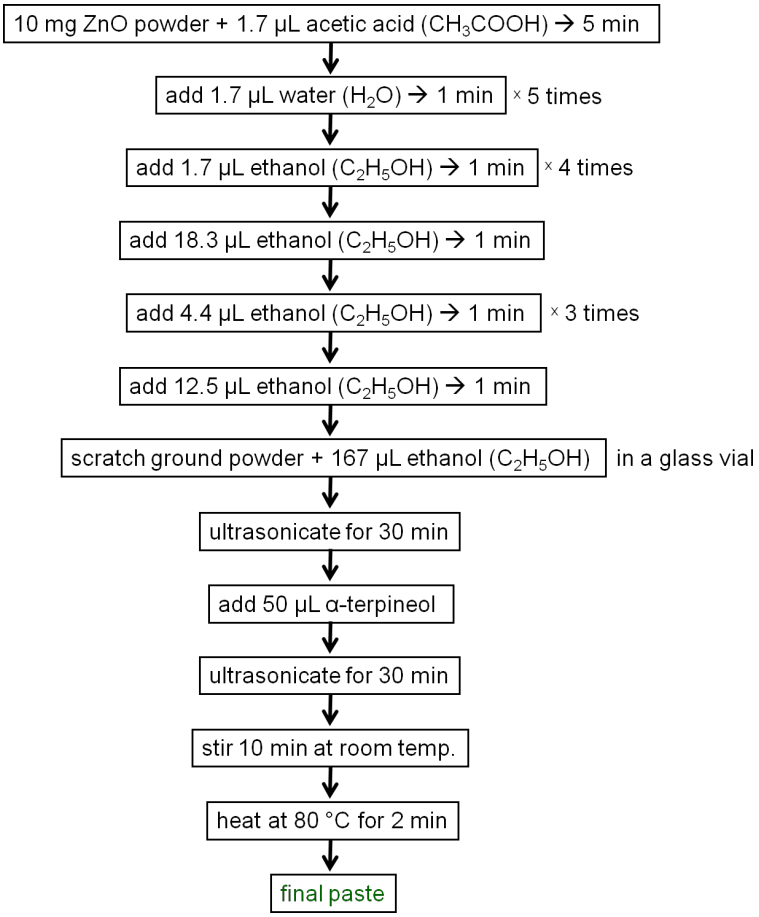

Figure 4.5.: Flow chart of the different steps involved in the fabrication of the ZnO paste from ZnO nanocrystalline powder. The time indicated in the boxed denote the grinding time and the numbers outside the boxes represent the number of times a particular step is repeated. The recipe presented is scalable depending on the number of substrates to be coated.

(section 4.2.2). For each substrate of (2.5 × 2.5) cm^2, 40 µL of the paste is blade-coated. After the first coat, the film is allowed to dry under ambient conditions for 15 min, after which, the film is heated to 120 °C on a heating plate (RET basic by IKA). The film is kept at this temperature for 5 min and then another blade coat is performed followed by drying and heating as mentioned after the first coat. The intermediate heating step ensures partial drying of the films, which helps in minimizing the distortion of the first film upon application of a subsequent coat.

In the presented investigations, the ZnO films prepared from the above-mentioned paste, are incorporated in ss-DSSCs. Hence, backfilling of the nanostructures is done using P3HT as the hole conductor via spin-coating (details about the deposition method is given in section 4.2.2). Various other routines are also established in literature in order to fill

the pores of the semiconductors using a suitable hole conductor, such as solution-casting or direct polymerization of monomers within the nanostructures [100]. In the present thesis, the backfilling procedure established by Rawolle et al. for TiO_2 nanostructures is implemented [61]. A 40 mg mL^{-1} P3HT solution in toluene is obtained after heating the solution up to 80 °C. Afterwards, the solution is cooled to room temperature and filtered with PTFE filters of 0.45 µm pore size into a pre-cleaned glass vial. The ZnO films are pre-soaked for 45 min in pure toluene bath. The films are taken out and directly put on the spin-coater. The purpose of this step is to remove the air trapped in the ZnO pores [101]. The P3HT solution is then dispersed on the ZnO film, which is still soaked with toluene. After waiting for 120 s, the spin-coater is started with the lowest acceleration to reach a speed of 500 rpm, where the sample is rotated for 60 s.

Annealing

Annealing is performed for the ZnO films backfilled with P3HT and for the films obtained from a sol-gel solutions containing EGMT. For the P3HT films, annealing is necessary for improving the crystallinity of the films which is an important aspect for charge transport (see section 2.1). The backfilled films are kept on a heating plate (RET basic by IKA), pre-adjusted to 140 °C. After 10 min of annealing, the samples are removed from the heating plate and cooled rapidly to room temperature by putting them directly on a metal plate at room temperature. This ensures quenching of the crystalline structures that evolved during the annealing process.

Annealing of the TiO_2 or ZnO-TiO_2 nanocomposite films is done after the deposition of the respective sol-gel solutions on the desired substrate. This is an essential step to define the nanostructures obtained after deposition of the sol-gel solutions. In the absence of this step, the PEO block of the P(S-*b*-EO) template tends to crystallize in the form of large spherulites as discussed in section 2.1. For the annealing step, a heating plate is pre-set to 90 °C and the freshly deposited films are placed on the heating plate as soon as the temperature is reached. It should be noted that the films after deposition should be transferred on the heating plate without any delay. The films are annealed for 30 minutes, before they are rapidly cooled to room temperature and calcined afterwards as described below.

Calcination

High temperature treatment is implied to the films produced via sol-gel synthesis. Calcination not only removes the diblock copolymer template from the films, but also provides crystallinity and structural organization to the nanostructures. Calcination of the films is

performed in air without exception in a tube furnace by GERO or Hereaus instruments. For this purpose, the films are inserted into the ceramic tube of the furnace, both ends of which are closed by ceramic wool. A calcination protocol is programmed to heat up the furnace slowly to the desired temperature. The time required for the calcination for all the films presented in the thesis is set to 30 minutes (if not specified differently), after which the samples are allowed to cool to the room temperature in the furnace. Different calcination temperatures ranging from 400 to 1000 °C are employed with varied heating rates of 2.5 or 5.78 °C min^{-1}, as mentioned in the chapters 5 to 8. If not specifically mentioned, a standard calcination temperature of 400 °C is employed for 30 minutes to the films with a heating ramp of 5.78 °C min^{-1}.

4.2.2. Deposition methods

ZnO, TiO_2 as well as ZnO-TiO_2 nanocomposite structures synthesized via sol-gel approach are deposited on solid substrates in the form of films for implementing the structures in practical applications. The commonly used substrates are glass substrates (26 × 76 mm^2, Carl Roth GmbH) and silicon substrates (wafer with diameter of 100 mm, boron-doped, (100)-orientation, Si-Mat), which are cut into smaller pieces with dimensions required for a specific experiment, using a diamond or a glass cutter. The substrates are then cleaned in an acid bath as described below. Several coating techniques have been developed for solutions in laboratory as well as industrial scale, such as spin-coating, solution-casting, blade-coating, spray deposition, ink-jet printing, slot-die coating and screen printing. For the investigations shown in the present thesis, spin-coating is used to obtain thin films. For slightly thicker films, needed for application in DSSCs, blade-coating and spray deposition are used, whereas, for powder films, solution-casting is implemented.

Substrate cleaning

In order to obtain comparable results, it is required to have reproducible samples. Hence, to ensure identical substrates for every experiment performed, a cleaning of the silicon and the glass substrates is of utmost importance. Cleaning also ensures a defined thickness of the native oxide layer on the substrates. It is performed via the procedure established in [102]. The required amounts of deionized water (H_2O), 30 % hydrogen peroxide (H_2O_2) and 96 % sulfuric acid (H_2SO_4), as mentioned in table 4.2, are mixed in that order and the temperature of the mixture is increased to 80 °C.

Once the temperature is attained, the pre-cut substrates are immersed into the bath, stacked in a teflon holder. The samples are kept in the bath for exactly 15 min and then taken out and subsequently put into a water bath. Afterwards, each substrate is

chemical	amount
deionized water (H_2O)	54 mL
hydrogen peroxide (H_2O_2)	84 mL
sulfuric acid (H_2SO_4)	198 mL

Table 4.2.: The composition of the acid bath used to clean the silicon and glass substrate. The required volumes of deionized water, hydrogen peroxide and sulfuric acid are listed.

separately rinsed with deionized water (approximately 250 mL per substrate), followed by drying them in an oil-free nitrogen flow. The cleaned substrates acquire a hydrophobic surface and are stored in clean Petri dishes. They are coated within six hours after cleaning. It is made sure that each bath is not used more than three times for cleaning 10 substrates per batch.

Spin-coating

Spin-coating is a fast non-equilibrium process to obtain thin homogeneous films. The entire process of spin-coating can be divided into three steps: first, most of the solution placed on the substrate is flung-off, already during the acceleration of the sample in a turbulent process. In the second step, convection is the dominating process, which is followed by the third step, which is diffusion of the solvent through the surface [103].

In order to coat the samples, described in the present thesis, a Delta 6 RC TT (Süss MicroTec Lithography GmbH) spin-coater is used. The sample is placed on a rubber mat, which is fastened to the rotation table of the spin-coater via vacuum. A defined volume of the solution is dispersed on the substrate to cover it entirely, before the spin-coater is started. The spin-coater is programmed to attain a certain rotation speed with a defined acceleration and to rotate for the selected time scale. The sample is dismounted from the vacuum chuck after the process and is wiped with a clean tissue at the back side to remove traces of left-over solution. For the present experiments, a standard acceleration of 400 rounds s^{-1} is used to attain the fixed rotation speed of 2000 rpm for a time of 60 s, if not mentioned otherwise. Also the temperature and the relative humidity are monitored in the range of 20-24 °C and 34-41 %, respectively. The thickness of the films obtained from pure polymer solutions can be predicted using an empirical formula which shows a linear relation between the film thickness and the concentration for a certain regime, where the viscosity of the solution can be neglected [104]. For the present investigations of spin-coating sol-gel solutions, film thicknesses in the range of 20 to 200 nm are achieved.

The thickness of the films can be tuned to a certain extent by using different rotation speeds and time. For slower rotation speeds, higher film thicknesses are reported [32].

Solution-casting

Thicker films as compared to the spin-coated films are achieved via solution casting. The thickness is tuned by the amount of solution placed on the substrate. The process of solution-casting is quite arduous, as it depends on a number of parameters for producing homogeneous films. For the drying of polymer solution during solution casting, often competing evaporation-driven flow and Marangoni counter-flow have been reported to result in the formation of inhomogeneous films [105]. Due to the presence of thermal fluctuations, capillary waves are always present which results in a different structure on the edges of the film as compared to the average film, at least on capillary length scales.

For the present experiments, the substrates are placed in a solution casting box or a desiccator and are horizontally aligned with respect to the base using an adjustment laser. A defined volume of the solution is dispersed on the substrate in a way that the entire area of the substrate is covered. Afterwards, the lid of the box or the desiccator is closed and the set up is left undisturbed for at least 48 hours. After calcination of these solution-cast films, it is observed that always a powder film composed of crystalline ZnO nanoparticles is obtained. The powder does not adhere strongly to the substrate unlike the solution-cast ZnO-polymer composite film before calcination. Hence, it is not possible to use the solution-cast films directly for applications. Due to this fact, the nanocrystalline powder is scratched off from the substrates and used for the fabrication of a paste (refer to section 4.2.1 for details), which is then coated on the substrates via blade-coating, as described in the next paragraph.

Blade-coating

The paste prepared using ZnO nanocrystalline powder as illustrated step-by-step in figure 4.5 is deposited on the substrates via blade-coating. The thickness of the films is defined by the scotch tape which acts as the spacer. A sketch of the blade-coating set up is shown in figure 4.6.

The strips of the scotch tape are attached to both sides of the pre-cleaned substrate as shown in figure 4.6. The ZnO paste is placed on the edge of the substrate as represented in green in the sketch. The material is then homogeneously dispersed over the whole substrate using a glass slide (cleaned by rinsing with ethanol) which is moved in the direction indicated by the arrow (figure 4.6). The angle of the glass slide with respect to the substrate is not more than 45°. After intermediate heating, a second blade coat can

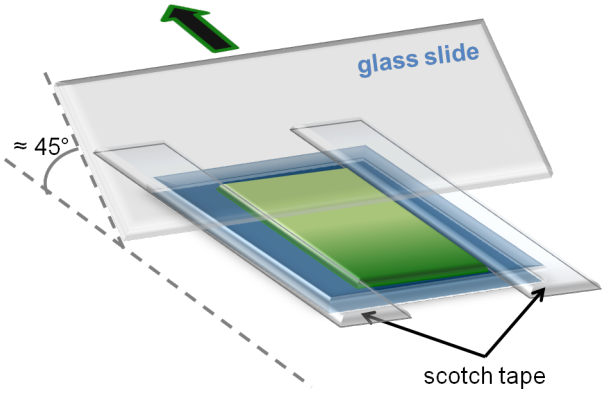

Figure 4.6: A sketch of the blade-coating set up. Two strips of scotch tapes are attached on the edges of the substrate in order to define the film thickness. The ZnO paste (green) is dispersed over the entire substrate with the aid of moving a glass slide in the direction indicated by the arrow.

also be applied to the same sample in order to increase the film thickness. The strips of the scotch tapes need to be removed before putting the samples on the heating plate in order to prevent the diffusion of the glue from the tape to the film. As an alternative, multiple strips of scotch tape can be fixed on top of each other to achieve a thicker spacer which yields a thicker film upon a single blade coat. For the presented films, a maximum thickness of 2 µm is achieved via this technique (using single strips of scotch tapes on each side of the substrate as spacers).

Spray deposition

Spray is commonly referred to a beam of small droplets coming out of a nozzle. These droplets are generated by the process termed as atomization, where a liquid is converted into small droplets with the aid of the energy provided by a compressed carrier gas [106]. The breaking up of the liquid jet basically depends on its density, kinematic viscosity and the surface tension. At the exit point of the nozzle (commonly named as orifice), the solution has an angular and downward velocity due to lateral pressure differences, which causes a widening of the spray, thereby forming the so-called spray cone.

The angular velocity of the droplets drive them apart from each other due to which the diameter of the cone enlarges and the density of the droplets in the beam decreases [107, 108]. This demonstrates that a large distance between the sample and the spray nozzle results in a more homogeneous deposition of the film due to smaller droplet size and a large coverage of the spray cone, but on the other hand, the amount of material that reaches the substrate is also significantly reduced. For the entire atomization process, the pressure of the carrier gas, the orifice diameter and the flow rate of the solution are also important factors and need crucial optimization in order to achieve reproducible films.

The temperature of the substrate has a major impact on the sprayed solution, in monitoring the evaporation of the residual solvent from the film, spreading of the droplets on the surface, chemical reactions in the sprayed solution and the final deposited material.

Viguié and Spitz have presented a model, schematically shown in figure 4.7 describing the processes occurring in the incoming spray cone when the substrate is at different temperatures [109].

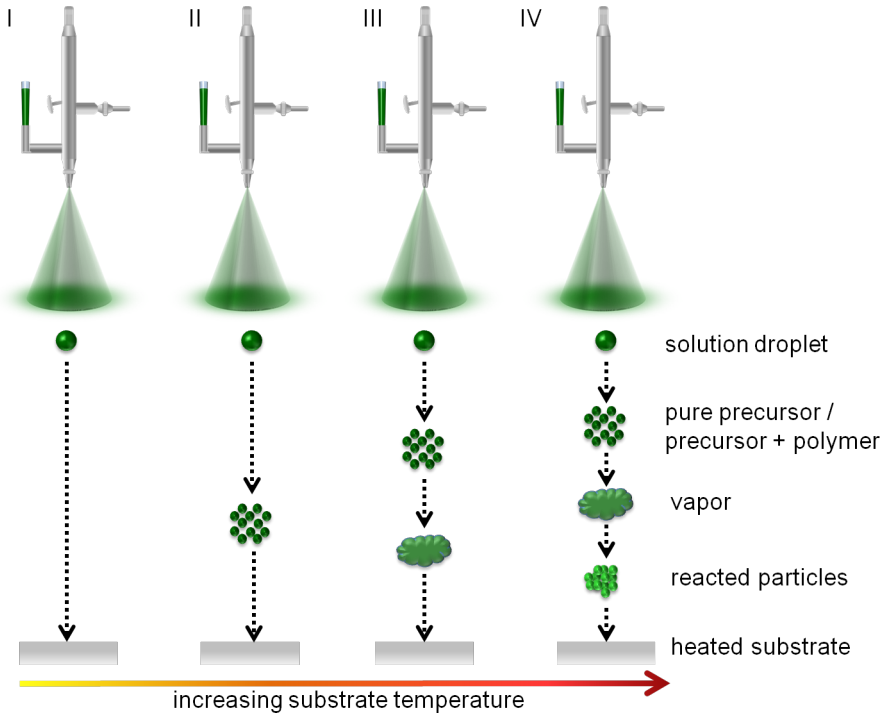

Figure 4.7.: Pictorial representation of the influence of different temperatures of the substrate on the spray-deposited solution. The nature of the material deposited with increasing substrate temperature is described in the text according to the reference [109].

According to the model represented in figure 4.7, four different processes are identified depending on different substrate temperatures as described below:

- **Process I:** At low temperatures of the substrate, the liquid droplet arrives and spreads over the substrate. The solvent dries over time, leaving behind a film of nanoparticles which may further react (figure 4.7I).
- **Process II:** At temperatures close to the boiling point of the solvent used for spray deposition, the small amount of solvents present in the incoming droplets, evaporates and solid material is deposited on the substrate as a dry film (figure 4.7II). The process is commonly termed as airbrush spray-coating [110].
- **Process III:** At even higher temperatures, the residual solvent in the incoming droplets evaporates gradually leading the particles to interact with each other or decompose during the flight and also on the substrate surface. This type of deposition is commonly termed as chemical vapor deposition (CVD) (figure 4.7III) and often guarantees high purity of the deposited material.

- **Process IV:** At very high temperatures of the substrates, the solvent evaporates completely from the incoming sprayed droplets. From the energy derived from the high temperature of the substrate, the incoming nanoparticles undergo chemical reactions. These reacted particles are then deposited on the substrate (figure 4.7IV).

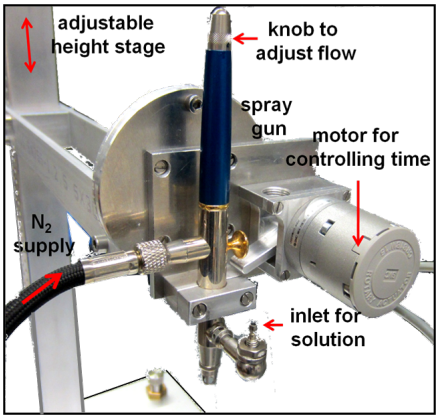

Figure 4.8: Photograph of the custom-made semi-automatized spray set up. The important parts are labeled.

An image of the automatized spray setup used for the present investigations is shown in figure 4.8. Different parts of the whole setup are depicted, the most important of which is the spray gun (Harder & Steenbeck; model Grafo T3, nozzle diameter = 0.4 mm). The spray gun is mounted on a stage with controllable height and angular axis. The distance and the angle of the spray nozzle with respect to the substrate is kept fixed to 16 cm and 90°, respectively. The trigger of the gun is coupled to a rotary actuator which is in turn connected to a time controller. For all the current spray depositions, a time of 10 s per shot is used. Nitrogen is chosen as the carrier gas for all the experiments shown in the thesis. The pressure of the carrier gas is kept fixed at 2 bars using a manometer for all the experiments. The flow rate of the solution is kept fixed to 20 to 25 µL s^{-1} by adjusting the knob present on top of the spray gun as shown in figure 4.8. The substrate is kept at 80 °C (if not specified otherwise), during the spray deposition. Multiple spray shots are delivered on a single substrate to attain film thicknesses up to nearly 40 µm for the presented films. Arrival of a fresh spray shot is always followed by cooling down of the substrate by 1-2 °C. Hence, a waiting time of 5 s is maintained between two consecutive spray shots. Thus, the used parameters cause the spray deposition to follow process I.

4.2.3. Solar cell assembly

The solar cells produced in this thesis are dye-sensitized solar cells (DSSCs) based on two different architectures; the liquid electrolyte-based and P3HT-based (solid state DSSCs, abbreviated as ss-DSSCs). The ss-DSSCs have the design of an inverted solar cell, where a blocking layer is used below the active layer. The individual steps involved in the

fabrication of the devices are sketched in figure 4.9. The individual steps are explained in more details below.

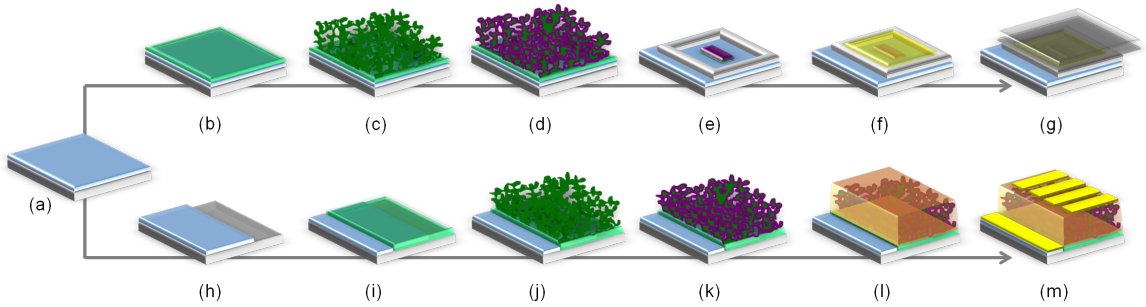

Figure 4.9.: Sketch of different steps for the fabrication of electrolyte-based and P3HT-based dye-sensitized solar cells (ss-DSSC). Both types of device architecture starts with a glass substrate coated with FTO. For electrolyte based DSSC: FTO-coated glass substrate is cleaned with organic solvents (a), and subsequently coated with a blocking layer (b). This is followed by the deposition of the nanostructured zinc oxide or zinc titanate film (c). The nanostructures are soaked in the dye (d). The active layer is scratched off, leaving behind only a small area, around which a teflon spacer is attached with grease (e). The electrolyte is filled within the spacer, covering the active area (f) and the platinum counter electrode is mounted on top (g) in order to obtain the final device.For ss-DSSC:One side of the FTO is etched and the substrate is cleaned (h), followed by the deposition of the blocking layer, leaving a small area of the FTO free as a contact for the I/V measurements (i). The active layer deposition (j) and the dye-soaking steps (k) are identical to the electrolyte-based DSSCs. (l) Backfilling by P3HT followed by the deposition of the gold electrodes on top (m) to obtain the final device.

Substrate preparation

The substrates used for all the solar cells reported are glass coated with fluorine-doped tin oxide (FTO, SnO_2), obtained from Solaronix (TCO10-10, (10×10) cm^2, 1.0 mm thickness, FTO sheet resistance $\approx 10\,\Omega$ cm^{-1}) which are cut into pieces of $(2 \times 2)\,$cm^2. For the electrolyte DSSCs, the pre-cut substrates are directly cleaned with the organic solvents (figure 4.9(a)), whereas, for ss-DSSCs, a thin area of the FTO is etched from one side of the substrate. For this, the FTO substrate is partially covered with adhesive tape (tesa), leaving a small area exposed which is treated by a paste of zinc powder in deionized (DI) water. 37 % HCl is then added dropwise on top of the paste in order to etch away the FTO layer underneath. The protective tape is removed and the substrate is rinsed with water and dried in nitrogen air-flow (figure 4.9(h)). Both the etched and the unetched substrates are first cleaned in an ultrasonic bath using Alkonox® (16 g L^{-1}) detergent for 10 minutes. The substrates are rinsed with DI water and directly placed

in a second bath of ethanol (C_2H_5OH) which is used to clean the substrates again for 10 minutes in the ultrasonic bath. After this, the substrates are individually rinsed with fresh ethanol and blow dried with nitrogen.

Blocking layer

For the ss-DSSCs, a compact ZnO hole-blocking layer is always used in order to minimize the recombination of the holes and electrons at the FTO electrode. In order to prepare the blocking layer, 150 mg of ZAD is mixed with 1 mL of 2-methoxyethanol in a pre-cleaned glass vial. The mixture is ultrasonicated for 10 minutes, after which a turbid solution is obtained. To this, 30 µL of diethanolamine is added and the solution is allowed to stir for 5 minutes at room temperature, until a clear solution is obtained. This solution is then directly spin-coated on the pre-cleaned substrates with a rotation speed of 1500 rpm for 30 s. The slowest acceleration of the spin-coater is used. It should be kept in mind that for the ss-DSSCs, a narrow area of FTO should be protected (figure 4.9(i)) using a piece of tape before spin-coating the hole-blocking layer in order to contact the FTO during I/V measurements. The tape is removed afterwards. For the elctrolyte DSSCs, the blocking layer is deposited on the entire substrate (figure 4.9(b)). The films are calcined afterwards as mentioned in section 4.2.1. This ZnO blocking layer is used for both types of solar cells when ZnO is used as the material for the active layer of the device.

However, for DSSCs based on zinc titanate active layers, a $TiCl_4$ (Sigma-Aldrich) treatment is given to the substrates in order to obtain a highly pure layer of thin titania. Since zinc titanate is only implemented in electrolyte-based DSSCs in the present thesis, etching of the FTO is not required. This thin titania layer not only acts as the blocking layer, but also improves the contact between the active layer and the substrate [11]. For the treatment, the pre-cleaned substrates are immersed in a bath of 50 mL DI water and then 1 mL of 2 M $TiCl_4$ solution (recipe for the preparation of the 2 M $TiCl_4$ solution can be found in [111]) is added drop-wise on top on the substrates. The bath is then heated up to 70 °C. The samples are removed from the bath after 45 min and rinsed with DI water followed by ethanol before drying with nitrogen.

Deposition of nanostructures

The ZnO and zinc titanate nanostructures are deposited by various methods, as described in section 4.2.2. The synthesis of the nanostructures is described in detail in section 4.2.1. For coating the substrates for ss-DSSCs with the active layer, again the protected FTO area is covered with adhesive tape (tesa) (figure 4.9(j)). For liquid DSSCs, the active layer is coated on the entire substrate (figure 4.9(c)). The deposited nanostructures are subse-

quently calcined in order to remove the copolymer template and to impart crystallinity to the nanostructures.

Dye

The samples with the calcined ZnO or zinc titanate nanostructures are heated to 200 °C for 5 min to remove any bound atmospheric water. The samples are then directly put into the D149 dye solution after they are cooled to 80 °C for 1 hour. During this time, the container is wrapped with aluminium (Al) foil and is stored undisturbed at room temperature. Afterwards, the samples are rinsed with 1 mL of ethanol per sample in order to remove superfluous dye solution and dried with nitrogen (figure 4.9(d) and (k)). For storing the dye-soaked substrates, cleaned Petri dishes wrapped with Al foil are used. For the liquid DSSCs, most of the active layer is scratched off using a teflon scalpel after dye soaking, leaving behind an area of about 0.15 cm^2. A (25 × 20 × 0.1) mm^3 teflon spacer with a hole of (18 × 12) mm^2 is used as the reservoir for the liquid electrolyte (figure 4.9(e)). The teflon spacer is coated with grease on both sides to prevent leakage of the liquid electrolyte.

Backfilling of nanostructures

For electrolyte DSSCs, 250 µL of the desired electrolyte is deposited drop by drop on the active area surrounded by the teflon spacer (figure 4.9(f)). All the steps involved in the fabrication of DSSCs after the dye soaking, are performed under minimized light conditions. For the ss-DSSCs, backfilling of the nanostructures by spin-coating P3HT solution is performed as described in section 4.2.1 (figure 4.9(l)).

Counter electrode

For the electrolyte DSSCs, platinum electrodes are prepared by blade-coating the commercial platinum (Pt) paste (PT-1, Dyesol) on pre-cleaned FTOs followed by a temperature treatment at 60 °C for 2 hours in an oven. Finally, the films are heated to 400 °C for 15 min with a ramp of 175 °C h^{-1}. It should be noted that for blade coating of the Pt paste, two strips of scotch tape are fixed one on top of the other on each side of the substrate, which acts as the spacer to obtain a film from the commercial paste. The electrode is placed on the electrolyte solution and pressed down to squeeze out the excess electrolyte solution. The grease applied to the teflon spacer, placed in between FTO and the Pt electrode, holds them together. However, for providing additional stability to the set up and make it convenient to contact the respective electrodes for the I/V measurements

without any leakage of the liquid electrolyte, Mauly paper clips are used to hold the FTO and the Pt electrode firmly in place (figure 4.9(g)).

For the ss-DSSCs, gold is deposited via a thermal evaporation setup, built by Robert Meier [79]. The samples are placed upside down into a shadow mask with 4 rectangular openings for the gold contacts. The area on the samples finally covered by gold are referred to as pixels. Between 160 to 190 mg gold is deposited within 2 min under a starting pressure of less than $3 \cdot 10^{-5}$ mbar and a working pressure of up to $8 \cdot 10^{-5}$ mbar. After the deposition of the electrodes, the annealing step to improve the crystallinity of P3HT is carried out as mentioned in section 4.2.1. The active area of one pixel of the solar cell is defined as the overlap of FTO and gold contacts, which is typically around 0.15 cm^2 (figure 4.9(m)). The accurate area is evaluated via the ImageJ v1.42q software from the optical microscopy images for each pixel. A short cut between the gold and the FTO is avoided during contacting of the cell at the outer edges, where the FTO is etched in the first step of solar cell preparation.

5. ZnO nanostructures using pure precursor

The considerable interest in the nanometer-sized particles having diameters in the range of 1 to 100 nm stems from their extraordinary properties such as high reactivity, high surface area and unusual electro-optical and magnetic properties [112]. Nanoparticles with these exceptional features have in turn, contributed largely in nurturing the field of electronic, optical and photonic applications over the recent decades [113]. Most of the nano-sized particles are synthesized via liquid, gas or solid-state routes [114, 115]. Sometimes, a combination of two or more conventional routes are also used for the development of complex nanomaterials. Among these approaches, the liquid route comprises of solution-based techniques, which can be largely used for the synthesis of elemental nanoparticles such as gold and platinum; binary nanomaterials such as titania (TiO_2), zinc oxide (ZnO) and cadmium telluride (CdTe) and complex oxide nanomaterials such as $BaTiO_3$ and magnesium hydroxide sulfate hydrate [113].

Among all these nanomaterials, ZnO is under consideration for the present chapter. It is a wide band gap II-VI compound semiconductor, which is transparent in the visible region and absorbs light in the UV region of the electromagnetic spectrum [34]. The material also shows piezoelectric properties [116]. Additional advantages include its stability towards thermal degradation as well as mechanical forces and its easy availability [117]. Combined with these advantageous properties of ZnO, the miniaturization of the material has resulted in an assortment of applications. Some examples include sensors fabricated using MEMS technology, ethanol, oxygen and ammonia gas sensors, probe for atomic force microscopy cantilevers, ultrasonic transducer arrays operating at 100 MHz and thin film transistors [118–122].

Solution-based approaches to synthesize ZnO nanoparticles mainly include emulsion and miniemulsion techniques, hydrothermal synthesis, low temperature wet chemical methods and sol-gel synthesis [113,123,124]. Most of these synthesis routes employ pure or hydrated zinc salts as the precursors for ZnO. Commonly used commercial precursors include zinc carbonate ($ZnCO_3$), zinc chloride ($ZnCl_2$), zinc sulfate ($ZnSO_4$), zinc nitrate hexahydrate

($Zn(NO_3)_2.6H_2O$) and zinc acetate dihydrate ($Zn(CH_3COO)_2.2H_2O$) in combination with various solvents acting as the reaction medium [125].

In the present chapter, the aim is to establish a straightforward routine to obtain ZnO nanoparticles. Zinc acetate dihydrate, abbreviated as ZAD, is chosen as the commercial precursor in association with the commonly used solvent, N, N-dimethylformamide (DMF). For most of the above-mentioned applications, two-dimensional thin films are required. Hence, the nanoparticles synthesized are deposited on silicon/glass/FTO-coated glass substrates via different deposition methods, which deliver thin films with varied thicknesses, specifically needed for a particular application. In the present chapter, three pathways of producing ZnO nanostructured films are investigated. The spin-coating technique results in a thin homogeneous film of ZnO nanoparticles, but with thicknesses limited to 80-100 nm. Solution-casting is selected as the second technique to obtain films with thickness in the range of 400-500 nm. The third method used is spray coating, which provides a high degree of flexibility in the achievable film thickness in the range of few microns.

The main focus of the present chapter is to develop the ZnO nanostructured films towards application in photovoltaics. Among the various categories of solar cells available, the dye-sensitized solar cells (DSSCs), since their discovery in 1991, have become most successful in terms of power conversion efficiency, although drawbacks regarding the lifetime of the devices and the sealing of the liquid electrolyte in the device impose inherent limitations [126]. Conventionally launched with TiO_2 as the electron conducting layer of the DSSCs, power conversion efficiencies up to 15 % has been achieved till date [13]. For a similar device using ZnO as the active layer, promising efficiencies have been reached over 6 % [127]. Given that the electron mobility in ZnO is almost twice than that of TiO_2, further investigations using ZnO as the material for the active layer is highly demanding to improve the device performance [128,129]. As mentioned in section 2.3.1, the thickness and the morphology of the active layer are the two most crucial parameters for efficient functioning of the device. Optimization of these features are performed, as described within this chapter. In order to obtain a reasonable film thickness, which is reported to be in the range of 18-20 µm for ZnO-based DSSCs, spray deposition is employed as the method for production of the active layer in the present chapter [127]. Active layers having thicknesses in the range of 200 nm to 35 µm are studied for their performance in DSSCs.

In order to investigate the film morphology on the surface and in the film volume, scanning electron microscopy (SEM) and grazing incidence small angle x-ray scattering (GISAXS) are employed. The crystallinity and the optical properties of the films are studied via x-ray diffraction (XRD) and UV/Vis spectroscopy, respectively. To probe the

structure-functional relationship, the films obtained via spray deposition are incorporated into active layers in DSSCs and the I/V characteristics of the solar cells are studied. The first section of this chapter entitles the spin-coated and the solution-cast films obtained from the ZnO nanoparticles (section 5.1). The morphology and crystallinity of these films are discussed in sections 5.1.1 and 5.1.2, respectively. This is followed by the results obtained for the thin films (section 5.1.3). The spray-deposited films are discussed separately in section 5.2. The structural characterization of these films is performed in a more sophisticated manner, using GISAXS during in-situ spray deposition. The experimental set up is explained in section 5.2.1 followed by the results obtained by probing the structural evolution in the film (section 5.2.2). The crystallinity of the films is investigated via XRD. The optical properties and the performance of the films as the active layer in DSSCs are reported in sections 5.2.3 and 5.2.4, respectively. The results obtained from these investigations are discussed in section 5.2.5. The summary of the entire chapter is enclosed in section 5.3.

5.1. Spin-coated and solution-cast films

The films investigated in this section are prepared from a solution of ZAD in DMF with varied concentrations. For the spin-coated films, three different concentrations are chosen: 15, 25 and 50 mg mL^{-1}. The solution is prepared by dissolving ZAD in DMF by stirring the contents for 30 minutes under ambient conditions. Every solution is passed through teflon filters with 0.45 µm pore size in order to remove dust particles before deposition on a substrate. The spin-coating parameters for all the films are kept constant at 2000 rpm for 60 s with an acceleration of 400 rounds s^{-1}. For the solution-cast films, the ZAD solution with 25 mg mL^{-1} concentration is used. The solution is dropped on a horizontally laser-aligned substrate and a waiting time of 48 hours is provided till the solvent is evaporated from the substrate leaving behind a solid film. Afterwards, all the films are calcined in air at 400 °C, as described in section 4.2.1 to obtain crystalline ZnO.

5.1.1. Morphology

All the spin-coated and the solution-cast films are investigated via scanning electron microscopy (SEM), which is a direct imaging technique probing the real-space local topography of the films. A good impression about the homogeneity of the film along with an approximate estimation of the particle sizes in the films is obtained via this technique. In addition, reciprocal-space analysis of the films is done via grazing incidence small angle x-ray scattering (GISAXS) for large scale information. Due to the low absorption and

the large footprint of the x-rays, not only the surface, but also the morphology within the volume of the films is probed, when the incident angle is chosen higher than the critical angle of the material under consideration. A combination of these two methods allows access to the film morphology both qualitatively and quantitatively.

Morphology of spin-coated films

The SEM topography images of the calcined spin-coated films from solutions with different ZAD concentrations are shown in figure 5.1. The bright regions in the image denote the ZnO (due to higher conductivity of the material) obtained after calcination of ZAD. The morphology of all the films appear similar stating that the change in concentration of the solution does not affect the surface morphology. The nanoparticles obtained from a solution with concentration of 25 mg mL^{-1} look inter-connected with one another (figure 5.1(b)), whereas the film obtained from the solution with 50 mg mL^{-1} shows clustered nanoparticles (figure 5.1(c)). The film with the lowest concentration appears darker (figure 5.1(a)) as compared to the other films signifying that the amount of material deposited on the substrate is drastically reduced. The average particle size observed for all the films is in the range of 15 to 20 nm.

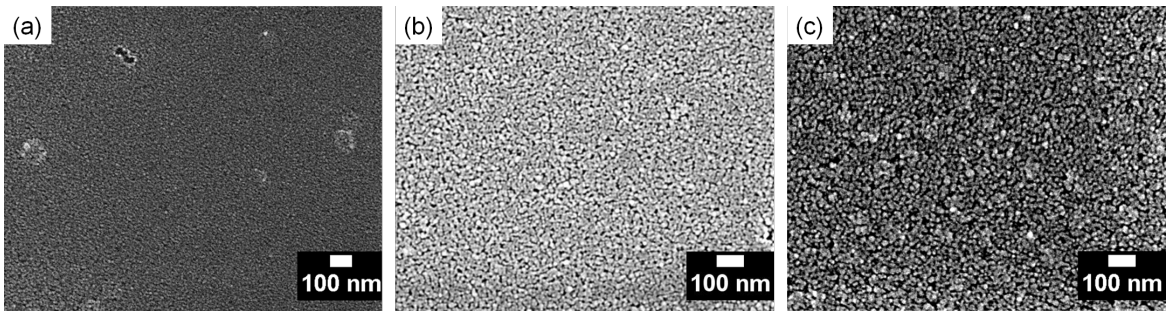

Figure 5.1.: SEM topography images of calcined ZnO spin-coated films, prepared with ZAD solutions with concentrations of (a) 15 mg mL^{-1}, (b) 25 mg mL^{-1} and (c) 50 mg mL^{-1}.

Among all the films, the one prepared using the solution having the concentration of 25 mg mL^{-1} shows the most homogeneous distribution of length scales of the nanostructures on the substrate. Hence, for further investigation of the morphology in the film volume for this particular sample, GISAXS measurements are performed at the P03 beamline of the PETRA III storage ring in DESY as described in section 3.1.5. The data obtained along with the analysis are shown in figure 5.2.

The 2d GISAXS data are obtained for the spin-coated films both before (as-prepared) and after calcination and are shown respectively in figures 5.2(a) and (b). Broad scattering features at low q_y are observed for the as-prepared film. Whereas, after calcination, very

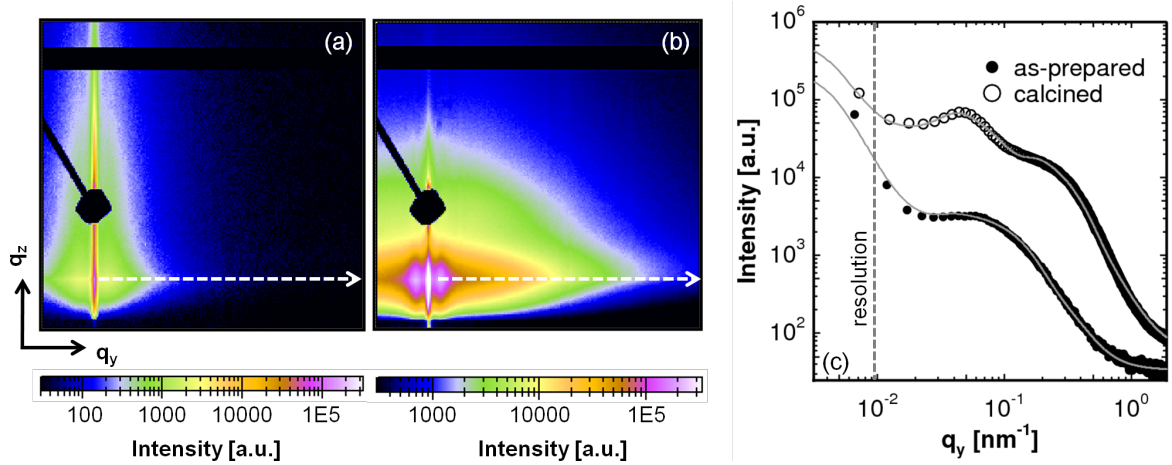

Figure 5.2.: 2d GISAXS data of spin-coated films obtained from ZAD solution (25 mg mL^{-1}) before (a) and after calcination (b), shown in q_y from -0.2 to 0.8 nm^{-1} and in q_z from 1.18 to 2.1 nm^{-1}. The intensity scale for each scattering signal is shown at the bottom of the images. The specular peak is covered by the point-shaped beamstop. The horizontal black stripe is the inter-module gap of the detector. The white dashed arrows indicate the position of the horizontal cuts. (c) Horizontal cuts (symbols) for both films along with the fits (solid gray lines) as described in the text. The vertical dashed line is the resolution limit towards larger structure sizes. The curves are shifted along the intensity axis for a clear demonstration of the structural features.

distinct scattering maxima at smaller q_y are observed along with a broad scattering signal in the lateral direction, indicating the origin of defined structural length scales in the volume of the film. Along q_z, the material characteristic Yoneda peak is clearly visible for both films. However, for the calcined film, the Yoneda peak shows a higher intensity due to the better scattering contrast with air, which arises from the crystalline regions.

In order to obtain quantitative information regarding the structure sizes for both the films, horizontal line cuts at the Yoneda peak position ($q_z = 1.326$ nm^{-1}) are performed as shown by the white dashed arrows in the images 5.2(a) and (b), integrated over 5 pixels along q_z direction for better statistics. The cuts also indicate an improvement in structural order after calcination (figure 5.2(c)), where the peak at high q_y becomes more prominent. The cuts are fitted with a model described in detail in section 2.4.2. Two form factors with cylindrical geometry are considered for each fit, distributed over a 1d paracrystalline lattice. These form factors correspond to the size of the scattering objects. The average center-to-center distance of the scattering objects is associated with the structure factors and are also obtained from the fits. In addition, a Gaussian distribution of the structure sizes and distances are derived for each fit.

For the as-prepared film, two characteristic length scales are resolved: the first structure size at lower q_y consists of a structure factor of (80 ± 10) nm with a Gaussian distribution of $\sigma_S = 28.5$ nm and a form factor radius of (8.4 ± 0.4) nm with a Gaussian distribution of $\sigma_F = 5.3$ nm. The second structure size at higher q_y consists of a structure factor of (62 ± 10) nm with a Gaussian distribution of $\sigma_S = 6.5$ nm and a form factor radius of (3.2 ± 1) nm with a Gaussian distribution of $\sigma_F = 1.9$ nm. Similarly for the calcined film, the structure factor at lower q_y indicates a length scale of (100 ± 5) nm with a Gaussian distribution of $\sigma_S = 23.5$ nm. The form factor associated produces a radius of (17.4 ± 0.7) nm with a Gaussian distribution of $\sigma_F = 8.3$ nm. Moving on to higher q_y values, the structure factor consists of (23 ± 2) nm with a Gaussian distribution of $\sigma_S = 5.5$ nm, whereas the form factor radius is fitted to be (4.2 ± 0.1) nm with a Gaussian distribution of $\sigma_F = 2$ nm.

A clear increase in both the form factors is observed after the calcination of the film indicating fusion of the nanoparticles to form larger objects. The structural rearrangement is driven by the energy provided to the system during the high temperature treatment. The formation of larger clusters in turn, results in a decrease in the average inter-particle distance from (62 ± 10) nm for the as-prepared film to (23 ± 2) nm for the calcined film, which matches with the average size of the pores observed in the calcined film via SEM (figure 5.1(b)). The structures of larger length scales, (80 ± 10) nm and (100 ± 5) nm for the as-prepared and the calcined films, respectively, are however not visible from the SEM investigations. This suggests the absence of these length scales locally and hence, are associated with the presence of some large domains, which are commonly observed for spin-coated films [32]. Although the length scales obtained for ZnO nanostructures via spin-coating seem promising for application as an active layer in a solar cell, the thickness of the films stay below 50 nm, which is still not feasible for implementation in high efficiency devices.

Morphology of solution-cast films

All the films produced via solution-casting show macroscopic cracks, which eventually leads to peeling of the films from the substrate. ZAD solutions of varying concentrations have been investigated, all of which have exhibited the same problem. The exemplary SEM images of a film prepared by ZAD solution with a concentration of 25 mg mL^{-1}, after calcination is shown in figure 5.3. As mentioned before, the cracks are visible on the film surface under a very low magnification (figure 5.3(a)). In the inset, a region of the film near the crack is depicted which shows the presence of ZnO nanoparticles within these cracks. Figure 5.3(b) shows the topography of the film in a crack-free region. The morphology of this part of the film appears very similar to that obtained for the films

produced from the same solution via spin-coating (figure 5.1(b)). The average pore size of the film ranges from 20 to 25 nm, which is slightly larger than that for the spin-coated films. Figure 5.3(c) shows the magnified region in one of the cracks present in the film. Spherical granules with a diameter in the range of 200 to 300 nm, consisting of aggregates of ZnO nanoparticles are visible.

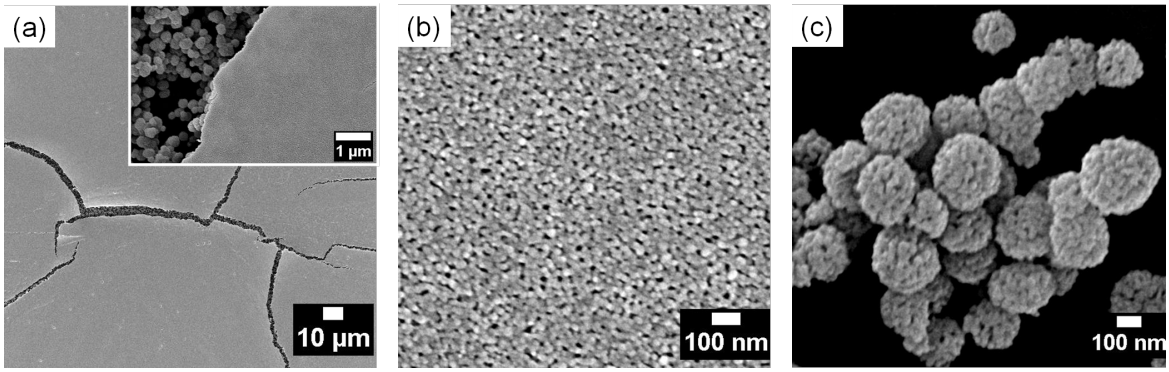

Figure 5.3.: Solution-cast ZnO films after calcination under different magnifications. (a) 350 × magnified, inset shows the same film under 10 k× magnification. (b) 50 k× magnified image focused on the homogeneous part of the film. (c) 50 k× magnified image focused on the cracks present in the film.

The complex modeling of the drying process during the film formation is reported by Tirumkudulu and Russel [130], where generally three stages of drying are identified. The drying mechanism can be correlated to the present scenario in order to explain the presence of cracks in the films. After deposition of the ZAD solution on the substrate, the first stage of drying involves spatially uniform drying of the film. Since the solution is composed of small ZAD molecules, the solvent leaving the surface is often responsible to drag the ZAD particles to the top. This mobility of the ZAD particles concentrates the solution at the liquid-air interface. The region richly incorporated with ZAD particles thus grows in thickness due to vertical convection which drives more particles towards the surface and is thus identified as the second stage of drying. The capillary pressure acts as the driving force for this process. The capillaries in turn, are depicted by the menisci of liquid formed between the ZAD particles present in the concentrated top surface. The third stage involves the movement of the lateral front during the drying process which mainly involves the edges of the film which are less concentrated. As a result, some ZAD particles start to diffuse towards the edges and thereby, two competing dynamic processes mutually exist in the film: the lateral convection and the propagation of the lateral front. Thereby, an imbalance in these two forces cause inhomogeneous drying of the film, meaning areas in the film with more and less deposition of particles. This

eventually leads to cracking of the films, which is exaggerated by heat treatment, where the particles with a close proximity are baked together leaving large gaps in the film where the particle concentration is very less. These are the regions in the present film where the spherical clusters are observed which are formed in order to minimize the surface area of the particles with the surrounding solvent. Besides the processes described, several other parameters such as the surface tension and deformation of individual particles also play important roles in the film formation process which are not fully detailed in the present study.

5.1.2. Crystallinity

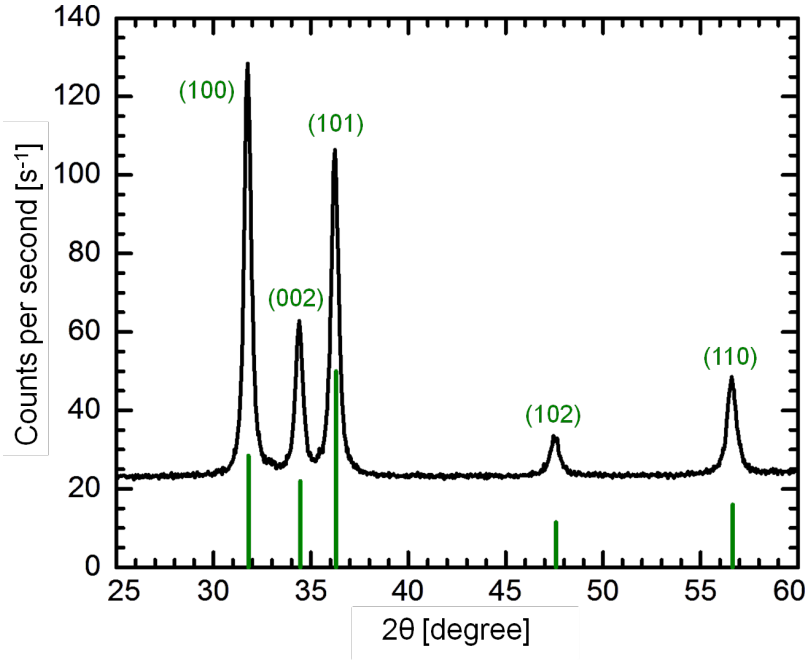

Figure 5.4.: XRD spectrum obtained for the solution-cast ZnO film after calcination at 400 °C. The green vertical lines indicate the theoretical peak positions with their relative intensities for the wurtzite ZnO phase [JCPDS reference database; card no. 36-1451].

The solution-cast films prepared from ZAD solution with a concentration of 25 mg mL^{-1} are investigated via XRD instrument II (section 3.1.4) after calcination in order to determine the crystalline phases present in the film. The solution-cast films are preferred over the spin-coated films due to higher film thickness, which contributes to an enhanced signal. For the spin-coated films, a thin film results in low count rate and hence, poor statistics. The diffraction pattern observed is shown in figure 5.4. As observed from the graph, the XRD pattern only shows peaks corresponding to the wurtzite crystalline phase

of ZnO, signifying the high purity of the film. The average FWHM of all the peaks are used for the calculation of the crystallite size using the Scherrer equation given in section 2.4.1. The value obtained for the present film corresponds to (12.5 ± 1.7) nm, where the error in the calculation is the standard deviation of the individual crystallite sizes obtained from all the peaks.

It is noticed that the intensity of the peak observed for (100) lattice plane is higher than the peak corresponding to (101) lattice plane, which is in contradiction to the theoretical relative intensities of the peaks. Since the intensity of the diffraction peaks depends on the total scattering from a particular lattice plane in the crystal structure of the material, for the present film, a preferred orientation of the lattice plane in (100) direction is found. Such deviation may occur based on the film preparation routine and the post production treatment given to the films, as also observed by Seghaier et al. for PbS thin films [131].

5.1.3. Results & discussion

An ample collection of nanostructures has been reported so far using zinc acetate dihydrate (ZAD) as the commercial precursor for ZnO [26]. However, all the solution-based approaches used, involve quite complicated chemical processing. In the present work, ZnO nanostructures with the same precursor are obtained by simply dissolving it in a suitable solvent. The simple chemistry of the production approach allows for a clear interpretation of the formation of the nanostructures. It is seen for the present analysis that for thin films produced by different deposition techniques, the morphology stays intact along with the length scales of the nanostructures depending on the concentration of the precursor solution used.

Two different deposition methods are used for the present investigation: spin-coating and solution-casting. It is observed that thin homogeneous films are obtained via spin-coating. For the solution-cast films, cracks are often produced on the surface of the films, the formation of which is associated to the complex drying process occurring during the film formation. However, the films obtained from both techniques display an interconnected morphology as opposed to isolated nanoparticles deposited on the substrate.

Although this simple system establishes desirable length scales in the film for applications in photovoltaics, each of the deposition methods suffer from its own disadvantages. The spin-coating method results in a very low film thickness as compared to the requirement for the active layers in dye-sensitized solar cells [127], whereas solution-casting results in inhomogeneous films.

Calcination of the films at a high temperature has shown an increase in the size of the aggregates due to baking of the structures together. The XRD investigation has shown

that pure crystalline wurtzite ZnO phase is obtained in the films after the high temperature treatment. In total, the presented approach to synthesize ZnO nanostructures is proved to be an efficient solution to understand the structural evolution in the films produced via spin-coating and solution-casting. However, the inherent limitation of the approach concerns the lack of tuneability of the length scales and morphology produced within the films. Additionally to the poor control of the structural order, thicker films without any cracks are not obtained successfully via solution-casting due to inhomogeneous distribution of particles in the film occurring during the drying process.

5.2. Spray-deposited films

The on-going progress in the development of dye-sensitized solar cells has stimulated research on promising nanomaterials in order to multiply the existing device efficiencies. Most of the successful results are obtained when sensitizing dyes are adsorbed on a porous network of an inorganic wide band gap semiconductor [132]. Since it is shown already in the previous section, that ZnO nanostructures with suitable length scales can be synthesized using zinc acetate dihydrate, the present section is dedicated towards improving film thickness. This is one of the most crucial parameters for efficient functioning of the device. Active layers in DSSCs utilize only a monolayer of adsorbed dye for absorption of light. Thicker layers of dye molecules have shown deteriorating influence on device performance [55]. Hence, a considerable film thickness and an improved surface area are the two possible ways to enhance the dye uptake without forming multiple layers. This in turn improves absorption of light. The thickness of the active layer as well as the available surface area obtained for dye adsorption depend to a large extent on the deposition technique employed for the active layer. The laboratory-based techniques discussed in the previous section pose limitations to the quality and thickness of the films. More recent and sophisticated methods include large-scale industrial techniques such as ink-jet printing, slot-die coating and spraying [120–122, 133].

Among all these methods, spray deposition has evolved as a very versatile approach to develop nanostructures of various materials. Lately, this approach has already been utilized for the fabrication of the P3HT:PCBM blend films for bulk heterojunctions [134]. Our approach to produce ZnO nanostructures is also suitable for being sprayed as the nanostructures are synthesized in solution. However, the kinetics of the spray procedure are not easy to monitor as several parameters (described in details in section 4.2.2) are involved, which affect the morphology, thickness and length scales generated in the sprayed films. In order to control these factors, numerous parameters need to be regulated to fulfill the requirements for a specific need. In order to govern these parameters with a high

degree of precision, a semi-automatized spray set up is custom-designed for the present research, the detailed functioning of which is given in section 4.2.2. The standard settings used for the spray experiments are also given in section 4.2.2. The framework maintained for the present experiments including their specifications are listed in table 5.1 as a recap. The ZAD solution with a concentration of 25 mg mL^{-1} is sprayed in all the experiments after filtering. All the sprayed films are subjected to a high temperature treatment of 400 °C in air for 30 minutes as described in section 4.2.1.

spray parameters	specifications
substrate-nozzle distance	16 cm
substrate temperature	80 °C
flow rate of the solution	20-25 µL s^{-1}
pressure of carrier gas	2 bars
spray time	10 s
waiting time in-between sprays	5 s
ambient temperature	20-25 °C
relative humidity	34-41 %

Table 5.1.: List of parameters used while spraying along with their specifications for designing ZnO nanostructured films using ZAD solution. A semi-automatized spray set up is used to control the parameters precisely.

5.2.1. Experimental details

Spraying being a solution-based route, is a desirable method for cost-effective and large-scale designing of nanostructures. However, to utilize the strength of the method to its maximum, a complete understanding of the underlying mechanism of the entire process is of paramount importance. The main aim of this section is to develop nanostructured ZnO films via spray deposition while following the structural evolution in these films during the spray process. The spraying scheme in general, involves a solution being deposited in terms of tiny droplets via a carrier gas, which makes the process highly dynamic. Real-time monitoring of such a fast process, having high degree of freedom, requires a high time resolution. As a consequence, most of the real space imaging techniques such as atomic force microscopy (AFM) and transmission electron microscopy (TEM) face acute challenges.

In order to address these challenges, the powerful reciprocal-space technique of grazing incidence small angle x-ray scattering (GISAXS) is applied to understand the spraying process in terms of uniformity of films, the drying time involved in the transformation of a solution to a solid film and the evolution of length scales in the film volume. These investigations become feasible due to the high time and spatial resolution accessible with GISAXS at modern synchrotron facilities. The present experiments are carried out at the P03 beamline of PETRA III storage ring in DESY as described in section 3.1.5. GISAXS is implemented in combination with in-situ spray deposition of ZAD solution on a substrate. To serve the purpose, the semi-automatized spray set up (as discussed in section 4.2.2) is installed in the P03 MiNaXS beamline of the PETRA III storage ring, DESY. The schematic of the experimental setup, which enables in-situ spray deposition and GISAXS measurements in parallel, is shown in figure 5.5.

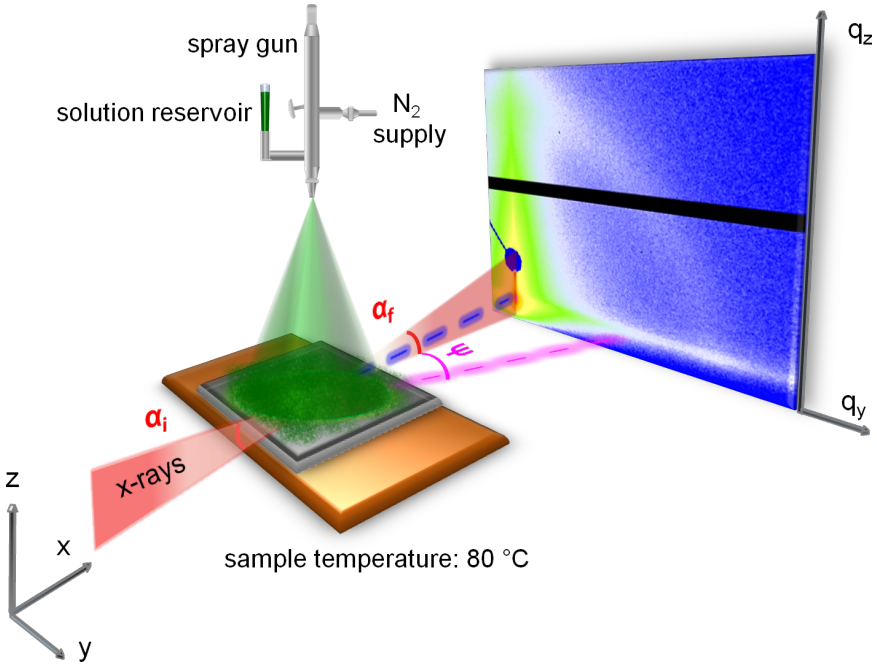

Figure 5.5.: A schematic representation of the experimental set up used for GISAXS measurements on the in-situ spray-deposited ZnO nanostructured film, from the ZAD solution.

The experiment is carried out under ambient conditions using the parameters listed in table 5.1 on a pre-cleaned silicon substrate. During the GISAXS measurements in the beamline, the motor of the rotary actuator of the semi-automatized spray set up (consult figure 4.8 for details) is controlled via giving a signal to the trigger of the spray gun using the main control program "ONLINE". This interfaces with the hardware control servers and clients and is also responsible for controlling the movement of the motors of the hexapod (on which the semi-automatized spray set up is mounted) and the height stage.

Another important unit for the experiment is the heating stage installed in the beamline to maintain a constant substrate temperature of 80 °C. The Anton Paar heating stage, DHS 1100 is installed on the hexapod as represented by the orange block underneath the substrate in figure 5.5. The holder material of the heating stage is composed of aluminium nitride having an operating temperature range between 25 and 1100 °C. The heating stage is calibrated using a blank silicon wafer prior to the measurements.

The entire spray protocol is designed and controlled by a script inserted in the control program of the beamline. The custom-programmed script ensures a perfect control of the steps involved in the experiment, which are listed in the following in the same order as they are executed:

- The temperature of the heating plate is adjusted to 80 °C and the pre-cleaned silicon substrate is placed on it. The sample-detector distance for the present experiment is 2.365 m.
- The substrate is aligned at half beam intensity ($\lambda = 0.957$ nm) for an incident angle $\alpha_i = 0°$. Once the substrate is aligned, α_i is fixed at 0.34°. Afterwards the beam shutter is closed.
- Information to the Pilatus 300k pixel detector (with a readout time of < 5 ms and pixel size of $(172 \times 172)\,\mu m^2$) is given.
- The beam shutter is opened, the high brilliance x-ray beam impinges the substrate at the same time as the spray shot is triggered. Pilatus starts taking images simultaneously (figure 5.5). The duration of spray lasts for the time pre-indicated in the script.
- After the spray shot is over, the sample stage is swept back-and-forth in the "y" direction (figure 5.5) over a distance of 2 cm continuously in order to average information over a large area of the film. A command for recording 1000 frames is given in the script.
- The sweeping of the stage stops when the desired number of frames indicated in the script is acquired, which include the scattering signals recorded during the course of the spray event and afterwards.
- Finally, after all the frames are recorded, the beam shutter is closed.

Each scattering frame is acquired over only 0.05 s (0.045 s measurement time + 0.005 s readout time by the detector) during the in-situ spray episode and afterwards. This low acquisition time is necessary for the high time resolution needed to follow the structural evolution in the film during the dynamic spray event without causing beam damage. However, after the measurements during and after the in-situ spray experiment are over, the same film is subjected to additional measurements in an area unexposed to x-rays

before for 41.205 s. This second measurement routine is divided into 41 frames, each acquired over 1.005 s (1 s measurement time + 0.005 s readout time by the detector) within 2 cm of the sample area. Each frame is obtained at a pristine spot separated from the next by 0.5 mm. The later experiment is performed in order to determine the homogeneity of the sprayed film in terms of structural length scales produced in the volume of the film after drying.

5.2.2. Structural & in-situ characterization

The inherent problem faced by the films prepared by multiple spin coats is partial dissolving or swelling of the underlying film by the solvent present in the additional film. With spray deposition of multiple layers to increase the film thickness, this problem is minimized to some extent due to fast drying of the solvent when the deposition is performed over a heated substrate. Hence, multiple spray depositions yield a more effective rise in the film thickness as compared to iterative spin-coated films. However, in the present section, only a single spray event of 10 s is studied in detail to monitor the structural evolution and arrangement in the film during the course of the spray process and afterwards.

Morphology investigation on an in-situ sprayed film

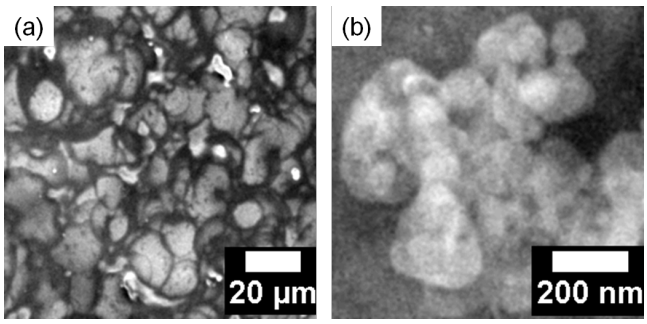

Figure 5.6.: SEM images under (a) 300 × and (b) 40 k× magnifications of the in-situ spray-deposited film, obtained from the ZAD solution.

The spray-deposited film studied in-situ with GISAXS, is investigated via SEM and the images obtained under low and high magnifications are shown in figure 5.6. The typical circular patterns are easily identified on the substrate (figure 5.6(a)). These result from the impact of individual droplets on the substrate during the spray process and their subsequent drying. The size of the discs vary according to that of the incoming droplets and their subsequent merger and dissolution. Under a higher magnification, (figure 5.6(b)), the agglomerates of ZnO nanoparticles are classified within these circular patterns. In

order to probe the drying time of the droplets and formation of a definite structural length scale in the film volume during the spraying episode, GISAXS investigations are performed on the in-situ spray-deposited film as described in section 5.2.1.

The system is probed during the 10 s in-situ spraying time followed by an additional 40 s measurement to track any structural evolution in the film, during and after the deposition. Hence, the total experiment lasts for 50 s and scattering data are recorded over 1000 frames (each acquired over 0.05 s) in total. It should be noted that during the last 40 s of the measurement performed after the spray event, the sample stage is swept constantly over a distance of 2 cm as mentioned in section 5.2.1. The data collected during the entire experiment is interpreted in the following:

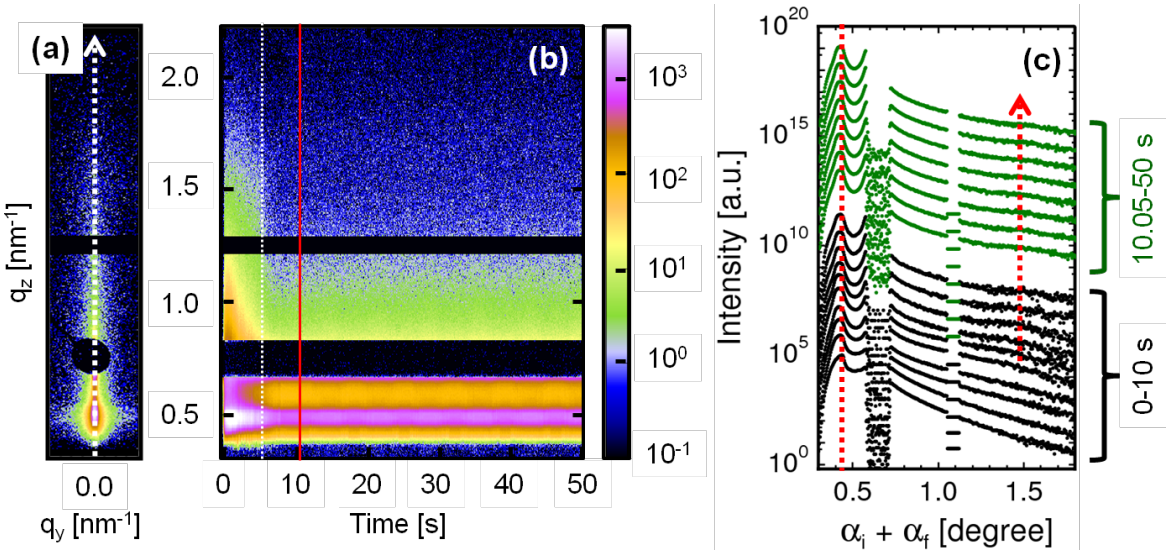

Figure 5.7.: (a) Example of a 2d GISAXS data acquired over 0.05 s during the in-situ spray deposition of ZAD solution. The white arrow indicates the vertical cut position. (b) Mapping of vertical line cuts at $q_y = 0$ nm^{-1} of all 2d frames plotted against the time axis. The black area between q_z 0.5 and 1.0 nm^{-1} is the specular beamstop and that between $q_z = 1.0$ and 1.5 nm^{-1} is the inter-module gap in the detector. The white dashed line marks the time of structural evolution and the red line marks the end of the spraying process. (c) Temporal evolution of vertical line cuts. Each black and green curve is integrated over 1 s and 5 s, respectively. The red dashed line indicates the Yoneda peak position and the arrow indicates the weak intensity modulation at $\alpha_i + \alpha_f = 1.5°$ arising after 5 s of spraying time. All the curves are shifted along the intensity axis for illustrative purposes.

A typical 2d GISAXS data (acquisition time = 0.05 s) obtained during the spray deposition process is shown in figure 5.7(a). Along $q_y = 0$ nm^{-1}, the highest intensity peak is the specular peak. It appears at the exit angle α_f equal to the incident angle ($\alpha_i = 0.34°$ in the present case), and is shielded by a circular beamstop. The material characteristic

Yoneda peak is visible at $q_z = 0.50$ nm^{-1}. In order to track the structural changes in the film, which occur following the measurement protocol, a mapping of all the 1000 scattering frames along the Yoneda region ($q_y = 0$ nm^{-1}) is presented against the time axis in figure 5.7(b). Each frame is integrated over 3 pixels in the horizontal direction. As seen from the mapping, in the initial 5 s (200 frames) of the spray shot, the scattering signals along q_z show an intense scattering. For the rest of the spray episode as well as after the end of the deposition, the scattering intensity along q_z decreases, but remains constant. The change in the scattering intensity along q_z is marked by the dashed vertical line in the image. The initial changes in the scattering signals observed along q_z is associated to the on-going structural changes in the vertical direction of the film when the fresh sprayed droplets arrive at the substrate. Surprisingly, the changes in structural ordering in the sprayed film seems to stabilize after 5 s of the spray event as the intensity of the scattering signals stays constant after this time scale. Particularly, the intensity in the Yoneda region is higher in the first 5 s of the spray experiment as compared to the rest, where the same gradually decreases. These observations can be explained as follows: The small amount of droplets approaching the substrate in the beginning of the experiment coalesce together. This results in formation of large clusters of the sprayed material, providing a higher contrast in the electron densities of the deposited material with air, which is observed as an enhanced intensity in the Yoneda region. This is also supported by the fact that large domains lead to more intense scattering, based on the relation between scattering intensity and mass of the scattering objects. The large clusters are also visible in the SEM image shown in figure 5.6(b). The growth of the clusters by coalescence of sprayed droplets is attributed to the energy supplied by the heated substrate to the system. The growth of the clusters by coalescence is also promoted by the preferred interaction of the material with itself rather than the substrate underneath. With increasing time, more material gets delivered on the substrate, which results in its complete coverage. As a consequence, the intensity drops due to smearing out of the contrast and possible origin of smaller clusters.

Vertical line cuts to the GISAXS data are performed at $q_y = 0$ nm^{-1} for all the frames recorded, as indicated by the white dashed arrow in figure 5.7(a). All the vertical cuts are plotted in figure 5.7(c). Information about the film profile perpendicular to the sample surface is obtained from these cuts. The black curves correspond to the data during the 10 s spray shot. This means that each of the black curves contains information obtained after summing up 20 frames, each acquired over 0.05 s. Hence, a single black curve represents a measurement time of 1 s. The green curves correspond to cuts performed for every 100 frames (each acquired over 0.05 s) summed up, from 10.05 s (after the spray shot) on, for additional 40 s (800 frames). Hence, each cut resembles to a total acquisition time of 5 s.

The Yoneda peak position at an exit angle of $\alpha_f = 0.1°$ (when $\alpha_i = 0.34°$) is marked by the red dashed line. It stays at a constant position after 5 s of spray. Also, the weak peak at the position $\alpha_f = 1.16°$ appears after 5 s of spraying and remains until the end of the experiment, as indicated by the red dashed arrow. Due to low counting time, this peak is nearly invisible in the 2d mapping as shown in figure 5.7(b). This peak corresponds to a real-space distance of 3.49 nm between the ZnO nanoparticle layers in z direction. The emergence of this modulation during the in-situ spray event also expresses increase in film thickness.

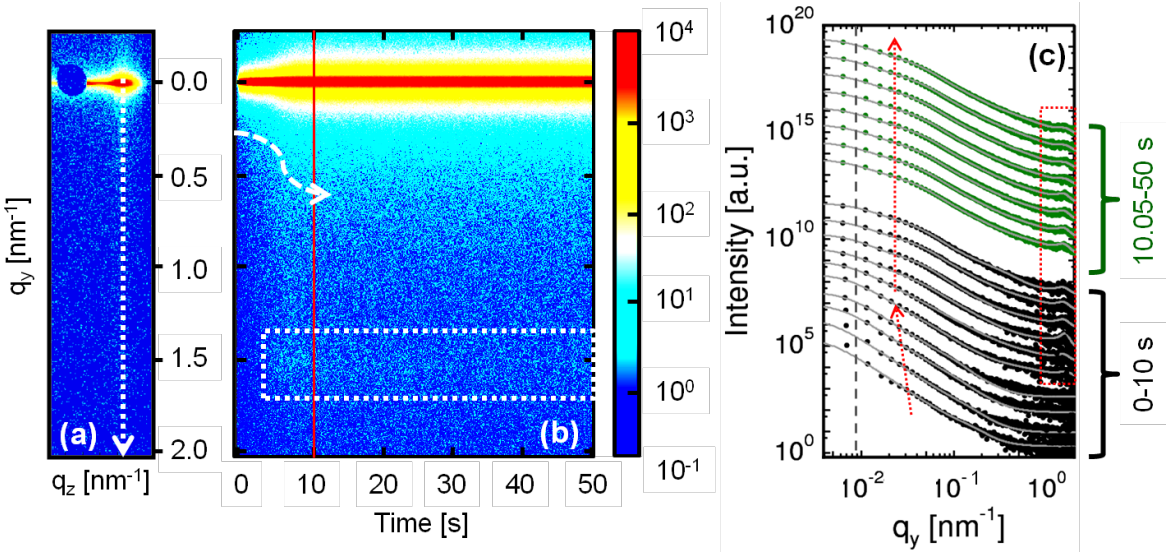

Figure 5.8.: (a) The same 2d GISAXS data as shown in figure 5.7(a), rotated by 90°. The arrow indicates the horizontal line cut position. (b) Mapping of horizontal line cuts at the Yoneda peak of all 2d frames plotted against the time axis. The arrow and the rectangle indicate the evolution of larger and smaller structures in the film after 5 s of spraying. The red line marks the end of the spray shot. (c) Summation of horizontal line cuts over increasing times, from bottom to top along with their respective fits (solid gray lines). Each black and green curve is integrated over 1 s and 5 s, respectively. The vertical dashed line is the resolution limit of the set up towards larger structure sizes. The arrows and the rectangle represents the growth of the larger structures in the first 5 s of the spray and evolution of smaller structures after this time, respectively. All the curves are shifted along the intensity axis for illustrative purposes.

Following the lateral structural evolution in the film is a bit more challenging due to the fast kinetics of the process as already proved by the analysis of the data for the vertical structural changes for the in-situ sprayed film. Also, to have a high time resolution, the data acquisition time is confined, causing the gradual structural changes in the film difficult to observe during spraying. The same 2d GISAXS data as shown in figure 5.7(a), is again shown in figure 5.8(a) with q_y axis plotted in the vertical direction. A different

intensity scaling is required to emphasize the weak signal from the lateral structures evolved during the spray deposition episode.

The scattering signal shown in figure 5.8(a) is acquired over 0.05 s, like every single frame in the present experiment. It should be noted from the image that an asymmetric set up of the detector is installed in order to probe a larger q_y region. In order to qualitatively visualize the sequence of 1000 frames acquired over a total measurement time of 50 s, horizontal frames are plotted in a 2d mapping presentation in figure 5.8(b) against the time axis. Each frame is plotted around the Yoneda peak over the entire q_y range and averaged over 5 pixels in the q_z direction. As observed from figure 5.8(b), the evolution of two distinct lateral scattering signals is visible at $q_y = 0.5$ nm^{-1} and 1.5 nm^{-1}. These are indicated by the white dashed arrow and the rectangle in the image, which mark the formation of predominant length scales in the film volume during the spray event. It is noteworthy that these side maxima appear prominently after 5 s of spraying, the same time during which structural reorganization has been observed in the vertical film profile. These lateral signals seem to stay constant in intensity after 5 s till the end of the experiment. However, the intensity of the signal originated at $q_y = 1.5$ nm^{-1} is very low as compared to the lateral structures observed at $q_y = 0.5$ nm^{-1}. This difference in intensities again signifies the formation of small and large domains during in-situ spray deposition.

For statistical representation of the data, horizontal line cuts are performed for all the 1000 frames in the direction indicated by the white dashed arrow in figure 5.8(a). Each of these horizontal cuts is integrated over exactly the same number of frames as discussed for the vertical cuts and are plotted with the same color code as figure 5.7(c), in figure 5.8(c). As in the case of the vertical cuts, the curves integrated over 100 frames (5 s per frame - the green curves), show better statistics as compared to those integrated over only 20 frames (1 s acquisition time per curve - the black curves). Three important observations are made from these cuts: firstly, the structural length scale in the lower q_y (appearing as a shoulder) increases in real-space as indicated by the red dashed arrow in figure 5.8(c) for the first 5 s of the experiment. Secondly, the prominent peak at higher q_y value, as marked by the red dashed rectangle in figure 5.8(c), originates after first 5 s of the spraying event. This is associated with the evolution of smaller length scales in the film volume in real-space. This observation agrees well with the explanation proposed for the scattering behavior observed from the vertical profile of the film during its formation during the in-situ spray shot of 10 s. Thirdly, the structures evolved in the film in the first 5 s of the experiment stay constant for the rest of the measurement time (indicated by the straight red dashed arrow in figure 5.8(c)).

For a further quantitative insight to the temporal evolution of characteristic length

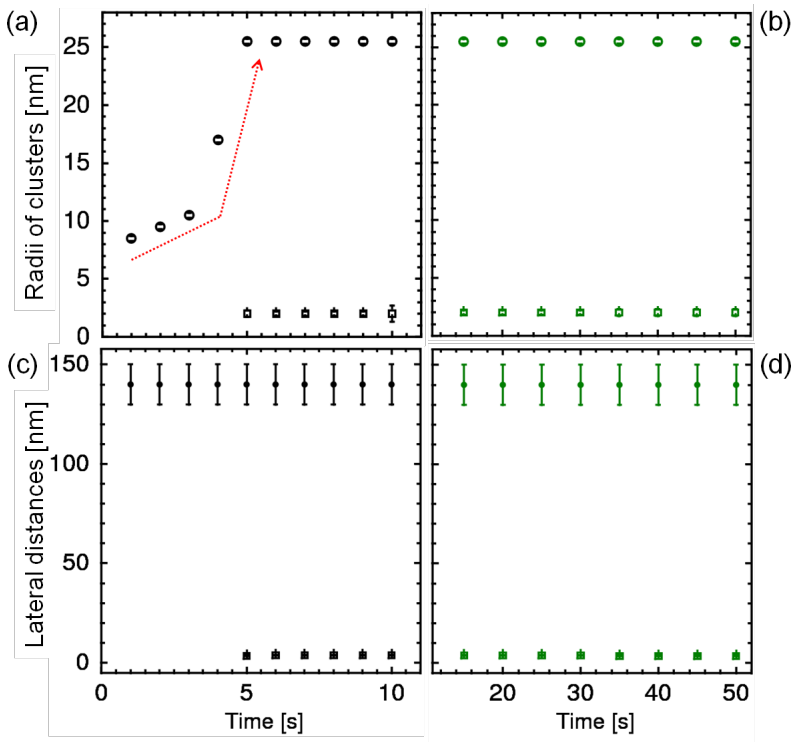

Figure 5.9.: (a) & (b) Radii of the clusters; (c) & (d) average center-to-center distances between these clusters, as extracted from the fits to the data shown in figure 5.8(c). The black data points represent the data acquired during the 10 s spraying event. The green data points corresponds to the measurements performed after the spraying event. This color coding is in accordance with the data shown in figure 5.8(c). The circle and the square symbols are linked to the larger and smaller length scales in the film volume, respectively. The red dashed arrow in (a) shows the increase in size of the larger clusters during the first 5 s of the spray experiment.

scales, all the above mentioned horizontal line cuts are fitted using a model consisting of form factors with cylindrical geometry distributed over a 1d paracrystalline lattice (details given in section 2.4.2). The center-to-center distance between the objects is associated with the structure factor, which is also derived from the fits. It should be noted that only one form factor is required for fitting the data corresponding to the first 5 s of the measurement, whereas for the rest of the data, two form factors are needed. The fits are also plotted along with the data points in figure 5.8(c). The average inter-particle distances and the radii of the particles deposited on the substrate are extracted from the fits, which are summarized in the plots shown in figure 5.9.

It is clearly evident from figures 5.9(a) and (b), that size of both the larger and the smaller clusters stay constant after 5 s of spraying. Before this time, no smaller structures are observed (figure 5.9(a)), whereas, the larger structures show a gradual increase in their

sizes as indicated by the red dashed arrow in figure 5.9(a) during the first 5 s of the spray event. However, interestingly, the center-to-center distances between both the smaller and the larger clusters remain unchanged during as well as after the spraying event as seen from the plots in figures 5.9(c) and (d). Upon a closer look to the cluster size and distances associated with the smaller length scales, it is clearly noticed that the clusters touch one another thereby forming a closed film. These smaller structures are not resolved by the SEM measurements presented in figures 5.6(a) and (b).

The homogeneity of the film is also tested in an additional measurement. After the first measurement of 50 s is accomplished, a pristine area of the same film is chosen to be probed with longer acquisition time. At this stage, the film is dry and hence, the structural features are fully evolved. Details of the measurement protocol are given in section 5.2.1. The results are summarized in figure 5.10.

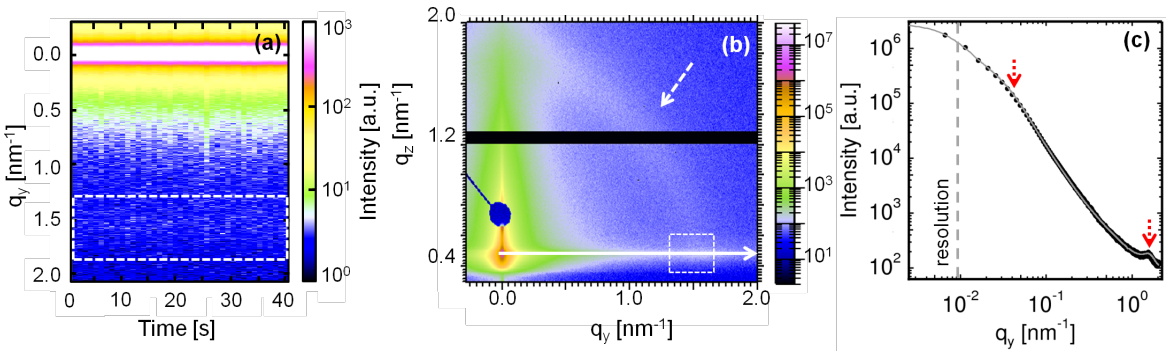

Figure 5.10.: (a) Mapping of horizontal line cuts at the Yoneda peak of all 2d frames obtained from the area scan of the in-situ spray-deposited ZnO film, after drying, plotted against time axis. The white rectangle marks the weak peak at q_y 1.5 nm^{-1}. (b) Summation of 41 2d GISAXS data obtained over the area scan. The specular peak is shielded by the point-shaped beamstop and the horizontal black stripe is the inter-module gap in the detector. The dashed rectangle indicates the weak peak observed in (a). The solid arrow marks the position of the line cut and the dashed arrow points towards the azimuthal scattering ring obtained. (c) Horizontal line cut at the Yoneda peak (symbols) shown with its fit (solid gray line). The dashed vertical line is the resolution limit to larger structure sizes. The red arrows points to the positions of the structures fitted to the data.

The horizontal slices of the 2d GISAXS data are chosen again at the Yoneda peak position, which are then composed into a mapping with respect to the time axis (see figure 5.10(a)). It is observed that the peak positions stay the same throughout the entire area of the sample probed (highlighted by the white dashed rectangle), indicating the high homogeneity of the film. For improving statistics, all the images in the mapping are added and plotted as a single 2d GISAXS data in figure 5.10(b). It is now clearly

evident that the peaks observed at $q_z = 1.8\ \mathrm{nm}^{-1}$ and $q_y = 1.5\ \mathrm{nm}^{-1}$ during the study of the vertical and horizontal film profiles respectively, belong to the weak and broad azimuthal (Debye-Scherrer) ring as indicated by the white arrow in figure 5.10(b). This ring essentially indicates the presence of randomly oriented ZnO particles in the film. The weak signal from the ring has not been easily identified for the in-situ measurement due to the low acquisition time used. The white dashed rectangle, shown in the image corresponds to the weak peak observed in the 2d mapping in figure 5.10(a). It should also be noted that the beam damage is avoided in the present experiments by careful adjustments of the experimental parameters.

Finally, to quantify the data obtained, a horizontal cut to the 2d GISAXS data shown in figure 5.10(b) is performed at the Yoneda peak position as marked by the white arrow. The cut along with the fit using the model described in section 2.4.2, is plotted in figure 5.10(c). The horizontal cut shows a prominent peak and a shoulder at high and low q_y values respectively, which are marked by the red dashed arrows. The structure size at higher q_y consists of a structure factor of $(3.6 \pm 0.2)\,\mathrm{nm}$ with a Gaussian distribution of $\sigma_S = 0.4\,\mathrm{nm}$ and a form factor radius of $(2 \pm 1)\,\mathrm{nm}$ with a Gaussian distribution of $\sigma_F = 1.2\,\mathrm{nm}$. Similarly, the structure size at lower q_y consists of a structure factor of $(140 \pm 10)\,\mathrm{nm}$ with a Gaussian distribution of $\sigma_S = 45\,\mathrm{nm}$ and a form factor radius of $(25.5 \pm 2)\,\mathrm{nm}$ with a Gaussian distribution of $\sigma_F = 20\,\mathrm{nm}$. Thus, the structural length scales acquired from the fit are identical to those obtained after the in-situ spray deposition of the film, as discussed above.

Model for lateral structure evolution during in-situ spray deposition

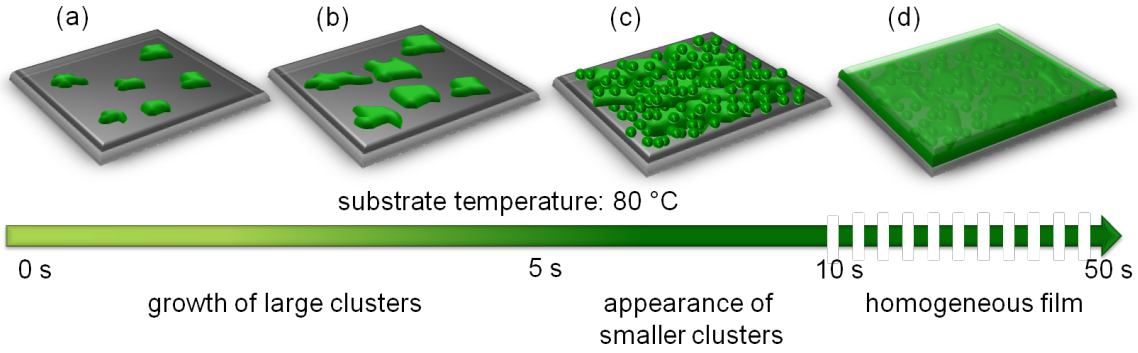

Figure 5.11.: (a) & (b) Formation of larger clusters of ZnO nanoparticles (represented by the green figures) in the first 5 s of the spray event. (c) Origin of smaller structures in the in-situ spray-deposited film as indicated by the green spheres during the last half of the spray shot. (d) The stable final film with both, large and small length scales, in the end of the experiment.

On the basis of the results derived from the GISAXS measurements for the lateral structures of an in-situ spray-deposited film (figure 5.9), a schematic representation of the formation of ZnO nanostructures is shown in figure 5.11. The large clusters show a gradual growth during the first 5 s of the spray event (figures 5.11(a) and (b)). This phenomenon is mainly attributed to the coalescence of incoming droplets. The distances between these clusters stay fixed throughout the entire experiment, which originates from the rapid evaporation of the solvent from the system. The evaporation of the solvent is further accelerated by the high temperature of the substrate onto which the droplets land. After removal of the solvent, the remaining ZnO nanoparticles get arrested on the substrate. However, the probability of deposition of more droplets in vicinity of these nanoparticles rises with time of spraying. Dissolution of the deposited ZnO nanoparticles by the solvent present in the fresh droplets results in coalescence of the material forming large clusters. Within 5 s, approximately 125 µL of the solution is sprayed which results in a considerable surface coverage. For the remaining half of the spray event, the droplets arriving the substrate get strongly bound to the already deposited ZnO clusters rather than forming big clusters among themselves (figure 5.11(c)). This process continues until a homogeneous surface coverage is attained in the end of 10 s. Thus, mostly vertical growth of the film can be estimated after 5 s of spray deposition. It should be noted that the small clusters might also be present during the initial stages of spraying, but are dominated by the presence of large clusters. Only after 5 s of spraying, these small clusters become more prominent and are distinguished in the scattering data as a sharp peak (figure 5.8(c)). The film obtained is highly stable and remains morphologically intact till the end of the experiment and afterwards (figure 5.11(d)). The final film thus consists of the large clusters formed during the first half of the spray experiment and the small clusters originated during the second half of the 10 s spray shot. Thus, a complete picture of the structure formation during the spray deposition process is revealed via GISAXS measurements.

Crystallinity investigation

The ZAD solution used for the in-situ spray deposition experiment in combination with GISAXS, is used to produce a similar film using the same spraying parameters as listed in table 5.1. For this duplicate sample, 1.5 mL solution is sprayed in order to obtain a film thickness of 200 nm. The purpose of preparing this film is to investigate the crystalline phases present in the spray-deposited film. Hence, the film is calcined afterwards at a high temperature of 400 °C in air for 30 minutes with a heating ramp of 5.78 °C min^{-1}. The film is then studied via x-ray diffraction (XRD instrument II, refer to section 3.1.4). A higher thickness of the present film than that of the in-situ sprayed film is necessary in

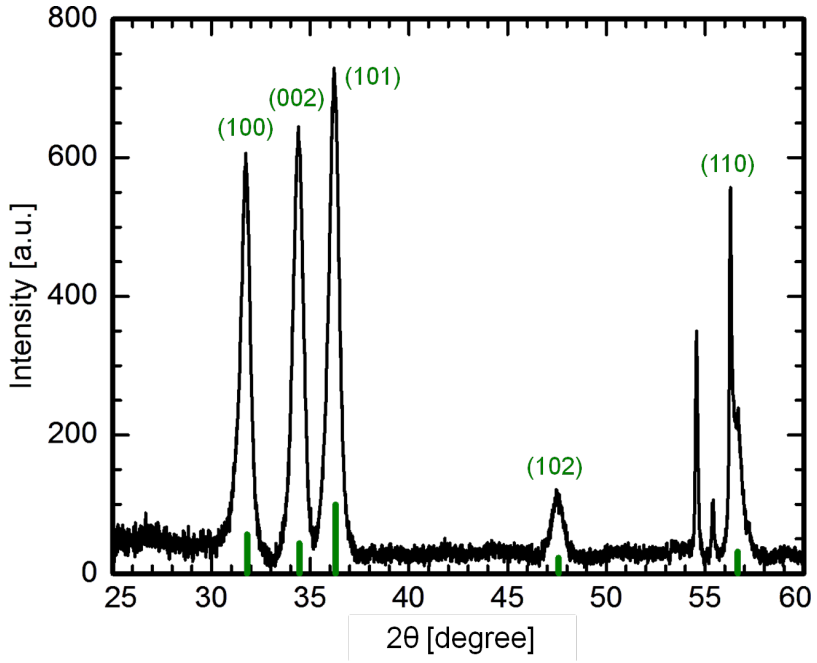

Figure 5.12.: XRD pattern of the ex-situ spray-deposited film obtained from ZAD solution with a concentration of 25 mg mL^{-1}, calcined at 400 °C. The green vertical lines represent the theoretical peak positions of wurtzite ZnO phase with their relative intensities.

order to obtain good signal in the detector. The XRD pattern of the corresponding film is shown in figure 5.12.

All the peaks observed are indexed as diffraction maxima belonging to the wurtzite crystalline phase of ZnO, according to JCPDS reference database (card no. 36-1451). The theoretical peak positions with their relative intensities are represented as green vertical lines in the graph. The average crystallite size calculated from all the diffraction peaks observed using the Scherrer equation (section 2.4.1), corresponds to (13 ± 3) nm. The diffraction peaks obtained from the (100) and (002) lattice planes show discrepancy with relation to the theoretical relative intensities. This signifies a preferred orientation of the lattice planes in (002) direction in the film, which may depend on the deposition method used for the fabrication of the film, as discussed in the previous section on spin-coated and solution-cast films.

5.2.3. Optical properties

For optical characterization of the spray-deposited films obtained from ZAD solution, a sample identical to the one studied for in-situ spray measurements discussed in section 5.2.2 is prepared on a pre-cleaned glass substrate. After spray deposition, the film is

calcined at 400 °C. The UV/Vis spectroscopic data is obtained in transmission mode using UV/Vis instrument I (section 3.2.1) and the corresponding absorption spectrum is plotted in figure 5.13(a). A typical absorption maximum at 370 nm is obtained for crystalline ZnO.

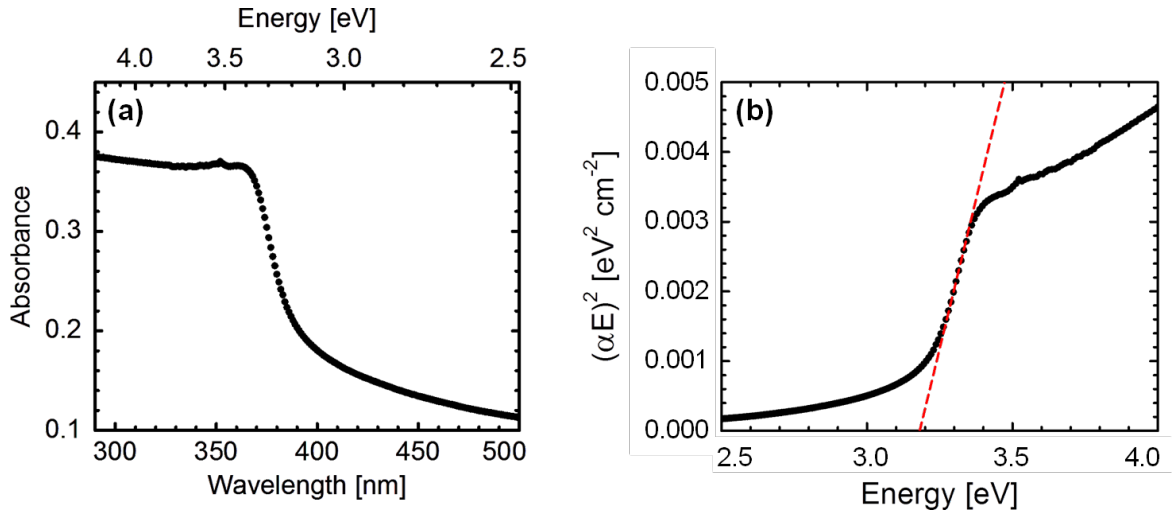

Figure 5.13.: (a) Absorption spectrum of spray-coated film obtained from ZAD solution, plotted against wavelength and the corresponding energy in the spectral range of 290 to 500 nm. (b) The corresponding Tauc plot for the same film. The band gap of the material is acquired by the linear extrapolation of the data to the energy axis.

The corresponding Tauc plot (following the Tauc equation for direct band gap semiconductors, discussed in section 3.2.1) for the same data is plotted in figure 5.13(b) for quantitative evaluation of the band gap energy of the material. On linear extrapolation of the data to the energy axis (as shown by the red dashed line in the graph), the direct band gap of the material is calculated to be (3.18 ± 0.02) eV. The error in the energy value originates from the uncertainty of the linear fit. The measured value lies within the range of band gaps obtained for wurtzite ZnO phase in different nanostructures, obtained via varied calculation methods [135]. The formation of crystalline wurtzite phase of ZnO after calcination of the film is also in good agreement with the results obtained from XRD measurements.

5.2.4. Solar cell performance

The thorough analysis of structural evolution in an in-situ spray-deposited ZAD film provided in section 5.2.2 establishes that the length scales obtained in the films after careful implementation of the spray deposition parameters, are reasonably suitable for being applied as active layers in dye-sensitized solar cells. However, in addition to morphology, the

thickness of the films also needs optimization in order to generate adequate numbers of charge carriers in the film in addition to sufficient light absorption. Three different solar cells are investigated in the present section, prepared by multiple spray coats using the parameters mentioned in table 5.1. All three films are directly sprayed on a ZnO blocking layer (spin-coated on FTO-coated glass substrates), the synthesis of which is provided in details in section 4.2.3. With every fresh shot, the temperature of the substrate decreases by 1-2 °C. In order to ensure the substrate temperature of 80 °C for every spray event, a time gap of 5 s is provided between two consecutive shots. Details about all the materials such as the electrolyte and the dye used for the fabrication of the DSSCs as well as the cell assembly, are given in section 4.2.3. Three different amounts of ZAD solution are sprayed for the three respective DSSC active layers. The total volume of solution sprayed is a more equitable measure for the control of the film thickness instead of counting the number of sprays due to the uncertainty in controlling the flow rate of the solution precisely for each spurt of spray. All the films are calcined as usual at 400 °C for 30 minutes to obtain ZnO in the conductive crystalline phase.

The three films are referred to as films I, II and III where a total volume of ZAD solution sprayed is 1.5 mL, 10 mL and 20 mL, respectively. The surface topography images of all the films after calcination are shown in figure 5.14 under different magnifications. Along with morphology, the thickness of the films are measured from the cross-sectional SEM images of the films as shown in the last row of figure 5.14.

As seen from the SEM images under 500 × magnification (figure 5.14, first row), all the films show sinuous surface morphology with the presence of micro and mesopores. In combination with the pores, larger aggregates of ZnO nanoparticles are observed for film I. On the other hand, the size of the ZnO clusters for film II is already restricted by the large amount of solution deposited (as discussed in section 5.2.2) and hence, instead of large clusters, high film roughness is prominent. The surface area of this film appears to be the maximum among the three and thereby, renders a promising morphology for higher dye uptake. The surface morphology of film III appears very similar to that of film II, but without the presence of the mesopores. This is explained by the high volume of the solution sprayed, which results in partial closing of the larger pores. From the magnified images of all the films, shown in the second row of figure 5.14, it can be seen that the average nanoparticle size lies in the range of 30 to 50 nm. Hence, the microscopic length scale in the film is preserved, which assures a precise control of the spraying parameters for different films. The ZnO nanoparticles observed in film III appear more densely packed than the other two films due to filling of the pores with the excessive amount of solution sprayed.

In addition to the length scale in the films, the thickness also rises with increasing

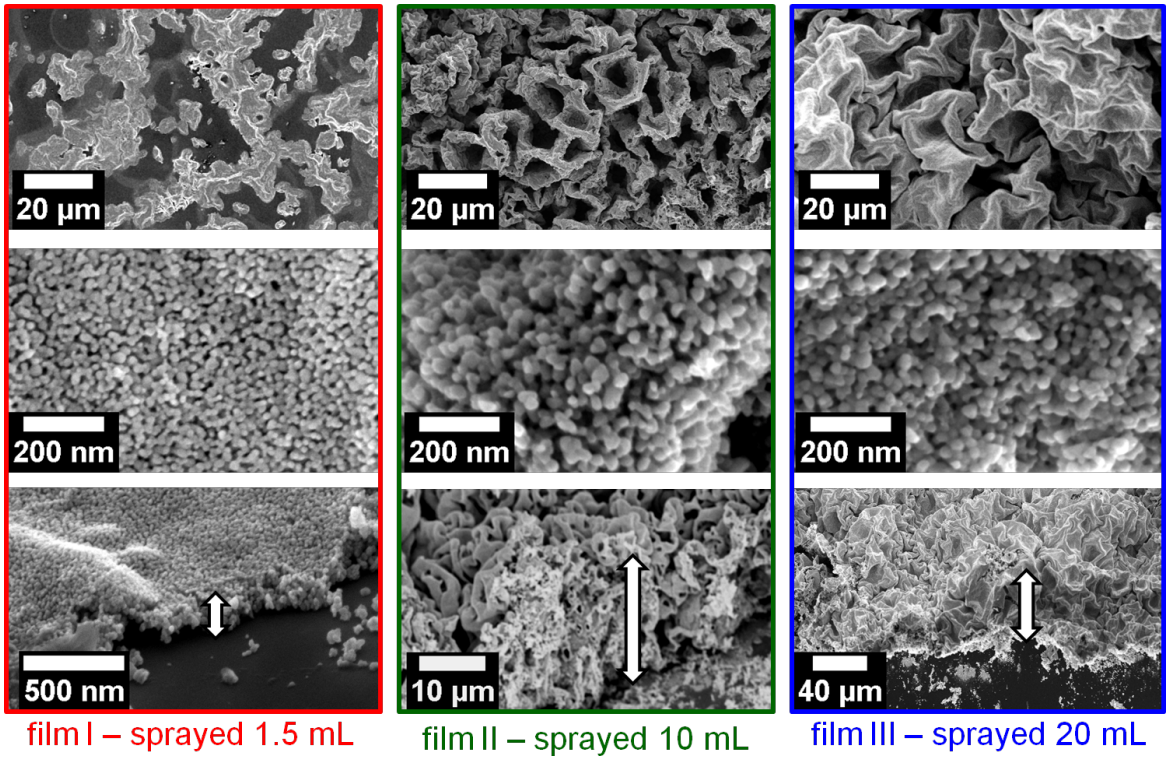

Figure 5.14.: SEM topography images of the ZnO nanostructured films obtained by multiple spray coats of pure ZAD solution. Different amounts of ZAD solutions sprayed, along with the film nomenclature are indicated at the bottom of the columns. The first and the second rows show the surface morphology with 500 × and 60 k× magnifications, respectively. The third row depicts the cross-sectional view of the respective films. The white arrows in the third row indicate the film thickness.

volume of ZAD solution deposited. However, the increase is not linear due to partial dissolution of the films during every fresh spray shot. But a signature of excellent control of morphology in terms of nanoparticle size is found for film thicknesses ranging from 200 nm to 40 µm. Finally, the three films are incorporated as the active layers in DSSCs, the performance of which is measured via I/V characterization. The corresponding I/V-curves are shown in figure 5.15 and the solar cell characteristics along with the film thicknesses are summarized in table 5.2. As observed from the I/V-plots, solar cell II having (20 ± 1) µm ZnO film thickness, shows the maximum short-circuit current density (I_{SC}). The open-circuit voltage (V_{OC}) for all the samples remains more or less the same, since this mainly depends on the choice of material combination. The slightly different fill factors (FF) result from the different series and sheet resistances seen from different slopes of the curves at I_{SC} and V_{OC}, respectively. The final power conversion efficiency (PCE) is therefore, depending mainly on I_{SC}. The low I_{SC} for solar cell I results from the low

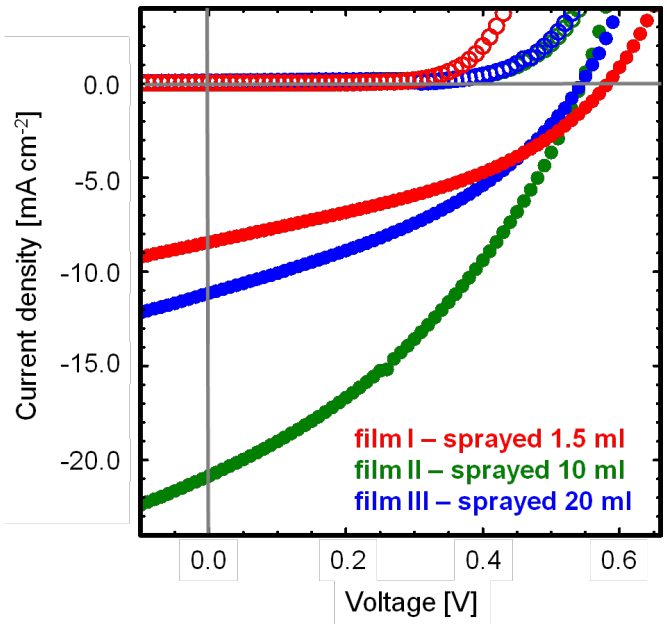

Figure 5.15: The I/V-curves are shown for dark measurements (open circles) and measurements under AM 1.5 illumination (closed circles) for the three solar cells with different ZnO film thicknesses obtained by multiple spray coats of pure ZAD solution (figure 5.14) as mentioned in the text with the corresponding color codes.

amount of charges generated. This in turn is caused by the low thickness of the ZnO active layer which has a limited dye uptake. The relatively high I_{SC} for solar cell II is attributed to both the thickness and morphology of the film. A nominal thickness of around 20 µm is necessary for sufficient light absorption as shown in literature [127]. Also the presence of both micro and mesopores (see figure 5.14 middle column) in the film enhances its surface area, thereby favoring the dye uptake by this cell more as compared to the other two. A high charge extraction also shows the presence of charge transport pathways in the film to the electrode. The performance of solar cell III is mainly restricted by the film thickness which hampers charge transportation due to their limited lifetimes. In addition to this, the surface area of the active layer is also decreased as the mesopores are filled

solar cells	film thickness	I_{SC} [mA/cm^2]	V_{OC} [V]	FF [%]	η [%]
film I	(200 ± 10) nm	-8.4	0.57	39.7	1.9
film II	(20 ± 1) µm	-20.8	0.54	36.2	4.1
film III	(35 ± 5) µm	-11.1	0.54	37.7	2.3

Table 5.2.: I/V characteristics of the DSSCs obtained from spray-deposited ZnO nanostructures obtained from spraying different amounts of ZAD solution (25 mg mL^{-1}) as the active layer; film I (indicated in red) - 1.5 mL sprayed, film II (highlighted in green) - 10 mL sprayed and film III (marked with blue) - 20 mL sprayed. The parameters are obtained from analyzing the I/V-curves shown in figure 5.15. Corresponding film thickness of the active layer for each cell is also listed in the second column, as obtained by cross-sectional SEM.

by the excessive material sprayed as seen form the morphology investigation (figure 5.14 third column).

5.2.5. Results & discussion

The fast kinetics and structural evolution of ZnO nanostructures during a spray deposition event is successfully studied using GISAXS. In conjunction with the length scales of the structures originating in the film during the spray process, the homogeneity of the film is also investigated using GISAXS and SEM techniques. For a ZAD solution of 25 mg mL^{-1} sprayed using the optimized parameters, a fast evolution of the nanostructures is noted within the first 5 s of the spray shot. After this time scale, no further evolution or reorganization of the structural domains are perceived confirming the fast drying of the film. For the spray-deposited film before calcination, the structure sizes evolved in the film volume are 3.6 × larger than those obtained for the as-prepared spin-coated films, for the same starting volume of ZAD solution (250 µL). This denotes faster coalescence of the deposited droplets for the sprayed films to produce larger structures. This is well-supported by the SEM images of the in-situ spray-deposited film where droplets of the ZAD solution are seen to merge together. However, the droplets arriving during the later stages of spraying on the substrate, which is already considerably covered by ZnO clusters, tend to form small aggregates. As a result, additional small structures are evolved in the film which are localized and lack mobility to fuse with other freshly deposited nanoparticles. This is attributed to the strong interaction of the fresh material with the existing ZnO clusters on the substrate. These small structures are almost the same size as those present in the as-prepared spin-coated films. The growth kinetics of similar systems in solution have been modeled, where most of the known systems follow the route of so-called Ostwald ripening [136]. Within this growth mechanism, the structures tend to grow via coalescence of the smaller particles to form larger clusters which are energetically more stable. However, from the results obtained via GISAXS measurements for the present system, such a growth mechanism is ruled out due to the absence of a linear relation between the increase in the volume of the particles and time. Morphological investigation on spray-deposited films obtained from the solution of the same precursor as the present study has been reported by Tarwal and coworkers. The structures evolved in the films are mainly attributed to agglomeration, coalescence and aggregation of the particles during the deposition process [137]. The present research has been successful in providing a kinetic insight to the complex evolution of ZnO nanostructures during the dynamic spray deposition event. The structural evolution of ZnO nanostructures in an in-situ spray deposition experiment is reported to be probed for the first time via GISAXS

measurements. It is also visible from the measurements that the film obtained is highly homogeneous.

Fast drying time and high homogeneity of the spray-deposited films have been utilized to translate the optimized spray protocol to multiple spray events to attain the desirable thickness for applications in DSSCs. A high control over morphology is sustained for even thicker films up to 35 µm. The nanostructures obtained from different number of spray coats show similar microscopic length scales on the film surface with the variation in the film roughness and the surface area, depending on the amount of material deposited. The spray-deposited films obtained from multiple coats are successfully incorporated as the active layers in DSSCs, which have shown promising performance. The optimized film thickness of (20 ± 1) µm yields a power conversion efficiency of 4.1 % and a short-circuit current density of 20.8 mA cm^{-2}, which is the highest recorded for ZnO-based DSSCs so far. The high surface area of this particular film contributed by the presence of the mesopores and micropores augment the dye uptake by the film, which in turn leads to a high number of charge carriers in the film, thereby lifting the I_{SC} value. In general, the overall power conversion efficiency of the cells is suppressed by the average low fill factor of 38 %. This is far below the required value of more than 70 % for high efficiencies [138, 139]. Surface defects and presence of oxygen vacancies are the most prominent drawbacks associated with most of the synthesis routes for ZnO nanostructures, specially those which are solution-based. Moreover, these defects along with the trap states increase with the surface area of the film. As a result, the fill factor deteriorates dramatically as compared to those obtained for bilayer cells. Additional source for this flaw might also be poor inter-connections between the different layers composing the final device [140–145].

The optical and crystallinity investigations have clearly indicated the presence of wurtzite ZnO phase in the system. The average crystallite size calculated for the spray-coated films is very similar to that obtained for the solution-cast films after calcination. Also the average crystallite size of 12.7 nm for both the systems is highly suitable for applications in DSSCs [146].

5.3. Summary

The synthesis of ZnO nanoparticles using a solution-based route is accomplished by dissolving the commercial ZnO precursor, ZAD in DMF. Three different modes of deposition of these nanoparticles are studied in order to retrieve nanostructured ZnO thin films. The morphology and the thickness of the films vary depending on the deposition method used. Spin-coating and solution-casting provide basically similar film morphologies. However,

the films obtained via spin-coating are more uniform than the solution-cast films which show macroscopic cracks due to inhomogeneous drying. The length scales of the structures obtained in the films is studied by SEM and GISAXS.

To overcome thickness limitations, spray deposition is used as the method to synthesize ZnO nanostructured films for applications in DSSCs. For a superior control of the morphology and thickness of the films, the spray parameters are strictly optimized. The combination of the GISAXS technique with the in-situ spray deposition of the films has revealed in-depth information about the evolution of structures during the course of the spray deposition. Fast structural kinetics of 5 s is derived from the GISAXS measurements on the in-situ sprayed film. The size of the nanostructures in the final film is tuned according to the amount of solution sprayed. The optimized spray protocol is also extended to production of multiple spray-coated films in order to tune the film thickness for a particular need. However, the shortcoming of the presented production process of ZnO nanostructures is the narrow available window to tune the structural length scales.

Incorporation of the multiple spray-coated films in DSSCs have shown promising power conversion efficiency and the highest short-circuit current density, reported so far. In summary, the present work provides a baseline to understand the morphology of spin-coated and solution-cast films along with the complicated structure formation during spray deposition. Spraying being the most successful method for producing ZnO nanostructured films with controllable film thickness and structural length scales using a simple solution-based route, can be extended to various other systems such as TiO_2, which has already achieved considerable attention for wide scale applications. The present contribution opens a new pathway to employ GISAXS as a method to resolve in-situ structure formation during other scalable manufacturing processes, such as screen-printing and slot-die coating.

6. ZnO nanostructures using P(S-*b*-EO) templates

Well-defined metal oxide nanostructures possessing extraordinary electro-optical properties have gained increasing interest in the field of photocatalysis, chemical/gas sensing, nanoscale electronic appliances, energy conversion devices such as solar cells and light-emitting diodes [147–156]. Zinc oxide (ZnO) being one of the most suitable candidates (based on its electronic and optical properties) for the above-mentioned applications, demands considerable attention to be improved in functionality. As such, the structure-function relationship is an important factor to be considered in order to address the improvement in nanoscale device performance [157]. ZnO is a versatile material which is easily molded in a myriad of morphologies, for example, nanorods [113, 158, 159], nanowires [160–162], tetrapods [163], spheres, discs [164], sponges [165] or others. Although these architectures have significantly contributed to widen the applicability of ZnO, a defined control over the length scales and structural order of such nanostructures via a solution-based technique is still lacking. The usefulness of a solution-based synthesis approach for ZnO nanostructures lies in the flexibility to choose from various methods available for deposition as thin films. This in turn provides numerous opportunities to control different structural parameters for instance morphology, area of coverage, surface roughness and film thickness.

A promising approach to meet the requirements is to apply the conventional sol-gel chemistry in combination with a suitable block copolymer template as introduced in chapter 1 section 2.2. Several studies have been documented to synthesize inorganic nanostructures using block copolymer templates, such as stable titania networks and carbon-based materials [25, 166–170]. However, synthesis of ZnO nanostructures using this route is not reported and hence, is the main focus of the present study. Among the various members from the amphiphilic diblock copolymer family, poly(styrene-*block*-ethylene oxide), abbreviated as P(S-*b*-EO) is selected as the structure-directing template for ZnO nanostructures, since it was successfully applied for synthesis of titania nanostructures in the past [15]. A solvent system consisting of a pair of good and selective solvents for the blocks of the copolymer is chosen in order to induce micro-phase separation of the block

copolymer. The presence of the selective solvent increases the surface energy of the polymer chains with the surrounding solvent environment. Thus the poorly dissolved block (hydrophobic block, PS in the present case) tries to minimize its interface with the selective solvent, which results in formation of micelles in the solution. The morphologies of these micelles are governed by the steric and the electrostatic forces among the copolymer chain segments. The shape and size of these micelles depend on the degree of stretching of the hydrophobic block, its interaction with the hydrophilic chain segments and with the surrounding solvent environment. A commercial zinc oxide precursor, namely, zinc acetate dihydrate (ZAD) is then added to the system which selectively gets incorporated in the hydrophilic block (PEO) of the template. As a result, by controlling the weight ratios of the solvents and the precursor added to the system, a large variety of nanostructures are obtained. The large morphological variety is a result of fusion of different copolymer aggregates which have the metal oxide precursor incorporated within. The fast chemical processes in the sol-gel result in several intermediate structures in their metastable states. Hence, the nanostructures often obtained via this approach are highly polydisperse.

In general, the process is limited by the range of structure sizes that can be obtained using a single template, although different film morphologies are synthesized. Four different morphologies produced by varying the weight ratio of the solvents and the precursors are discussed in section 6.1. One workaround to overcome the challenge of length scale limitation, is to use a similar copolymer template with different lengths of the blocks. This tailors the volume in which the precursor molecules are integrated and react, thereby changing the range of length scales accessed by a specific template. The impact of using a template with different block lengths on the morphology and the length scales generated in the film is demonstrated for a foam-like network morphology using a high molecular weight derivative of P(S-*b*-EO), as a function of increasing ZnO precursor weight fraction in the system (section 6.2). Section 6.1.1 presents the investigations on morphology and crystallinity of ZnO films synthesized by the low molecular weight P(S-*b*-EO) template-assisted sol-gel route. An overview of the structural length scales formed in the films is given. The electro-optical properties of selected morphologies are investigated in section 6.1.2. The results are then summarized in section 6.1.3. The morphology of the ZnO nanostructured film obtained by using high molecular weight P(S-*b*-EO) as the template are discussed in section 6.2.1. This is followed by the summary of results in section 6.2.2. For practical device engineering, an optimum thickness of the nanostructured film is necessary which is accomplished by the blade-coating (commonly known as doctor-blading) technique in section 6.3. A ZnO paste is synthesized from custom-tailored ZnO nanoparticles obtained by the sol-gel technique, for this purpose. The morphology and crystallinity of such films are discussed in sections 6.3.1 and 6.3.2 respectively. Afterwards, the films

are used to fabricate both solid-state and liquid electrolyte-based dye-sensitized solar cells (section 6.3.3). The results obtained are assembled in section 6.3.4. Finally, the summary of results for synthesis of ZnO nanostructures using P(S-*b*-EO) templates is unified in section 6.4. The investigations presented in section 6.1 and 6.2 in this chapter are published in references [26] and [171], respectively.

6.1. ZnO nanostructures using low molecular weight P(S-*b*-EO)

The samples investigated in this section are synthesized by the sol-gel technique described in section 4.2.1. The structure-directing template used is a low molecular weight P(S-*b*-EO) as described in section 4.1. Different sol-gels are prepared using different combinations of weight fraction ratios of N,N-dimethylformamide (DMF; good solvent), water (H_2O; selective solvent) and zinc acetate dihydrate (ZAD; ZnO precursor). The polymer concentration for all the sol-gels is kept constant at 25 mg mL^{-1}. The resulting sol-gels are then spin-coated or solution-cast on pre-cleaned silicon or glass substrates as described in section 4.2.2.Followed by deposition of the films, a high temperature calcination step is performed in order to remove the polymer template and to impart crystallinity to the nanostructures as described in section 4.2.1. Typically after the calcination of the solution-cast films, a white ZnO powder film is obtained on the substrates. Both polymer-ZnO hybrid films and the calcined films are characterized in the present chapter.

6.1.1. Structural characterization

The morphology of the polymer-ZnO hybrid films and the pure ZnO films obtained after calcination is studied majorly by two different techniques. For the preliminary structural investigation (surface morphology and thickness), the real-space technique of scanning electron microscopy (SEM), is employed (as described in section 3.1.1). For the in-depth characterization of the length scales in the film volume, the reciprocal-space technique grazing incidence small angle x-ray scattering (GISAXS) is employed (as described in section 3.1.5). Finally, the crystallinity of selected films is approved by x-ray diffraction (XRD) measurements (as described in section 3.1.4).

Morphology investigation

Table 6.1 lists all the different combinations of weight fractions of the solvents and the precursor used to prepare sol-gel solutions. These sol-gels are spin-coated to obtain thin

films with different morphologies. The resulting morphologies are majorly classified into four different categories: worm-like aggregates (coded in black), circular vesicles (indicated in blue), spherical granules (indicated in red) and foam-like structures (represented in green). All these morphologies are plotted in the form of a ternary phase diagram as shown in figure 6.1. The compositional boundaries for different nanostructures are drawn based on surface and volume morphology investigation on the films by SEM and GISAXS respectively. The evolution of these different nanostructures and their length scales are discussed in the following:

composition	$w_{DMF} : w_{H_2O} : w_{ZAD}$	composition	$w_{DMF} : w_{H_2O} : w_{ZAD}$
I	0.980 : 0.010 : 0.010	XVI	0.955 : 0.025 : 0.020
II	0.940 : 0.030 : 0.030	XVII	0.952 : 0.021 : 0.027
III	0.925 : 0.025 : 0.050	XVIII	0.910 : 0.080 : 0.010
IV	0.925 : 0.010 : 0.065	XIX	0.970 : 0.025 : 0.005
V	0.902 : 0.006 : 0.092	XX	0.990 : 0.005 : 0.005
VI	0.970 : 0.010 : 0.020	XXI	0.975 : 0.015 : 0.010
VII	0.960 : 0.010 : 0.030	XXII	0.910 : 0.040 : 0.050
VIII	0.940 : 0.040 : 0.020	XXIII	0.890 : 0.050 : 0.060
IX	0.940 : 0.020 : 0.040	XXIV	0.925 : 0.045 : 0.030
X	0.980 : 0.005 : 0.015	XXV	0.915 : 0.060 : 0.025
XI	0.975 : 0.005 : 0.020	XXVI	0.925 : 0.050 : 0.025
XII	0.906 : 0.022 : 0.072	XXVII	0.920 : 0.040 : 0.040
XIII	0.930 : 0.025 : 0.045	XXVIII	0.900 : 0.070 : 0.030
XIV	0.960 : 0.025 : 0.015	XXIX	0.905 : 0.045 : 0.050
XV	0.940 : 0.005 : 0.055	XXX	0.912 : 0.046 : 0.042

Table 6.1.: List of all the different weight fraction (w) combinations of the solvents (DMF, H_2O) and the precursor (ZAD) used for preparing sol-gel solutions using the low molecular weight P(S-*b*-EO) template. Different colors indicate different morphologies: green = foam-like structures, black = worm-like aggregates, blue = circular vesicles, red = spherical granules.

Worm-like aggregates: Figure 6.2 represents the exemplary SEM images of the morphology obtained from sol-gels containing a very low weight fraction of ZAD (0.01 or less) and a variable weight fraction of H_2O. The specific weight fraction combination used for the sol-gel producing the depicted films is listed as composition XVIII in table 6.1. The polymer-ZnO hybrid film (figure 6.2(a)) shows an intermingled wavy network where the brighter regions represent the ZnO and the darker regions correspond to the non-

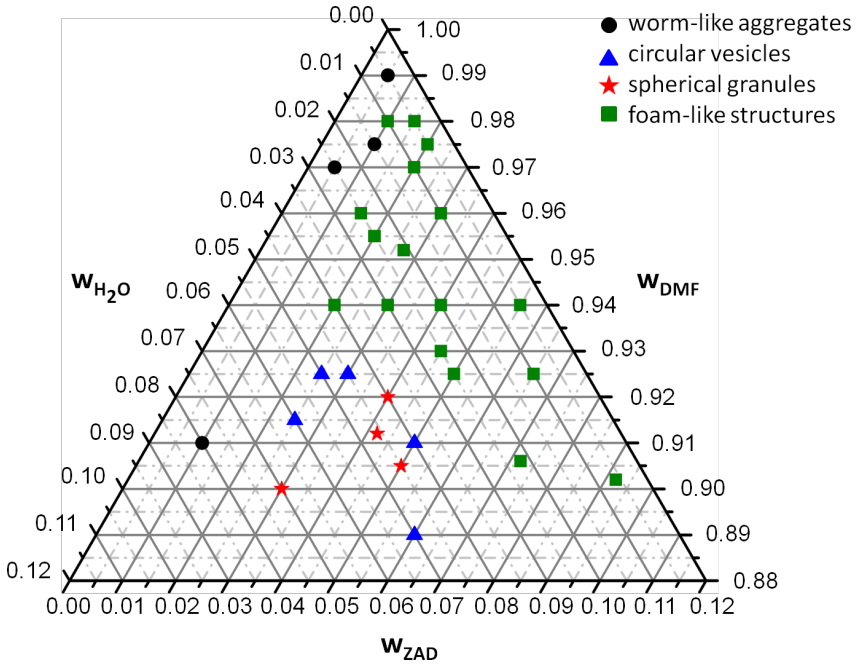

Figure 6.1.: Ternary phase diagram of ZnO morphologies obtained via sol-gel route using low molecular weight P(S-*b*-EO) as a template. The compositions of all the plotted morphologies are listed in table 6.1 following the respective color codes. The nanostructured films are obtained after calcination of the polymer-ZnO hybrid films produced by spin-coating technique. (w represents the weight fraction).

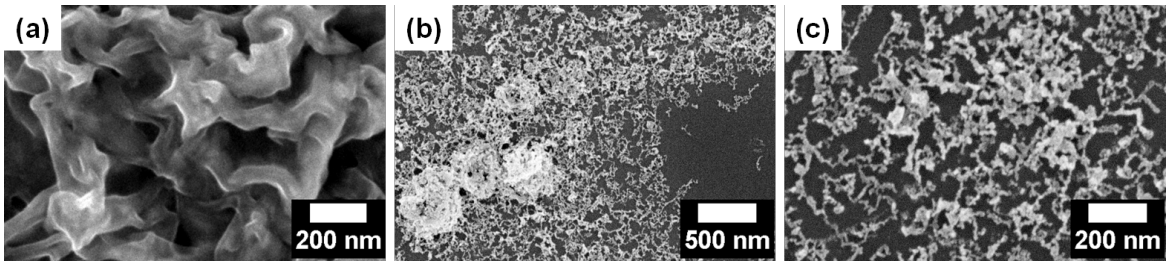

Figure 6.2.: (a) SEM topography image of polymer-ZnO hybrid spin-coated film for morphology corresponding to worm-like aggregates. (b) & (c) Surface view of the same film after calcination under low and high magnifications respectively.

conducting copolymer template. After calcination, the SEM surface images essentially appear sharper and brighter as compared to the former due to the removal of the non-conducting template from the system. The SEM image under low magnification (figure 6.2(b)) shows an incomplete coverage of the substrate, which appears as the dark background. Moreover, the remaining ZnO nanostructures on the substrate form aggregates having different geometries. Predominantly, the wavy cylindrical structures resemble tiny

worms scattered on the surface. In addition to these, larger structures of approximately 500 nm in size are also observed which appear like clusters of the small worm-like structures (figure 6.2(b)). The polymer-ZnO hybrid film shows no such clustering, which indicates the onset of aggregation during the spin-coating process or even afterwards, during calcination of the hybrid film. The high temperature during calcination provides enough energy to the system to allow the ZnO nanoparticles to bake together forming clusters of different shapes and sizes (the so-called pattern collapse). A magnified view of the sample is provided in figure 6.2(c), where it is observed that the smaller worm-like nanostructures are connected to one another thereby forming a network-like morphology. As seen from figure 6.2(c), these elongated worm-like structures form of only a monolayer over the substrate. This is attributed to the fact that the precursor weight fraction ($w_{ZAD} = 0.03$) used for the present sol-gel is extremely low which results in the formation of limited number of Zn-O bonds in the polymer matrix.

Circular vesicles: In the ternary phase diagram (figure 6.1) the circular vesicular morphology constitutes only small islands. Keeping the w_{ZAD} above 0.02, if the w_{H_2O} is gradually increased over 0.03, such a morphology appears. The spin-coated hybrid and calcined films are shown in figure 6.3. The exact weight fraction of the ingredients of the sol-gel used to produce these films is listed as composition XXII in table 6.1.

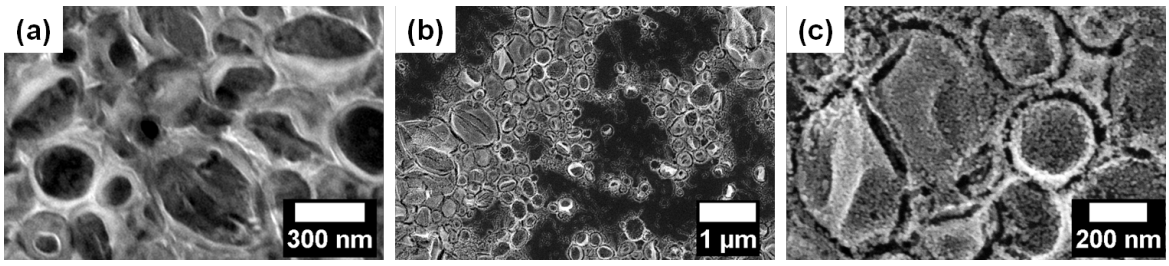

Figure 6.3.: (a) SEM topography image of polymer-ZnO hybrid spin-coated film for film morphology resembling circular vesicles. (b) & (c) Surface view of the same film after calcination under low and high magnifications respectively.

The vesicles are commonly reported nanostructures [172,173], which are basically characterized by their thicker walls and shallow inner structures. As apparent from the topography images (figure 6.3), the morphology exhibits predominantly two different length scales both before and after calcination of the film. The larger vesicles possibly arise by the fusion of the smaller vesicles either in the solution or during the film processing. Similar to the worm-like aggregates, the hybrid film (figure 6.3(a)) shows bright and dark regions corresponding to ZnO and polymer-rich regions respectively. This gives an impression of the vesicles being hollow in the center, which is majorly because of the fact that the rim of the vesicles are abundantly enriched with ZnO. The size of these vesicles is determined

by the w_{H_2O}, whereas, the thickness of the shell depends on w_{ZAD} in the system [174]. Upon calcination of the polymer-ZnO hybrid film, it is seen that the surface coverage is not homogeneous (figure 6.3(b)), same as for the previous case. This is again attributed to the low weight fraction of w_{ZAD} in the sol-gel. However, the surface morphology after calcination remains unaltered. Additionally, after calcination, it is clearly visible that the vesicles are indeed not hollow, but are sparsely populated with ZnO nanoparticles as compared to the boundary. The diameter of the vesicles formed after calcination ranges up to 500 nm as evident from the surface information provided by SEM. The formation of such large structures by the fusion of two or more small vesicles is clearly demonstrated on the left side of figure 6.3(c). However, the population of these very large structures is less as compared to those of the smaller vesicles. Majorly the size of the vesicles resides in the range of 40 to 200 nm.

For an in-depth analysis of the film, the reciprocal-space technique of GISAXS is used, where a high x-ray flux penetrates the volume of the sample. The GISAXS measurements are performed as described in chapter 2.4.2 in the BW4 beamline of DORIS III storage ring at DESY. The 2d GISAXS data obtained from the measurements are shown in figure 6.4(a) and (b).

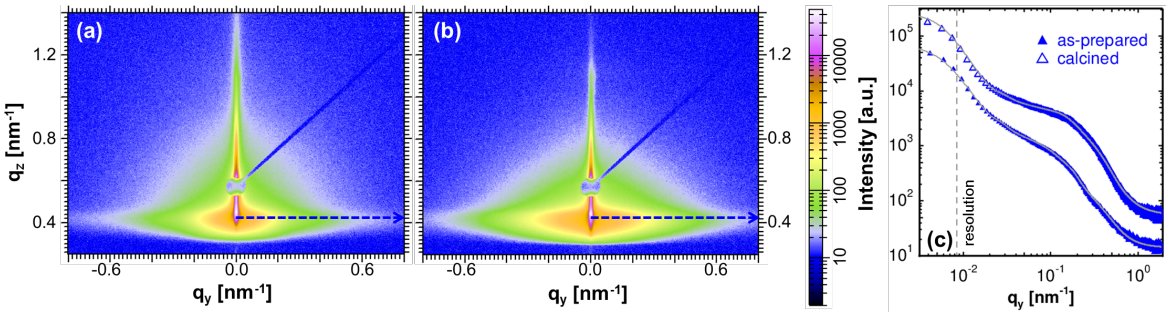

Figure 6.4.: (a) & (b) 2d GISAXS data obtained for the hybrid and the calcined films respectively, showing circular vesicular morphology (composition XXII, table 6.1). The blue dashed arrows indicate the cuts to the data at the respective Yoneda peak positions. The circular beamstop shields the specular peak. (c) Horizontal cuts (symbols) and the fits (solid gray lines) for the hybrid (as-prepared) and calcined films. The curves are shifted along the intensity axis for illustrative purpose. The gray dashed line is the resolution limit to larger structure sizes.

The broad scattering signal in figures 6.4(a) and (b) already give an idea about the polydispersity of the structures in the film. For further quantitative analysis of the structural length scales present in the film volume, horizontal cuts as indicated by the blue dashed arrows at the material-sensitive Yoneda peak positions are performed. These cuts along with the fits considering cylindrical form factors distributed over an 1d paracrystalline lattice as described in section 2.4.2, are shown in figure 6.4(c). Two characteristic length

scales are resolved for both the hybrid film, referred in this context as the as-prepared film and the calcined films. For the polymer-ZnO hybrid film, the first structure size at lower q_y consists of a structure factor of 190 nm with a Gaussian distribution of $\sigma_S = 33.5$ nm and a form factor radius of 8.5 nm with a Gaussian distribution of $\sigma_F = 5.8$ nm . The second structure size at higher q_y consists of a structure factor of 32 nm with a Gaussian distribution of $\sigma_S = 4.5$ nm and a form factor radius of 3 nm with a Gaussian distribution of $\sigma_F = 1.9$ nm. Similarly, for the calcined films, the structure sizes are also determined. At lower q_y, a structure factor of 170 nm with a Gaussian distribution of $\sigma_S = 33.5$ nm is predominant along with a form factor radius of 6 nm having a Gaussian distribution of $\sigma_F = 5.2$ nm. Moving to higher q_y value, a structure factor of 32 nm with a Gaussian distribution of $\sigma_S = 7$ nm is resolved along with a form factor radius of 4 nm with a Gaussian distribution of $\sigma_F = 1.9$ nm. It is noteworthy for the present case, that the above-mentioned structure and form factors correspond to the average distance between the scattering objects and their average size respectively. For both the hybrid and the calcined films, the larger structure factor is attributed to the distance between the rim of the vesicles, thereby representing the average size of the vesicles. This is based on the observation that the rim of the vesicles are thicker and elevated compared to the rest. Hence, the two opposite sides of the vesicle contribute to scattering. The wide Gaussian distribution confirms the presence of vesicles of different sizes in the films. The smaller structure factor on the other hand is associated with the average distance between the vesicles for both the films. On having a closer look, the vesicles of all sizes in the film are constructed of ZnO nanoparticles and their clusters. The form factors obtained from the fits correspond to these ZnO nanoparticles and their aggregates. The larger form factor in case of both the films is correlated to the ZnO nanoparticle aggregates forming the boundary of the vesicles, whereas, the smaller form factor is linked to the average radii of the nanoparticles composing the interior of these vesicles. The assigning of different length scales to the corresponding vesicular structures is well-supported by the SEM data. Another fruitful observation made from the obtained results directs to a shrinkage of the larger structure sizes upon calcination. This is an established fact for the nanostructures synthesized via block copolymer templates and is denoted as the so-called pattern collapse due to removal of the polymeric scaffold [15].

Spherical granules: Spherical granules constitute only a very small region in the phase diagram (figure 6.1) and have no distinctive compositional boundary with the circular vesicles. Increasing the w_{H_2O}, the circular vesicular morphology is transferred to spherical granules. Due to the increasing w_{H_2O}, the interfacial energy of ZnO increases with the surrounding solvent environment. The spherical granular structure arises as a result, when the ZnO nanostructures tend to minimize their surface energy. The SEM topography

images of the polymer-ZnO hybrid and the calcined films are shown in figure 6.5. The exact combination of the weight fraction of the solvents and the ZnO precursor used for the sol-gel to synthesize the present morphology is given as composition XXVIII in table 6.1.

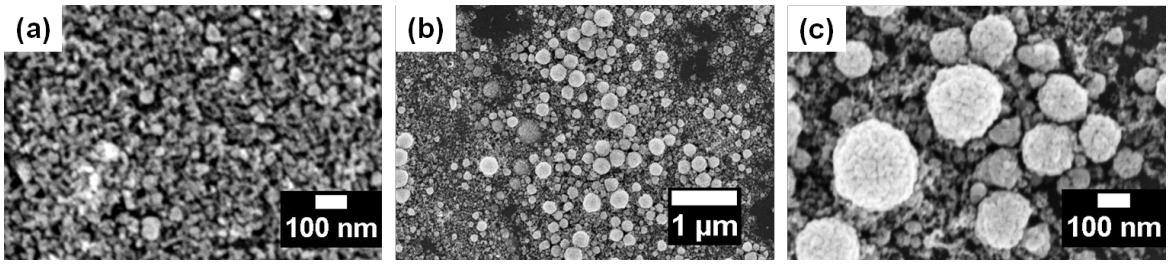

Figure 6.5.: (a) SEM surface image of polymer-ZnO hybrid film obtained after spin-coating the sol-gel for spherical granular morphology. (b) & (c) Surface topography of the calcined film displaying ZnO nanostructured morphology consisting of spherical granules, under low and high magnifications respectively.

The surface morphology observed for the polymer-ZnO hybrid film indicates the formation of ZnO clusters, but with very low concentration of prominent spherical granules (figure 6.5(a)). However, after the film is calcined, a structural rearrangement leads to the evolution of spherical granules which have a high polydispersity in the size (figures 6.5(b) and (c)). Therefore, the formation of this granular morphology occurs during calcination. The surface coverage in this case is more uniform than the morphologies discussed previously. It is observed from the images that the surface of the granules are composed of ZnO nanoparticles. The nanoparticles are also present underneath the granules representing the amount of material which fails to get transformed into bigger spherical granules and occur only as small agglomerates. Also like the vesicular morphology, the larger granules are believed to evolve over fusion of smaller granules. This phenomenon requires additional energy which is provided during the calcination of the films, when the polymer template is removed and the remaining ZnO nanoparticles bake together. The energy provided to the system during calcination in the present case is however not enough to promote the fusion of all the ZnO nanoparticles to form large spherical granules. The granular sizes, based on the surface investigation range up to approximately 260 nm.

The volume average information about the structure sizes in the film is again extracted via GISAXS as mentioned for the circular vesicles. The 2d scattering data along with the horizontal cuts at the Yoneda position (marked by red dashed arrows) are shown in figure 6.6. As seen from the 2d GISAXS data (figures 6.6(a) and (b)), a broad scattering signal along the q_z direction is observed indicating presence of different structure sizes along the depth of the film. After calcination, the scattering signal along q_y direction gets reduced

indicating formation of larger structures in the film. For quantitative information about the structure sizes, the horizontal cuts along with their fits are shown in figure 6.6(c).

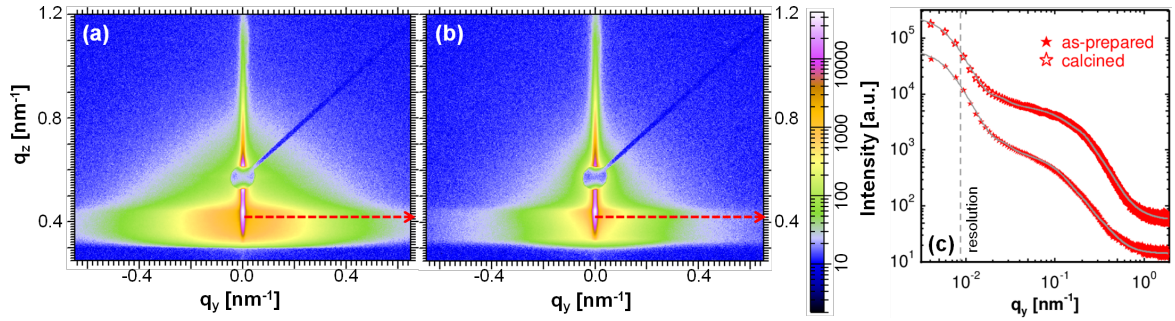

Figure 6.6.: (a) & (b) 2d GISAXS data obtained for the hybrid (as-prepared) and the calcined films respectively, showing spherical granular morphology (composition XXVIII, table 6.1). The specular peak is covered by the beamstop. The red dashed arrows show the position of the cuts along q_y. (c) The horizontal cuts (symbols) to the 2d data along with the fits (solid gray lines) to probe the length scales of the lateral structures. The dashed gray line shows the resolution limit for the larger structures. Both the curves are shifted along the intensity axis for clarity.

Two predominant structure sizes are obtained for both the polymer-ZnO hybrid and the calcined films from the corresponding fits. For the polymer-ZnO hybrid film, the first feature at lower q_y consists of a structure factor of 190 nm with a Gaussian distribution of $\sigma_S = 33.5$ nm and a form factor radius of 9 nm with a Gaussian distribution of $\sigma_F = 6$ nm. This large structural length scale is attributed to the average domain sizes present in the film rather than any particular feature observed via SEM. Such large scale domains are known to arise during the film formation via spin-coating process [32]. The second structure size at higher q_y value consists of a structure factor of 25 nm with a Gaussian distribution of $\sigma_S = 4$ nm and a form factor radius of 3.5 nm with a Gaussian distribution of $\sigma_F = 1.9$ nm. This smaller length scale correspond to the small spherical granules present in the films as illustrated in the SEM image (figure 6.5(a)). The form factors on the other hand, are associated with the larger and smaller clusters of ZnO nanoparticles in the film volume.

For the calcined films, the structure factor obtained at lower q_y values represents a length scale of 205 nm having a Gaussian distribution of $\sigma_S = 37.5$ nm. The form factor radius obtained for this structure size corresponds to 6.5 nm with a Gaussian distribution of $\sigma_F = 5$ nm. The larger length scale is attributed to the size of the spherical granules formed in the film after calcination. The sizes obtained via fitting of the GISAXS data are in very good agreement with the length scales retrieved via SEM investigation. For higher q_y values, a structure factor of 25 nm having a Gaussian distribution of $\sigma_S = 4$ nm

and a form factor radius of 4 nm with a Gaussian distribution of $\sigma_F = 2$ nm are extracted. The smaller length scale is again associated with the smaller granules. The form factors are linked to the ZnO nanoparticle clusters, which are present underneath the distinctive spherical nanostructures. The average size of the large spherical granules increase after calcination as confirmed by the SEM measurements as well, whereas, the smaller granules retain their dimensions. The shrinkage in the form factor for larger structures once more reconfirms the concept of pattern collapse.

Foam-like structures: The network-like ZnO nanomorphology occupying the maximum area in the investigated ternary phase diagram is referred to as foam-like structures. These nanostructures are obtained for a wide range of combinations of different weight fractions of the solvents and the precursor, specially w_{ZAD} ranging from 0.01 to 0.92. For the present discussion, four different network structures grouped under the foam-like morphology are investigated. The different combinations of the sol-gel ingredients are shown as compositions I, II, III and IV in table 6.1. The hybrid polymer-ZnO and the calcined films obtained from these compositions are investigated using SEM for the local surface morphology. The corresponding SEM micrographs are shown in figure 6.7.

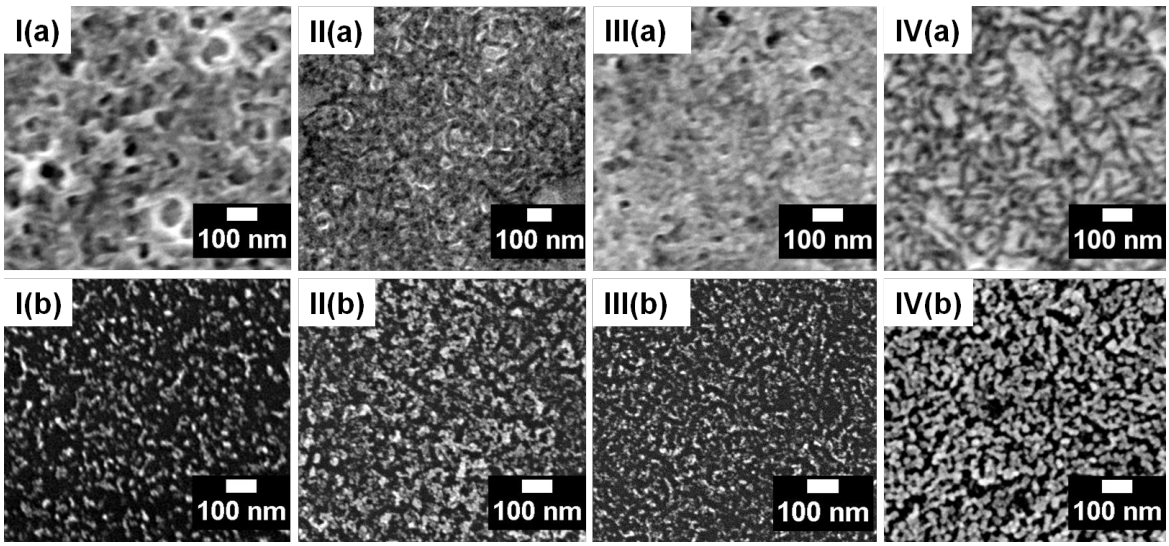

Figure 6.7.: I(a)-IV(a) SEM images for the polymer-ZnO hybrid films obtained after spin-coating from sol-gel with compositions I, II, III & IV (table 6.1) respectively. I(b)-IV(b) The corresponding films after calcination showing foam-like appearance.

The structural investigation for the different compositions is performed as a function of increasing w_{ZAD} in the system from 0.010 to 0.065. The impact of increasing w_{ZAD} in the system is clearly visible for the hybrid samples (figures 6.7I(a)-IV(a)) by an increase in the brighter proportions of the gray-scale SEM images. The film obtained from composition

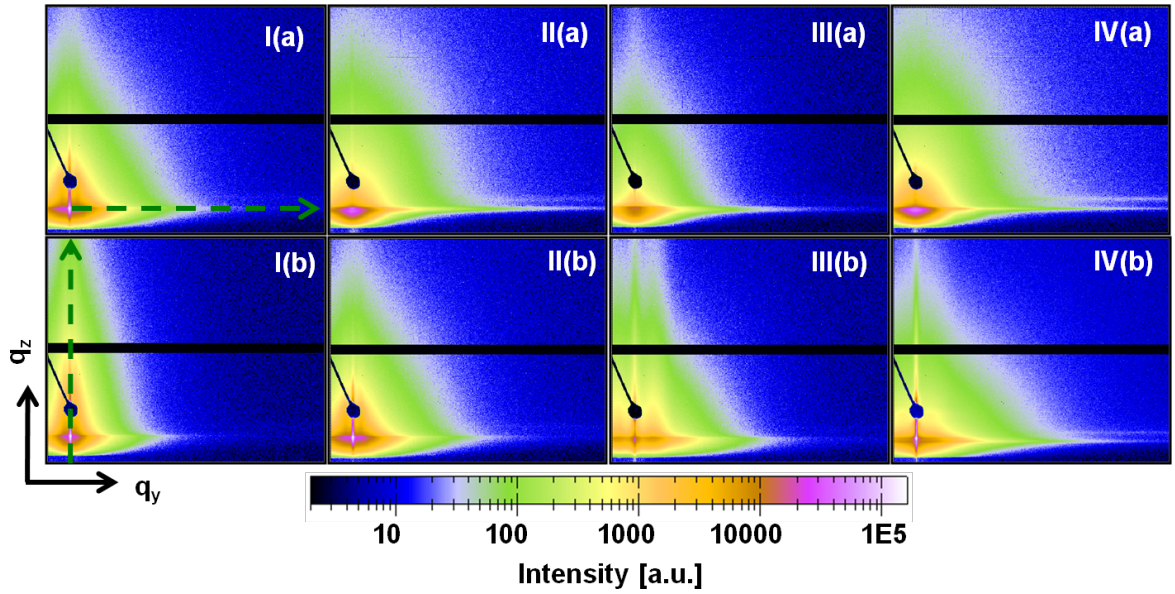

Figure 6.8.: 2d GISAXS data shown in the range of -0.16 to 1.8 nm^{-1} in the q_y direction and 0.3 to 1.9 nm^{-1} in the q_z direction for the polymer-ZnO hybrid films I(a)-IV(a) and corresponding films after calcination I(b)-IV(b) obtained from sol-gels with compositions I, II, III & IV respectively. The vertical and the horizontal green dashed arrows in I(a) and I(b) show the cut positions to access quantitative information. The point-shaped beamstop shields the specular peak and the black horizontal segment is the inter-module gap of the detector.

I (figure 6.7I(a)) shows already a network-like scaffold of the polymer matrix in which the precursor is incorporated. Due to the fact that the polymer appear darker in the SEM images, the film seems highly porous. Upon increasing the w_{ZAD} (figures 6.7II(a)-IV(a)), the morphology of the films becomes more compact with diminishing porous appearance. The continuous foam-like morphology prominently shows up after calcination without the presence of discontinuities or inhomogeneities in the films as seen for the previous morphologies. It is also observed that the calcined films resemble the hybrid films and hence the ZnO morphology is preserved upon removal of the template. All the films show highly porous morphology having a foam-like appearance which becomes denser with increasing w_{ZAD}. However, for all the films, the pore size of the foam stays highly polydisperse.

In order to explore the foam-like nanostructures thoroughly, the structures in the film volume are probed using GISAXS as described in section 3.1.5. The measurements are carried out at the P03 micro and nano-focused x-ray scattering (MiNaXS) beamline of the PETRA III storage ring at DESY. The 2d GISAXS data for all the hybrid and the calcined films are shown in figure 6.8. It is observed that the scattering signals of the films obtained from different sol-gel compositions are different indicating presence of varied length scales

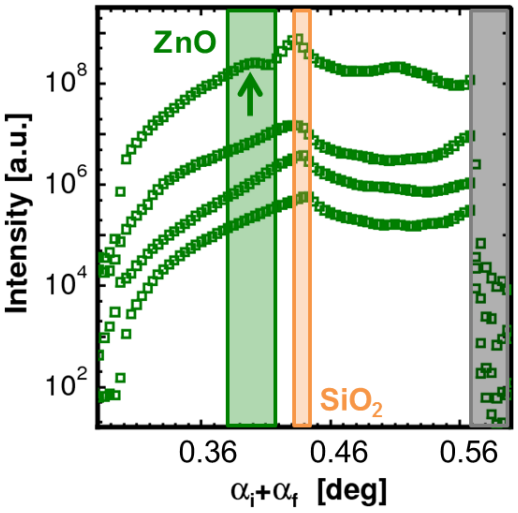

Figure 6.9: Vertical cuts at $q_y = 0\,\mathrm{nm}^{-1}$ for the calcined films exhibiting foam-like morphology plotted as a function of increasing w_{ZAD} from bottom (composition I; $w_{ZAD} = 0.010$) to top (composition IV; $w_{ZAD} = 0.065$). Refer to table 6.1 for the compositions of all the sol-gel solutions used. The gray shaded region corresponds to the specular peak shielded by the beamstop (figure 6.8I(b)-IV(b)). The Yoneda peak for ZnO is most prominent for the film with $w_{ZAD} = 0.065$ as indicated by an arrow.

in the volume of the films. The signal from the calcined films show higher intensity at the Yoneda positions, clearly showing that the contrast between air and ZnO is higher than the contrast provided by the polymer-ZnO nanocomposite. Again to quantify the length scales present in the film volume, cuts to the data are performed along q_y and q_z directions.

The vertical cuts made at $q_y = 0\,\mathrm{nm}^{-1}$ provide average depth-sensitive information about the structures present perpendicular to the substrate plane. These vertical cuts for all the calcined films are plotted in figure 6.9. Considering the incident angle $\alpha_i = 0.3°$, the peak obtained at an exit angle $\alpha_f = 0.14°$ for all the cuts, corresponds to the theoretical critical angle α_c of silicon dioxide (SiO_2) which is used as a support for all the films. This common peak is shaded by an orange bar in the graph 6.9. The low film thickness of the films results in a scattering contribution from the substrate as well. For the highest w_{ZAD} in the film (synthesized using composition IV), another peak at $\alpha_f = 0.10°$ (marked by the green arrow) is observed (the topmost curve in figure 6.9). This peak corresponds to the α_c of ZnO. The detection of the α_c in the films with lower w_{ZAD} is difficult due to the stronger contribution from the substrate. Hence, the Yoneda region in the signal corresponding to ZnO for all the films is marked by a green shaded area in the graph. Comparing the scattering length density (SLD) for the ZnO foam calculated for $\alpha_f = 0.10°$ obtained for $w_{ZAD} = 0.065$, with the theoretical SLD for bulk ZnO (equation 2.32), a porosity of 77 % is obtained.

In addition to the porosity information, the modulations in the cuts at $\alpha_i + \alpha_f > 0.54°$ give information about the thickness of the films. The shorter reciprocal distance between these oscillations for the film containing the highest $w_{ZAD} = 0.065$ indicates an increase in the film thickness in real space. Thus, the thickness of the calcined films shows an increase with the increasing w_{ZAD} as more ZnO remains on the substrate.

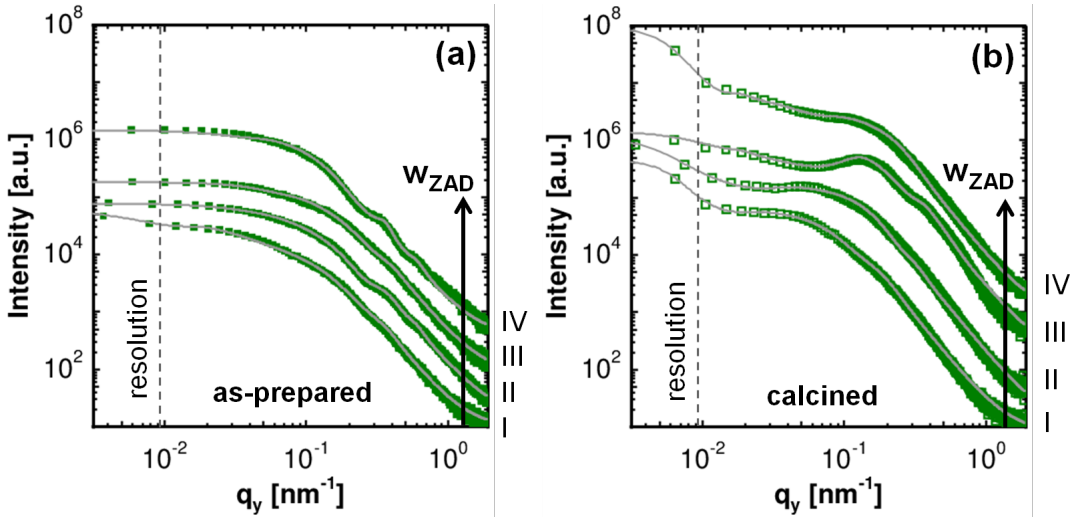

Figure 6.10.: Horizontal cuts (symbols) at the Yoneda peak position of ZnO, $q_z = 0.47\,\mathrm{nm}^{-1}$ for the hybrid (as-prepared) (a) and calcined films (b) exhibiting foam-like morphology plotted as a function of increasing w_{ZAD} from bottom (w_{ZAD} = 0.010) to top (w_{ZAD} = 0.065) as indicated by the arrows. The respective compositions (refer to table 6.1) of the sol-gel solutions are marked on the right axis of both plots. The solid gray lines are the fits to the data. All the curves are shifted along the intensity axis for clarity and the vertical dashed lines correspond to the resolution limit towards larger structures.

The horizontal cuts along q_y for the hybrid and the calcined films shown in figure 6.10 allow to probe the lateral structural length scales in the film volume. The prominent peaks visible in the horizontal cuts denote the dominant length scales in the films. The horizontal cuts are fitted with the two cylindrical form factors and structure factors distributed on a 1d paracrystalline lattice as described in chapter 2.4.2. The structure and form factors with their respective distributions for each sample are summarized in table 6.2. It is worth noting at this point that the listed form factor diameters are linked to the size of the clusters of ZnO nanoparticles in the film and are in good agreement with the length scales obtained via SEM. The structure factors on the other hand, is the representative of the average center-to-center distance between the ZnO clusters. Additional to this set of information, more thorough analysis also reveals the average pore size in the films (more prominent for the hybrid films). The presence of mesopores in all the films has been already confirmed by the SEM images.

The average pore size in the film volume is calculated using the following equation:

$$\text{pore size} = \text{center-to-center cluster distance} - \text{cluster diameter} \tag{6.1}$$

Thereby, the average pore sizes obtained for all the films along with the average ZnO

composition	polymer-ZnO hybrid (as-prepared) films			
	structure factor [nm]	σ_S [nm]	form factor [nm]	σ_F [nm]
I	50 ± 5	18	20 ± 1	5.5
II	45 ± 2	20	26 ± 1	2.2
III	35 ± 2	12	24 ± 1	2.2
IV	16.5 ± 1	1.7	12 ± 1	3.6
composition	calcined films			
I	130 ± 10	45	46 ± 2	5.5
II	75 ± 2	28	24.4 ± 1	3.0
III	34 ± 5	7	18 ± 1	2.8
IV	38 ± 5	13.5	12 ± 1	3.3

Table 6.2.: Summary of different length scales obtained in the volume of the films showing foam-like morphology, prepared using different sol-gel compositions (table 6.1). The form factor diameter and the structure factor with their respective Gaussian distributions (σ_F & σ_S respectively) are obtained from the fits to the horizontal line cuts of the GISAXS data as shown in figure 6.10.

cluster sizes present in the films are plotted as a function of increasing w_{ZAD} in figures 6.11(a) and (b) respectively. For the data shown for the pore sizes in the films, two conclusions are clearly drawn: firstly, the average pore size of the foam-like films increases after calcination due to the removal of the polymer template. Secondly, it is also observed that the average pore size in the film volume decreases with increasing w_{ZAD}. This is attributed to the presence of more material in the film after calcination for higher w_{ZAD}, which limits the size of the pores.

From the plot of the average cluster sizes in the films before and after calcination (figure 6.11(b)), it is clearly noted that the ZnO clusters decrease in size when w_{ZAD} is increased. This is explained by the limited mobility of the ZnO nanoparticles for high w_{ZAD}. When the amount of ZnO precursor incorporated in the system is low, the ZnO nanoparticles have high mobilities and therefore, the probability of finding one another to form large clusters during the film processing is intensified. The possibility of formation of large clusters which later disintegrates into smaller clusters also exists for the films containing higher w_{ZAD}. But, the same average cluster size for the film with $w_{ZAD} = 0.065$ before and after calcination, supports the former assumption of limited mobility of ZnO nanoparticles. Interestingly, it is also realized that the cluster size for the calcined

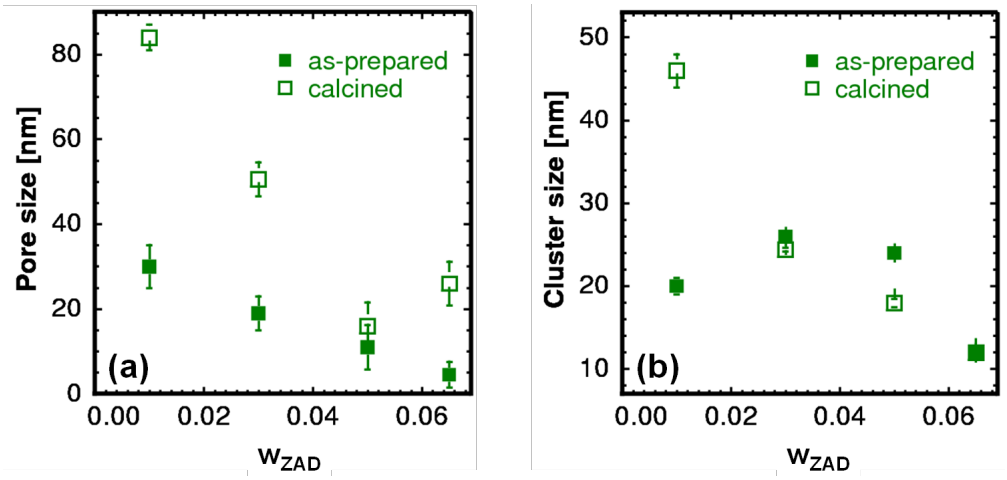

Figure 6.11.: (a) Average pore sizes for hybrid (as-prepared) and calcined films prepared using compositions I, II, III & IV showing foam-like morphology. (b) Average cluster sizes for the same films plotted as a function of increasing w_{ZAD} in the system. The results are obtained from the fits to the horizontal cuts of the GISAXS data (figure 6.10) and applying equation 6.1.

films for $w_{ZAD} > 0.04$, are within the exciton diffusion length [175], which accounts for the usability of these films as an active layer in hybrid solar cells. The network-like morphology also allows for further development of the films towards applications in dye-sensitized solar cells (DSSCs).

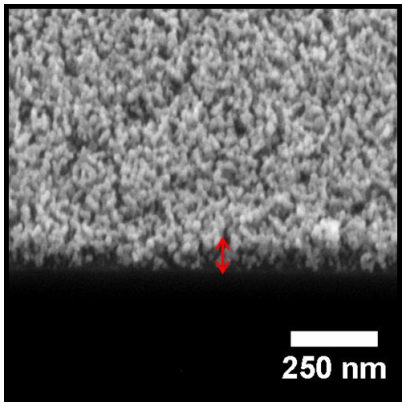

Figure 6.12: The SEM cross-sectional view of the calcined film showing foam-like morphology, prepared from sol-gel with w_{ZAD} = 0.065 (composition IV) in table 6.1. The red arrow shows the height of the ZnO film on the dark SiO_2 substrate of (525 ± 25) µm.

In summary, the length scale of the various nanostructures in film synthesized via sol-gel approach using P(S-*b*-EO) as the structure-directing template lies in the range of 40 to 200 nm. Studies have also been carried out in order to obtain length scales larger than 200 nm. This has mainly involved varying the w_{ZAD} in the sol-gel solution. Extremely low w_{ZAD} provides inhomogeneous films, whereas, higher amounts of w_{ZAD} restricts the mobility of the ZnO nanoparticles synthesized in the sol-gel solution. As such, a tendency towards precipitation of the ZnO nanostructures is observed in the sol-gel. This phenomenon sets

the limits to the structural length scales of the nanostructures that are possible to obtain using a single diblock copolymer template.

Besides a suitable length scale in the nanostructured film volume, the thickness also plays an important role in deciding the device performance as explained in detail in section 2.3. As seen from the exemplary cross-sectional SEM image of the film with foam-like morphology (obtained using sol-gel composition IV) in figure 6.12, it is observed that even for the highest w_{ZAD} investigated, the film thickness ranges up to 50 nm. Several attempts have been made to tune the film thickness via adjusting the spin-coating parameters such as the rotation speed. Maximum thickness of up to 85 nm has been achieved, which is still well below the optimum thickness required for a practical application, for example, as an active layer in hybrid solar cells or in DSSCs. To expand the thickness of the films, alternative deposition method, such as solution-casting is investigated for the most promising foam-like morphology obtained from composition IV.

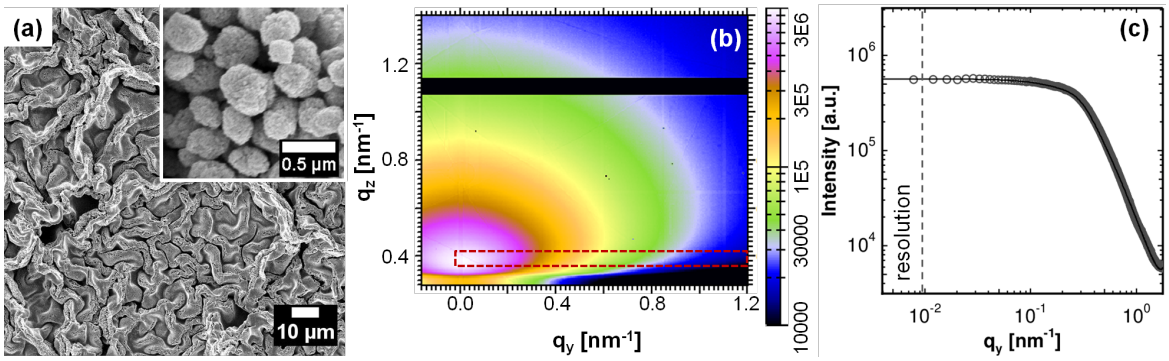

Figure 6.13.: (a) SEM topography image of the solution-cast film after calcination, prepared using composition IV. An image of the same film under higher magnification is shown in the inset. (b) The corresponding 2d GISAXS data of the calcined film. The red dashed rectangle shows the region where the horizontal cut to the data is made averaged over 7 pixels. The black horizontal stripe is the inter-module gap of the detector. (c) The horizontal cut to the GISAXS data (symbols) along with the fit (gray solid line). The vertical dashed line shows the resolution limit towards larger structure sizes.

As seen from the SEM surface images (figure 6.13(a)), the calcined solution-cast film shows a high surface roughness and structural length scales in the range of several hundreds of nanometers up to micrometers. It is clearly seen from the magnified image (as an inset in figure 6.13(a)) of the same film, that the morphology of the film is quite different from that obtained via spin-coating from the same sol-gel solution. The solution-cast film is rather composed of ZnO nanoparticles resembling spherical morphology instead of the expected foam-like morphology. This is interpreted from the thermodynamic point of view, where the solution-casting process provides considerable time for reorganization

of the structures in the film. The energy for rearrangement of the structures is provided by the surrounding solvent environment which increases the mobility of the nanostructures. This finally leads to the formation of spherical granular morphology as it is highly energetically favorable. Although, a high effective surface area of the film is evident, it suffers the disadvantage of being transformed to a powder film on the substrate after calcination. Although a higher film thickness of around 400 nm is reached as compared to the spin-coated films, lack of proper adhesion of this powder to the substrate limits its practical application.

However, for a complete study, a detailed investigation of the morphology in the film volume is performed via GISAXS measurements as described before. The 2d GISAXS data for the calcined films looks very different from the patterns obtained for the films fabricated via spin-coating (figure 6.13(b)). No prominent specular peak and Yoneda peak are observed. This is due to the large diffuse scattering of the x-rays caused by the highly polydisperse structures, due to which the reflection is considerably reduced. Hence, to obtain fruitful information from the data, the scattering signal is obtained at an incident angle of $\alpha_i = 0.21°$ which is very close to the critical angle, α_c of ZnO. Horizontal cuts are performed to the data averaged over 7 pixels along q_z as shown in figure 6.13(b) by the dashed rectangle and plotted in figure 6.13(c). The plateau-like feature of the horizontal cut results from the lack of a well-defined structure size in the film. Upon fitting the data using the model described in section 2.4.2, a structure size of (25 ± 5) nm is observed. This corresponds to the average distance between the ZnO nanoparticles. The larger length scales of the order of few microns as observed by SEM are not resolved due to limitations imposed by the set up of the beamline.

Crystallinity of ZnO

The polymer-ZnO hybrid films obtained after spin-coating or solution-casting of the sol-gel solutions discussed in the previous section consist of amorphous ZnO phase. However, for practical applications in nano-electric devices, crystalline phase of ZnO is required for better charge transport as discussed in section 2.2.2. Crystallinity is imparted to the films via a high temperature calcination step as discussed in section 2.2.2.

For the crystallinity investigation, the foam-like structures are chosen which are prepared using the sol-gel with composition IV and measured using XRD instrument I (see section 3.1.4). For the spin-coated film, as seen from the XRD data (figure 6.14), the signal is very weak, whereas, for the solution-cast film, a considerable intensity is received. This is attributed to the difference in film thicknesses of the samples. Due to very low thickness of the spin-coated films, approximately 50 nm, the sample for the XRD measurement has been prepared by 3× iterative spin-coating. Both the films exhibit signal corresponding

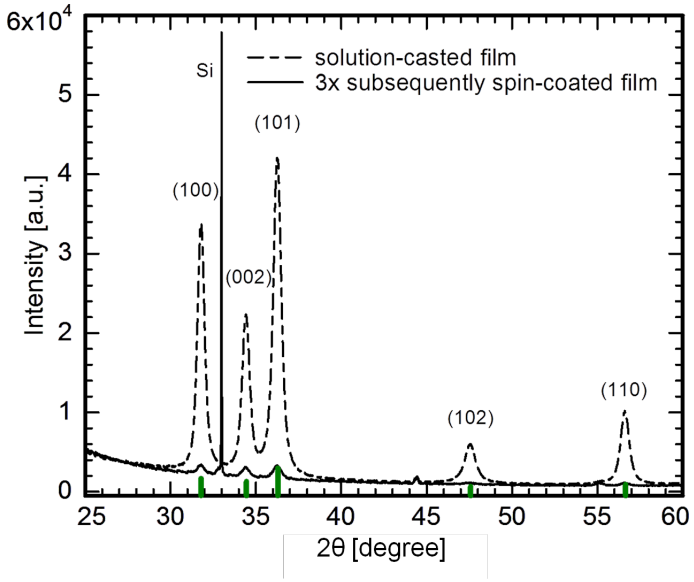

Figure 6.14.: XRD patterns of the spin-coated (black solid line) and the solution-cast (black dashed line) films after calcination. Both the films are prepared using a sol-gel having composition IV. The vertical solid green lines show the theoretical peak positions for crystalline wurtzite phase of ZnO with their relative intensities.

to the wurtzite polymorph of ZnO. The strong peak obtained at $2\theta = 33°$ comes from the silicon (Si) substrate underneath. It is a Si (100) peak and is well observed in the spin-coated sample due to its low film thickness. The data from both samples are fitted with Gaussian peaks and the average crystallite sizes in the films are calculated using the Scherrer equation (section 2.4.1). It should be noted that for the calculation of the average crystallite size, the full width at half maximum intensity of the respective peaks is taken into account. Although from the SEM and the GISAXS measurements performed on the same films, it is concluded that the size of the ZnO nanocrystals present on the samples are highly polydisperse, this is not resolved via the XRD measurements. Average crystallite sizes of 16 nm and 20 nm are obtained for the spin-coated and the solution-cast films respectively. The average crystallite size for the solution-cast film is observed to be higher than that of the spin-coated film.

6.1.2. Optical properties

For optical characterization of the ZnO films synthesized via sol-gel, UV/Vis spectroscopy (using UV/Vis instrument I, see section 3.2.1) is performed. In addition, Fourier-transformed infrared spectroscopy (FTIR) is carried out in order to determine the various constituents present in the film, so as to investigate the film composition.The absorption of foam-

like ZnO nanostructured film obtained from composition IV, is exemplarily studied via UV/Vis spectroscopy. For the UV/Vis measurements, the film is prepared on a glass substrate in order to measure the transmitted light through it. Figure 6.15(a) shows the corresponding absorbance spectra for the calcined foam-like film measured over the optical spectrum range from visible to ultraviolet. A typical absorption in the UV region of the spectrum for crystalline ZnO is observed. In figure 6.15(b), the square of absorption coefficient of the film times the energy is plotted against energy axis in order to determine the bandgap of the material present in the film. The band gap is obtained by linear extrapolation of the data as shown by the black dashed line, and is calculated to be 3.3 eV. The Tauc equation for direct band gap semiconductors as described in section 3.2.1, is used for calculating the band gap in the present case. The band gap corresponds to the theoretical value of wurtzite phase of ZnO confirming the crystallinity of the film in agreement with the results obtained from XRD measurements.

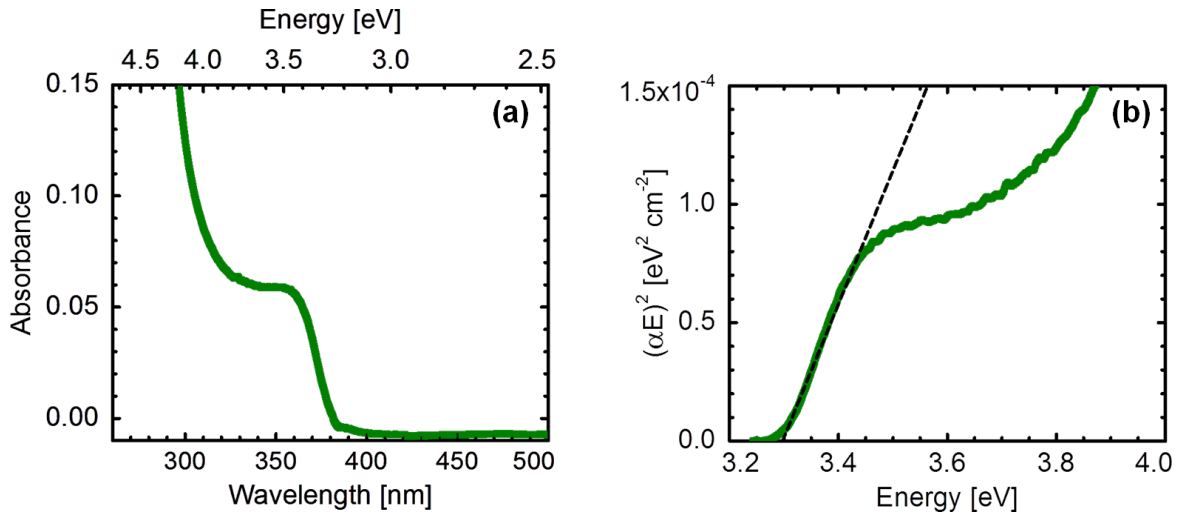

Figure 6.15.: (a) Absorption spectrum of ZnO foam-like film (prepared from composition IV) plotted against wavelength and the corresponding energy in the spectral range of 260 to 500 nm. (b) The respective Tauc plot for the same same film. The linear extrapolation to the energy axis reveals the bandgap of the material.

In addition to the UV/Vis measurements, FTIR spectroscopy, as explained in section 3.2.3 is executed on the ZnO powder obtained via solution-casting using composition IV of the sol-gel (table 6.1). For this particular measurement, the sample in the powder form is essentially required in order to obtain a pellet which can be inserted in the sample holder to be measured in transmission mode. The pellet is prepared using the ZnO powder in combination with potassium bromide (KBr) crystals under a high pressure. The FTIR spectrum obtained is depicted in figure 6.16. It is observed that the data acquired contains

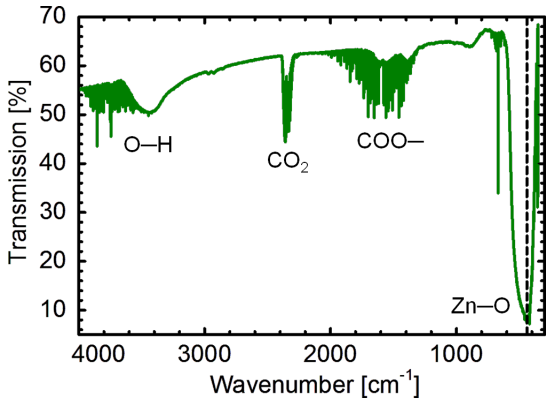

Figure 6.16.: FTIR spectrum of ZnO powder obtained after calcination of the solution-cast film (prepared using sol-gel composition IV). The vertical dashed line shows the signal corresponding to Zn-O bond. The presence of all the other signals is indicated and described in details in the text.

some noise which has resulted from the fact that very little amount of ZnO powder is used for the preparation of the pellets and the homogeneous distribution of the ZnO nanoparticles in the final pellet is not assured even if a homogeneous pressure is exerted on the entire material. Nevertheless, the characteristic absorption lines obtained in the spectrum are associated with the absorption by the corresponding components present in the sample. The most significant signal at 450 cm^{-1} corresponds to the Zn-O bond [176]. Next, a weak signal between 1600 and 1400 cm^{-1} signifies the COO- stretching modes. The occurrence of this signal in the FTIR spectrum for ZnO is often reported [177]. However, its presence is still under discussion. The COO- stretching can be mainly observed in this context during two different scenarios. First, this signal may arise from the presence of acetate groups in the sample. It should be noted that although, zinc acetate dihydrate is used as the precursor, its presence after the calcination of the sample, performed at a high temperature of 400 °C, is quite unexpected. All the unreacted precursor molecules, if present in the system in the first place, should be removed after the high temperature calcination step. The second possible explanation for the signal observed, as reported, comes from the fact that the ZnO powder in the pellet absorbs carbon dioxide (CO_2) from the surrounding environment [117]. The signal at 2342 cm^{-1} is due to the presence of CO_2 [178]. This might be preset in the sample as impurities or might be absorbed from the surrounding environment. Another possibility for the presence of this group is their formation during the combustion of the diblock copolymer at a high temperature. Finally, the signal obtained at 3400 cm^{-1} is associated to the stretching of O-H bond and is commonly observed in most of the FTIR spectra of compounds [179]. This signal confirms the presence of water molecules, absorbed by the sample from the ambient atmospheric

moisture. Another conclusion which can be drawn from the FTIR analysis is the complete removal of the copolymer template after calcination. This observation is confirmed by the fact that any signal corresponding to the C-H bond, which generally appears in the range of 2800 to 3000 cm^{-1} is missing in the present spectrum. Thus, both UV/Vis and FTIR spectroscopies confirm the formation of crystalline ZnO phase in the films, synthesized via sol-gel route.

6.1.3. Results & discussion

Sol-gel synthesis is explored in combination with a structure-directing diblock copolymer in order to successfully produce a complex assembly of various zinc oxide (ZnO) morphologies. The nanostructures obtained for ZnO are quite different from the previously reported TiO_2 synthesized using the same approach [15]. The different nanostructures result from the varied interactions between the components in the systems, which highly depends on the thermodynamic conditions and interfacial energies between the components. The ternary phase diagram for four different ZnO nanomorphologies shows the respective compositional boundaries. Such a phase diagram for ZnO is investigated for the first time using P(S-*b*-EO) template as per the existing literature. From the SEM and GISAXS investigations, it is observed that the structures in the film are obtained in the range of 40 to 200 nm. These different nanostructures obtained are suitable for different applications, such as catalysts, sensors, drug-delivery and energy storage [180–182].

Out of the different morphologies, the foam-like nanostructures are of the most interest as several on-going studies have already shown their high potential in the field of organic photovoltaics [183]. The foam-like inorganic scaffold is used for the injection of a suitable hole conductor, which is either a conducting polymer or a liquid electrolyte in case of hybrid and dye-sensitized solar cells respectively [184–186]. However, for an efficient functioning of the final device, the inorganic matrix needs to fulfill certain criteria such as a high surface area, the right film thickness and suitable pore sizes. Backfilling of a solid-state hole conductor is very closely related to the size of the pores obtained in the films. If they are too small, the large polymeric molecules of the hole conductor find it difficult to get incorporated into the film. This directs towards the suitability of having larger pores in the films. However, if the pore sizes are increased beyond a certain limit, the excitons generated in the system need to travel longer distances to reach the interface, which is essential for the separation of charges. Since, the excitons have a limited diffusion length and lifetime, the overall efficiency of charge separation in the device is hampered. As an example, for P3HT as the hole-conducting material, the distance that the exciton can travel is in the range of 10 to 20 nm [175]. To overcome these theoretical limits for

the pore sizes, sol-gel technique is very promising as the average pore size is shown to be tuned effectively in the range of (84 ± 3) to (26 ± 5) nm (when low molecular weight P(S-*b*-EO) is used as the template) by monitoring the w_{ZAD} in the sol-gel recipe. The porosity of of the films for the investigated foam-like morphologies is calculated to be about 77 % via GISAXS measurements. This high porosity is very promising for the practical applications and is in good agreement for the porosities obtained for titania systems [187]. However, the film thickness remains low in the range of 50 nm which is not sufficient for any of the above-mentioned device applications.

Alternative deposition routines such as solution-casting provides films with a high film thickness of about 400 nm with an average structure size of (25 ± 5) nm in the film volume. However, for practical applications, these films are not used since, they are in the form of powder which has a poor stability and contact with the substrate surface.

The crystallinity and the optical properties of the foam-like nanostructures are investigated via XRD, UV/Vis and FTIR spectroscopy. All these measurements give a clear signature of the presence of ZnO in the wurtzite crystalline phase. This polymorph of ZnO has a higher electron mobility than that of the other phases and hence is highly potential for being applied in nanoelectronic devices. It is also reported that the electron mobility of ZnO is higher than that of titania and hence is considered as an extremely important material as an alternative to titania [128]. For the calcined films obtained after solution-casting, a larger crystallite size is obtained as compared to those obtained for the spin-coated films. This phenomenon is explained by the fact that spin-coating is a fast drying process. The structures obtained are quenched rapidly due to fast solvent evaporation, which does not allow for further rearrangement of the structures. However, for the slow solution-casting process, enough time is provided for the structural rearrangement and formation of larger crystallites. In conclusion, the results show a good agreement with the findings from SEM and GISAXS measurements. Additionally, the calculated band gap of 3.3 eV is in good agreement with the theoretical band gap for crystalline wurtzite phase of bulk ZnO [188]. Finally, the FTIR measurements indicates a complete removal of the polymer template after calcination.

6.2. ZnO nanostructures using high molecular weight P(S-*b*-EO)

ZnO nanostructured films with a foam-like structure have found applications in photocatalysts, gas/chemical sensing and as energy storage materials in the recent years. Although the synthesis of such foam-like nanostructures in the form of thin films might appear rea-

sonable as described in the previous section, a real challenge is to develop a route to control two important parameters related to these nanostructures: the porosity and the pore size. Optimization of these parameters is necessary to suite the structures to any particular end application. The sol-gel synthesis route already allows for fine-tuning these parameters depending on the diblock copolymer template used and the various combinations of the weight fractions of the sol-gel ingredients, but only to a limited extent. The limitation is imposed by the block lengths of the template which act as the sites for the reaction of the precursor molecules, thereby giving rise to the final nanostructures. Hence, additional tuneability to the pore size and porosity of the foam-like ZnO films is imparted by the use of a template with different molecular weight. P(S-*b*-EO) is used as the structure-directing agent for the sol-gel synthesis of the foam-like ZnO thin films, in the same way and under similar conditions as described in section 6.1. The only difference lies in the chain lengths of the present template, which are longer than that used before. Hence, the molecular weight of this template is higher than the former. Details about the molecular weights and the polydispersity indices of the templates are provided in table 4.1. Since both the hydrophobic and the hydrophilic blocks of the template used in this section are longer than the previous one, more amount of the ZnO precursor (ZAD) is possible to be incorporated in the system. The different weight fraction combinations of the solvents and ZAD chosen for the present study are listed in table 6.3. A thorough morphological analysis of the films obtained is performed in terms of porosity and average pore size at the film surface and volume via SEM and GISAXS investigations respectively. In the end, a comparison of the porosity and the average pore sizes in the volume of the films (extracted via GISAXS measurements) obtained from both the templates, is shown. This gives a complete picture of the range of different structural length scales achievable in the system depending on the molecular weights of the templates used. Throughout the discussion, the two templates are referred to as the low and high molecular weight templates. Based on the analysis of the GISAXS data, a schematic model is proposed in order to understand the underlying principle regarding tuneability of the structural length scales.

6.2.1. Morphology

It is observed that due to the longer chain lengths of the PEO block for the high molecular weight template, it is possible to incorporate more amount of ZAD in the system (table 6.3), as compared to the sol-gel compositions for the low molecular weight template (compositions I, II, III and IV in table 6.1).

composition	w_{DMF}	$w_{\mathrm{H_2O}}$	w_{ZAD}
A	0.99	0.005	0.005
B	0.91	0.08	0.01
C	0.94	0.03	0.03
D	0.91	0.01	0.08

Table 6.3.: List of different sol-gel compositions chosen for the synthesis of foam-like ZnO nanostructures using a high molecular weight P(S-*b*-EO) template. w represents weight fraction.

Surface and inner film morphologies

Figure 6.17 shows SEM images of the calcined films (top row) prepared via spin-coating of the sol-gels listed in table 6.3. It is evident from the SEM surface images that all the films show a foam-like appearance, similar to the ones obtained using the low molecular weight template. It is also observed that the ZnO nanostructures are more densely packed on the substrate with increasing w_{ZAD}, thereby giving an impression of reduced porosity.

In order to confirm the morphological changes as a function of increasing w_{ZAD} in the volume of the film and to quantify the structural length scales, GISAXS measurements are performed as described in section 3.1.5. The bottom row in figure 6.17 depicts the corresponding 2d GISAXS data obtained from the respective films. It is observed that higher coverage of the substrate by the ZnO nanostructures also contributes to an effective increase in the contrast of the scattering signal followed by an enhanced lateral scattering in q_y direction. This enhancement is strongly visible for the film prepared from composition A to B. However to obtain quantitative information from the GISAXS analysis, vertical and horizontal cuts, as indicated in figure 6.17(e) by the dashed arrows, are performed.

Information about the morphology perpendicular to the substrate plane is essentially obtained from the vertical cuts as plotted for all the samples in figure 6.18. The most important information obtained from the analysis of these cuts is the average porosity in the film volume which is calculated from the scattering length density (SLD) of the material obtained. In order to obtain the SLD, the critical angle of the material is determined which is obtained at the position of the Yoneda peak in the scattering data. As observed from the vertical cuts, a prominent Yoneda peak is only visible for the film with the highest w_{ZAD} as indicated by the arrow. The peak position is determined at $\alpha_f = 0.12°$ when the incident angle, α_i is at 0.38°. An additional peak for the film obtained using composition D is observed at $\alpha_f = 0.14°$ which matches with the theoretical critical angle, α_c of silicon dioxide, coming from the substrate underneath. This peak is clearly

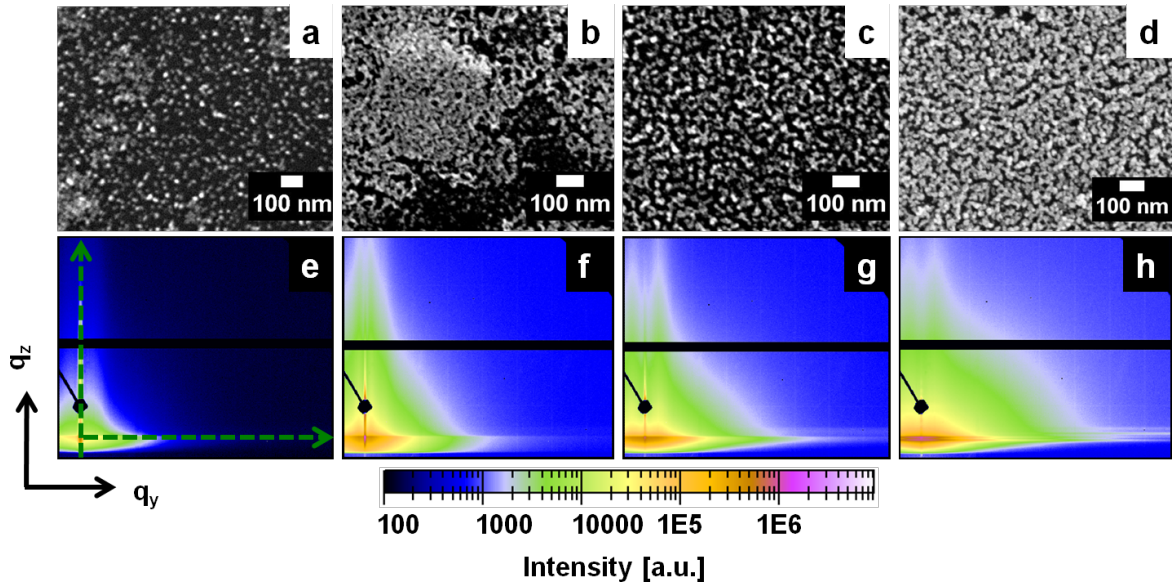

Figure 6.17.: Top row: SEM surface topography images of the calcined films obtained using the high molecular weight P(S-*b*-EO) template plotted from (a) to (d) for compositions A to D as listed in table 6.3. Bottom row: 2d GISAXS data for the respective films plotted in q_y from -0.16 to 1.8 nm^{-1} and in q_z from -0.18 to 2.8 nm^{-1}. The intensity scale bar is shown below the images and the dashed arrows schematically indicate the cut positions in the images for the quantitative analysis of the data. The point-shaped beamstop shields the specular peak and the horizontal black stripe visible in the scattering signals corresponds to the inter-module gap of the detector.

visible for all the films and is indicated by the orange shaded area in the graph. The Yoneda peak area, shaded in green, however, does not show a prominent peak except for the film with the highest w_{ZAD}. This is due to the low film thickness and coverage for the films obtained with compositions A, B and C. The SLD of the material extracted from the ZnO Yoneda peak (for composition D) is compared to the theoretical SLD for bulk ZnO, which yields an average porosity of 61 % in the film volume. Along with the porosity information, it is also clearly observed that modulations in the cut for the highest w_{ZAD} is smaller and is rather prominent at $\alpha_i + \alpha_f > 0.53°$ as compared to the other cuts. This indicates an increase in film thickness in the real space which also agrees with the increased coverage of the substrate for highest w_{ZAD} as observed from the SEM image (figure 6.17(d)).

For information regarding the lateral structures in the film volume, the horizontal cuts for the 2d scattering data are performed for both the copolymer-ZnO hybrid (as-prepared) and the calcined films for all the compositions mentioned in table 6.3. These cuts are obtained at the Yoneda peak position of ZnO for all the films and are fitted using the

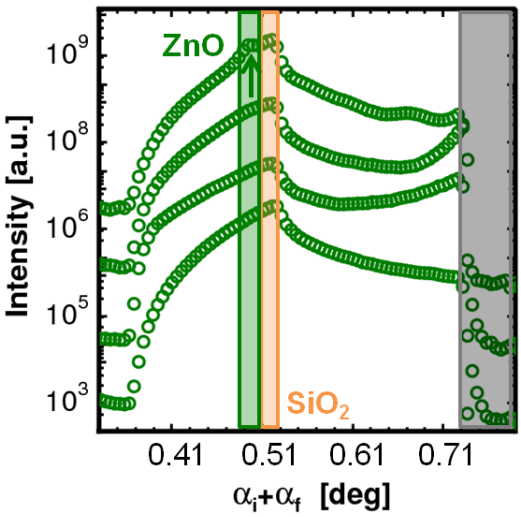

Figure 6.18: Vertical cuts at $q_y = 0\,\mathrm{nm}^{-1}$ for the calcined films exhibiting foam-like morphology, obtained from the high molecular weight P(S-*b*-EO) template, plotted as a function of increasing w_{ZAD} from bottom (composition A with $w_{ZAD} = 0.005$) to top (composition D with $w_{ZAD} = 0.08$). For the composition of the sol-gel solutions, refer to table 6.3. The gray shaded region corresponds to the specular peak shielded by the beamstop. The Yoneda peak for ZnO is most prominent for the film with $w_{ZAD} = 0.08$ as indicated by an arrow. The SiO_2 Yoneda peak, as shaded by the orange region is observed for all the films.

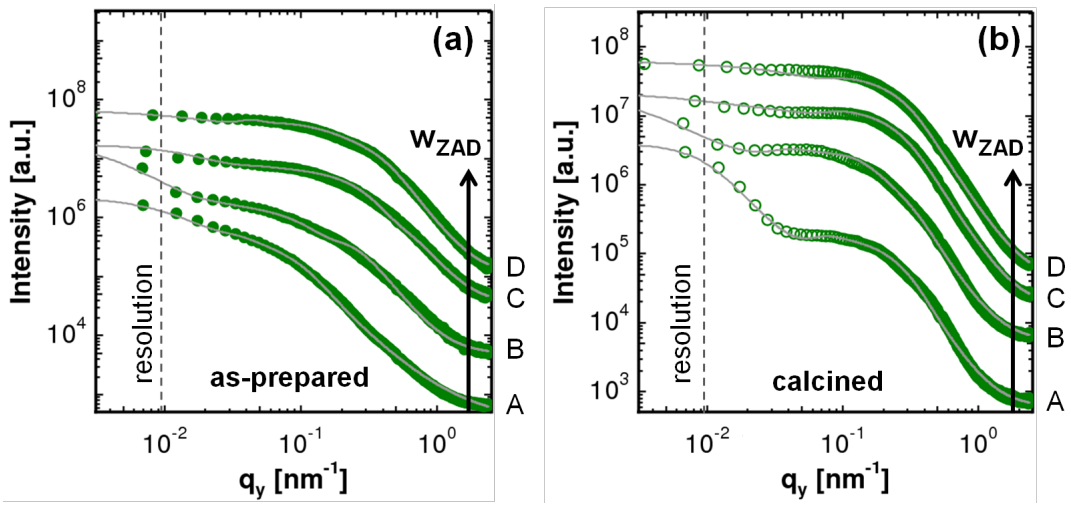

Figure 6.19.: Horizontal cuts (symbols) at the Yoneda peak position of ZnO, for the hybrid (as-prepared) (a) and calcined films (b) exhibiting foam-like morphology, obtained from the high molecular weight P(S-*b*-EO) template, plotted as a function of increasing w_{ZAD} from bottom ($w_{ZAD} = 0.005$) to top ($w_{ZAD} = 0.08$) as indicated by the arrows. The respective sol-gel compositions (see table 6.3) are mentioned on the right axis of the plots. The solid gray lines are the fits to the data. All the curves are shifted along the intensity axis for illustrative purpose and the vertical dashed lines correspond to the resolution limit for larger structures in the film.

cylindrical form factors distributed over a 1d paracrystalline lattice as described in detail in section 2.4.2. The data along with their fits are plotted in figure 6.19 as a function of increasing w_{ZAD} in the system. The plateau-like feature observed in the horizontal cuts for the as-prepared and the calcined films, in general indicate a high polydispersity in the system. However, comparatively the peaks are more pronounced after calcination. This indicates a narrower distribution of the lateral length scales after the combustion of the

polymer template. Quantitatively, the average cluster and pore sizes (calculated using equation 6.1) for all the films are extracted from the fits to the horizontal cuts and are depicted in figure 6.20 as a function of increasing w_{ZAD} in the system. Additionally, the values obtained from the fits for the structure and the form factors with their respective Gaussian distributions are listed in table 6.4.

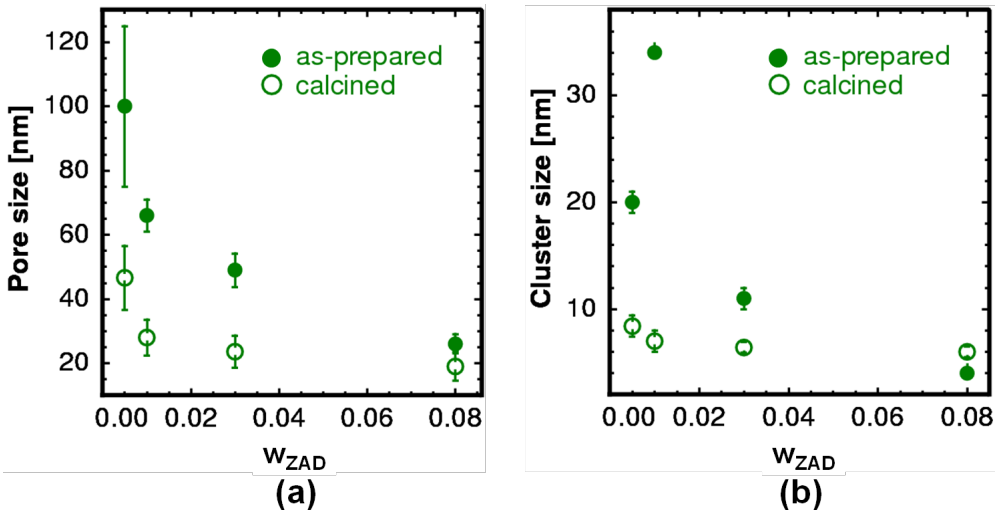

Figure 6.20.: (a) Average pore sizes for hybrid (as-prepared) and calcined films prepared using compositions A, B, C & D showing foam-like morphology. (b) Average cluster sizes for the same films plotted as a function of increasing w_{ZAD} in the system. The results are obtained from the fits to the horizontal cuts of the GISAXS data (figure 6.19) and applying equation 6.1.

As observed from figure 6.20(a), the average pore size in the volume of the film decreases after calcination. Additionally, the pore size also decreases with an increase in w_{ZAD}. The same trend is observed for the average ZnO cluster size in the film volume when the w_{ZAD} is increased (figure 6.20(b)). The suppression in the aggregation of ZnO particles in the system, which finally results in the formation of smaller aggregates is associated with the limited mobility of the ZnO nanoparticles synthesized in the sol-gel when the w_{ZAD} is increased. As also observed in case of the average pore size, the average cluster size in the film volume is reduced after calcination due to removal of the polymer matrix.

Structural comparison of ZnO foam-like nanostructures synthesized using P(S-*b*-EO) templates with different molecular weights

The comparison of the average pore and cluster sizes of the foams obtained from the different templates is presented in figure 6.21. The values are extracted from the fits of the horizontal cuts of the GISAXS data of the corresponding films. The average cluster

composition	polymer-ZnO hybrid (as-prepared) films			
	structure factor [nm]	σ_S [nm]	form factor [nm]	σ_F [nm]
A	120 ± 5	29	20 ± 1	7.5
B	100 ± 2	48.5	34 ± 1	3.8
C	60 ± 2	24	11 ± 1	2
D	30 ± 1	15	4 ± 1	2.25
composition	calcined films			
A	55 ± 10	13.5	8.4 ± 2	2.8
B	35 ± 2	27.5	7 ± 1	2.7
C	30 ± 5	12	6.4 ± 1	3
D	25 ± 5	11	6 ± 1	2.9

Table 6.4.: Summary of different length scales obtained in the volume of the films showing foam-like morphology, prepared using different sol-gel compositions (table 6.3). The form factor diameter and the structure factor with their respective Gaussian distributions (σ_F & σ_S respectively) are obtained from the fits of the horizontal line cuts to the GISAXS data as shown in figure 6.19.

and pore sizes of the ZnO foam-like nanostructures in general are lower for the films synthesized via the high molecular weight template. In order to visualize the on-going structural arrangements in the film volume giving rise to such trends, a schematic model of nanostructure formation is presented in figure 6.22.

The red spheres represent the hydrophobic PS blocks forming the core of the micelles, whereas the blue chains indicate the hydrophilic PEO blocks forming the corona. The small green spheres represent the ZAD molecules which are selectively incorporated in the PEO chains in the micelles. This color code is maintained for both the templates and are indicated accordingly in figure 6.22(a) and (b). As seen from the pictorial presentation, the size of the micelles for the high molecular weight template is bigger than that of the low molecular weight template. This is attributed to the different chain lengths of the polymers used. It gives rise to an initial prediction of obtaining larger pores for the ZnO foam obtained from the high molecular weight template as the PS block forming the core is bigger. It should be noted that the geometry of the micelles shown in figure 6.22 is just for understanding of the processes and may vary in reality depending upon the weight fraction of the solvents present in the sol-gel. For both cases of templating, after calcination, the organic polymer molecules are combusted leaving behind the Zn-O

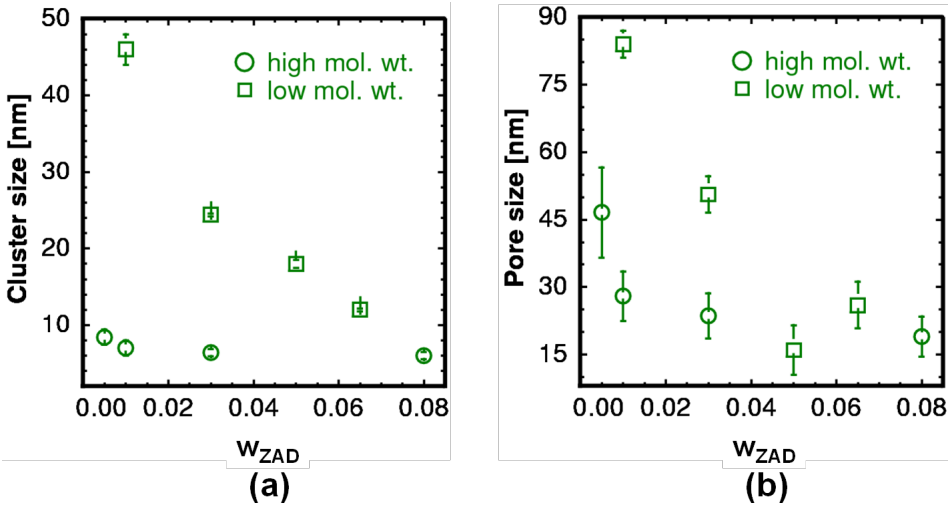

Figure 6.21.: Average cluster (a) and pore sizes (b) in the volume of the films showing foam-like ZnO nanomorphology after calcination. The films are prepared via the sol-gel route using the low and high molecular weight P(S-*b*-EO) templates.

network structures in an amorphous phase (the conversion of ZAD to ZnO during the sol-gel process in the solution is already explained in section 4.2.1). The results obtained via GISAXS (summarized in figure 6.21) are correlated to the schematic model (figure 6.22). For the low molecular weight template, smaller amount of ZAD is incorporated in the micelles which have considerable mobility and therefore, have high probability to cluster together, thereby producing large pores in the film volume. On the other hand, for the high molecular weight template, the presence of higher amount of ZAD in the system restricts their mobility and as a result, smaller clusters are produced (figure 6.21(a)). Additionally, since the clusters are confined due to their lack of mobility, only smaller pores are obtained in the end (figure 6.21(b)). As a consequence, the average porosity of the films is also reduced as observed before. Moreover, a decrease in the overall cluster and the pore size of the films derived from both templates is observed with an increasing w_{ZAD} in the sol-gel. This further confirms the hypothesis of limited mobility of ZnO particles in the system for the high molecular weight template. This is also supported by the fact that the average pore size of the ZnO foam synthesized from the high molecular weight template does not decrease with an increasing w_{ZAD} in the sol-gel as severely as in the case of low molecular weight template, as shown in figure 6.21.

However, an increased incorporation of ZAD molecules (for high molecular weight template) lead to formation of higher number of Zn-O bonds which might also enhance the interaction between the ZnO molecules. As such, larger clusters are produced which undergo structural arrangement in the film volume during the calcination process. These

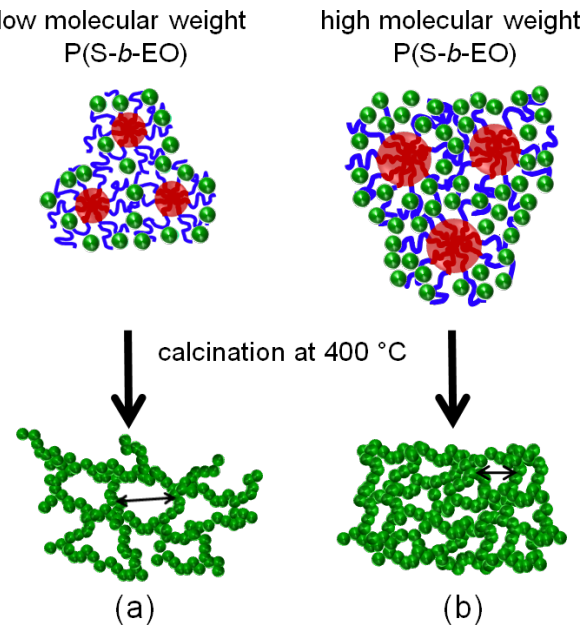

Figure 6.22.: Schematic representation of the formation of foam-like morphology in the ZnO thin films after calcination when a low (a) and high (b) molecular weight P(S-*b*-EO) are used as templates. The model is explained in more details in the text.

clusters then can also disintegrate into smaller clusters due to the pattern collapse after the calcination process, which reduces the average pore size of the films. The exact mechanism of the formation of larger or smaller pores highly depends on the interaction of the various constituents of the sol-gel and the thermodynamic equilibrium among all these interactions. Additionally, the structural rearrangement in the films during the calcination process also plays an important role in deciding the final morphology of the films.

6.2.2. Results & discussion

The foam-like ZnO morphology is obtained via sol-gel synthesis using the high molecular weight template of P(S-*b*-EO) for different composition of the respective sol-gel solutions. The morphology obtained has a high resemblance to those obtained from the low molecular weight template. The homogeneity and surface coverage of the films improve with increasing w_{ZAD} in the system. A clear decrease in the average cluster and pore sizes in the film is observed after calcination. This behavior is contrary to that observed for nanostructures obtained from low molecular weight P(S-*b*-EO) in terms of the trend observed for the average pore sizes in the films. However, the decrease in the cluster size after calcination is expected due to the removal of the polymer template from polymer-ZnO hybrid film. Generally, a reduced cluster size is often accompanied with increasing

cluster-to-cluster distance, referred to as the pore size. However, this is not the outcome of the present investigation. This observation is related to the restricted mobility of the high amount of ZAD molecules used for synthesizing the foam-like nanostructures using the high molecular weight template. It is concluded that after the removal of the polymer matrix, the ZnO nanostructures show little mobility, which is confirmed by the reduction in the average pore size. However, the phenomenon of complete pattern collapse is not observed where the synthesized ZnO nanostructures are supposed to bake together creating large distances (pores) among themselves. Evidence for structural rearrangements in the films during the calcination step is also found, which might lead to the disintegration of the larger clusters into smaller ones. Absence of larger pores on the surface as well as the volume of the film is confirmed by SEM and GISAXS investigations respectively. The average pore size in the film volume (of calcined films) ranges from 46 nm to 19 nm as a function of increasing w_{ZAD} in the sol-gel. The average cluster size of the calcined films on the other hand, lies in the range of 6 nm to 8 nm. This shows that these structures are highly promising for the applications in photovoltaics as the average cluster size is in the range of exciton diffusion length [175]. However, the practical application for the present nanostructures are restricted by the low film thickness which is in the range of 50 to 80 nm.

In summary, the possible limitation to the otherwise highly versatile route of synthesizing varied ZnO nanostructures, is overcome by the use of derivatives of the diblock copolymer template having different molecular weights. It is successfully shown that the same copolymer template is capable of producing similar morphologies even if the molecular weights and hence, the sol-gel compositions are varied. It is observed that a diblock copolymer template with a higher molecular weight of around 1.4 times yields a smaller average pore size and porosity by 21 %. Thus, on the basis of a specific end product for practical application, a correct choice of the molecular weight of the template produce the desired length scale keeping the morphology intact. The thorough analysis by SEM in combination with the powerful technique of GISAXS manifests an efficient way of harvesting the various possibilities related to device engineering via the template-assisted sol-gel approach. Additionally, the present findings further extends the scope to manipulate the length scales of other suitable morphologies and several different metal oxide nanostructures.

6.3. Blade-coated films from custom-made ZnO paste using high molecular weight P(S-*b*-EO)

Recent developments in the field of organic photovoltaics have promoted the use of numerous production techniques which involve mass production in an energy-efficient manner. The most commonly exploited industry-based techniques include roll-to-roll printing, spray deposition and screen-printing. In order to use the just-mentioned deposition methods, the material to be deposited needs to be processed in a distinct way. The nanostructures discussed previously are synthesized in the solution mainly constituting of DMF, which is not practical for commercial applications from the point of view of environmental protection. One workaround to the problem is to synthesize pastes of nanostructures which are directly applied for the printing process. The fabrication of such pastes are majorly reported for TiO_2 nanostructures [99]. Basically, these pastes are based on terpineol which pose no known danger to the environment. On the other hand, tepineol-based pastes are often stable over a large time scale and give reproducible results [99]. Another advantage of using a paste for large-scale deposition methods is the easy upscaling of the film thickness, which is often demanded for the efficient functioning of DSSCs. Till date the most successful results are obtained from only the commercially available terpineol-based pastes of TiO_2 and ZnO. However, the non-toxicity of ZnO and its easy availability is beneficial for the development of a custom-made paste for ZnO nanostructured films for applications in dye-sensitized solar cells.

In the present section, thin films prepared using self-made ZnO pastes via blade-coating technique are investigated in terms of structural characteristics, crystallinity and performance as an active layer in solid-state and liquid electrolyte-based dye-sensitized solar cells. The basic preparation routine of the terpineol and ethanol-based paste using ZnO nanostructures is described in details in section 4.2.1. The parameters used for blade-coating of the pastes on silicon substrates is noted in section 4.2.2. The surface and volume morphology of the films are studied using SEM and GISAXS and are discussed in section 6.3.1. This is followed by an overview of crystallinity of the films measured using XRD (section 6.3.2). Two kinds of solar cells are constructed using the blade-coated films, namely the solid-state dye-sensitized solar cell in combination with a hole-conducting polymer, P3HT and the dye-sensitized solar cell in combination with a liquid electrolyte. The performances of these cells and the impact of morphology on the device performance is discussed in section 6.3.3.

6.3.1. Morphology

The ZnO nanoparticles synthesized via solution-casting as described in section 6.1.1 is the starting material for the production of the ZnO custom-made paste. In this case the sol-gel solutions are prepared using the high molecular weight P(S-*b*-EO) template. The concentration of the copolymer template is kept fixed at 15 mg mL^{-1} for all the films prepared. Six different sol-gels are studied in the present section which are solution-cast on pre-cleaned silicon substrates. After a waiting time of 48 hours for each sol-gel, the films are subjected to calcination at 600 °C for 30 minutes in air with a heating ramp of 5.78 °C min^{-1}. After the calcination step, ZnO nanoparticles are obtained on the substrate in the form of powder-like films. The nanoparticles are then scratched off from the substrates and processed further to obtain a paste. The different compositions of sol-gels used are listed in table 6.5. Thus, six batches of pastes are obtained which are blade-coated on silicon substrates. In addition to the paste preparation from six different sol-gel compositions, different calcination temperatures (400, 600, 800 and 1000 °C) are also chosen to obtain the ZnO nanoparticles from the solution-cast films. In order to study the influence of calcination temperature, the sol-gel composition in this case is kept fixed and hence, sol-gel composition VI (see table 6.5) with the highest w_{ZAD} is chosen. All the films are prepared by blade-coating the paste on the same substrate twice, without any intermediate calcination step. However, finally, all the films are heat treated at 400 °C for 30 minutes with a heating ramp of 5.78 °C min^{-1}. Since the films are obtained from the pastes containing already crystalline ZnO nanoparticles, the final combustion of the films is used just to ensure the complete removal of the organic constituents of the paste. For the sake of clarity in the text, this temperature treatment step to the final films (at 400 °C) is named as combustion step.

Morphology of blade-coated films obtained from different sol-gel compositions

Figure 6.23 shows SEM images of the blade-coated films obtained after combustion (at 400 °C) from different batches of ZnO pastes containing nanoparticles, synthesized via different sol-gel solutions (see table 6.5). All the different batches of ZnO nanoparticles mentioned in the present section are calcined at 600 °C.

Based on different sol-gel compositions, the ZnO nanoparticles obtained have different sizes. However, after the final paste is obtained from the nanoparticles, hardly any difference is observed in the physical quality of the paste such as viscosity. This is expected as all the pastes are prepared identically and the amount of ZnO nanoparticles used for individual paste preparation is kept fixed (4.2 wt. %). All the films show a granular morphology with spherical nanoparticles having diameters in the range of 20 to 100 nm

composition	w_{DMF}	$w_{\mathrm{H_2O}}$	w_{ZAD}
sol-gel I	0.92	0.05	0.03
sol-gel II	0.92	0.04	0.04
sol-gel III	0.92	0.03	0.05
sol-gel IV	0.92	0.02	0.06
sol-gel V	0.92	0.01	0.07
sol-gel VI	0.92	0.005	0.075

Table 6.5.: List of six different sol-gel compositions used for the synthesis of ZnO nanoparticles via the solution-casting technique. The different batches of ZnO nanoparticles are used for the fabrication of custom-made ZnO pastes based on terpineol and ethanol, which are in turn blade-coated in order to obtain thin films.

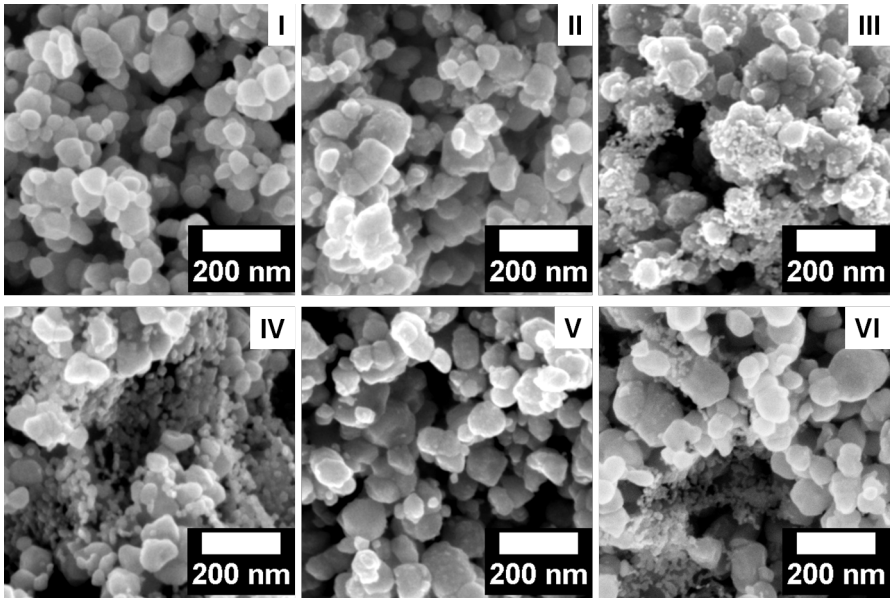

Figure 6.23.: SEM topography images of blade-coated films after combustion at at 400 °C. Labels of the images refer to the compositions of the sol-gel solutions used to prepare the nanocrystalline powders (table 6.5), which in turn are used to prepare the pastes for blade-coating.

(figure 6.23). Hence, all the films are highly polydisperse. In addition to larger granules, several smaller granules ranging in diameter between 10 to 20 nm are present. The smaller granules lie in close vicinity to the larger granules and are more prominently observed for films containing ZnO nanoparticles obtained from sol-gels III, IV and VI (figure 6.23).

Nonetheless, all the films show a homogeneous coverage and are devoid of large cracks, even after combustion.

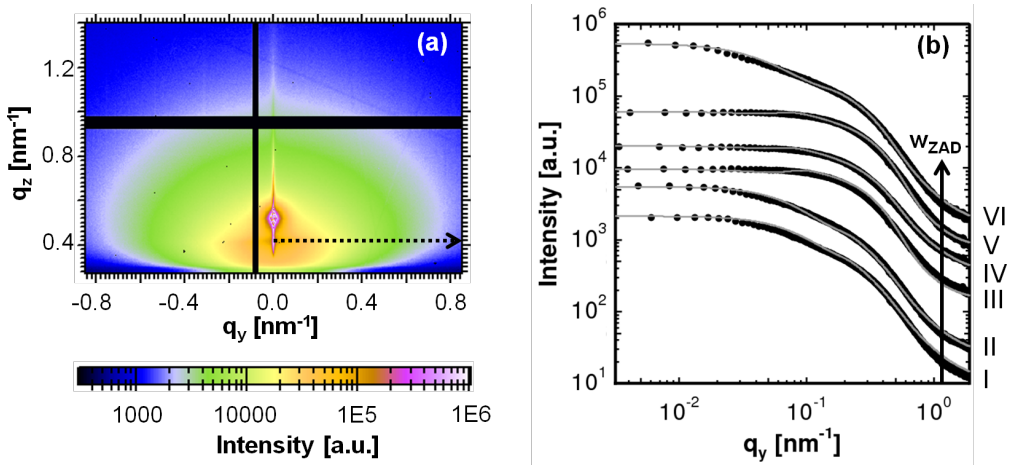

Figure 6.24.: (a) Exemplary 2d GISAXS data obtained from a calcined blade-coated film obtained from ZnO nanoparticles synthesized using sol-gel composition I (table 6.5). The dashed arrow indicates the position for the horizontal cut. The intensity bar is given in the bottom of the image. (b) Horizontal cuts (black circles) along with their fits (solid gray lines) plotted for all the blade-coated films, obtained from sol-gel I (bottom) to sol-gel VI (top), as indicated in the right axis of the graph. All the curves along with their fits are shifted along the intensity axis for clarity.

composition	structure factor [nm]	σ_S [nm]	form factor [nm]	σ_F [nm]
sol-gel I	20 ± 5	4.5	7 ± 1	2
sol-gel II	20 ± 2	4.5	7 ± 1	2
sol-gel III	38 ± 2	11.5	22 ± 1	2
sol-gel IV	45 ± 1	14.5	7.5 ± 1	1.8
sol-gel V	45 ± 1	14.5	7.2 ± 1	1.6
sol-gel VI	20 ± 1	6.5	7.4 ± 1	2.2

Table 6.6.: Summary of different length scales obtained in the volume of the blade-coated films after combustion. The pastes used for blade-coating are synthesized from ZnO nanoparticles obtained via varied sol-gel compositions (table 6.5). The form factor diameter and the structure factor with their respective Gaussian distributions (σ_F & σ_S respectively) are obtained from the fits of the horizontal line cuts of the GISAXS data as shown in figure 6.24.

For structural information from the film volume, GISAXS experiments are performed on all the combusted blade-coated films as described in section 3.1.5. The experiments

reported in this section are carried out at I07 beamline of the Diamond Light Source, Oxfordshire. To account for the high polydispersity of the films, the incident angle is chosen very close to the critical angle of ZnO, $\alpha_i = 0.23°$. Exemplary 2d GISAXS data obtained from the film containing ZnO nanoparticles synthesized from sol-gel I (see table 6.5) is shown in figure 6.24(a). Unlike the 2d GISAXS data obtained for the highly polydisperse solution-cast film (shown in figure 6.13), a prominent specular peak and a Yoneda peak are observed in the present case. The broad scattering along q_y and q_z is created by the broad distribution of length scales present in the film volume. The horizontal cut to the data is obtained at the Yoneda position for all the films and are shown in figure 6.24(b) with their respective fits using the model described in chapter 2.4.2. Although the plateau-like features for all the cuts suggest a broad distribution of structure sizes in the film volume, the most prominent length scales obtained from the fits are summarized in table 6.6.

It is clearly seen that the structural dimensions for all the films are in a similar range as observed via SEM measurements. The form factors obtained from the fits, representing the average inter-particle distances show a close packing of the ZnO granules in the blade-coated films. This is mostly due to the contribution from the smaller granules which exist on the surface of the larger ones. On the other hand, the structure factors obtained from the fits correspond to the average size of the granules. The length scales obtained from the films are within a suitable exciton diffusion length reported for conducting polymers [189, 190]. This directs towards the application of these films as an electron-acceptor in an ss-DSSC.

Morphology of blade-coated films prepared from pastes of ZnO nanoparticles obtained at different calcination temperatures

The sol-gel with composition VI (see table 6.5) is chosen for the present study. After solution-casting of this sol-gel, different calcination temperatures are chosen in order to obtain ZnO nanoparticles with different sizes. These nanoparticles are then transformed into a paste which is then used for blade-coating on pre-cleaned silicon substrates. Finally, all the films are combusted at a high temperature of 400 °C in air to remove the organic solvents.

Figure 6.25 shows the SEM surface images of blade-coated films prepared from corresponding ZnO custom-made pastes constituting ZnO nanoparticles, which are obtained at four different calcination temperatures. The morphology of the final blade-coated films are affected depending on the size of the ZnO nanoparticles present in the paste. As observed from figure 6.25, all the films show a foam-like appearance under low magnification. Figure 6.25(a) corresponding to the paste containing nanoparticles obtained after calci-

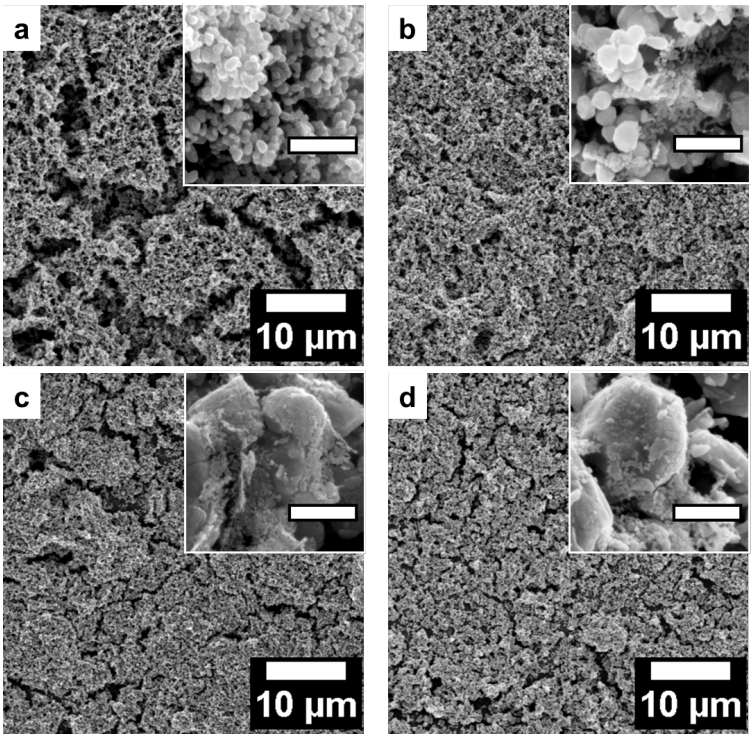

Figure 6.25.: SEM surface images (1 k× magnified) of blade-coated films after combustion at 400 °C, obtained from self-made pastes. Different pastes contain ZnO nanoparticles obtained from the calcination of solution-cast films at (a) 400 °C, (b) 600 °C, (c) 800 °C & (d) 1000 °C. The sol-gel composition VI (as listed in table 6.5) is used for solution-casting. The SEM images in the inset represent the same corresponding films obtained under 60 k× magnification. The scale bar for all the images in the insets corresponds to 200 nm.

nation at 400 °C shows an uneven surface with the presence of large depths all over the films. However, these gaps do not extend to the bottom of the film giving rise to cracks. This is evident from the foam-like structures present also within the gaps (figure 6.25(a)). The film visible through the large gaps is associated to the first blade-coated film applied, while the film showing the gaps is the second blade coat applied on the first film. Under a higher magnification, ZnO granular nanoparticles are observed with an average diameter ranging from 20 to 50 nm. In addition, clusters of these particles are also visible giving rise to cluster sizes in the range of 50 to 70 nm (figure 6.25(a)-inset). The films obtained from the ZnO nanoparticles calcined at 600 °C show no cracks or large depth on the film surface (figure 6.25(b)) under low magnification. However, unlike the previous film, ZnO granules with two prominent length scales are observed under high magnifications (figure 6.25(b)-inset). The larger granules range up to 100 nm and the smaller ones up to 10 nm in diameter. For the film obtained from ZnO nanoparticles calcined at 800 °C, similar morphologies are obtained. However, under low magnification, some cracks are visible in

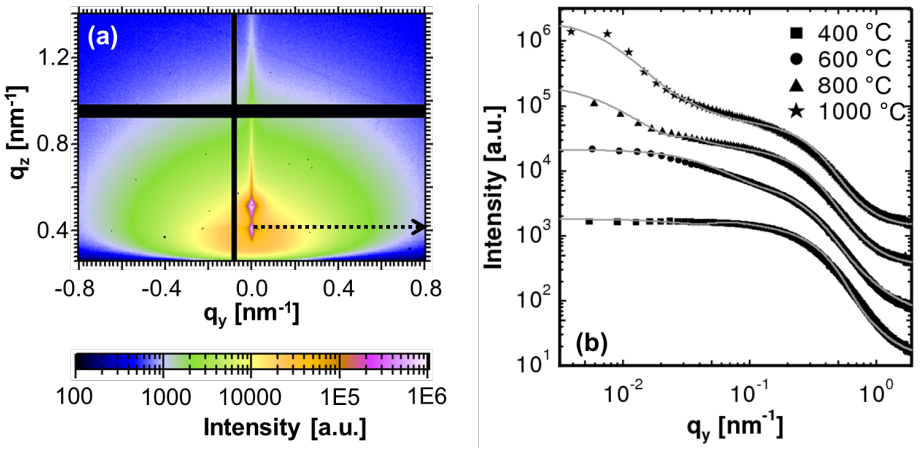

Figure 6.26.: (a) Exemplary 2d GISAXS data obtained from a combusted blade-coated film obtained from ZnO nanoparticles synthesized using sol-gel composition VI (table 6.5) and calcined at 600 °C. The dashed arrow indicates the position for the horizontal cut. (b) Horizontal cuts (black symbols) along with their fits (solid gray lines) plotted for all the blade-coated films, obtained from self-made pastes containing ZnO nanoparticles calcined at 400, 600, 800 and 1000 °C. All the curves along with their fits are shifted along the intensity axis for illustrative purpose.

the film through which the dark silicon substrate is visible (figure 6.25(c)). These cracks are in the order of 1 to 2 µm in width. The ZnO nanoparticles observed in the inset of figure 6.25(c) denotes a very large diameter of up to 500 nm. This indicates that the initial dimensions of the ZnO nanoparticles obtained after the calcination of the solution-cast film is retained in the self-made paste. During the paste preparation routine (as described in section 4.2.1), grinding of the ZnO nanoparticles might lead to formation of smaller granules as compared to the starting material. But their agglomeration to form large particles is less likely. Similar morphology is obtained for the films obtained from ZnO nanoparticles calcined at 1000 °C (figure 6.25(d)). The cracks in the film remains in this case as well. The granules observed in the inset of figure 6.25(d), are however larger than the previous film. The diameter of these granules vary in the range of 500 to 700 nm.

As mentioned earlier, the custom-made ZnO pastes used to prepare the films shown in figure 6.25 consist of ZnO nanoparticles synthesized from a single sol-gel composition (sol-gel VI in table 6.5). Hence, an identical size of the nanoparticles is expected in the final blade-coated films which are all combusted at the same temperature of 400 °C. On the contrary, it is observed that the final length scales evolved in the blade-coated films is dependent on the calcination temperature at which the ZnO nanoparticles are obtained for the paste formation. The different calcination temperatures of the solution-cast films provide additional energy to the system to undergo structural reorganization.

It is observed that upon increasing the temperature, the mobility of the nanoparticles increases and so does the probability of fusion of these nanoparticles. Temperatures higher than 600 °C produce considerable large clusters of nanoparticles as seen in figures 6.25(c) and (d), where the trend in the nanoparticle size is replicated for the combusted blade-coated films.

Furthermore, the presence of prominent cracks on the films is observed, mainly for the blade-coated films obtained from the ZnO nanoparticles calcined at temperatures of 400, 800 and 1000 °C. This phenomenon is explained as follows: The first film from the paste deposited on pre-cleaned silicon substrate increases the resistance for the second film to be deposited by blade-coating. For the application of the second film, the interaction between the ZnO nanoparticles in the paste and those already present in the first film is very high, which makes it difficult to drag the paste over the first film without deforming it to some extent. It should also be kept in mind that the two subsequent coating steps are done without any intermediate calcination step. The resulting second film thereby, inherits surface inhomogeneities and incomplete coverage over the first film. Depending on the size and hence, the surface area of the nanoparticles in the paste, the strength of interaction between the two subsequent ZnO films vary. For the films obtained with ZnO nanoparticles calcined at 400 °C (figure 6.25(a)) the cracks have the maximum width. For the film obtained with ZnO nanoparticles calcined at 600 °C, no prominent crack is visible on the film surface (figure 6.25(b)). This implies the optimized size of ZnO nanoparticles showing the most effective interaction. For the larger particles, the cracks on the surface appear again (figures 6.25(c) and (d)) due to the restricted mobility of the nanoparticles as a function of their size and surface area. It is noteworthy that the cracks present in the blade-coated films get more pronounced after the final combustion step due to the shrinkage of the film upon removal of all the organic solvents. The cracks are easily propagated in the areas of the films which are covered with less material.

Similar to the previous blade-coated films, all the films of the temperature series are also investigated by GISAXS for in-depth structural information as described in section 3.1.5. Figure 6.26(a) shows an exemplary 2d GISAXS data for the film shown in figure 6.25(b). A broad scattering signal already indicates the large distribution of structure sizes in the film volume. The horizontal cuts performed at the Yoneda position along with the fits (see section 2.4.2 for the description of the model) for all the films shown in figure 6.25 are plotted in figure 6.26(b). The quantitative information obtained from the fits for the data of different films is listed in table 6.7.

According to the quantitative information obtained from the fits, the structure factors representing the average size of the ZnO nanoparticles in the blade-coated film shows an increasing trend, when the ZnO nanoparticles used as an ingredient for the paste

temperature	structure factor [nm]	σ_S [nm]	form factor [nm]	σ_F [nm]
400 °C	50 ± 5	16.5	7.4 ± 1	1.6
600 °C	20 ± 2	6.5	7.4 ± 1	2.2
800 °C	140 ± 2	29.5	6 ± 1	2.7
1000 °C	120 ± 1	32.5	6.4 ± 1	2.4

Table 6.7.: Summary of different length scales obtained in the volume of the blade-coated films after combustion. The self-made pastes used for blade-coating are synthesized from ZnO nanoparticles obtained via calcination at different temperatures, as noted in the first column. The sol-gel composition to obtain the ZnO nanoparticles is kept fixed to composition VI of table 6.5. The form factor diameter and the structure factor with their respective Gaussian distributions (σ_F & σ_S respectively) are obtained from the fits of the horizontal line cuts of the GISAXS data as shown in figure 6.26.

preparation is obtained after a calcination at temperatures higher that 600 °C. This trend is in good agreement with the observations made from SEM. However, the values obtained in the present case are not as high as that observed via SEM mainly due to two reasons: the structure sizes larger than 200 nm are not resolved by the GISAXS measurements due to the resolution limit of the beamline set up and the presence of smaller particles in the range of 10 to 20 nm reduces the average size of the ZnO granules. The form factors on the other hand, corresponding to the average distance between the ZnO granules in the blade-coated films show an average of 6.8 nm. This indicates a very close packing and good inter-connectivity of the ZnO granules for all the films. The larger cracks seen for the samples obtained from ZnO nanoparticles calcined at 800 and 1000 °C are beyond the resolution limit of the beamline set up and hence are not observed.

6.3.2. Crystallinity

The blade-coated films obtained from the temperature series are investigated for their crystallinity using XRD instrument II (see section 3.1.4). The XRD patterns are plotted in figure 6.27 from bottom to top with increasing temperatures at which the ZnO nanoparticles are obtained for the fabrication of the paste.

As mentioned before, the final combustion temperature for all the films is 400 °C. Hence, the difference in the degree of crystallinity imparted to the films is a function of the calcination temperature at which the ZnO nanoparticles are obtained for the paste preparation. It is observed from figure 6.27 that all the films crystallize in the wurtzite phase of ZnO. The peak positions as well as their relative intensities are in good agreement with the

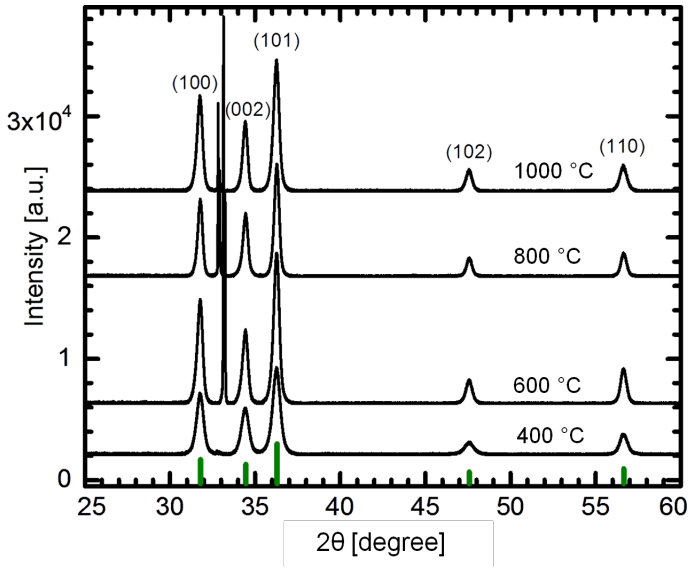

Figure 6.27.: XRD patterns of the blade-coated films prepared from pastes containing ZnO nanoparticles obtained at different calcination temperatures as indicated in the plot, increasing from bottom to top. The vertical solid green lines show the theoretical peak positions for crystalline wurtzite phase of ZnO with their relative intensities.

theoretical values. Furthermore, the crystallite size for the films increases with increasing calcination temperature of the nanoparticles. For the film composed of nanoparticles calcined at 400 °C, the lowest crystallite size of (16.2 ± 1) nm is obtained. Upon increasing the calcination temperature up to 600 °C, larger crystallites are produced with (21.3 ± 1) nm size. For even higher calcination temperatures, the average crystallite size increases to 22.5 nm, which is in accordance to the conclusions drawn from the SEM and GISAXS investigations.

6.3.3. Solar cell performance

Two batches of solar cells are discussed in the present section prepared from the blade-coated nanostructured ZnO films studied in detail in the previous section. The blade-coated films obtained from the paste consisting of ZnO nanoparticles synthesized using different sol-gel compositions (section 6.3.1), are used for the fabrication of dye-sensitized solar cells in combination with a solid-state hole conductor. For this purpose, an organic hole conductor, P3HT is used. A 40 mg mL^{-1} concentration of the P3HT solution in toluene is used for all the cells. The backfilling as well as the steps involved in the assembling of the solar cells is illustrated in section 4.2.3. On the other hand, the blade-coated films prepared from the ZnO nanoparticles obtained from different calcination

temperatures (section 6.3.1), are used for the synthesis of dye-sensitized solar cells in combination with a liquid electrolyte (electrolyte system I as introduced in section 4.1). For both solar cell types, D149 is used as the dye. The preparation routine for the cells along with the details about the materials used is elaborated in section 4.2.3. For all the solar cells, a ZnO blocking layer is used, which is prepared as also discussed in section 4.2.3.

Solid-state dye-sensitized solar cells (ss-DSSCs)

In order to test the functionality of all the morphologies produced by blade-coating of a custom-made paste, the films shown in figure 6.23 are used as the active layers of solid-state dye-sensitized solar cells. The resulting I/V-curves obtained for each cell for measurements in dark and under illumination of AM1.5 solar spectrum conditions (intensity: 1000 W m^{-2}) are shown in figure 6.28. All the measurements shown correspond to the best pixel in the cell.

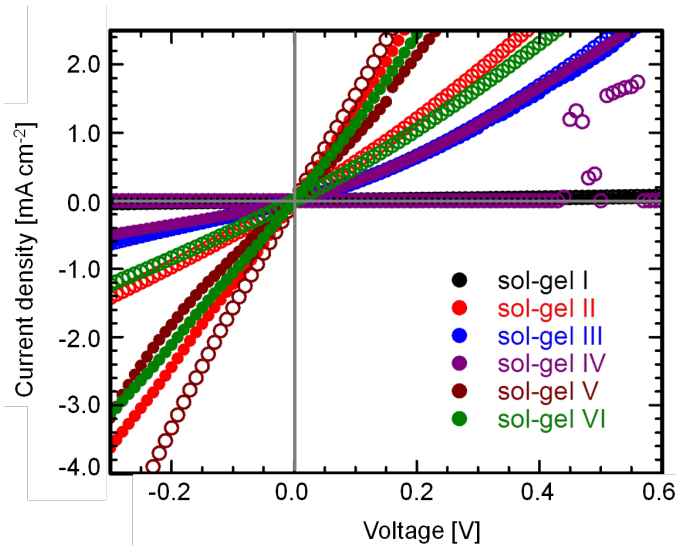

Figure 6.28.: I/V-curves of the ss-DSSCs obtained from the blade-coated films containing ZnO nanoparticles synthesized from different sol-gel compositions (table 6.5). The open and the closed circles correspond to the measurements performed in dark and under AM1.5 simulated solar spectrum conditions.

As seen from the I/V-curves, the prepared samples do not show a solar cell behavior. Hence, no power conversion efficiency has been extracted from these devices. Several attempts have been made in order to produce ss-DSSCs, even without using the dye, but the tests have remained unsuccessful. In order to understand the reason behind failure of the devices to perform as a solar cell, cross-section SEM images of all the ss-DSSCs are

studied and are shown in figure 6.29. To ensure a clear edge of the device without any material being peeled from the surface, the samples are broken over a scratch with the aid of liquid nitrogen.

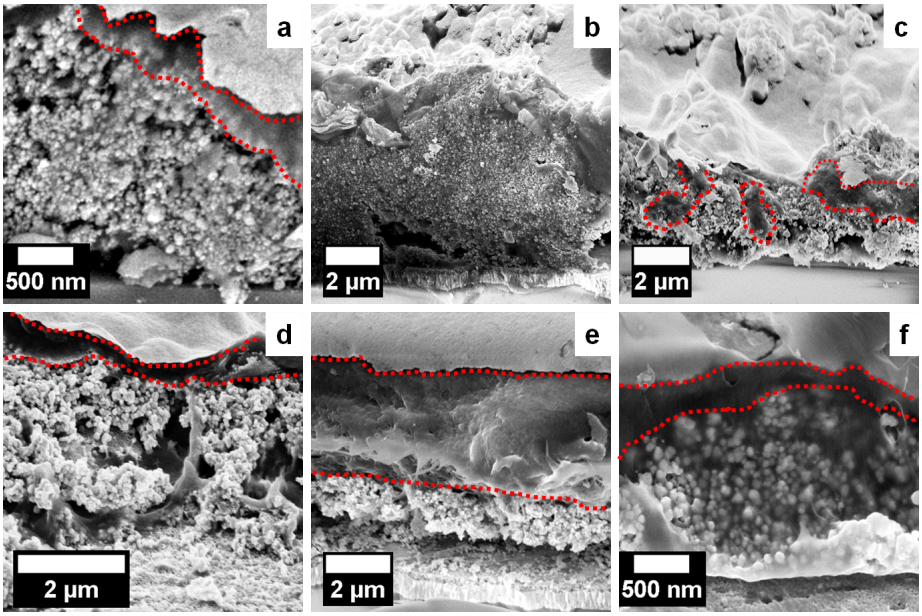

Figure 6.29.: (a)-(f) Cross-section SEM images of the ss-DSSCs prepared from the corresponding blade-coated films shown in figure 6.23. The red dotted lines indicate the P3HT overlayer on the ZnO active layers.

The bright spherical granules visible in all the images are the ZnO nanoparticles, whereas, the darker regions represent the less conducting polymer. The top surface of all the images appear bright due to the presence of the top gold electrode. The blocking layer underneath the ZnO active layer is present in all the samples, but are clearly visible specially in images 6.29(d) and (e). As observed from the different scale bars of the images, the thickness of the ZnO film varies from sample to sample and lies in the range of 1 to 7 µm. This wide thickness range occurs as a consequence of the different particle sizes in the film as discussed before. In addition, the thickness of the P3HT overlayer for each cell also varies in the range of 200 nm to 4 µm. These phenomena are explained as follows: the size of the ZnO nanoparticles present in the film influences the amount of dye-uptake by the film and hence affects the device efficiency. Additionally, the amount of dye adsorbed on the surface of the ZnO nanoparticles modifies their surface properties which has an impact on the penetration of the hole-conducting polymer into the system. Although the average size of the ZnO nanoparticles for the above-mentioned films is concluded to be in the range of 20 to 45 nm from the SEM and GISAXS measurements, the presence of smaller particles in combination with the bigger particles cannot be neglected specially

for the films prepared from ZnO nanoparticles obtained from sol-gel compositions III, IV and VI (figures 6.23(c), (d) and (f)).

For the first two films (figures 6.23(a) and (b)), the smaller ZnO nanoparticles are not observed which gives a hint towards low dye uptake by these films. As the amount of smaller nanoparticles increase from the third film on, (figures 6.23(c), (d) and (f)), the dye uptake is expected to rise. Also observed from the figure 6.29, the increased infiltration of P3HT is clearly noticed for films synthesized from nanoparticles obtained from sol-gel III, IV and VI (figures 6.29(c), (d) and (f)). This points towards the fact that enhanced dye uptake refers to an enhanced coverage of the ZnO nanoparticles by a dye monolayer, thereby favoring the penetration of P3HT into the films. An efficient backfilling as well as the presence of a P3HT overlayer are the two most essential facts for the proper functioning of an ss-DSSC [61, 191]. As marked by the red dotted lines in figure 6.29, the P3HT overlayer is not well-defined for the samples obtained from sol-gel II and III (figures 6.29(b) and (c)). Films prepared using ZnO nanoparticles obtained from sol-gel I, IV, and V show a defined P3HT overlayer on the other hand, but the backfilling is poor (figures 6.29(a), (d) and (e)). An extra thick P3HT overlayer for the ZnO film obtained from ZnO nanoparticles synthesized from sol-gel V (figure 6.29(e)), is attributed to the fact that the ZnO film in this case has the largest particles amongst all the films (see table 6.6). This indicates the lowest surface area of the film which reduces the dye uptake and hence negatively influences the backfilling. However, the device fabricated from ZnO nanoparticles obtained from sol-gel VI (figure 6.29(f)), shows the best backfilling. The ZnO spherical granules are visible with unsharp edges beyond the P3HT layer in the cross-section. The hole conductor seems to penetrate the entire film. In addition, a well-defined P3HT overlayer in the range of 200 to 300 nm is distinctly visible. Hence, the film obtained from ZnO nanoparticles produced by sol-gel VI shows the best backfilling and from previous observations, can be concluded to have the best dye uptake.

Besides the dye uptake and P3HT infiltration, other important factors also govern the functioning of the device. These include the roughness of the film leading to the formation of a top contact highly populated with cracks and perforations. The high roughness of all the films is mainly caused by the uneven drying of the films which involves evaporation of a high boiling point solvent, terpineol. A tendency of the film to dry from the edges to the center is observed, which drives the nanoparticles in an uneven manner throughout the film causing the high roughness. The P3HT spin-coated on top of these films then in turn replicates the surface roughness. Evaporation of the gold electrode in the end, on top of the highly rough active layers leads to formation of huge cracks on the electrode surface as clearly visible from the images of the real devices, shown in figures 6.29(b), (c) and (f). These cracks highly oppose lateral charge transport in the device. In total, all

the above-mentioned factors contribute to the failure of the devices as observed in the present case.

Dye-sensitized solar cells based on liquid electrolytes (DSSCs)

In spite of the negative behavior of the ss-DSSCs discussed in the previous section, it is concluded that the blade-coated film obtained from ZnO nanoparticles synthesized by the sol-gel composition VI (table 6.5) shows the highest dye uptake and a film thickness in the range of 1.7 to 2 µm. In order to test the performance of this particular film in a set up using liquid electrolyte, dye-sensitized solar cells (DSSCs) are prepared from the blade-coated films obtained from ZnO nanoparticles produced by sol-gel VI, but calcined at different temperatures (as discussed in section 6.3.1). All the cells are prepared in the same manner as described in the previous section and in details in chapter 4.2.3. As compared to the ss-DSSCs, the DSSCs investigated in the present section are filled with a liquid electrolyte instead of a polymeric hole conductor. The resulting I/V-curves obtained from the four different DSSCs are plotted in figure 6.30.

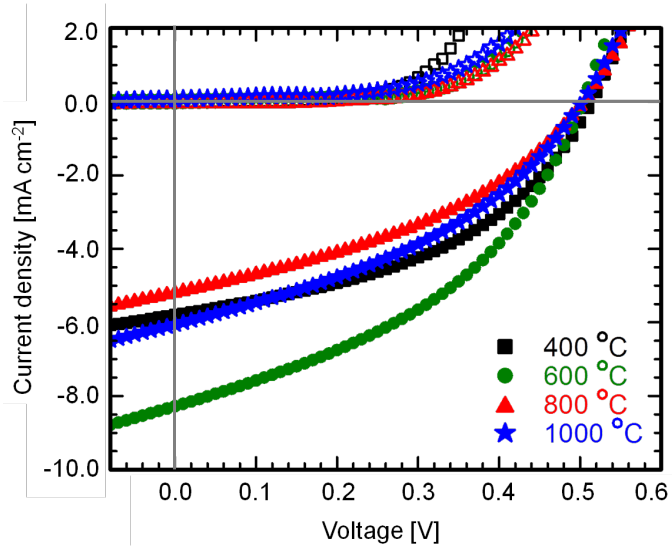

Figure 6.30.: I/V-curves of the liquid electrolyte-based DSSCs obtained from the blade-coated films containing ZnO nanoparticles synthesized from sol-gel composition VI (table 6.5), but calcined at different temperatures as indicated by the legends. The open and the closed symbols correspond to the measurements performed in dark and under AM1.5 simulated solar spectrum (1000 W m^{-2}) conditions.

The I/V-curves prove an efficient functioning of all the devices unlike the ss-DSSCs. The details about the device characteristics of each cell is summarized in table 6.8. It is observed that the open-circuit voltage (V_{OC}) of all the devices stay nearly equal, which is

expected due to the similar materials used for the fabrication of the cells. On the other hand, the short-circuit current (I_{SC}) and the fill factor (FF) of all the cells vary. In general, the I_{SC} of all the cells stays low indicating a very low density of charge carriers which is justified by the low film thickness of the films.

temperature	I_{SC} [mA/cm^2]	V_{OC} [V]	FF [%]	η [%]
400 °C	-5.79	0.49	45.37	1.31
600 °C	-8.28	0.49	42.58	1.72
800 °C	-5.56	0.54	43.45	1.32
1000 °C	-6.06	0.49	39.47	1.17

Table 6.8.: I/V characteristics of the liquid electrolyte-based DSSCs obtained from self-made ZnO pastes containing ZnO nanoparticles calcined at different temperatures as noted under the first column. The parameters are obtained from analyzing the I/V-curves shown in figure 6.30.

It is clearly seen that the short-circuit current density is highest for the cell obtained from ZnO nanoparticles calcined at 600 °C and hence, this cell shows the best performance. This is in very good agreement with the conclusion drawn from the study of ss-DSSCs from blade-coated films. In addition, the morphology of the film obtained from ZnO nanoparticles calcined at 600 °C is the most promising according to the SEM measurements (figure 6.25(b)). It has been observed from both SEM and GISAXS that the size of the ZnO nanoparticles increases when the constituent ZnO nanoparticles are calcined at a temperature higher than 600 °C (in the present case, 800 and 1000 °C; section 6.3.1). This indicates towards an expected reduction in the dye-adsorption by these films. As supported by the I/V-curves (figure 6.30), the power conversion efficiency (η) of the devices obtained from ZnO nanoparticles calcined at 800 and 1000 °C indeed show a decreasing trend as compared to the film obtained from ZnO nanoparticles calcined at 600 °C. Additionally, for the film obtained from ZnO nanoparticles calcined at 400 °C, a better solar cell performance is expected as compared to the cells containing ZnO nanoparticles calcined at 800 and 1000 °C, due to the smaller ZnO particle size obtained for the former (table 6.7). However, this is not the case as the solar cells prepared from the paste containing ZnO nanoparticles calcined at 800 °C shows slightly better performance. This is associated to the large depths in the film obtained with ZnO nanoparticles calcined at 400 °C, as observed in figure 6.25(a), which lowers the surface area for dye adsorption.

6.3.4. Results & discussion

A suitable technique to prepare ZnO custom-made pastes, without the involvement of any complex instrument is introduced. The paste synthesized in the process is highly stable and can be used for screen-printing in addition to blade-coating, as tested in the present study. The only drawback of this manufacturing route lies in the lengthy preparation procedure which takes four days in total. However, this time includes the synthesis of self-tailored ZnO nanoparticles. Transferring the same preparation routine to commercially available ZnO nanoparticles would significantly contribute to shorten the whole procedure to obtain nanostructured films in a day. Moreover, this simple routine can be extended to other inorganic metal oxides such as titania. Several complicated paste processing routines have already been reported with titania [99]. But a simple recipe to obtain a paste, specially with custom-made ZnO nanoparticles is studied for the first time in the present thesis.

Solution-casting is chosen as the initial method to obtain ZnO nanoparticles via sol-gel synthesis. The use of the high molecular weight P(S-*b*-EO) as the structure-directing agent controls the reaction of the precursor molecules within a restricted volume thereby producing nanoparticles of the desired size. Since solution-casting is a slow process, sufficient time results in agglomeration of the ZnO nanostructures synthesized in the sol-gel. Being the energetically favorable geometry, spherical nanoparticles of ZnO are obtained after calcination.

As discussed in section 6.3.1, different sol-gels are used to obtain ZnO nanoparticles of various sizes which are then composed to a paste for blade-coating in order to obtain nanostructured films. As observed from the morphology study, the spherical granular morphology stays intact in the blade-coated films even after calcination. Hence, the paste preparation routine preserves the nanostructures synthesized by the sol-gel route. It is observed that the average size of the ZnO nanoparticles obtained in the blade-coated films after combustion stay within a narrow range. However, additional smaller nanoparticles become visible for films obtained from pastes having ZnO nanoparticles synthesized via sol-gels containing a higher w_{ZAD} (sol-gel III, IV, V and VI). This indicates that the higher amount of precursor (ZAD) in the sol-gel hinders the mobility of the molecules thereby forming smaller particles. Whereas for the sol-gels containing lower w_{ZAD}, comparatively larger particles are obtained (sol-gel I and II). This is supported by the high mobility of the precursor molecules which increases the probability of clustering to form bigger structures. However, all the blade-coated films obtained contain structural length scales suitable for charge transport and separation in a solid-state or liquid electrolyte-based DSSC [146].

In addition, the impact of temperature on the average size of the ZnO nanoparticles is

also studied, which confirms the formation of larger granules with increasing calcination temperature. This determines that additional energy is provided to the system during calcination which leads to structural reorganization in the films resulting in the formation of bigger particles. Pastes prepared from the large ZnO nanoparticles also provide large structure sizes in the final blade-coated film after combustion. All the observations mentioned so far, are confirmed via SEM and GISAXS measurements. The crystallinity of the films is proved using XRD measurements. An increasing trend in the crystallite sizes is observed for the films obtained from ZnO nanoparticles with higher calcination temperatures, thereby supporting the observations made from SEM.

Regarding the performance of these films as an active layer material in solar cells, two different studies are performed. In case of the devices based on a solid-state hole conductor, no success has been achieved due to the high film thickness of the films. The high roughness of the films contributes to the failure of the devices as well. However, from the study concerning the performance of ss-DSSCs prepared using the blade-coated films prepared from pastes with ZnO nanoparticles synthesized from different sol-gel compositions, an important insight is obtained for determining the suitable morphology for the best dye-uptake. The presence of combination of smaller and larger ZnO nanoparticles in the blade-coated film obtained from the paste containing ZnO structures synthesized from the sol-gel with the highest w_{ZAD}, makes it the morphology with the highest surface area with the highest dye uptake capacity.

Films blade-coated from pastes containing ZnO nanoparticles synthesized at different calcination temperatures are studied for the performance in liquid electrolyte-based DSSCs because of suitable film thickness. All the nanoparticles in this series are synthesized from sol-gel composition containing the highest w_{ZAD}. The thickness of the investigated films stays below the optimum thickness required for sufficient light absorption [127]. This is due to the drawback of the blade-coating technique, which limits the number of coats that can be applied on the same substrate as the underlying layer often gets scratched off from iterative coatings and does not significantly multiply the film thickness. Due to the low thickness of the active layer, the short-circuit current stays at a low value. Nonetheless, the performance obtained from these devices are very reasonable and are comparable to the already achieved power conversion efficiencies using ZnO paste obtained from commercial nanoparticles [192–195]. From the study it is established that the blade-coated film obtained from the paste containing ZnO nanoparticles synthesized using a sol-gel having $w_{ZAD} = 0.075$ and calcined at 600 °C, gives the best power conversion efficiency of 1.72 % in a DSSC based on liquid electrolyte.

6.4. Summary

For the first time, sol-gel chemistry in combination with a diblock copolymer template is established as a suitable route to synthesize ZnO nanostructures. Several complex morphologies are obtained via this route, namely worm-like aggregates, circular vesicles, spherical granules and foam-like nanostructures. The possibility to fine-tune the structural length scales is shown using this approach. Surface and volume morhologies of the nanostructured films are studied via SEM and GISAXS, respectively. P(S-*b*-EO) is used as the template with two different molecular weights for foam-like nanostructures synthesized in the present study. Different molecular weights of the same template allows for further manipulating the structural length scales of the films while keeping the morphology intact, in order to suit it for a specific device application. It is found that the nanostructures obtained with the low molecular weight template show higher porosity than the ones synthesized using the high molecular weight template. In general, the lateral length scales obtained in the film volume is found to be highly promising for using them as active layers in dye-sensitized solar cells. All the morphologies show a good crystallinity and optical properties after being calcined at 400 °C. The XRD and UV/Vis measurements show the presence of wurtzite phase of ZnO in the nanostructured films. The FTIR measurements confirm the absence of impurities in the ZnO films.

In addition, different deposition techniques such as spin-coating, solution-casting and blade-coating are applied for obtaining ZnO nanostructures in form of thin films. Different coating techniques provide different thicknesses to the films obtained. Spin-coating produce films ranging in thickness between 50 and 80 nm. The thickness of the nanostructured films is enhanced to 400 nm via solution casting. Lastly, blade-coating provide the highest film thickness in the range of 1 to 7 µm. Moreover, it is observed that ZnO nanoparticles are obtained in the form of a white powder after calcination of the solution-cast films. This powder is then used to synthesize a ZnO paste, which is free from any toxic organic solvent and is based on terpineol. The blade-coated films obtained from such ZnO pastes show poor performance as active layers in solid-state dye-sensitized solar cells. Major reasons for the failure being high surface roughness, unoptimized film thickness and poor backfilling of the hole-conducting polymer. However, the blade-coated films show promising behavior as active layers in dye-sensitized solar cells based on liquid electrolytes.

In summary, efficient routes are developed for obtaining nanostructured ZnO thin films from solutions as well as pastes. Both the solution-based approach and the paste processing are studied for the first time with respect to ZnO nanostructures. A complete investigation of the films in terms of morphology, crystallinity, optical and electronic

properties offers a solid backbone towards efficient device engineering using the suitable morphology with the required structural and opto-electronic properties. These methods also broadens the scope of research for the development of other inorganic metal oxides or combination of metal oxides.

7. ZnO nanostructures using P(S-*b*-4VP) templates

Block copolymers on the basis of their volume fraction, molecular weight and interaction parameter of the different blocks are known to yield variety of morphologies in the nanometer correlation length scale arising from micro-phase separation [196–199]. Geometries such as lamellae, gyroids, spheres, cylinders, etc. can be achieved in bulk [172, 200]. Transferring these morphologies to thin films increases the complexity of the process as the interaction of the different blocks of the copolymer with the substrate also plays a role in deciding the final morphology [201]. As such, it is possible to produce several morphologies in their non-equilibrium states. The scope to freeze-in metastable nanostructures, provides further opportunities to synthesize a broad collection of morphologies that can then be used as patterns or templates for chemical, biological, magnetic, optical and electronic applications [202]. In the present study, amphiphilic diblock copolymers are essentially used as templates to provide ordered nanostructured morphologies using a sol-gel precursor for ZnO. Several ZnO nanostructured morphologies in thin films, synthesized with P(S-*b*-EO)-assisted sol-gel approach are presented in chapter 6. In order to expand the assortment of complex assemblies of ZnO nanostructures, a different diblock copolymer is used in the present chapter.

Poly(styrene-*block*-4-vinylpyridine), abbreviated as P(S-*b*-4VP) is used as the template with two different molecular weights as listed in table 4.1. P(S-*b*-4VP) has been reported to produce spatially ordered morphologies when used as a template for inorganic small molecules such as titania and metal nanoparticles, which are anchored to the P4VP block via hydrogen bonds or electrostatic and van-der-Waals interaction [203]. Successful templating of inorganic moieties using P(S-*b*-4VP) template also depends on the domain structure which in turn is influenced by the surface energies of the different blocks when they face geometrical constraints, being confined to a thin film [202]. In the present chapter, zinc acetate dihydrate (ZAD) is used as the source for ZnO and is incorporated in the P(S-*b*-4VP) matrix to study different nanomorphologies.

Furthermore, additional orientation of the microdomains obtained as a result of microphase separation of the diblock copolymer, can be provided with the aid of external stimuli

such as interfacial tension between the blocks, application of an electric field, introduction of a patterned substrate or by subjecting the system to a gradient of temperature and shear [204–207]. Russell and coworkers have reported structural rearrangements in P(S-*b*-4VP) under the influence of a suitable solvent vapor stimulus [208, 209]. This process is mainly termed as solvent vapor annealing or simply solvent annealing and has been successfully applied to bulk samples in addition to thin films. More recently, the self-assembling properties of the block copolymers has been exploited by anchoring a suitable salt to one of the blocks of the copolymer via non-covalent interactions, thereby forming supramolecular assemblies (SMAs) [196]. Such systems in bulk and thin films have shown highly ordered structures, which can be transferred to various nanotechnological applications [202]. Several different systems of P(S-*b*-4VP) in thin films, associated with small molecules such as 3-pentadecylphenol (PDP) or hydrogen tetrachloroaurate(III) trihydrate ($HAuCl_4.3H_2O$) have shown improvement of structural order under the influence of a suitable solvent vapor such as tetrahydrofuran (THF) [210–212]. On the other hand, performance of other systems such as P(S-*b*-4VP) with 2-(4'-hydroxybenzeneazo)benzoic acid (HABA) is studied under the influence of chloroform vapor [213, 214]. For these studies, the phase behavior and terrace formation of the resulting structures are investigated for different molecular weights of the copolymer, different vapor pressures of the solvents used for annealing and different concentration of the salt integrated into the copolymers. The solvent vapor annealing is implemented in the present study to the ZnO nanostructures templated using P(S-*b*-4VP). For the purpose, it should be noted that the presence of P(S-*b*-4VP) in the films is essential, which is sensitive to the solvent vapor. The reorganizations in the polymeric template are then transferred to the ZnO nanostructures embedded in the copolymer matrix. In the present study, solvent annealing of ZnO-polymer films is used to tune the length scales of the ZnO nanostructured morphology. This is an important routine for tuning the length scale of a desired morphology to match the requirements for a specific application, as it is not always feasible to have templates with different block lengths to achieve desired length scales in the film. Once the nanostructures with suitable length scales are obtained, the template can be be removed depending on the final application via solvent extraction, UV or temperature treatment.

The major advantage of using block copolymer templates for inorganic nanostructures lies in large-scale opto-electronic applications due to solution processibility of the system. Also, the approach can be cost-effective when roll-to-roll printing of devices is realized [215]. In the present chapter the synthesized nanostructures are optimized towards applications in dye-sensitized solar cells (DSSCs). Along with tuning length scales in the nanomorphology, the scalability of film thickness is also taken into account, which

plays a significant role in the device performance. For the active layers tested in DSSCs, spray deposition method is employed to achieve suitable film thickness.

Section 7.1 is dedicated to the synthesis of ZnO nanostructures using low molecular weight P(S-*b*-4VP) as the template. The surface and volume morphologies of films spin-coated from the sol-gel solutions are discussed in section 7.1.1, as probed by SEM and GISAXS, respectively. The optical properties of the films are investigated via UV/Vis spectroscopy and photoluminescence (section 7.1.2). The results and discussion are given in section 7.1.3.

The solvent annealing approach to tune the length scales of ZnO nanostructures, synthesized using low molecular weight P(S-*b*-4VP) is discussed in detail in section 7.2. Two different solvents, chloroform and tetrahydrofuran, having different selectivity towards the different blocks of the copolymer are investigated in order to tune the pore size of the nano grid-like morphology of the ZnO films (section 7.2.1 and 7.2.2). The results are discussed in section 7.2.3.

Finally, the nanostructures obtained from the high molecular weight P(S-*b*-4VP) are deposited on the substrate via spray-coating as presented in section 7.3. The morphology and crystallinity of the films are investigated via SEM and XRD, respectively, in section 7.3.1. Results for the film thickness measurements using height profilometry are also discussed in the same section. The optical properties of the spray-coated films are studied via UV/Vis spectroscopy and are reported in section 7.3.2. Finally, the selected films with optimized morphology and thickness are incorporated as active layers in dye-sensitized solar cells (section 7.3.3). The results are discussed in section 7.3.4 and the chapter closes with a summary (section 7.4).

Some of the experiments are performed together with Kai Müller and Stefan Pogorzalek. Parts of the investigations made with the low molecular weight P(S-*b*-4VP) template is published in the bachelor's thesis of Kai Müller [216]. Parts of the study regarding tuning the pore size of the ZnO nano grids is published in reference [217]. Parts of the results obtained for the high molecular weight P(S-*b*-4VP) template is published in the bachelor's thesis of Stefan Pogorzalek [218].

7.1. Films obtained via spin-coating using low molecular weight P(S-*b*-4VP)

Five different weight fraction combinations of the sol-gel ingredients are reported in this section (as listed in table 7.1), from which thin films are successfully prepared via spin-coating. Several other sol-gel compositions are also tested, which have always resulted in

precipitation of the material in the solution, due to which the deposition of these solutions are not carried out. Nonetheless, these different compositions are listed in appendix A. For all the successful compositions, the concentration of the copolymer template (P(S-*b*-4VP)) is kept fixed at 15 mg mL^{-1}. Details about the molecular weights of the different blocks of the polymer are given in table 4.1. The standard spin-coating parameters, as mentioned in section 4.2.2, are used for deposition of thin films on pre-cleaned silicon substrates. Afterwards, all the films are calcined at a high temperature of 400 °C as described in section 4.2.1.

composition	w_{DMF}	$w_{\mathrm{H_2O}}$	w_{ZAD}
I	0.86	0.01	0.13
II	0.84	0.01	0.15
III	0.81	0.02	0.17
IV	0.79	0.03	0.18
V	0.79	0.04	0.17

Table 7.1.: List of different sol-gel compositions chosen for the synthesis of nano grid-like ZnO films using a low molecular weight P(S-*b*-4VP) template. w represents weight fraction. DMF and H_2O are the good and the selective solvents for the sol-gel solution. Zinc acetate dihydrate (ZAD) is the ZnO precursor.

7.1.1. Morphology

Figure 7.1 shows the SEM topography images of all the spin-coated films obtained from the different sol-gel compositions, as listed in table 7.1. All these images are obtained from the calcined films. The nano grid-like morphology of the thin films prepared from sol-gel compositions I, II and III is clearly observable. The nano grids appear highly ordered locally with the presence of large domains with different orientations. The average pore sizes of these grids are in the range of 17 to 22 nm. In the bottom row of figure 7.1, the fast Fourier transformation (FFT) patterns for the corresponding SEM images are provided. It is evident that the nano grid-like morphology becomes less ordered with an increasing weight fraction of water in the sol-gel composition. The quadratic arrangement of the nano grids is clearly seen from the anisotropic signal from the FFT patterns for the films prepared using the compositions I, II and III (figures 7.1(a), (b) and (c)). For the films obtained from compositions IV and V, the ring-like FFT pattern indicates no preferred orientation of the lattice in the film. The distortion of the grid-like arrangement is also noticeable from the SEM surface images (figures 7.1(d) and (e)).

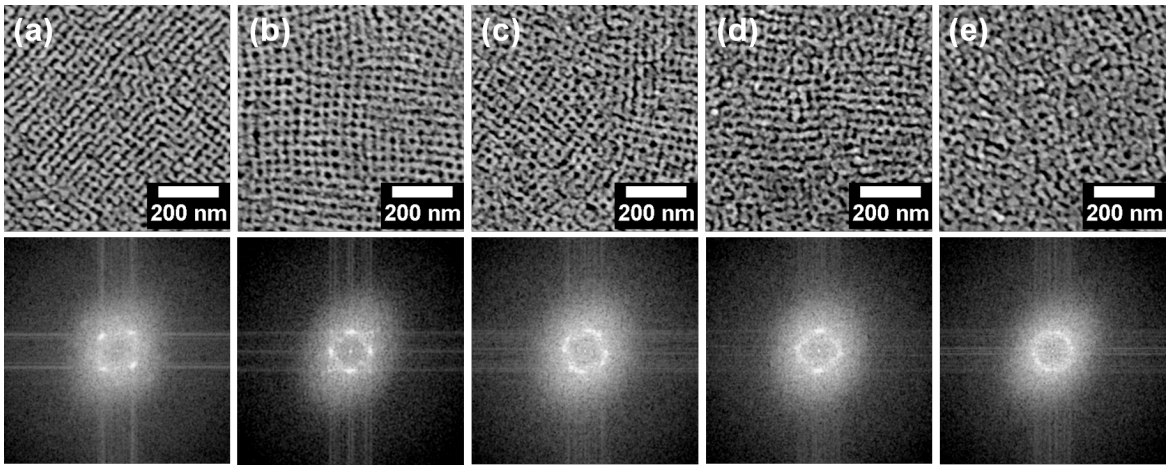

Figure 7.1.: Top row: SEM topography images of the spin-coated films after calcination obtained from compositions (a) I, (b) II, (c) III, (d) IV and (e) V, as listed in table 7.1. Bottom row: the FFT patterns of the corresponding films showing arrangement of the ZnO crystalline lattice.

The loss in order of the morphology can be explained by the complex interaction of the constituents of the sol-gel solutions. Upon deposition of the sol-gel solution via spin-coating, rearrangement in the film takes place depending on the drying time provided. If the polymeric interactions are favored over the ones occurring among the inorganic moieties, more ordered morphologies are produced. On the contrary, if the interaction among the inorganic particles is dominant, a less ordered and ill-defined morphology is obtained. For the present samples, the weight fraction of H_2O increases from sol-gel compositions I to V along with the w_{ZAD}. Based on this, the strength of the polymeric interactions decreases and the cross-linking of the precursor particles gets enhanced. As a consequence, the final film morphology after calcination loses the structural order from compositions I to V.

Due to highly ordered morphology, the film obtained via composition I is further investigated by grazing incidence small angle x-ray scattering (GISAXS) (see section 3.1.5) to probe structures in the volume of the film. The measurements are performed at the BW4 beamline of the DORIS III storage ring in DESY, Hamburg. Figures 7.2(a) and (b) show the SEM topography images of the film before and after calcination, respectively. The grid-like pattern is also clearly visible for the as-prepared film, denoting a successful templating by the diblock copolymer. Figures 7.2(c) and (d) show the characteristic 2d GISAXS data of the corresponding films. The prominent lateral peaks are observed for both the films. For the as-prepared film, the arc-shaped scattering signal (see figure 7.2(c)) indicates the presence of short-range order of the lateral structures provided by the diblock copolymer template [219]. However, after calcination, the peak gets extended

along q_z in the form of Bragg rods, indicating the improvement in structural order in the film in the direction perpendicular to the substrate. The modulations in the scattering data along q_z for the calcined film (figure 7.2(d)) corresponds to stacking of planes in the film. In addition, the broader diffuse scattering obtained after calcination results from the enhanced polydispersity of the length scales emerged in the film volume.

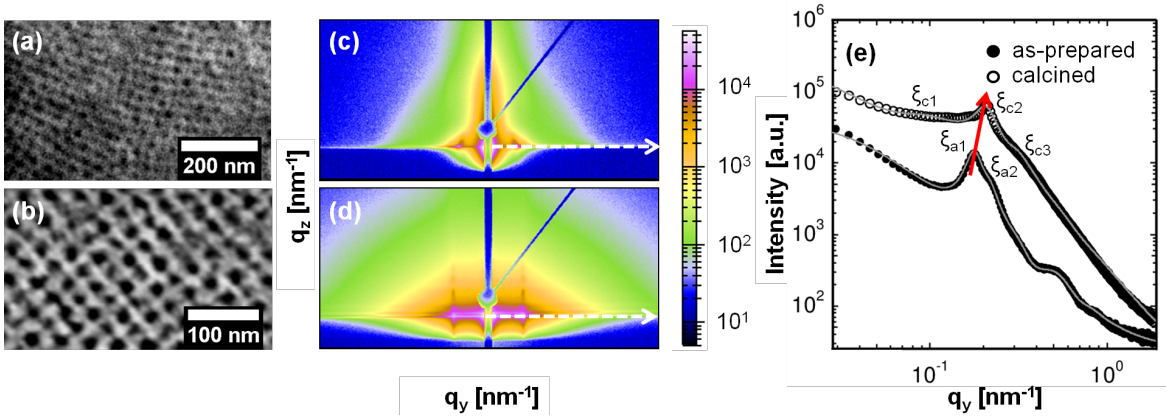

Figure 7.2.: SEM topography images of the spin-coated film obtained from sol-gel composition I, as listed in table 7.1, before (a) and after calcination (b). (c) & (d) Show the corresponding 2d GISAXS data plotted in q_y from -1.0 to 1.0 nm^{-1} and in q_z from 0.3 to 1.2 nm^{-1}. The point-shaped beamstop shields the high intensity specular peak. The vertical rod-shaped beamstop is installed in the set up in addition, to enhance the lateral scattering features. The white dashed arrows mark the position of the horizontal cut to the data. (e) Horizontal line cuts for the as-prepared and the calcined films (symbols) along with the fits (solid gray lines) as described in the text. The curves are shifted along the intensity axis for clarity. The red arrow indicates the shift of the prominent lateral structure peak after calcination. The prominent peak positions for both films are labeled. For the as-prepared film, the peaks obtained at high q_y are the higher orders of ξ_{a1}.

For visualizing the structural order in the film volume in a more quantitative manner, horizontal line cuts to the data are performed as indicated by the dashed white arrows in figures 7.2(c) and (d). These cuts along with the fits to the data are plotted in figure 7.2(e). From the cuts, two principle conclusions are drawn: Firstly, the presence of the prominent length scale, along with the short-range higher orders, is seen clearly for the as-prepared films. On the other hand, after calcination, the higher order peaks have vanished, leaving only one very prominent length scale. This indicates that the presence of the highly ordered morphology in the film is given by the scaffold of the diblock copolymer template. Secondly, the most prominent peak, as indicated by the red arrow in figure 7.2(e), shifts towards a larger q_y value after calcination, which is ascribed to the formation of smaller

length scales in the film. This decrease is well-known for inorganic nanostructures obtained from organic templates due to the pattern collapse as discussed in chapter 6.

In order to access the structure sizes, both cuts are fitted using objects with cylindrical geometry as described in section 2.4.2. For the as-prepared film, two prominent lateral distances (ξ_{a1} and ξ_{a2}, see figure 7.2(e)) are obtained for a cylindrical form factor with a radius of (9.7 ± 0.2) nm, each. The lateral distances correspond to (34.5 ± 0.3) nm and (28 ± 0.3) nm with narrow Gaussian distributions of $\sigma_{S_{a1}} = 2.7$ nm and $\sigma_{S_{a2}} = 2.2$ nm for the structure factors, respectively.

In case of the calcined films, three lateral distances representing the structure factors along with three different sizes of the ZnO nanoparticles, corresponding to the form factors are acquired from the fit to the data. The structure factor corresponding to the most prominent peak in the cut (figure 7.2(e)) is found to be (29 ± 0.1) nm with a narrow Gaussian distribution of $\sigma_{S_{c2}} = 2.7$ nm. This length scale is the intermediate length scale (ξ_{c2}) in the calcined film. In addition to this, a bigger structure (ξ_{c1}) of (45 ± 3) nm is fitted at low q_y, with a Gaussian distribution of $\sigma_{S_{c1}} = 10.8$ nm. The third structure factor (ξ_{c3}) obtained at the highest q_y corresponds to (19 ± 2) nm with a Gaussian distribution of $\sigma_{S_{c3}} = 2$ nm. The analogous form factor radii ranging from low to high q_y, are fitted to be (8.8 ± 0.1) nm, (7.2 ± 0.3) nm and (4.8 ± 0.2) nm, with Gaussian distributions of $\sigma_{F_{c1}} = 2.9$ nm, $\sigma_{F_{c2}} = 2.8$ nm and $\sigma_{F_{c3}} = 1.3$ nm, respectively.

For the calcined film, the structures marked by ξ_{c1} are associated with domain sizes which are also observed in the SEM images with different orientations within the same film (figure 7.1). Structures described by ξ_{a2} and ξ_{c3} are small scale defects in the as-prepared and the calcined films, respectively. The highest scattering intensity is obtained from the structures represented by ξ_{a1} for the as-prepared film and ξ_{c2} for the calcined film. These structures are used to extract the most prominent pore sizes in the film using equation 6.1. The pore sizes thus retrieved for the as-prepared and the calcined films are (15.2 ± 0.3) nm and (14.6 ± 0.2) nm, respectively which agrees very well with the range of pore size observed from the SEM images for the calcined film obtained from composition I (table 7.1).

Thickness of the calcined films is studied via AFM measurements over a scratch on the film. In order to measure the film thickness, a sharp scratch is made (using a pre-cleaned razor blade) on the film, in a way that it reaches down to the silicon substrate underneath, without scratching the later. Figure 7.3 shows an exemplary AFM image taken for the calcined film prepared using composition IV (table 7.1).

The dark region in the AFM image corresponds to the silicon substrate (which appears black as it is lower compared to the film) and the brighter portion of the image shows the ZnO nanostructured film, as indicated in figure 7.3(a). It is observed that at the edge

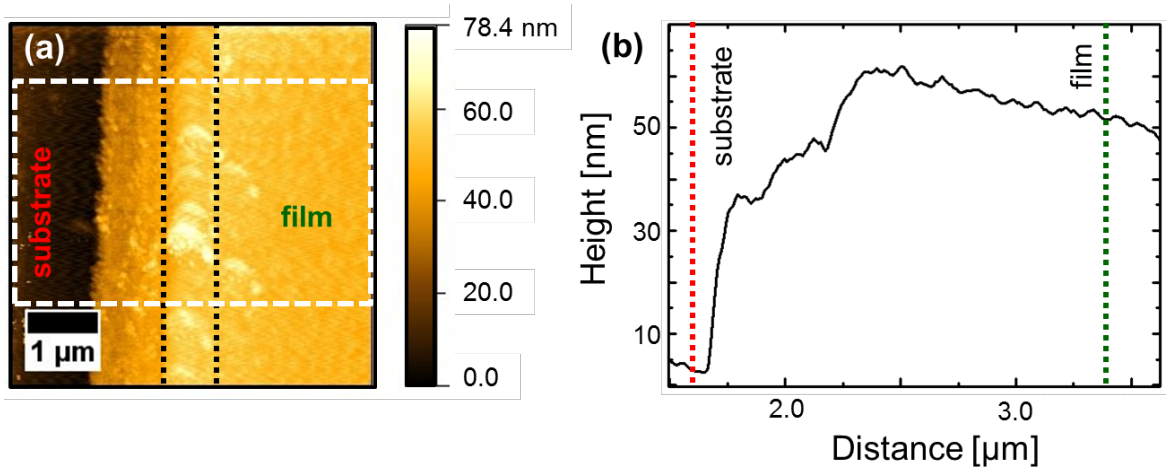

Figure 7.3.: (a) Exemplary AFM topography image of the scratched calcined film obtained using the sol-gel composition IV (table 7.1). The substrate and the film are labeled. The vertical dashed lines outline the material pile-up created during the scratch. The white dashed area is the region over which the thickness of the film is integrated. (b) The integrated line cut over the area indicated in (a). The dashed lines on the film and the substrate indicate the positions chosen for the calculation of the height corresponding to the film thickness.

of the scratch, the area appears a bit brighter than the rest of the film (outlined by the dashed black lines in figure 7.3(a)). This is due to the excess material that is piled up at this position, when the scratch is made. To obtain quantitative idea about the film thickness, several line cuts are performed over the entire image and integrated over the film area represented by the dashed rectangle in the image 7.3(a). The integrated line cut is shown in figure 7.3(b). The difference in height of the substrate and the film is taken as the thickness of the film. The thickness of all the calcined films obtained in a similar manner, lies in the range of 52 to 59 nm.

7.1.2. Optical properties

Optical properties of the calcined films obtained from the sol-gel compositions listed in table 7.1, are probed via UV/Vis instrument I and photoluminescence spectroscopy as described in sections 3.2.1 and 3.2.2, respectively. For the absorption measurements, the films are prepared on glass substrates, whereas for detecting photoluminescence, films on silicon substrates are used.

Figure 7.4(a) shows UV/Vis plots for the calcined grid-like film obtained from sol-gel compositions I to IV (table 7.1). The absorption spectra correspond to the typical behavior shown by crystalline wurtzite ZnO, which absorbs in the UV range. Figure

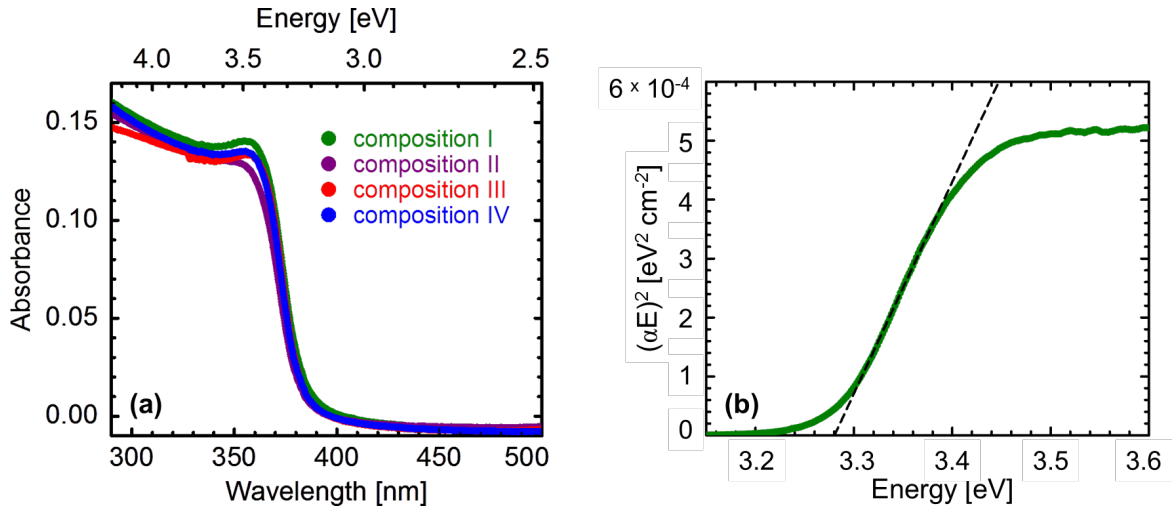

Figure 7.4.: (a) UV/Vis absorption spectra obtained for the calcined films prepared using compositions I to IV (table 7.1), plotted in a spectral range from 290 to 500 nm. (b) Exemplary Tauc plot for the film obtained using sol-gel composition I. The band gap is calculated by linear extrapolation of the data to the energy axis.

7.4(b) shows an exemplary Tauc plot (for the film obtained from sol-gel composition I), which is used to calculate the band gap of the material as described in section 3.2.1. For the film obtained using composition I, a band gap of (2.8 ± 0.01) eV is obtained. Similar measurements are performed for the films prepared using sol-gel compositions II to IV (table 7.1). The average band gap calculated via the Tauc equation (equation 3.2) for all the films is 3.29 eV, which matches with the wurtzite phase of crystalline ZnO as reported in literature [188].

Photoluminescence spectroscopy (PL) for all the calcined films prepared using the different sol-gel compositions (table 7.1) is plotted in figure 7.5(a). The instrumental settings used for the measurements are stated in section 3.2.2. PL measurements are important in order to understand the optical properties of a material in addition to its surface properties, such as presence of defect states and crystallinity. Since, the dimension of the material under investigation strongly influences the above-mentioned factors, PL is widely used for characterizing nanostructured materials. Band-band transitions and excitonic PL are the major processes contributing to the overall signal [37].

Figure 7.5(b) exemplarily shows Gaussian fits to the emission peaks obtained for the nano grid-like ZnO film prepared using sol-gel composition IV. The PL spectra for all the films show a prominent UV emission peak and at least one broad peak in the visible region of light. The position for the former peak is at 375.5 nm (for the film obtained for sol-gel composition IV), which corresponds to the band gap energy of wurtzite crystalline

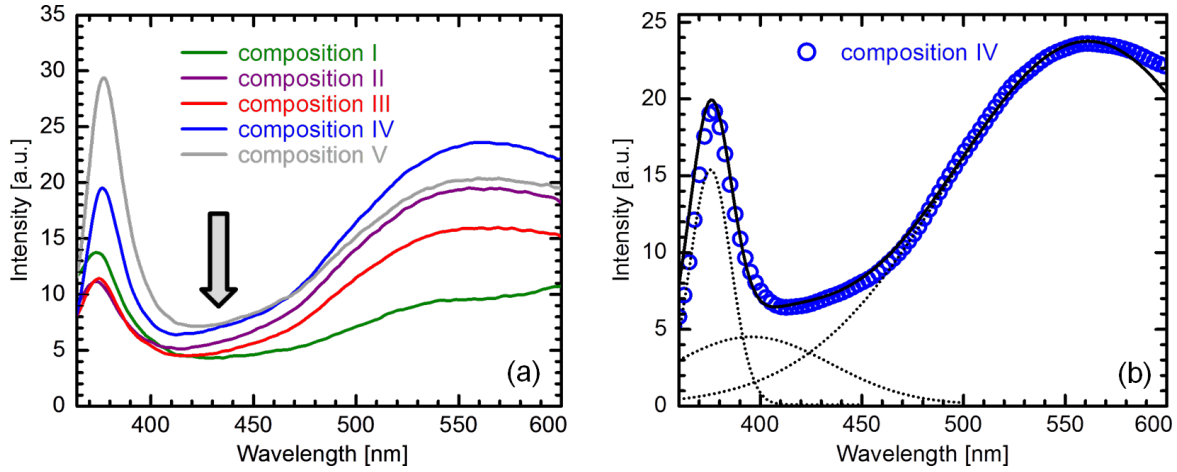

Figure 7.5.: (a) Photoluminescence spectra for all the calcined ZnO films showing nano grid-like morphology, prepared using the different sol-gel compositions as listed in table 7.1. The arrow indicates the weak photoluminescence signal. (b) Exemplary fit to the emission spectrum of the nano grid-like ZnO film obtained from the sol-gel composition IV (table 7.1). The three dotted curves represent the Gaussian peaks used to fit the data (open symbols). The final fit is plotted as the solid black curve.

phase of ZnO (3.3 eV), is in good agreement with the UV/Vis measurements. This peak (as obtained from the fit) signifies the radiative recombination of the electronic transitions from the conduction band to the valence band of wurtzite ZnO. In addition to this peak, a broad peak ranging from 460 to 600 nm (corresponding approximately to 2.1 to 2.7 eV) is present for all the films. A less intense and broader peak is also present in the range of 390 to 460 nm (corresponding approximately to 2.7 to 3.1 eV) for all the films as indicated by the arrow in figure 7.5(a) and by the fit shown in figure 7.5(b). Hence, these peaks are at longer wavelengths (lower energies) than the band gap of the material. The broadness of these peaks is attributed to a superposition of many deep level transitions [220]. The origin of these broad peaks is associated with the imperfections in the crystal lattice, which may arise due to native or intrinsic defects [37]. Such defects mainly include vacancies (missing atoms at regular lattice positions), interstitial (additional atoms occupying the interstices in the lattice) and antisites (Zn atoms occupying the sites for O atoms and vice versa). The presence of these defects and combination of two point defects largely depend on their formation energies [141, 142].

According to already reported investigations, the violet-blue emission (390 to 460 nm) might result due to and electronic transition between the zinc interstitial and the valence band, or due to a transition between the conduction band and the zinc vacancy [141]. Balandin et al. have additionally attributed this broad emission peak to oxygen antisites

[143]. On the other hand, the emission peak ranging from 460 to 600 nm (green emission) is linked to transitions from the conduction band to the oxygen or zinc vacancies [144,145]. In addition to the just mentioned sources for PL signal, the presence of trap states also significantly influence the PL response of a material. Mainly the oxygen vacancies are reported to be quite prone to capture photo-excited electrons and thereby, contribute to the PL signal [37]. Hence, a material contributing to a strong PL signal gives the signature of poor crystallinity and large number of defect states.

For the calcined ZnO nano grid-like films, composition IV and V (figure 7.5) show the highest PL signal among all. Films with compositions II and III (figure 7.5) show similar intensity for the the signal obtained at the band gap of wurtzite ZnO. However, the film with composition II denotes an enhancement in the signal for the PL signal in the violet-blue and green emission regions. The signals in the range of 400 to 600 nm for the film with composition I, is remarkably quenched as compared to all the other films.

7.1.3. Results & discussion

Unlike the P(S-*b*-EO) templates with low and high molecular weights (discussed in chapter 6), the low molecular weight P(S-*b*-4VP) template provides limited variation in film morphologies within the investigated sol-gel compositions. To obtain a stable sol-gel from P(S-*b*-4VP) is very critical using the same solvent environment (DMF as good and H_2O as selective solvents) and the precursor used before (chapter 6). This can be explained with regard to the interactions of the polymer chains among themselves and with the precursor particles in the given solvent surrounding. Depending on the weight fractions of the good solvent (DMF) and the selective solvent (H_2O), two opposing processes commences in the system: the interaction of the polymer micelles with each other resulting in fusion and formation of larger aggregates with different geometries and the interaction between the ZAD molecules. For the low molecular weight templates, the number average molecular weight (M_n) of P4VP block (which acts as a host for the metal oxide nanoparticles) is slightly more than double as compared to that for the PEO block of P(S-*b*-EO) template. Hence, for most of the combinations of the weight fractions of the sol-gel ingredients in the present case, the interaction between the polymer chains overrates that between the metal oxide nanoparticles with the P4VP block of the template. As a result only a narrow window is attained for the preparation of stable sol-gel solutions with a balance between the interactions mentioned above within the system.

A unique nano grid-like morphology is predominantly produced from the sol-gel synthesis using low molecular weight P(S-*b*-4VP) as the template. The sol-gel solution with the lowest weight fraction of the ZnO precursor (ZAD) among the five different compositions,

tends to have less interaction withing themselves and thereby, duplicates the structural arrangement of the template the best, hence showing the most ordered morphology among all the films studied in the present section. With increasing weight fraction of ZAD in the sol-gel, the interaction among ZAD molecules intensifies and hence, they cease to follow the structural ordering of the template. As a consequence, the morphology turns from a well-defined grid to a more foam-like appearance. The volume morphology of the films is studied by GISAXS measurements. All films are modeled to be composed of cylindrical scattering objects. The scattering signal perpendicular to the substrate becomes stronger after the calcination of the films, whereas, before the high temperature treatment, broad lateral scattering features are observed. The morphology is believed to be highly promising for applications demanding high structural order, such as photocatalysts and gas/chemical sensing [161,221,222]. Moreover, this length scale is within the range of the exciton diffusion length, which is interesting for applications in the field of dye-sensitized solar cells [223]. However, these practical applications are restricted by the rather low film thickness as measured by AFM. Some of the possible alternatives to increase the film thickness are multiple spin-coating, blade-coating, solution casting, spray deposition or printing. Such thickness upscaling methods have, in turn, their own inherent limitations. The first method is inefficient to increase the film thickness in a reasonable way, whereas, for the others, keeping the morphology of the films intact is a challenging task. This is due to the fact that all these methods have much slower kinetics as compared to spin-coating and hence, the nanostructures get additional time in order to reorganize themselves and evolve into different morphologies. The optical characterization of the films has revealed the presence of wurtzite phase of ZnO along with certain defect states.

7.2. Tuning grid-like morphology obtained using low molecular weight P(S-*b*-4VP) via solvent vapor annealing

The highly ordered nano grid-like morphology of ZnO obtained using the low molecular weight P(S-*b*-4VP) as discussed in the previous section, has a high potential for practical applications in nano-electronic devices. It is also shown that the occurrence of such a beneficial nanostructure is highly stimulated by the templating diblock copolymer used. However, this nano grid-like morphology shows limitation regarding the length scales, e.g., the pore size obtained in the films prepared from different sol-gel compositions (section 7.1.1). This drawback is mainly confined to the length of the blocks of the template involved. The main aim of the present section is to develop a pathway in order to impart

additional flexibility and widen the range of the pore sizes obtained using a single sol-gel composition, while keeping the unique morphology intact.

Long range order has been established in P(S-*b*-4VP) and similar polymers belonging to the same family by subjecting the system to a suitable solvent vapor [210, 224]. However most of the investigations are performed on pure block copolymer films which undergoes self-assembly upon exposure to a solvent vapor. The uniqueness of the investigations reported in the present section lies in the fact that the block copolymers present in the thin films are already micro-phase separated and are in addition incorporated with ZnO nanostructures. Solvent vapor annealing in the present study is thus a medium to manipulate the length scales of the micro-phase separated domains of the block copolymer. These changes are then expected to be imparted to the ordered ZnO nanostructures, hosted by the block copolymer domains. Various other methods such as anodized aluminium oxide template-assisted sol-gel, chemical treatment on ZnO nanostructures, electrodeposition methods, imprinting or selective plasma etching have also been used to tune the length scales of the generated metal oxide nanostructures [215]. However, all these methods face a difficulty to be implemented for large scale production and do not provide long-term stability of the nanostructures. The workaround to these problems is provided by the solvent annealing method as discussed in the following.

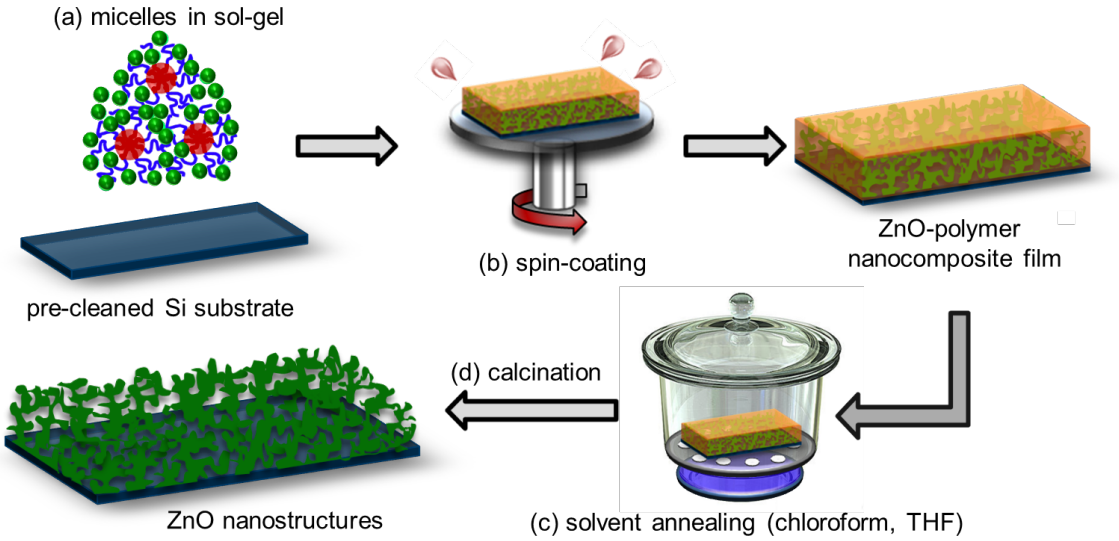

Figure 7.6.: Schematic representation of the steps involved in the fabrication of ZnO-polymer nanocomposite thin films and their solvent annealing: (a) preparing ZnO sol–gel solution, (b) spin-coating the ZnO-polymer nanocomposite film, (c) solvent annealing in THF/$CHCl_3$ vapor for different times, (d) high temperature calcination step to obtain the nanostructured ZnO film.

Two different solvents are used for the present study, namely, chloroform ($CHCl_3$) and tetrahydrofuran (C_4H_8O; THF). The choice of these solvents are based on their selectivity

towards the blocks of the copolymer template. $CHCl_3$ tends to dissolve both the blocks of the copolymer equally well, whereas, THF is slightly more selective towards the PS block [225, 226]. The ZnO-polymer hybrid films are treated with the vapor of the above mentioned solvents for different time intervals in order to control the degree of structural organization in the film. Depending on the solvent, the kinetics of the process also vary and hence, different time intervals for the treatment of the films with the respective solvent vapors is chosen. For all the experiments, composition I (see table 7.1) is taken in the following, due to the highest degree of order of the nano grid-like morphology as investigated in previous section. A short description of the different steps involved in a typical solvent annealing experiment is shown in figure 7.6. In order to perform the solvent vapor treatment, the micellar sol-gel solution is spin-coated on pre-cleaned silicon substrates in order to obtain the ZnO-polymer nanocomposite films (figures 7.6(a) and (b)). These nanocomposite films are then horizontally placed in desiccators of 0.7 L volume. Each of the desiccators contain a single sample which is placed on a perforated ceramic plate as shown in figure 7.6(c). 20 mL of the solvent used is then filled in the bottom as represented by the blue liquid inside the desiccator (figure 7.6(c)). The lid of the desiccator is closed and sealed with Parafilm. The whole set up is then kept undisturbed under ambient conditions for the required time. The effect of the structural reorganization in the block copolymer template, which get transferred to the ZnO nanostructures, is studied. For this purpose, the solvent-annealed films are calcined at 400 °C in order to combust the polymer (figure 7.6(d)). To follow the changes in the morphology of the films, SEM and GISAXS measurements are performed on the films treated with both solvents for different times scales.

7.2.1. Influence on morphology by $CHCl_3$ vapor annealing

Chloroform is used as the non-selective solvent towards both blocks in P(S-*b*-4VP). Figure 7.7 shows the SEM topography images of the hybrid films after solvent annealing and the subsequently calcined films.

Structural modifications in the hybrid films are clearly visible already after 4 hours of solvent vapor treatment. Additionally, it is evident that the modifications induced by the solvent vapor to the morphology of the hybrid films, are also transferred to the films after the calcination step. Compared to the untreated films shown in figure 7.2(a) and (b), the morphology of the films upon treatment with chloroform vapor for 1 hour (figure 7.7), stays very similar without any drastic transitions. The scenario changes with the appearance of larger pores or cracks for longer solvent annealing times ranging from 4 to 6 hours (figure 7.7). The nano grid-like morphology is maintained till 6 hours of solvent

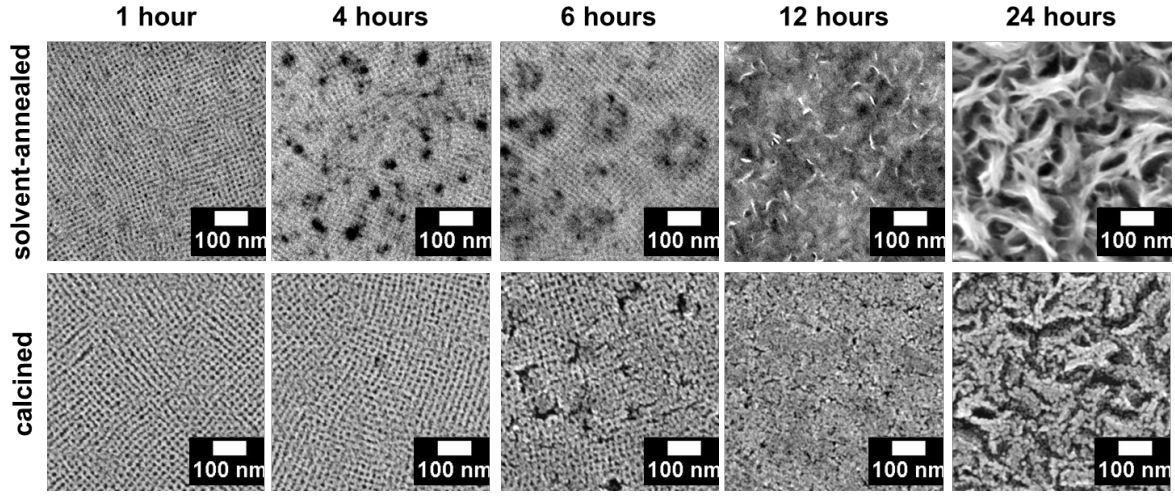

Figure 7.7.: Top row: SEM topography images of the ZnO-polymer hybrid films after chloroform vapor annealing for different times as indicated. Bottom row: the corresponding films after a high temperature treatment of 400 °C.

treatment time, after which the ordered morphology is lost (figure 7.7). Hence, this time sets the maximum limit for the exposure of the hybrid films to the chloroform vapor where preservation of the grid-like morphology is desired. Moreover, the porosity of the films is also highly reduced, but with an enhancement of the surface roughness. Nonetheless, the morphology of the film evolved after 24 hours of solvent annealing is interesting due to the enhanced surface area as seen from the SEM image in figure 7.7. Such morphologies with an optimum film thickness and high surface area can be used as active layers in devices for energy storage and conversion.

Chloroform, being a good solvent for both the blocks of the templating polymer, equally swells the core and the corona of the micelles (from the sol-gel solution), which get arrested on the substrate after spin-coating. After a considerable degree of swelling, the micellar structure of the template is disrupted. The ZAD molecules, selectively embedded in the P4VP block of the copolymer template, thereby loose their preferential ordering and tend to cluster among themselves. This phenomenon is supported by the increase in the size of ZnO clusters seen after calcination of the films in figure 7.7. The largest clusters are observed for the film treated for the longest time with chloroform vapor.

In order to follow the structural changes in the volume of the films upon chloroform vapor annealing for different times, GISAXS experiments are performed at the BW4 beamline of DORIS III storage ring in DESY, as described in section 3.1.5. The data obtained from the measurements are shown in figure 7.8.

Figure 7.8(a) shows all the 2d GISAXS data obtained for the grid-like films after dif-

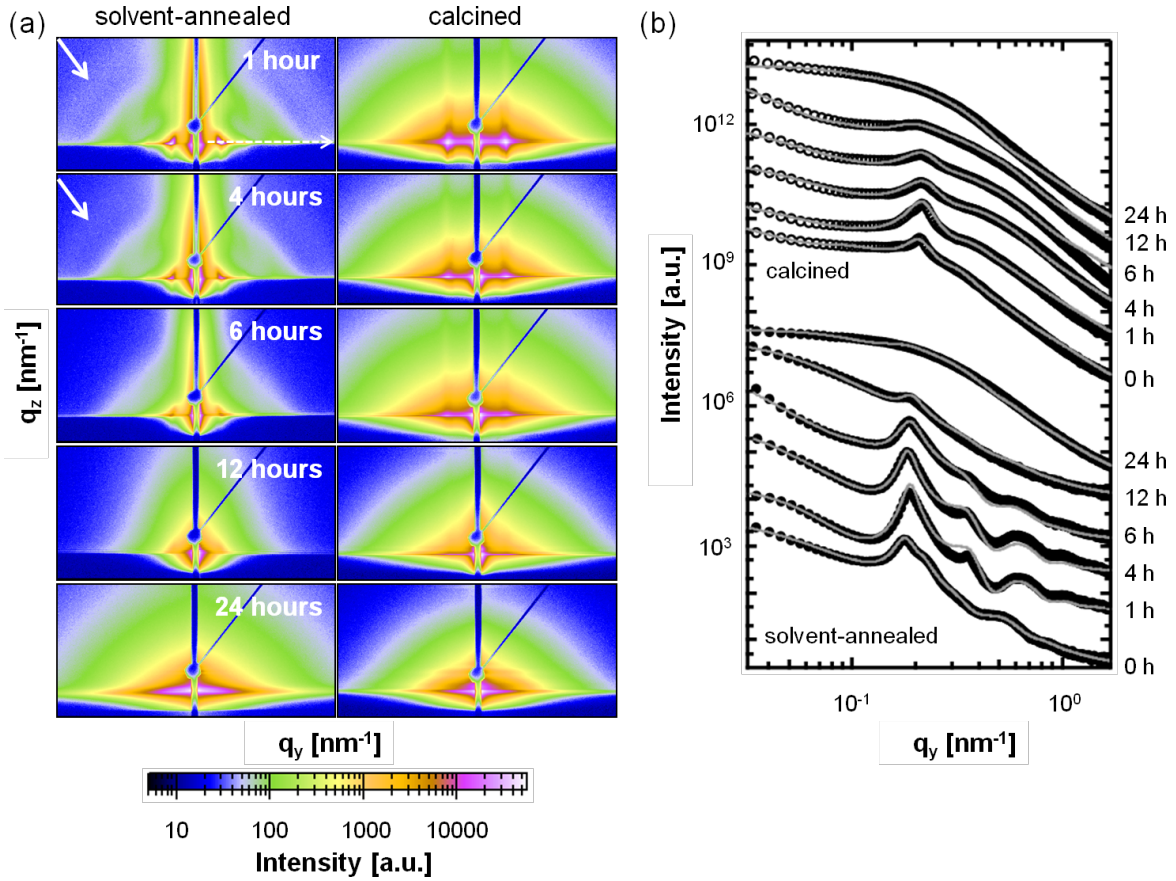

Figure 7.8.: (a) 2d GISAXS data obtained for the solvent-annealed films (left column) for different time scales as indicated. The 2d images are plotted in q_y from -1.0 to 1.0 nm^{-1} and in q_z from 0.3 to 1.2 nm^{-1}. The arrows in the first two images point towards the azimuthal scattering ring. The white dashed arrow in the first image exemplarily shows the position chosen for performing the horizontal line cuts for all the films. The right column shows the scattering data obtained from the respective solvent treated films after calcination at 400 °C. (b) Horizontal line cuts (symbols) along with the fits (solid gray lines) for all the films as mentioned are plotted with the increasing time of solvent annealing from bottom to top as marked on the right axis of the plot. All the curves are shifted along the intensity axis for clarity.

ferent times of solvent annealing. The point shaped beamstop present in all the images shields the specular peak which occurs at the exit angle equal to the incident angle. In addition, a rod beamstop is also installed to cover the scattering along $q_y = 0$ nm^{-1} in order to further enhance the scattering signal in the higher q_y region. Up to a solvent annealing time of 6 hours, pronounced lateral peaks are visible for both solvent-annealed and calcined films. This peak for the solvent-annealed films appears slightly arc-shaped as discussed for the scattering data obtained from the as-prepared films before any solvent vapor treatment (section 7.1.1). After calcination, the lateral peaks become more promi-

nent and show an enhanced Bragg scattering along the q_z direction. The solvent-annealed films for 2 and 4 hours, in addition show an azimuthal scattering ring as indicated by the white arrows in the first two images of the left column in figure 7.8(a). The azimuthal signal arises from the Debye-Scherrer scattering for the solvent-annealed films, associated with the disorder of the out-of-plane orientation such as bending and tilting of the ZnO domains embedded in the polymer matrix, with respect to the beam [227]. This signal is however lost upon calcination of the respective films as seen from the data on the right column of figure 7.8(a). Instead, the so-called crystal truncation rods (CTRs) appear which indicate the improvement of perpendicular ordering of the domains. The scattering intensity for these CTRs is found to be higher at the exit angle equal to the critical angle of the material. For solvent annealing times of 12 and 24 hours, also the calcined films show high degree of randomness and loss of structural order as scattering intensity corresponding to the CTRs diminish and a broad scattering signal is obtained, which is characteristic of a polydisperse system. The data obtained from GISAXS measurements is in good agreement with the conclusions drawn from the SEM investigations.

The above-mentioned observations are more clearly identified in the horizontal line cuts for all the films, performed at the Yoneda peak position of ZnO, as indicated by the white dashed arrow in figure 7.8(a), for the chloroform-annealed film for 1 hour. These cuts along with their fits (model explained in section 2.4.2) are shown in figure 7.8(b). For reference, the data for the hybrid and the calcined films without any solvent treatment (marked as 0 h curves) are also plotted in figure 7.8(b). From the cuts to the solvent-annealed films, the presence of higher orders of the uniform grid-like structure is visible till the solvent annealing time of 6 hours. Afterwards, the higher orders vanish and a broad scattering behavior is established. The length scales obtained from the fits do not show any sequential influence of the solvent annealing time on the pore size or the size of the ZnO clusters. The averaged information retrieved from the GISAXS measurements show that the average pore size of the calcined films increases from (9.4 $\pm$ 0.3) nm to (14.4 $\pm$ 0.3) nm with solvent annealing time from 1 hour to 24 hours, respectively. However, from the SEM images, the size of the pores seem to decrease in the same range of solvent annealing time with a collapse of the ordered nano grid-like morphology for a solvent annealing time of 24 hours. Hence, the increase in the prominent length scale observed from the fitting of the GISAXS data is associated with the contribution from the large voids formed in the calcined film after 24 hours of solvent annealing (figure 7.7). Moreover, the prominent length scale observed after 24 hours of solvent annealing is less than the pore size ((14.6 $\pm$ 0.2) nm) obtained in the calcined film which is not treated with any solvent vapor. Hence, with $CHCl_3$ vapor treatment, around 36 % decrease in the pore size is observed for an exposure time of 1 hour, thereby indicating the high mobility imparted

to the block copolymer domains in the thin films by the $CHCl_3$ vapor. This in turn, increases interaction between the ZAD molecules embedded in the domains, which results in an overall shrinkage of the average pore size.

In summary, variation in morphology and length scales of nanostructures produced by the sol-gel technique assisted with the P(S-*b*-4VP) copolymer template, is possible via chloroform vapor treatment of the spin-coated films. This is largely governed by the selectivity of the solvent towards both of the blocks of the copolymer and the volatility of the solvent. The major problem encountered while using the present solvent is the non-systematic alteration of the pore sizes as well as a rupture of the nano grid-like morphology for a longer annealing time.

7.2.2. Influence on morphology by THF vapor annealing

In order to further explore the possibility to tune the pore size of the ZnO nano grid-like morphology, tetrahydrofuran (THF) is used as the solvent, which is slightly selective towards the PS block of the template, P(S-*b*-4VP). Solvent annealing of the ZnO-polymer hybrid films is performed in similar manner as stated in section 7.2.1, using the spin-coated ZnO-polymer nanocomposite films obtained with sol-gel composition I (table 7.1). Solvent vapor annealing times of up to 48 hours are used in the present case. The structural evolution in the film is studied via SEM, AFM and GISAXS. A combination of all these techniques allows to probe the morphological rearrangement on the film surface as well as in the volume.

Surface morphology

The SEM surface images of the ZnO-polymer hybrid films subjected to THF solvent vapor annealing are shown in figure 7.9 (top row) for different annealing times as indicated. The solvent-annealed films are subsequently calcined in order to investigate the structural modifications on the remaining ZnO film. The SEM images of these calcined films are shown in figure 7.9 (middle row). Like in the previous case for films treated with chloroform vapor, the present films also show identical morphologies before and after the calcination step as well as high surface homogeneity. It is observed that the films annealed with THF vapor maintains the nano grid-like morphology up to at least 12 hours of solvent annealing time. This time scale is double the time when the films preserve the surface morphologies after chloroform vapor treatment (section 7.2.1). However, for a longer solvent annealing time of 48 hours, a collapse of the grid-like morphology is observed for the solvent-annealed and the calcined films. The white clusters seen from the SEM image (figure 7.9: 48 hours), represent aggregates of ZnO particles. In addition,

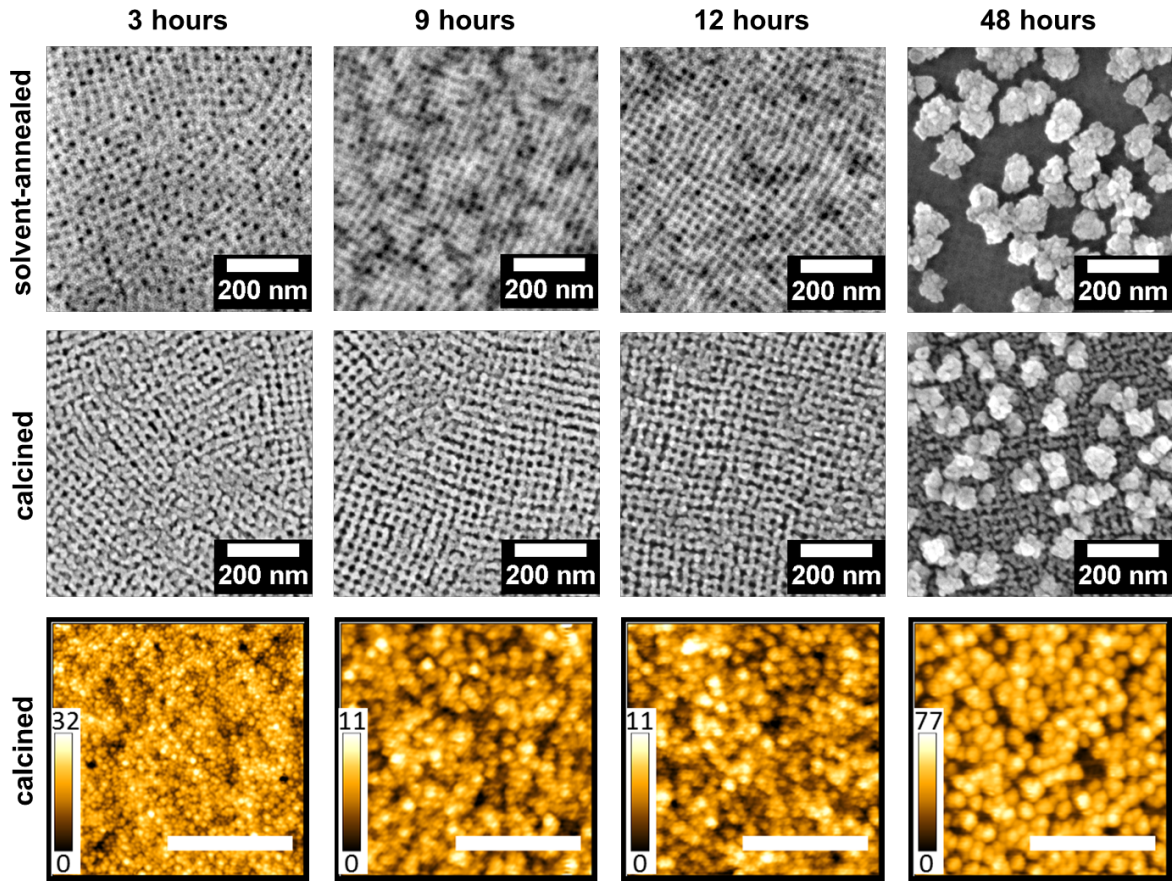

Figure 7.9.: Top row: SEM surface images of the ZnO-polymer nanocomposite films obtained via sol–gel synthesis showing a nano grid-like morphology, being subjected to THF vapor annealing for different time scales as indicated. Middle row: the corresponding films calcined at 400 °C after the THF solvent vapor treatment. Bottom row: AFM topography images of the calcined ZnO nanostructured films subjected to THF vapor treatment beforehand. All the images are (2 × 2) μm^2 and the scale bar for all the images is 1 µm long. The color bars as insets in the AFM images indicates the height of the nanostructures in nm.

the distorted grid-like morphology is present underneath these clusters. The variation in the pore size of the nano grid is however, not easily visible. Upon thorough analysis of the SEM data, it is found that the average pore sizes of the ZnO grid for the calcined films increase with increasing solvent annealing time, from approximately 14.6 nm for the untreated film to up to 20 nm for the film calcined after a solvent vapor treatment of 12 hours.

Since the calcined films, containing only the crystalline ZnO network is of interest for practical applications such as in sensors and energy storage devices, the morphology of these films is studied in further details. The height of the structures as well as the surface

roughness of the calcined films are investigated via AFM. The AFM topography images of all the calcined films are shown in the bottom row of the figure 7.9. A clear morphological trend towards larger surface structures is observed with increasing solvent annealing time. The brighter regions are associated with the domains of larger heights which contribute to the surface roughness of the films. The rms roughness of the films for shorter solvent annealing times of up to 12 hours is in the range of approximately 2 nm, whereas, after 48 hours of solvent annealing, it increases to (12.6 ± 1) nm.

Inner film morphology

It is quite challenging to follow the modifications in length scales of the nanostructures occurring during short annealing times. Nevertheless, a quantitative analysis of the length scales is important in order to develop an accurate routine to tune the structures for a specific requirement. To effectively address the prerequisite, grazing incidence small angle X-ray scattering (GISAXS) has been performed on the solvent-annealed and calcined films to probe the structural transitions in the bulk of the films. This powerful technique enables even to probe the minor structural fluctuations in the length scale of nanostructures in a quantitative manner.

The 2d GISAXS data obtained from the measurements for all samples are shown in figure 7.10(a). Similar to the 2d GISAXS data obtained for the chloroform-annealed films, the THF-annealed films show the Debye-Scherrer ring. In the present case, the signal from the ring is observed up to an annealing time of 12 hours (figure 7.10(a) - left column) unlike for the films annealed with $CHCl_3$ vapor, where the ring-like scattering disappeared after 4 hours of solvent annealing. This is a good indication that the grid-like columnar structures are maintained until this time scale after solvent annealing. However, the azimuthal scattering, as marked by the white arrows in the 2d GISAXS data of the solvent-annealed films (figure 7.10(a) - left column) represents the presence of random orientation of these features with respect to the substrate surface. Only after the longest solvent annealing time of 48 hours, these scattering characteristics are lost (figure 7.10(a) - left column), and a broad scattering signal is obtained. This observation is in good agreement with the structural arrangement derived from the SEM investigations, where formation of large ZnO clusters with the loss of structural order is seen after 48 hours of solvent annealing (figure 7.9 - top row). For the calcined films, similar CTRs are visible as those observed for the calcined films exposed to chloroform vapor (figure 7.10(a) - right column). This again indicates an improvement in the structural order of the grid-like columnar structures in the vertical direction with respect to the substrate. The film treated with THF vapor for 48 hours, however, shows the broad scattering signal, similar to that of the solvent-annealed film, confirming the loss of order in the morphology.

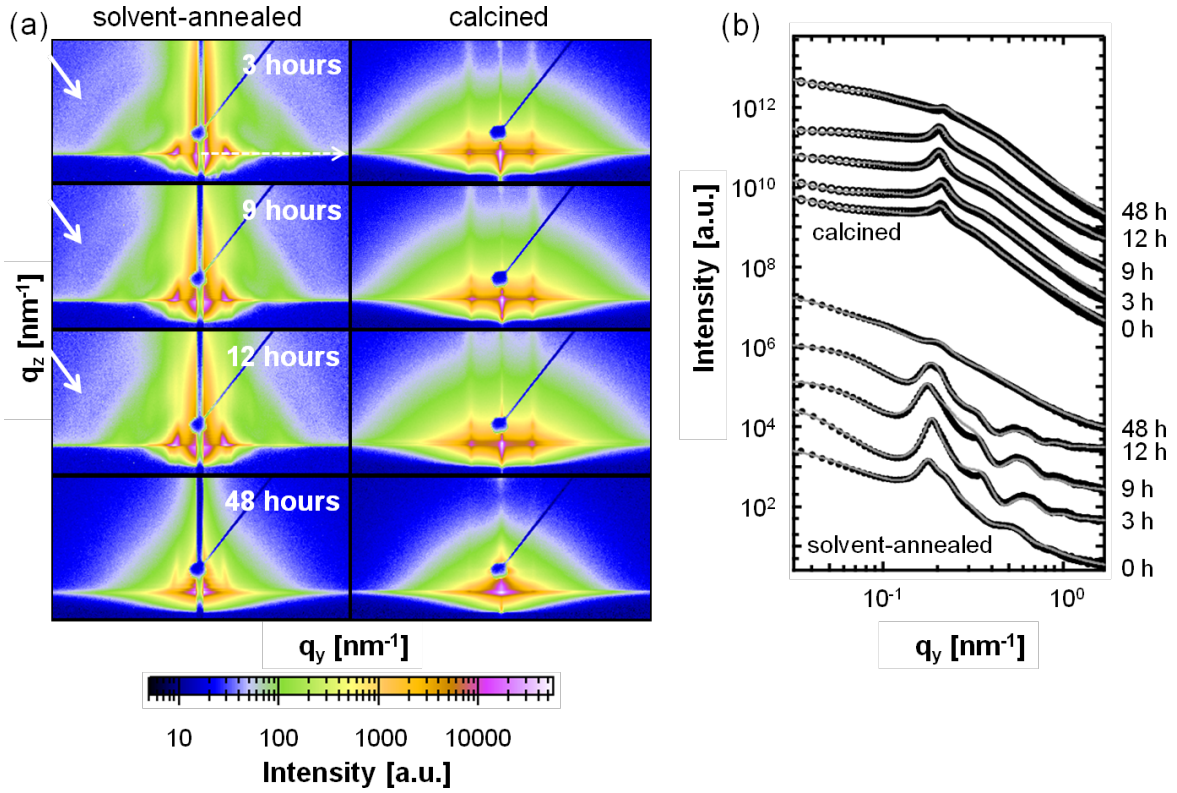

Figure 7.10.: (a) Left column: 2d GISAXS data obtained for the THF-annealed films for different time scales as indicated. The 2d images are plotted in q_y from -1.0 to 1.0 nm^{-1} and in q_z from 0.3 to 1.2 nm^{-1}. The arrows in the images for samples annealed for 3, 9 and 12 hours point towards the azimuthal scattering ring. The white dashed arrow in the first image exemplarily shows the position chosen for performing the horizontal line cuts for all the films. Right column: the scattering data obtained from the corresponding solvent treated films after calcination at 400 °C. (b) Horizontal line cuts (symbols) along with the fits (solid gray lines) for all the films are plotted with the increasing time of solvent annealing from bottom to top as marked on the right axis of the plot. All the curves are shifted along the intensity axis for clarity.

Horizontal line cuts to all the scattering data are performed in the position exemplarily shown by the white dashed arrow in figure 7.10(a) for 3 hours THF-annealed film. These line cuts are plotted along with their fits (explained in section 2.4.2) in figure 7.10(b). Horizontal line cuts are used to gain information about the structural length scales parallel to the substrate. The cuts are plotted for increasing solvent annealing times from bottom to top (figure 7.10(b)). Again for reference, the lowest curve denotes the film without any solvent annealing. The position of the most pronounced peak observed for all the films determines the predominant structural length scale in the volume of the film. The secondary peaks in case of the solvent-annealed films indicate the higher orders of the nanostructures. For the solvent-annealed films these higher orders are suppressed after

solvent annealing for 48 hours. Also, for all calcined films, the higher orders are no longer present, even after the shortest solvent annealing time investigated. Hence, the presence of higher orders in the system is assigned to the copolymer template. The loss in order after calcination is attributed to the collapse of the structures due to removal of the polymer template, which is well-known for these systems.

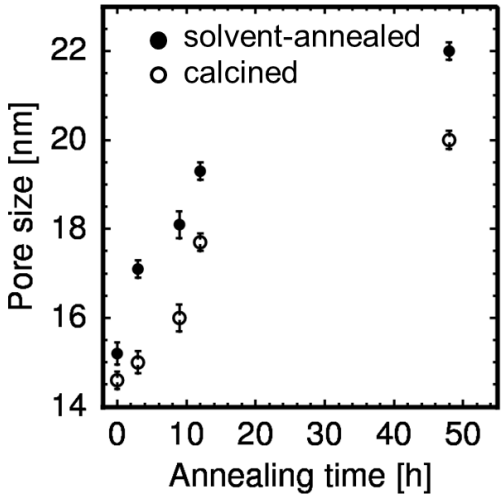

Figure 7.11: The average pore size of the THF-annealed films obtained before and after calcination for different solvent annealing times, as derived from the fits shown in figure 7.10(b).

The structure and the form factors extracted from the fits, as described previously, are used to calculate the average pore size in the volume of the films using equation 6.1. The pore size of the films with respect to the solvent annealing times are plotted in figure 7.11. The increase in the average pore size is clearly visible with increasing solvent annealing time for the hybrid films. It should be noted that the so-called pores in the hybrid films are not hollow, but are rather occupied by the copolymer template. The contrast between the pore walls (composed of ZnO precursor particles incorporated in P4VP block of the copolymer template) and the template-filled pores arises due to the difference in the electron densities of the two materials. For the films calcined afterwards, a similar trend is manifested. The average pore size of the solvent-annealed films decreases after they undergo the calcination step which is related to the pattern collapse. The average pore sizes extracted from the GISAXS measurements are in good agreement with those obtained from the surface investigation of the films via SEM. It is noteworthy that the average pore size mentioned for the solvent-annealed film for 48 hours is represented by the distorted grid present underneath the large ZnO clusters observed on the film surface (figure 7.9 - top and middle row). An increase in pore size from (14.6 $\pm$ 0.2) nm for the untreated film to (17.7 $\pm$ 0.2) nm after annealing time of 12 hours. Finally, the pore size of the collapsed grid after 48 hours of solvent annealing is found to be (20 $\pm$ 0.2) nm. Along with the distorted grid, large clusters of ZnO are also present in the film after 48 hours of solvent annealing (as seen from the SEM and AFM images in figure 7.9). The

average distance between the large ZnO clusters of an average size of 60 nm, is also probed by GISAXS and corresponds to a length scale of around 40 nm for the calcined film.

Model representing pore size tuning of the ZnO nano grid via THF vapor annealing

To summarize the results obtained via the real- and the reciprocal-space analysis, figure 7.12 shows a pictorial representation of the on-going modification processes in the ZnO-copolymer hybrid films as a function of time-dependent THF annealing. In the sketch, the micelles formed in the solution during sol–gel synthesis, as a result of micro-phase separation are shown. The micro-phase separation occurring due to the interaction of the blocks with the good and the selective solvents in the sol-gel process is described in detail in section 2.1.1.

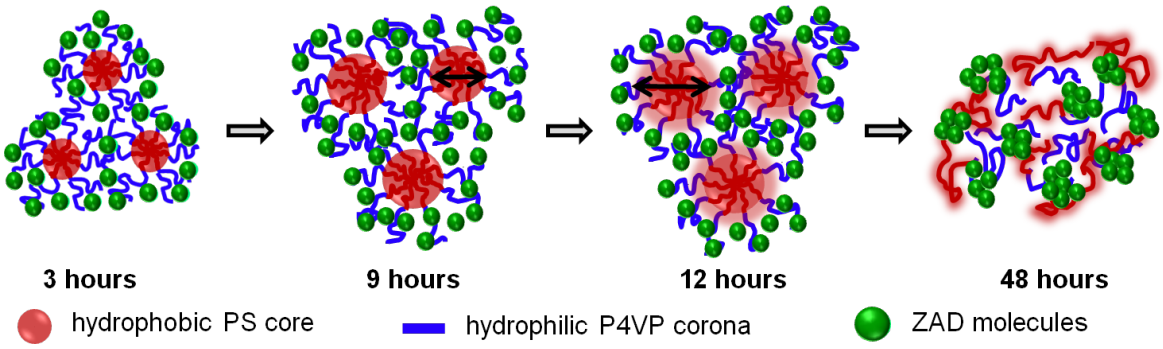

Figure 7.12.: Schematic illustration of the structural evolution of the ZnO-copolymer nanocomposite film (prepared from sol-gel composition I; table 7.1) for different THF annealing times as indicated. The black arrows indicate the swelling of the PS cores over time by the THF vapor, thereby, increasing the pore size of the nano grid.

The hydrophobic PS block is indicated in red. It is shown to form the core of the micelles, whereas the corona formed by the blue chains represents the hydrophilic P4VP block. The small green spheres indicate the ZnO precursor (ZAD) particles. Although the solvent annealing is performed on thin films, the sketch describes the structural modifications in the micelles. These micelles produced in the sol–gel are frozen on the substrate after spin-coating. However, the micelles retain the potential to rearrange under an external applied field which in the present case is THF vapor. As the ZAD molecules get preferentially incorporated in the P4VP block of the template, its mobility is hindered to a large extent. On the other hand, THF being slightly selective towards the PS block, tends to swell it faster than P4VP block. Since the PS block constitutes the core of the micelles, the average pore size of the ZnO nano grid increases after solvent annealing as marked by the black arrows in figure 7.12. It is observed from the SEM images that

the grid-like morphology stays intact even after 12 hours of solvent annealing. The slow kinetics of the system is explained by the fact that the PS core is protected from the THF vapor by the ZAD particles which are incorporated in the P4VP corona. Hence, considerable time is needed by the solvent vapor in order to penetrate the ZnO shielding and finally swell the PS block. Nevertheless, for sufficiently long solvent annealing times, THF vapor considerably swells both the PS and the P4VP blocks of the template, which results in a collapse of the micellar arrangement (figure 7.12 - 48 hours of solvent annealing). With time, both the blocks attain sufficient mobility. Thus, big clusters of ZnO are formed. Also, for the calcined film after 48 hours of solvent annealing, a distorted nano grid of ZnO, as observed from the SEM images is present underneath the big ZnO clusters. This indicates that the solvent affects the top part of the film first and then gradually penetrates the rest of the film as shown for many other solvent annealing studies.

7.2.3. Results & discussion

Solvent annealing is a simple and efficient strategy to control the length scales of a nanostructured film. It promotes the advantage of preserving the thin film morphology for a given time frame, as compared with other techniques [209, 228]. The exclusive ZnO nano grid-like morphology obtained via sol-gel synthesis, is treated with chloroform and THF vapor in order to tune the pore size of these nanostructures. Depending on the kinetics of the interaction of the polymer to the solvent vapor, the structural reorganizations in the volume of the film is successfully probed by the combined investigations using real- and reciprocal-space imaging methods.

For annealing using chloroform vapor, a fast response time of the polymer is noticed. This is explained by the fact that $CHCl_3$ has equally good selectivity towards both the blocks of the copolymer due to which, the $CHCl_3$ vapor reduces the interfacial energy between the two blocks. This leads to swelling of both blocks and disruption of the micellar structures produced during the sol-gel synthesis process. Moreover, ZnO precursor particles present in the P4VP blocks also get affected by this structural arrangements and thereby start loosing the highly ordered grid-like network already after 4 hours of annealing. Finally, the interaction of the solvent vapor with the polymer chains increases which result in random distribution of the ZAD particles in the film. This is why they tend to form aggregates with a reduced porosity towards a longer chloroform annealing time of 12 hours. The change in the morphology observed by SEM is also supported by GISAXS measurements probing the morphology in the volume of the films. The results obtained are also in good agreement with the variation in morphology of thin films containing P(S-*b*-4VP) template loaded with PDP molecules, studied by Zoelen et al. [211]. They have

thermodynamically explained the swelling behavior of the block copolymer template in the presence of a non-selective solvent. It has been shown that in case of non-preferential swelling, the effective interaction parameter of the template decreases as the difference in the interaction parameters of any of the two blocks with the solvent is negligible. This leads an ordered system to transform into a disordered one, as is observed for the nano grid-like morphology in the present investigation [211].

Solvent annealing of the same ZnO nano grid-like morphology using THF has shown that the morphology remains intact for longer solvent annealing times. Additionally, the desired tuneability of the pore sizes is achieved. The increase in the average pore size is around 37 % after 48 hours of solvent annealing. The success of using THF vapor for tuning the pore size of the nano grid is again explained by a slightly better selectivity of the solvent towards the PS block of the polymer template. For a longer THF annealing time of 48 hours, the grid-like morphology gets disrupted and the high order is lost. Instead, large ZnO clusters are produced, which is attributed to the intermicellar fusion. In addition to the large ZnO clusters, a distorted grid is also present. Similar investigations on variations in morphological orientation of P(S-*b*-4VP) template in combination with PDP molecules is studied by Huang et al. and have reported a preferential parallel orientation of the microdomains with respect to the substrates, when oxygen-containing solvents such as THF are used for annealing the films [210]. However, this is not observed in the present case due to different film thickness and also different interaction of the ZAD molecules with the P4VP block.

In conclusion, the solvent annealing method is shown to be successful in providing additional flexibility to the length scales of a desired morphology without any aggressive treatment to the system, such as high temperature treatment, which might alter the desired morphology of the films. The thorough investigation of the structural evolution via SEM, AFM and GISAXS indicates that the selectivity of the solvent towards different blocks of the copolymer plays an important role in tuning the length scales along with the solvent annealing time. This strategy seems competent to be extended to other inorganic metal oxides in order to tune the length scales or orientation of the nanostructures. Also, exploring other solvents and time scales can establish suitable routines to alter the length scales of the nanostructures in accordance to the needs.

7.3. Spray-deposited nanostructures using high molecular weight P(S-*b*-4VP)

A high molecular weight P(S-*b*-4VP) is explored in the present section to synthesize ZnO nanostructures via the spray deposition route. Details about the polydispersity and molecular weights of the different blocks of the copolymer are provided in table 4.1. Via spray deposition, the common challenge regarding low thickness of the spin-coated films is overcome. In addition, the films obtained via spray deposition (see section 4.2.2) show high surface area due to the surface roughness caused by the impact of the droplets on the substrate.

ZnO nanostructures synthesized in the present chapter are directly applied as active layers in dye-sensitized solar cells. The sol-gel approach (as described in section 4.2.1) is used for the synthesis of sol-gel solutions. For all the sol-gel solutions used during the entire study, the concentration of the polymer is fixed to 15 mg mL^{-1}. The weight fraction combinations of the different constituents in the sol-gel is chosen as $w_{DMF} : w_{H_2O} : w_{ZAD} = 0.82 : 0.16 : 0.02$. The standard spraying parameters are used as noted in section 4.2.2. For all the films discussed in this section, three subsequent spray shots are delivered on the same substrate, with a 5 s waiting time in between and without any intermediate calcination step. The temperature of the substrates during the deposition is varied from 80 °C to 160 °C in steps of 20 °C. Afterwards, all the sprayed films are calcined at 400 °C for 30 minutes with a heating ramp of 5.78 °C min^{-1}. The effect of different substrate temperatures during the deposition of inorganic metal oxides or organic polymers on the morphology of as well as crystalline phases obtained in the films have been previously reported [229–231]. Therefore, optimizing the deposition temperature plays an important role in deciding the final performance of the device. In the present section, the impact of different substrate temperatures during spray deposition of the sol-gel solution mentioned above, on the morphology of the final ZnO nanostructured films is studied along with the performance of these films as active layers in dye-sensitized solar cells. For this purpose, a temperature range including values both below and above the boiling point of the major solvent present in the sol-gel solution (DMF in the present case with a boiling point of 154 °C), is chosen.

7.3.1. Structural characterization

The morphology of the films sprayed at different temperatures are investigated by scanning electron microscopy (SEM). In addition, the thickness of the films is also measured by DEKTAK height profilometry. Along with the morphology and film thickness, the

crystallinity of the films is also an important factor for acquiring suitable efficiencies in dye-sensitized solar cells. Hence, the crystallinity of all the films is studied via XRD.

Film morphology

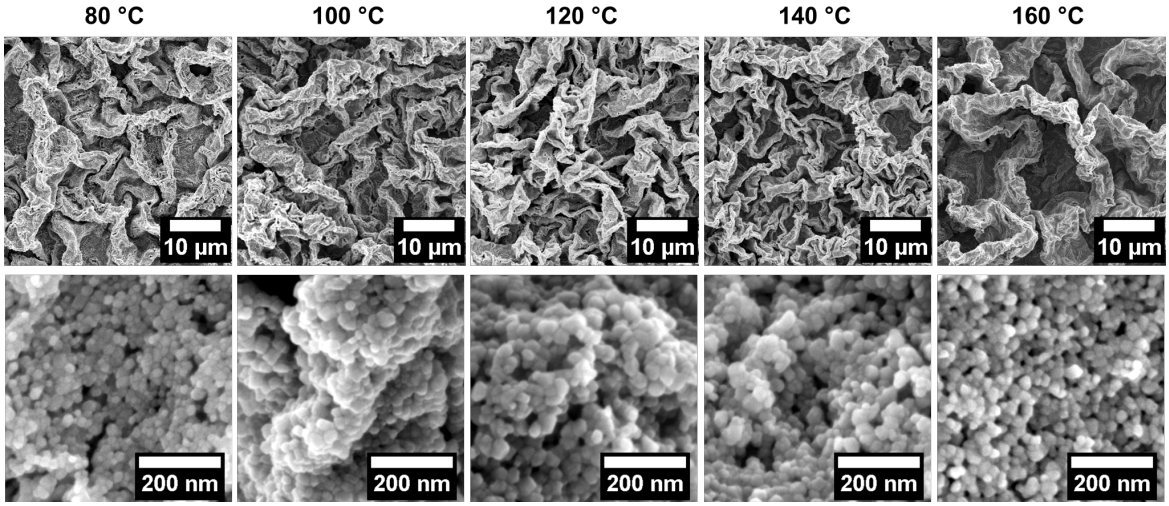

Figure 7.13.: SEM topography images of the spray-deposited ZnO nanostructures obtained on substrates heated to different temperatures as indicated. Top and bottom rows depict images taken under 1 k× and 80 k× magnifications, respectively.

Figure 7.13 shows the SEM topography images (under low and high magnifications) of all the spray-deposited films after calcination obtained at different substrate temperatures. For all the films, the wavy surface of the films is visible, which indicates a high roughness, and in turn a high surface area as compared to the spin-coated films, discussed before. From the SEM images under low magnifications (figure 7.13 - top row), it is evident that the density of the surface modulations decreases with an increasing temperature of the substrate. This observation is explained by the model governing the deposition depending on the substrate temperature, as described in details in section 4.2.2. At lower substrate temperatures, the droplet spreads on the surface after landing due to the presence of the solvent (boiling point of the solvent DMF = 154 °C). Afterwards, the solvent evaporates gradually, during which, it drags some of the components in the sol-gel (polymer with ZAD molecules) along with it to the surface. Even at these low temperatures, e.g., 80 °C, the evaporation of the solvent is rather quick, which does not allow for an arrangement of the deposited material to attain equilibrium morphology. Hence, the material which gets dragged on the surface during the evaporation of the solvent, stays there, producing the wavy modulations as observed from the SEM images (figure 7.13 - top row). With further increase of the substrate temperature, the evaporation of the solvent is accelerated. Thus,

for spray deposition on substrates kept at a temperature higher than the boiling point of the solvent, faster kinetics are involved during film formation as compared to the films obtained at temperatures chosen below the boiling point of the solvent. For the films obtained at 160 °C, depending on the size of the incoming droplets, for the relatively small droplets reaching the substrate, the solvent is already evaporated. As a result, only the polymer with ZAD nanoparticles land on the substrate. Whereas, for big droplets, the residual solvent reaches the substrate and dries within a short time, during the course of which, the modulations on the film surface appear again (figure 7.13 - top row).

However, despite the variation of the surface modulations for different substrate temperatures, all the films show a spherical granular morphology in SEM under high magnification (figure 7.13 - bottom row). A dense packing of these spherical granules is observed with an average granule diameter of (28 ± 7) nm.

Film thickness

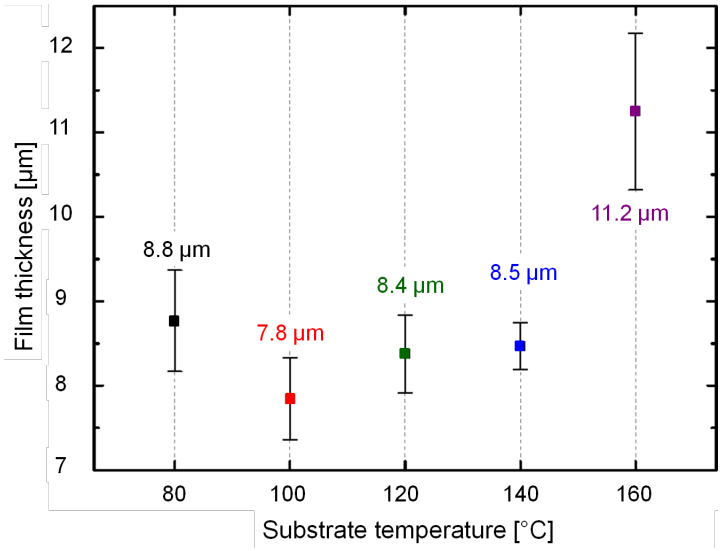

Figure 7.14.: Thickness of the films obtained via spray deposition on substrates heated to 80 °C, 100 °C, 120 °C, 140 °C & 160 °C. The values over the data points are the values of the corresponding film thicknesses.

Figure 7.14 summarizes the thickness of all the films obtained after deposition on substrates at different temperatures, as indicated in the plot. It should be noted that the same volume of sol-gel solution is sprayed for all the films. The films obtained at substrate temperature of 80 °C to 140 °C nearly show similar film thickness, in the range of 8 µm. However, for the film deposited on a substrate maintained at a relatively high temperature of 160 °C, a higher film thickness of 11.2 µm is achieved. This is explained

by the time for which the solvent resides in the incoming droplets and in the deposited material, depending on the temperature of the substrate. For 160 °C, the evaporation of solvent present in the droplets arriving the substrate is fast, due to which, mainly the polymer with the ZAD nanoparticles are deposited on the substrate. In the subsequent shots, similar phenomenon occurs and results in an effective increase in the film thickness. However, for the films, which are deposited on substrates, kept at temperatures lower than 160 °C, the solvent present in the incoming droplets evaporates slower as compared to the films deposited on substrates at 160 °C. As a consequence, each fresh spray shot tends to partially dissolve the pre-deposited film underneath due to longer residual time of the solvent in the sprayed droplets and the deposited material. As such the increase in the film thickness is not as efficient as for films deposited on a substrate with a temperature higher than the boiling point of the solvent (160 °C for the present case).

Crystallinity

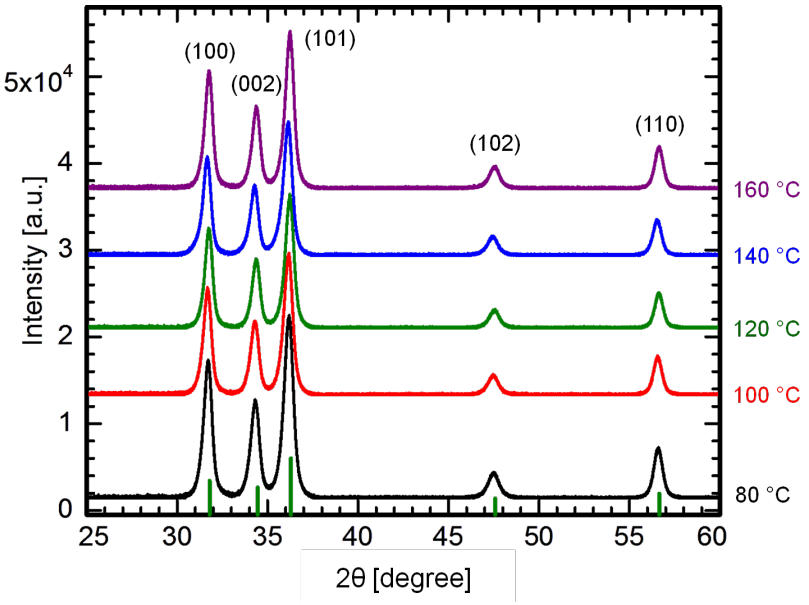

Figure 7.15.: XRD patterns of the ZnO films sprayed on substrates heated to different temperatures, as indicated to the right of the graph. The vertical green lines at the bottom axis are the theoretical peak positions with their relative intensities for wurtzite ZnO, as obtained from JCPDS database, card no. 36-1451. The Miller indices are indicated exemplarily for all the curves.

The crystallinity of the spray-deposited ZnO films plays a crucial role in efficient functioning of dye-sensitized solar cells investigated in the present work. In order to use the

spray-deposited films directly as active layers in dye-sensitized solar cells, they are subjected to calcination at 400 °C. XRD patterns (measured using XRD instrument II, see section 3.1.4) for all these films are shown in figure 7.15. The peak positions observed in the measured diffraction pattern for all the films resembles the theoretical peak positions for wurtzite crystalline phase of ZnO.

substrate temperature	80 °C	100 °C	120 °C	140 °C	160 °C
crystallite size [nm]	14.2 ± 1.1	14.8 ± 1.1	15.4 ± 1.1	15.1 ± 1.1	15.2 ± 1.2

Table 7.2.: Summary of crystallite sizes obtained as an average of all the diffraction peaks for the ZnO nanostructures heated to different temperatures as mentioned in the top row. The error bar for each value is the standard deviation from all the diffraction peaks obtained for individual films as reported in figure 7.15.

The average crystallite size calculated for each film from the Scherrer equation (section 2.4.1) is listed in table 7.2. An average crystallite size of 15 nm is observed for all the spray-deposited films after calcination. The similar crystallite sizes for all the films is also in good agreement with the SEM investigations, where all the films show identical granular nanoscale morphology.

7.3.2. Optical properties

Figure 7.16(a) shows absorption spectra of all the spray-deposited films obtained at different substrate temperatures, measured using UV/Vis instrument II (see section 3.2.1). Before the measurements are performed, all films are calcined at 400 °C in order to obtain pure ZnO crystalline phase. As seen from the plot, all films show very low absorption in the visible range and attain an absorption maximum at 375 nm, which typically corresponds to the absorption reported for the wurtzite ZnO crystalline phase. The absorption for all films stay high as seen from the plateau in the plot over the measured UV range. This phenomenon is attributed to the direct electronic transitions from the valence band to the conduction band. The band gap of the films is calculated by the Tauc equation for direct band gap semiconductors, as detailed in section 3.2.1. Exemplary Tauc plot for the film deposited on the substrate at 120 °C is shown in figure 7.16(b). The individual band gap acquired for each film is listed in table 7.3.

The obtained band gap for ZnO is slightly lower than that of the bulk crystalline wurtzite phase of ZnO (3.3 eV). Depending on the preparation methods, the band gaps of single and polycrystalline ZnO has shown several band gap energies in the range of 3.1

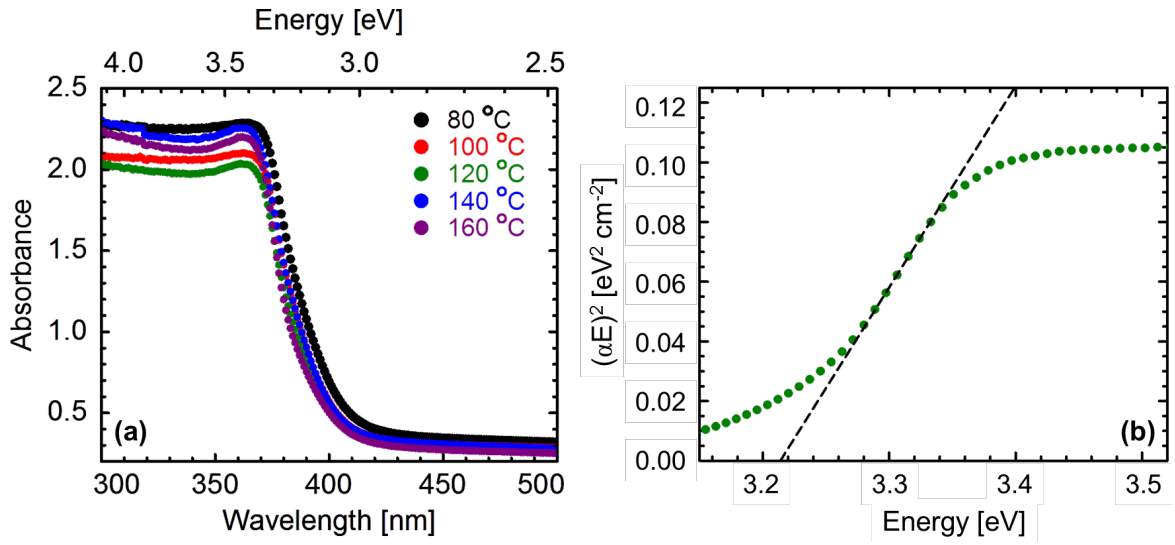

Figure 7.16.: (a) Absorption spectra of the ZnO nanostructured spray-deposited films on substrates maintained at different temperatures, plotted in the spectral range of 300 to 500 nm. (b) Exemplary Tauc plot for the ZnO film deposited on a substrate heated to 120 °C. Linear extrapolation of the data to the energy axis reveals the band gap of the material.

to 3.3 eV [114, 232]. This lowering of the bang gap energy is often explained in literature by the presence of intrinsic donor levels, present under the conduction band of ZnO. The density of these donor levels vary, depending on the synthesis and deposition of the material and under certain circumstances, might dominate the absorption spectrum. The origin of such donor levels is attributed to the intrinsic defects in ZnO crystalline lattice, such as oxygen vacancies and zinc interstitials [83,233]. From the band gaps calculated for the present films, it is noteworthy that this increases with the temperature of the substrate maintained during the deposition. The band gap energy of 3.24 eV obtained for the film deposited on the substrate at 160 °C is very close to that reported for bulk crystalline ZnO. Hence, this shows that the substrate temperature during the spray deposition of

substrate temperature	80 °C	100 °C	120 °C	140 °C	160 °C
band gap [eV]	3.18 ± 0.01	3.20 ± 0.01	3.21 ± 0.01	3.21 ± 0.01	3.24 ± 0.01

Table 7.3.: Band gap energies extracted from the UV/Vis measurements shown in figure 7.16, for ZnO nanostructured films, heated at different temperatures as mentioned in the top row.

ZnO nanostructures influences the defect levels in the film and thereby, manipulates the band gap of the deposited material.

7.3.3. Solar cell performance

Dye-sensitized solar cells are fabricated with all the films deposited at different substrate temperatures, using the device assembly protocol as illustrated in section 4.2.3. A compact ZnO blocking layer (refer to section 4.2.3 for preparation details) is pre-deposited and calcined for each cell before the deposition of the active layer, under different temperatures. The measured I/V-curves obtained for all the DSSCs are shown in figure 7.17. For a clear overview of the performance shown by each cell, the I/V characteristics are listed in table 7.4.

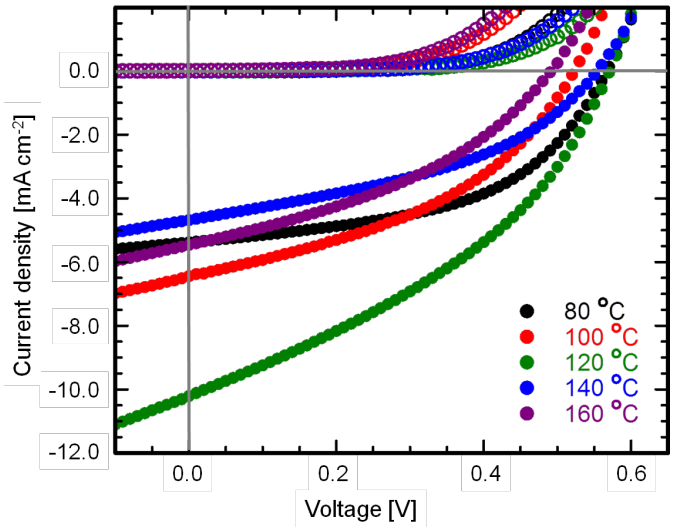

Figure 7.17.: I/V-curves of DSSCs fabricated from spray-deposited ZnO nanostructured films on substrates heated to different temperatures. The open and the closed circles correspond to the measurements performed in the dark and under AM1.5 simulated solar spectrum conditions.

All the devices show successful solar cell characteristics. Surprisingly, the solar cell prepared with the ZnO active layer deposited at a substrate temperature of 160 °C shows the worst performance amongst all the devices, despite having the thickest active layer (see table 7.4). This behavior is attributed to the worst V_{OC} of the cell (see figure 7.17), which indicates possibly higher recombination of the charge carriers in the film. This can be related to the longer pathways that the charges need to travel in order to reach the FTO electrode.

substrate temperature	I_{SC} [mA/cm^2]	V_{OC} [V]	FF [%]	η [%]
80 °C	-5.38	0.57	51.65	1.54
100 °C	-6.45	0.52	42.35	1.39
120 °C	-10.21	0.57	38.34	2.18
140 °C	-4.68	0.55	42.01	1.06
160 °C	-5.46	0.49	38.85	1.02

Table 7.4.: I/V characteristics of the DSSCs obtained from ZnO nanostructured films deposited on substrates at different temperatures as noted under the first column. The parameters are obtained from analyzing the I/V-curves shown in figure 7.17.

On the other hand, the ZnO active layer deposited on a substrate heated to 120 °C, shows the best performance, with a promising short-circuit current density (I_{SC}) of 10.21 mA cm^{-2}. This is comparable to some of the most successful DSSCs employing ZnO as the active layer [234, 235]. The overall performance of the device is limited by the poor fill factor (FF). The loss in FF is mainly assigned to the decreased shunt resistance in the device indicating a reduction in the leakage current [236]. This shows the effect of different deposition temperatures on the morphology of the device, which significantly influence the final performance of the device.

7.3.4. Results & discussion

Morphology and film thickness of ZnO nanostructured films are investigated via the spray deposition method. The uniqueness of the study lies in the fact that spray-deposited ZnO nanostructures are studied for the first time using a sol-gel solution prepared with P(S-*b*-4VP) copolymer, serving as the structure-directing template and ZAD as the ZnO precursor. Spray deposition of ZnO nanostructures from different precursors have been already studied, mostly on substrates heated to different temperatures. For most of the reported investigations, the substrates are maintained at temperatures of 200 °C or above in order to ensure the deposition of pure ZnO particles on the substrate and also, to allow for an efficient increase in the film thickness with a relatively low quantity of material [229, 230]. In the present study, a direct influence of the substrate temperatures chosen during spray deposition on the film morphology, film thickness and device performance is reported.

For the present investigations, the temperatures of the substrates are kept below 200 °C. This shows an additional possibility to redissolve a pre-deposited film by subsequent spray

coats. This in turn gives rise to the formation of diffused interfaces between the consecutively sprayed films on the same substrate. As such, the increase in film thickness is not that drastic depending on the number of spray shots applied. However, this shortcoming is compensated by the improved connection obtained between the films, which is suitable to provide continuous charge carrier pathways for applications in DSSCs. Nevertheless, the trend observed of an increase in the film thickness for high temperature of the substrates is in accordance with literature [237]. Not only the film thickness and the interfacial connections between different films are tuned by spray deposition of the sol-gel on substrates at different temperatures, but also the overall morphology of the film is affected. A more detailed study on the film morphology has revealed that all the films are composed of granular nanostructures closely connected together. From the investigations regarding the crystallinity and the optical properties of the calcined films, it is shown that wurtzite phase of ZnO is present.

A successful application of the ZnO nanostructured films as active layers in DSSCs has been shown. Better device performances at deposition temperature lower than the boiling point of the solvent also confirms that the diffused interfaces between multiple films allow for an efficient charge transport in the final solar cell. The maximum power conversion efficiency is achieved from the DSSC which has a ZnO active layer, spray-deposited on a substrate heated at 120 °C. The highest power conversion efficiency obtained is 2.18 % for the presented study. The highest reported power conversion efficiency obtained for spray-deposited ZnO-based DSSCs is above 7.5 % [14]. However, for these cells, unlike the present investigation, commercial nanoparticles are used. The present research provides suitable opportunities to be expanded to other, more robust systems such as titania (TiO_2) or composite ZnO-TiO_2 nanostructures synthesized via sol-gel approach.

7.4. Summary

The strength of the template-assisted sol-gel routine to synthesize ZnO nanostructures is established using yet another diblock copolymer template, P(S-*b*-4VP) in the present chapter. The use of the present polymer produces an ordered and unique ZnO nano grid-like morphology. The long range order present in the films showing this morphology is lost after the calcination step. However, an improvement in ordering of the nanostructures along the plane perpendicular to the substrate surface is gained, as observed via GISAXS measurements. Different compositions of the sol-gel solutions are studied, showing a decrease of ordering of the nano grid-like morphology with increasing weight fraction of the precursor in the system. Optical characterization of the films reveals their promising photoluminescence behavior. Thus, with reference to the results obtained from chapter 6,

it is clear that different nano morphologies and length scales can be achieved using varied diblock copolymer templates via the sol-gel route. At the same time, due to limited scope of tuning the length scales of the grid-like morphology imposed by the copolymer template used, an alternative way to tune the pore size of the nano grid is successfully investigated via solvent vapor treatment of the ZnO-polymer hybrid films. Selective as well as non-selective (towards the different blocks of the copolymer) solvents are used for manipulating the pore size of the nano grid. The change in the pore size as a function of different solvent annealing times is fruitfully quantified by GISAXS measurements. Chloroform, being a good solvent for both the blocks, equally swells the entire polymer chain due to which, the ordered pattern of the nano grid is disrupted. On the other hand, THF selectively swells the pores of the nano grid-like structures, which is the PS block and thereby preserves the morphology for a long time. A successful increase in the average pore size of the films is established via THF vapor treatment. These modifications in the length scales induced via solvent annealing to the ZnO-polymer hybrid films, are also translated to the films after their subsequent calcination to remove the polymer template, allowing for fine-tuning of the pore size to tailor the structure to meet the needs for a specific application.

Thicker ZnO nanostructured films are produced via spray deposition method. A good control over the film morphology and thickness is established via different substrate temperatures while spraying. All the films essentially show granular morphology on the nanoscale. The film deposited at the highest substrate temperature shows the highest film thickness and the lowest surface roughness. The films obtained at substrate temperatures below the boiling point of the solvent present in the sol-gel solution that is sprayed, show similar thicknesses to one another. The spray-deposited films show reasonably good performance as active layers in DSSCs. In summary, the substrate temperature shows a significant influence on the film morphology, thickness and the interfacial connection between the films for subsequent spray depositions on the same substrate. All these factors also show their signature in the final output given by the DSSCs. Lastly, the active layer deposited at 120 °C shows the best power conversion efficiency.

8. ZnO-TiO_2 nanocomposites

A substantial momentum gained towards the development of ordered nanostructures from inorganic metal oxides has resulted in a huge development in upgrading the nanotechnology, mainly in the field of sensing, drug delivery, photocatalysis, energy storage and conversion [238–241]. All these applications depend on the extraordinary structural and electronic properties that are imparted with advanced material engineering of the metal oxides. Among the wide range of inorganic metal oxides, the two materials that have gained the most interest in scientific research are titanium dioxide, commonly known as titania (TiO_2) and zinc oxide (ZnO) [242]. The structural design to tune the physical and chemical properties of the metal oxides is not restricted to the pure materials, but has also been extended to binary/ternary nanocomposites, compounds and alloys of different inorganic metal oxides for example TiO_2-SiO_2, TiO_2-MoO_3, TiO_3-WO_3, ZnO-Al_2O_3 and ZnO-TiO_2 [243, 244]. The tremendous demand for nanoscale devices in the recent decades requires a larger variety of materials. Production of complex functional nanomaterials as the combination of different materials, is an efficient way to cover a wider horizon of required properties in order to improve the technology specializing in nanoscale opto-electronics. Hence, the last chapter of the present thesis contributes towards the development of a compound of ZnO and TiO_2 and to study its structural, optical and electronic properties.

As reported in literature, the simultaneous synthesis of ZnO-TiO_2 nanocomposites gives rise to three different compounds and some minor impurities [245]. These three compounds are: zinc orthotitanate (Zn_2TiO_4) with a cubic spinel structure, $Zn_2Ti_3O_8$ with a cubic defect spinel structure and zinc metatitanate ($ZnTiO_3$) with a rhombohedral ilmenite structure. The minor impurity phases consist of rutile TiO_2 or ZnO. $Zn_2Ti_3O_8$ is a metastable form of $ZnTiO_3$ and is known to occur at temperatures lower than 800 °C, whereas, $ZnTiO_3$ is well-known to decompose to Zn_2TiO_4 and rutile TiO_2 at temperatures above 945 °C [245]. Hence, the production of a pure compound is a challenge resulting from the temperature requirements. Most of the compounds synthesized in mixed phases have been widely used in paints and pigments industries so far. Among the three reported common compounds, zinc orthotitanate (Zn_2TiO_4) is studied in the present work due to its high-potential for several applications. Zn_2TiO_4 has been established as one of the

most important regenerable photocatalysts, additionally showing wide-scale applications in the removal of sulfur during coal gasification, photocatalytic splitting of water and degradation of organic compounds, as an active anode material in Li-ion batteries and microwave dielectrics [245, 246]. All these successful applications arise from promising electrical and optical properties of the zinc orthotitanate phase. Hence, in the present chapter, Zn_2TiO_4 is developed towards the applications in photovoltaics, more precisely as the active layer in dye-sensitized solar cells (DSSCs).

The most common technique reported in literature to synthesize Zn_2TiO_4 is the direct solid-state route employing a high temperature of 1000 °C [245]. Other methods producing pure and mixed phases of Zn_2TiO_4 involve metal-organic chemical vapor deposition [247], ball milling [248, 249], sol-electrospinning [250] and synthesis using inorganic metal oxide templates via sputtering [251]. However, most of these techniques face the problems of using high energy-consuming instruments as input and the lack of tuneability of the nanostructures produced as output in terms of their length scales. Although a few morphologies of zinc orthotitanate are proclaimed, such as nanorods, twinned nanowires [251], fibres [250] and nanocrystalline powders [252], a thorough investigation about the possible nanomorphologies is still lacking, which is crucial for final device applications in DSSCs. In order to meet these challenges, the block copolymer template-assisted sol-gel synthesis, which is a well-established route for the development of multiple morphologies in pure TiO_2 and ZnO systems, is applied for the present study. The high molecular weight diblock copolymer poly(styrene-*b*-ethylene oxide) (P(S-*b*-EO)), as used in section 6.2 for the synthesis of pure ZnO nanostructures, is employed as the template for the present system. Thereby, a series of complex morphologies is synthesized using two different precursors, each for ZnO and TiO_2. The variation in the final morphology is studied as a function of different volume fraction compositions of zinc acetate dihydrate (ZAD; commercially available ZnO precursor) and ethylene glycol-modified titanate (EGMT; custom-synthesized[1] TiO_2 precursor). The major advantages provided by this approach involve the ability to obtain multiple morphologies using the same copolymer template and the flexibility to tune the length scales of the nanostructures at the same time for a specific need.

Since, the synthesis route is solution based as discussed in section 4.2.1, mixing of the individually synthesized nanostructures in the solution might seem feasible, however, to produce a single ternary compound phase is challenging. In order to ensure the formation of a single phase in the end, different series of morphologies are prepared under different calcination temperatures. Hence, the present study gives a clear overview of various

[1]synthesized by Thomas Fröschl, group of Prof. Nicola Hüsing, Paris-Lodron University Salzburg, Hellbrunnerstr. 34, 5020 Salzburg, Austria

morphologies of different combinations of ZnO-TiO_2 nanocomoposite films. In addition to a suitable morphology including favorable length scales for applications in DSSCs, an appropriate film thickness is also essential in order to ensure sufficient light absorption. A commercial approach to achieve the desired film thickness is spray deposition of the final solution on pre-cleaned substrates. The spray-deposited film is then calcined afterwards to remove the polymer template and to obtain crystalline phases in the film, essential for charge transport in DSSCs.

A series of eleven different spray-deposited films is produced, which are then analyzed by scanning electron microscopy (SEM) for surface morphology investigation. The crystallinity of all the films is studied by x-ray diffraction (XRD) method. In addition, the surface composition of selected films is characterized using energy-dispersive x-ray spectroscopy (EDX) (section 8.1.1). The optical properties of all the films are investigated via UV/Vis spectroscopy (section 8.1.2) and finally selected films are incorporated as an active layer in DSSCs. The performance of the DSSCs is discussed in section 8.1.3. Sections 8.1.4 and 8.2 give the results obtained and the summary from the entire study respectively. Parts of the experiments were performed together with Erik Braden and are published in the masters' thesis of Erik Braden [253].

8.1. Spray deposition of ZnO-TiO_2 nanocomposite films

The sol-gel solutions for ZnO and TiO_2 are prepared separately as described in section 4.2.1, using different weight fractions of the constituents. For the ZnO sol-gel, $w_{DMF} : w_{H_2O} : w_{ZAD}$ is chosen to be $0.92 : 0.005 : 0.075$, which corresponds to the composition D as discussed in section 6.2. In order to keep the volume of the titania precursor (EGMT) equal to that of ZnO precursor (ZAD) in the final sol-gel, a different weight fraction combination of the ingredients for TiO_2 sol-gel is chosen, $w_{DMF} : w_{HCl} : w_{EGMT} = 0.905 : 0.08125 : 0.01375$. The compositions of both sol-gel solutions are kept constant for all the films synthesized in the present section, along with the diblock copolymer template (P(S-*b*-EO)) concentration (15 mg mL^{-1}). However, the volume ratio of the two sol-gels are varied in order to obtain a mixed sol-gel as the final product. The different combination of volume fractions are listed in table 8.1. As seen from the table, the volume percent of ZnO sol-gel is varied from 100 % to 0 % in steps of 10 % in the final sol-gel solution. Hence, a series of eleven different sol-gel solutions with varied compositions are prepared which are then spray-deposited on pre-cleaned substrates as graphically illustrated in figure 8.1. Three kinds of substrates are used throughout the study. Silicon substrates are used for structural characterization of the films by SEM, XRD and EDX. Plain glass substrates are used for optical characterization (UV/Vis spectroscopy) and

FTO substrates are used for the fabrication of dye-sensitized solar cells, DSSCs (I/V characterization). The specifications and cleaning procedures of all the substrates are provided in section 4.2.2.

sol-gel composition	volume ratio ZnO : TiO_2	ZAD [mol/L]	EGMT [mol/L]	molar ratio ZAD : EGMT
I	10 : 0	0.3527	0.0	pure ZnO sol-gel
II	9 : 1	0.3174	0.0084	37.92 : 1
III	8 : 2	0.2821	0.0251	16.86 : 1
IV	7 : 3	0.2468	0.03	9.82 : 1
V	6 : 4	0.2116	0.0335	6.32 : 1
VI	5 : 5	0.1763	0.0419	4.21 : 1
VII	4 : 6	0.1411	0.0502	2.81 : 1
VIII	3 : 7	0.1058	0.0586	1.81 : 1
IX	2 : 8	0.0705	0.0670	1.05 : 1
X	1 : 9	0.0353	0.0753	0.47 : 1
XI	0 : 10	0.0	0.0837	pure TiO_2 sol-gel

Table 8.1.: Overview of the different sol-gel compositions (1^{st} column) with varying volume ratios (2^{nd} column) and molar concentrations (3^{rd} & 4^{th} column) of ZnO and TiO_2 precursors. The ratio of the molar concentrations of ZAD : EGMT in the final sol-gel solutions are listed in the last column.

The final sol-gel solutions obtained after the combination of individual ZnO and TiO_2 sol-gels (figures 8.1(a) and (b)), are spray-deposited as shown in figures 8.1(c) and (d). The standard parameters used for spray deposition are given in section 4.2.2. For the structural and optical characterization, 500 µL of each sol-gel is spray-deposited using 10 s spray shots with a waiting time of 5 s between two subsequent sprays. For the DSSCs, a thicker film is essential which is obtained by spray deposition of 5 to 10 mL sol-gel solution on a single substrate (figure 8.1(e)). All the spray-deposited films are annealed on a heating plate at 80 °C for at least 15 minutes. The temperature and humidity for all the steps involved is controlled (temperature: 20 to 24 °C; relative humidity: 34 to 41 %). Afterwards, all the films are calcined in air at 400 and 600 °C with a heating ramp of 5.78 °C min^{-1} in order to obtain ZnO-TiO_2 nanocomposite structures (figure 8.1(f)). It should be noted that the different sol-gel mixtures result in the synthesis of different phases. In general, all the mixed phases obtained in the present study are termed as nanocomposites. This is due to the fact that along with the mixed phases, parts of pure

ZnO phase is also obtained for certain compositions. However, the aim of the study is to establish a compound of ZnO and TiO_2, where the pure ZnO and TiO_2 phases do not exist anymore. For the thick films prepared via spray deposition of 10 mL of sol-gel for applications in DSSC, a slower heating ramp of 2.5 °C min^{-1} is used to avoid peeling-off or cracking of the films.

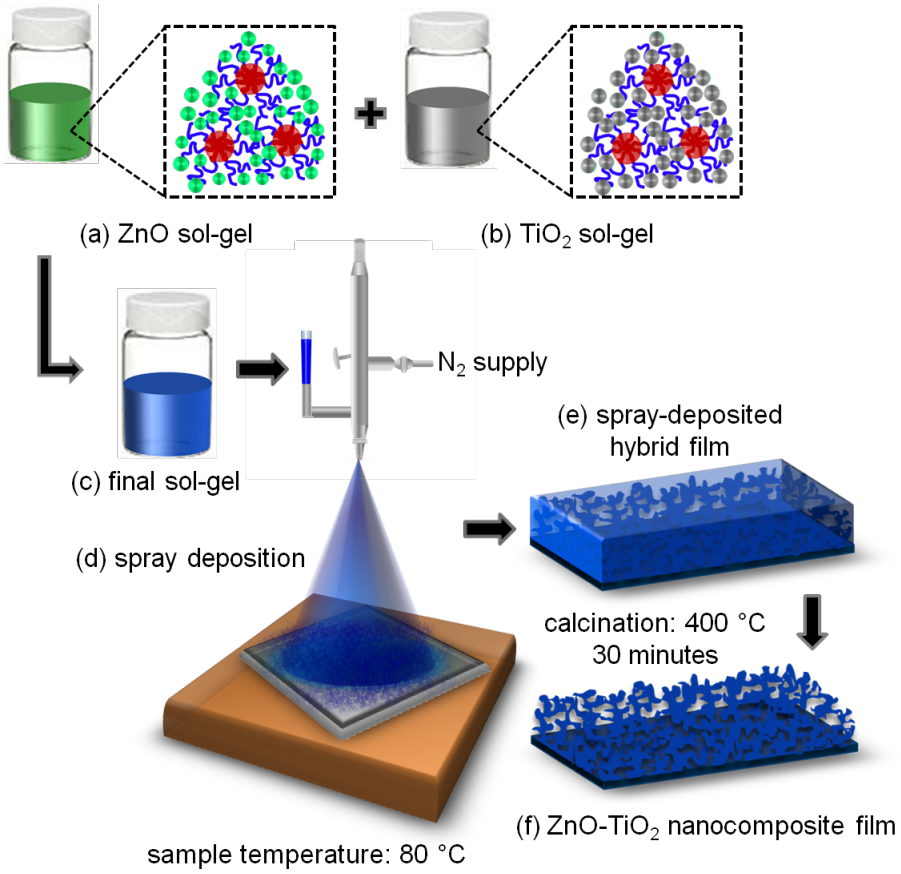

Figure 8.1.: Schematic illustration of the steps involved in the synthesis of nanocomposite films using different mixing ratios of pure ZnO and TiO_2 sol-gel solutions. A high molecular weight P(S-*b*-EO) is used as the structure-directing template in the sol-gel synthesis. The polymeric micelles are represented by red cores formed from the PS block and blue coronas composed of the PEO chains. (a) Preparation of ZnO sol-gel solution using ZAD as the precursor (green spheres). (b) Preparation of titania sol-gel solution using EGMT as the precursor (gray spheres). (c) Mixing the two solutions together in the required volume ratio to obtain the final sol-gel solution. (d) Spray deposition of the final sol-gel solution using nitrogen as the carrier gas on a heated substrate. (e) Spray-deposited hybrid film. (f) Final calcination step to remove the polymer template yielding pure nanostructured film with mixed ZnO-TiO_2 phases or a single compound phase.

8.1.1. Structural characterization

All the calcined films produced by using the different sol-gel compositions listed in table 8.1 are investigated by a series of different techniques in order to probe the morphology, crystallinity and the surface composition. The eleven different films are denoted analogous to the composition numbers depicted in the first column of table 8.1, throughout the text. A pure compound phase of ZnO and TiO_2, namely zinc orthotitanate (Zn_2TiO_4) is developed among the series of these eleven different sol-gel compositions. Since, the calcination temperature of the films has a huge impact on the final phases obtained in the films, two different temperatures are studied for the calcination of all the films: 400 °C and 600 °C. Hence, in total a set of twenty-two samples are characterized to obtain the pure zinc orthotitanate phase.

Structure and crystallinity investigation on spray-deposited films obtained after calcination at 400 °C

Figure 8.2 presents an overview of the surface topography of all the spray-deposited films obtained from different sol-gel compositions listed in table 8.1, after calcination at 400 °C.

The SEM topography images only provide a qualitative information about the nanostructures and hence, this method is not feasible to determine the different crystalline phases present in the films. Nonetheless, it is an important technique to investigate the surface morphology of the films which is one of the crucial parameters for efficient device functioning. As seen from figure 8.2, the bright regions depict the inorganic metal oxide and the darker regions correspond to the pores or cavities left behind after the removal of the diblock copolymer template. First of all, the templating effect of the copolymer is verified by the different morphologies obtained. Secondly, it is observed for the films obtained from sol-gel compositions I and II (figures 8.2) result in similar morphologies. The film surface is mainly dominated by the presence of spherical granular structures, which are also observed as the most common morphology obtained for the spray deposition of ZnO sol-gels, as discussed in chapter 5. The similar morphology in the present case is explained by the fact that the first two films of the series are obtained from sol-gel solutions with the highest ZAD concentrations (see table 8.1). The average diameter of the granules for both the films is found to vary in the range of 24 to 30 nm. This shows a narrow size distribution, meaning the presence of a dominant length scale in the nanostructures obtained. It is also evident from figure 8.2, that the surface morphology of the films obtained from sol-gel compositions X and XI are similar and consist of dense and porous regions. According to the film compositions, these films are rich in titania. The average size of the pores for both the films lies in the range of 39 to 44 nm, again

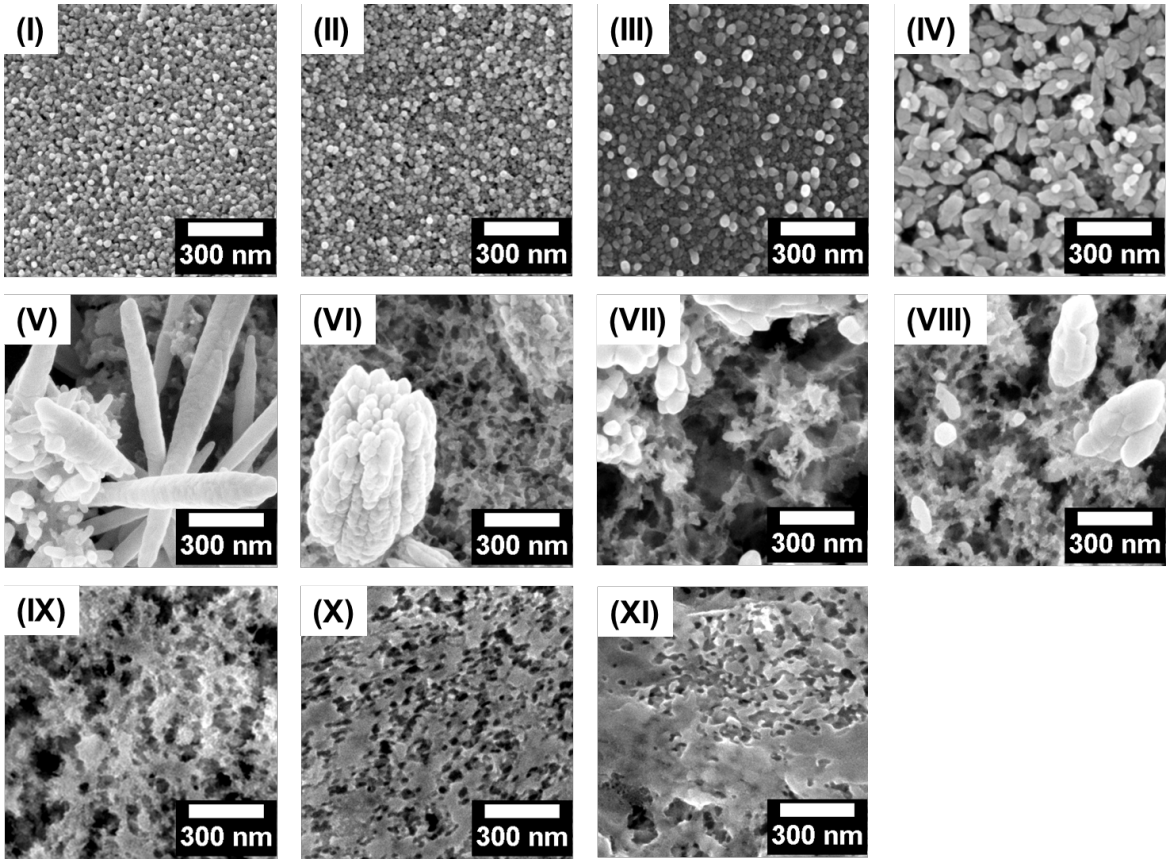

Figure 8.2.: SEM surface images of the spray-deposited films obtained from sol-gel compositions I to XI (as indicated, see table 8.1). The images are taken after calcination of the films at 400 °C.

showing a narrow distribution of length scale of the nanostructures. However, complex morphological changes take place for the films obtained from sol-gel compositions III to IX (figure 8.2).

The films obtained from compositions III-VIII have significantly higher molar concentrations of ZAD in the system as compared to EGMT. Hence, the morphologies obtained are expected to show strong seggregation of the two phases. This is explained by the fact that the large difference in the concentrations between the ZnO and the TiO_2 systems tends to drive the similar particles to cluster together which is energetically more favorable. The degree of clustering in turn affects the size of the nanostructures obtained. This hypothesis is proved by the SEM images of the corresponding films shown in figure 8.2III-VIII. All these films show the presence of large aggregates along with the presence of interconnected network structures, giving an impression of coexistence of two morphologies in the same film. Especially for films synthesized from sol-gel compositions III, V and VI (figure 8.2), the larger structures resembling nanorods, seem to have a preferred orientation perpendicular to the substrate. These upright structures are very small for

the film obtained from composition III, where they only appear as bright spots and have an average diameter of 38.6 nm. On the other hand, these larger structures for the films obtained from sol-gel compositions V and VI (figure 8.2), are significantly long and tilted with respect to the substrate. The larger aggregates observed for the films obtained from sol-gel compositions IV, VII and VIII (figure 8.2) ranges from 100 to 250 nm in length and do not appear to have any preferred orientation to the substrate unlike the films just discussed. An additional interconnected network morphology is prominent for the films obtained from sol-gel compositions VI, VII and VIII (figure 8.2) with a varied pore size in the range of 20 to 100 nm.

For the film obtained with composition IX (figure 8.2), multiple morphologies are not observed anymore. This is explained by the fact that the molar concentration of ZAD and EGMT are quite similar in this sol-gel (see table 8.1). The morphology appears like a foam with an average pore size of 38.25 nm.

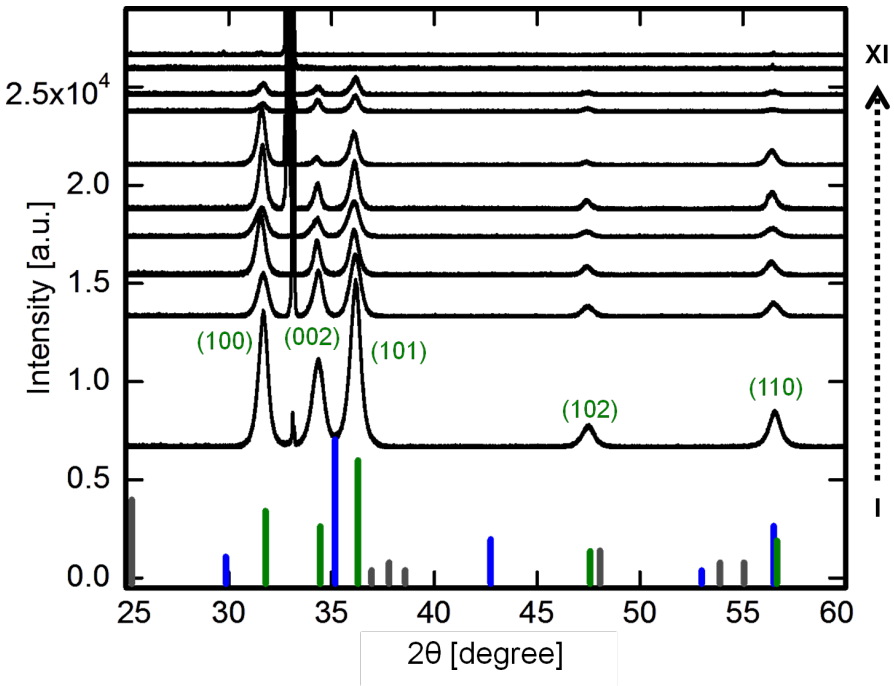

Figure 8.3.: XRD spectra of all spray-deposited films obtained from sol-gel compositions I to XI (table 8.1), plotted from bottom to top (as indicated by the dashed arrow) after calcination at 400 °C. The vertical lines at the bottom axis represent the theoretical peak positions with their relative intensities for wurtzite ZnO (green), anatase TiO_2 (gray) and Zn_2TiO_4 (blue). All the curves are shifted along the intensity axis for clarity. The lattice planes are indicated for the signal obtained from wurtzite ZnO.

At this stage, it is difficult to comment about the composition of the spherical granules, large clusters and the foam-like network visible for the films shown in figures 8.2I-XI.

Hence, to further explore the crystallinity and film compositions, x-ray diffraction (XRD) measurements are performed (using XRD instrument II) on all the above-mentioned films. As observed from the XRD spectra (figure 8.3), films prepared from the sol-gel compositions I to IX show peaks corresponding to the wurtzite crystalline phase of ZnO. No additional peak, either for titania or any other mixed phases is observed in the XRD spectra of any sample. The peak observed at $2\theta = 33°$ for all the films is related to the (100) lattice plane of silicon which is used as the substrate for the films. Even for the films prepared using the compositions X and XI, which contains the maximum molar concentration of EGMT in the system, no crystalline peak corresponding to anatase or rutile titania is observed. As the amount of titania present in the films with compositions II to XI is significant, the XRD investigation indicates the presence of titania in the films in amorphous phase. The same holds true for any other intermediate phases of ZnO-TiO_2 nanocomposite or Zn_2TiO_4. Due to the possible amorphous nature of these phases, no crystalline contribution are obtained in the XRD signals.

Additionally, the intensity of the peaks corresponding to wutzite ZnO is not constant for all the films. The most intense peaks are obtained for the pure ZnO film obtained from composition I (figure 8.3). The intensity of the peaks decreases afterwards for films obtained from compositions II to VI (figure 8.3). For the films obtained from compositions VII to IX, the intensity of the peaks decreases further till they become non-existent for the films prepared from compositions X and XI (figure 8.3). Decrease in intensity of the peaks is a clear indication of reduced crystallinity in the system. The lack of crystallinity in the films along with the complete absence of any crystalline phase for the pure TiO_2 film (composition XI), implies that the calcination temperature chosen in the present case might not be sufficient to attain crystallinity.

It is noted from the theoretical peak intensities plotted for wurtzite ZnO (figure 8.3), that the peak corresponding to (101) lattice plane is the most intense. However, the XRD signals obtained for the films prepared from compositions III, V and VI show the highest intensity for the peak related to the (100) lattice plane. Comparing this result with the SEM images of the same films as reported in figure 8.2III, V and VI, it is observed that these are the same films where the large clusters have indicated a preferred orientation with respect to the substrate in the morphology study. This suggests that the large clusters observed from the SEM images might be related to the crystalline ZnO phase in the system. This outcome can be extrapolated to all the other films where the preferred orientation is not visible via SEM, but large clusters still prevail. However, the presence of mixed amorphous phases in these large clusters cannot be ruled out completely. Hence, the complete analysis of the films via SEM and XRD suggests that the interconnected network-like nanostructured morphology visible in the films (specially for compositions

VI, VII and VIII, shown in figure 8.2, represents any mixed phase present in the system, with some probable inclusion of the amorphous TiO_2.

The average crystallite size for all the films are obtained from the average FWHM of all the diffraction peaks of the XRD spectra, using the Scherrer equation and are plotted in figure 8.4. A clear increase in the average crystallite size is observed for the films prepared from compositions I to VIII. This is in very good agreement with the conclusions drawn from the SEM images. For the film obtained from spray deposition of composition IX, the error bar associated with the measurement is very large which is attributed to the low intensity and broadening of the peaks obtained (figure 8.3). For the films obtained from compositions X and XI, no diffraction peak is obtained in the XRD spectrum and hence, the crystallite sizes for these two samples are not shown.

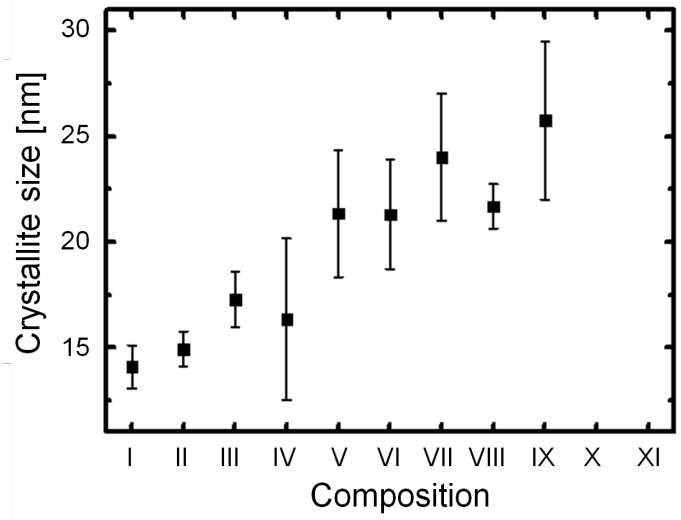

Figure 8.4.: Average crystallite sizes obtained for the spray-deposited films, calcined at 400 °C. The films are obtained from different sol-gel compositions as indicated in table 8.1. The error bars are the standard deviation of the sizes obtained from all the diffraction peaks obtained in figure 8.3.

Structure and crystallinity investigation on spray-deposited films obtained after calcination at 600 °C

The SEM surface images of the films spray-deposited from the different compositions listed in table 8.1 after calcination at 600 °C are shown in figure 8.5. Similar to the films obtained after calcination at 400 °C (figures 8.2I-XI), changes in morphology of the films are observed with increasing EGMT molar concentration in the final sol-gel (table 8.1). In general, the surface topography of both sets of films obtained at 400 and 600 °C,

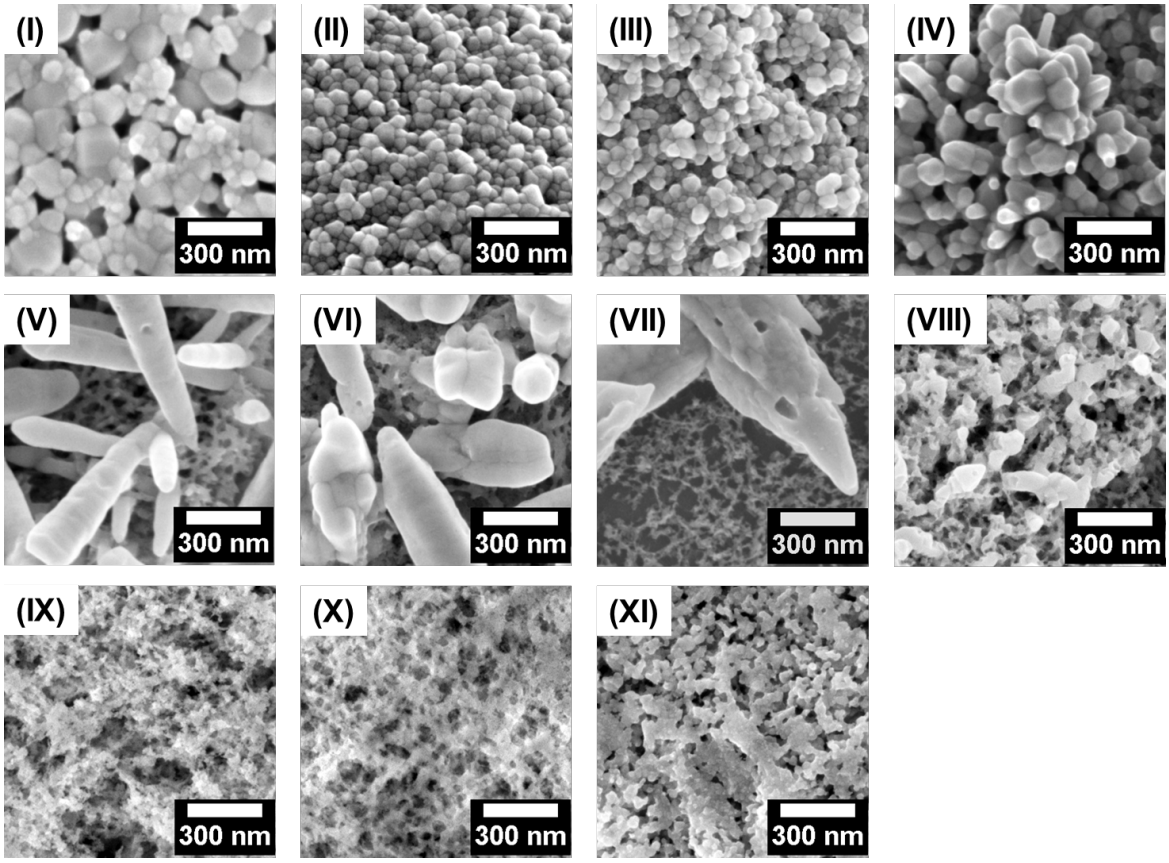

Figure 8.5.: SEM topography images of the spray-deposited films obtained from sol-gel compositions I to XI (table 8.1) respectively. The images are taken after calcination of the films at 600 °C.

appear very similar with respect to the sol-gel compositions. This manifests that the difference in temperature treatment influences only the structural length scales keeping the morphology of the films intact.

The films obtained from composition I, II and III (figure 8.5), show spherical granular morphology, similar to the films obtained after calcination at 400 °C (figures 8.2I, II and III). However, the granules for the films calcined at 600 °C show larger diameters supporting the fact that higher temperature provides more energy to the system which leads to fusion of the nanostructures. The film obtained at 600 °C from composition I shows two different classes of spherical granules, the smaller ones range in the diameter from 50 to 100 nm, whereas, the larger granules have a diameter range of 150 to 200 nm. The films obtained from compositions II and III (figure 8.5) show similar granular sizes in the range of 30 to 100 nm and appear to have a more compact morphology as compared to the film obtained from composition I. Also similar to the films obtained at 400 °C, the films obtained after calcination at 600 °C from compositions IX and X (figure 8.5) show a

foam-like morphology with an average pore size in the range of 40 to 100 nm. Similarly, the film obtained from composition XI (figure 8.5) shows denser and porous regions, with an average pore size of 30 to 100 nm. Thus, it is clear that the pore sizes obtained for the films obtained after calcination at 600 °C are larger than those of the films obtained at a calcination temperature of 400 °C. The major variations in the surface morphology of the films of the present series occur between compositions IV to VIII (figure 8.5).

Similar to the films obtained after calcination at 400 °C, the films obtained from compositions IV to VIII after calcination at 600 °C (figure 8.5), also show the presence of large elongated clusters in the films. Apart from these upright rod-like structures, a film of foam-like network structures is also visible for the films obtained from compositions V to VIII (figure 8.5). The appearance of the two different prominent morphologies (rod-like and foam-like) in the same films in case of compositions V to VIII is again explained by the strong seggregation of the two phases with an increasing molar concentration of EGMT in the final sol-gel solution. Thus, it is evident that the compositions of the different sol-gels has a strong impact on the film morphology and the different phases obtained in the system.

It should be kept in mind that the main purpose for undertaking calcination of the films at two different temperatures is to obtain a single compound phase of Zn_2TiO_4. XRD is performed on all the films using XRD instrument II (see section 3.1.4) and the diffraction peaks obtained are plotted in figure 8.6. As observed from the diffraction spectra, the crystalline phases present for the films obtained after calcination at 600 °C are very different from those obtained from films after calcination at 400 °C (figure 8.3), although the surface morphologies of the two series appear very similar. The films obtained from compositions I to III show pure ZnO wurtzite crytstalline phase (figure 8.6). For films obtained from compositions IV to VII, two additional peaks corresponding to Zn_2TiO_4 (220) and (311) lattice planes start to appear at $2\theta = 29.9°$ and 35.2° respectively. The intensity of these two peaks is still very low compared to the peaks related to the wurtzite ZnO phase. Hence, films obtained from compositions IV to VII have mixed phases of ZnO and Zn_2TiO_4 in the system. For the film with composition VIII, the contribution from the (220) and (311) lattice planes of Zn_2TiO_4 becomes even stronger and at the same time the signal belonging to the wurtzite ZnO phase is suppressed indicating the transformation of the crystalline phase towards Zn_2TiO_4.

On further increasing the molar concentration of EGMT in the final sol-gel, the film obtained from composition IX purely shows all the peaks corresponding to the crystalline phase of Zn_2TiO_4. The presence of any other crystalline phase for ZnO or TiO_2 is not observed for this film. The relative intensities of the peaks obtained for this film is also in a very good agreement with the theoretical values.

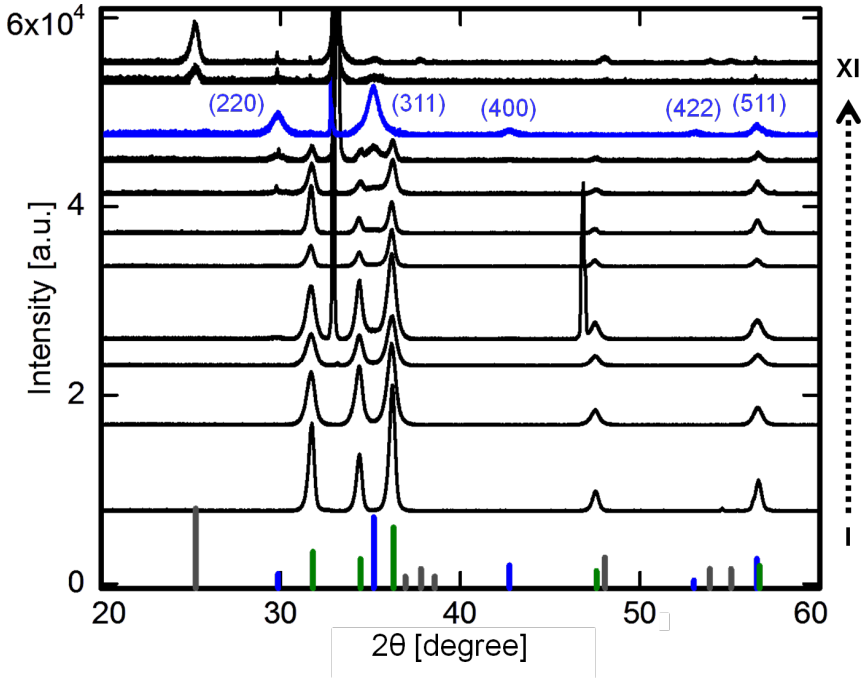

Figure 8.6.: XRD spectra of all spray-deposited films obtained from sol-gel compositions I to XI (table 8.1), plotted from bottom to top (as indicated by the dashed arrow) after calcination at 600 °C. The vertical lines at the bottom axis represents the theoretical peak positions with their relative intensities for wurtzite ZnO (green), anatase TiO_2 (gray) and Zn_2TiO_4 (blue). All the curves are shifted along the intensity axis for clarity. The lattice planes are indicated for the signal obtained from Zn_2TiO_4. Additionally, the XRD spectrum corresponding to the film having a pure Zn_2TiO_4 phase is also highlighted in blue. The peak obtained at $2\theta = 33°$ corresponds to the (100) lattice plane of the silicon substrate.

The film with composition X shows mixed phases of crystalline Zn_2TiO_4 with crystalline anatase phase of TiO_2. The peak at $2\theta = 25.3°$ clearly corresponds to the (101) lattice plane of anatase titania. Apart from this peak, diffraction from any other lattice plane either from titania or Zn_2TiO_4 is not observed. The minor amount of ZnO present in composition X also results in the absence of any signal obtained from ZnO. For the films obtained from pure EGMT sol-gel (composition XI), the peak corresponding to the (101) anatase phase is the strongest and all the other signals for crystalline anatase polymorph of TiO_2 are also present. This proves that a higher calcination temperature of 600 °C is favorable to obtain the crystalline phases of TiO_2 when EGMT is used as the precursor. This behavior is quite surprising, as the crystalline phases of titania are reported to be achieved at room temperature already when EGMT is used as the precursor [27, 88, 90]. Additionally, the intensity of the peaks obtained for the film prepared from pure EGMT sol-gel is very low which is due to the lower film thickness as compared to the film obtained

from pure ZAD sol-gel. This originates from the fact that the weight fraction of EGMT in composition XI is lower than that of ZAD in composition I. Hence, less amount of particles are deposited for the film prepared from composition XI, thereby resulting in a reduced film thickness.

It is confirmed that both the composition of the sol-gel and the calcination temperature are equally important to ensure the formation of pure Zn_2TiO_4 crystalline phase in the system. In the present investigation, a sol-gel solution having the molar ratio of ZAD : EGMT = 1.05 : 1 (composition IX) is most suitable to produce pure Zn_2TiO_4 crystalline phase when the films are calcined at a temperature of 600 °C. The sol-gel solutions having a higher molar concentration of ZAD as compared to the optimized composition, result in mixed phases of wurtzite ZnO and Zn_2TiO_4 in the system, whereas, sol-gel compositions containing a higher molar concentration of EGMT result in mixed phases of anatase and Zn_2TiO_4 in the final films.

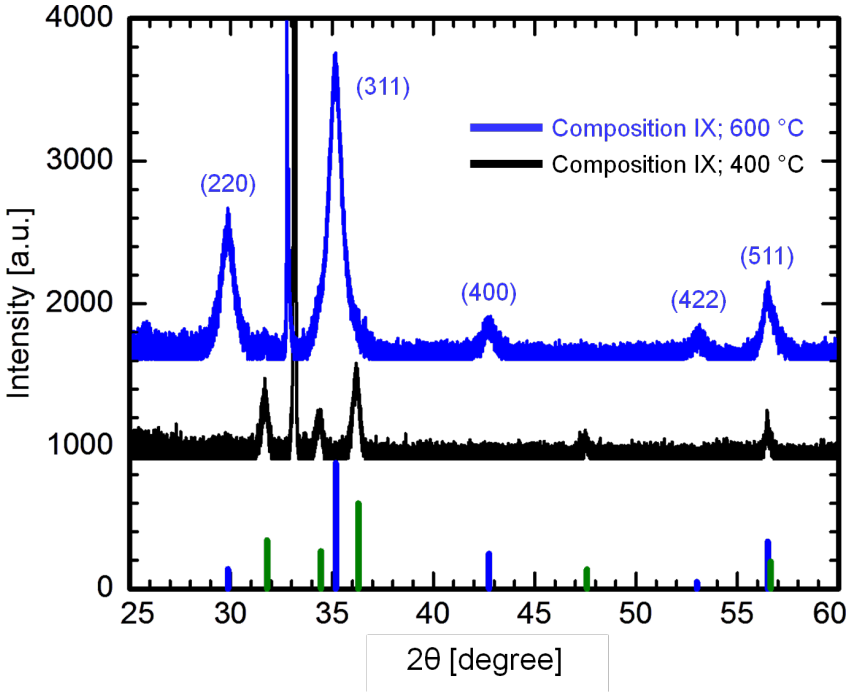

Figure 8.7.: XRD spectra of the spray-deposited films obtained from sol-gel composition IX (table 8.1), plotted after calcination at 400 °C (black) and 600 °C (blue). The vertical lines at the bottom axis represent the theoretical peak positions with their relative intensities for wurtzite ZnO (green) and Zn_2TiO_4 (blue). The curves are shifted along the intensity axis for clarity. The lattice planes are indicated for the signal obtained from Zn_2TiO_4. The peak obtained at $2\theta = 33°$ corresponds to the (100) lattice plane of the silicon substrate.

In order to better illustrate the influence of the calcination temperature on the spray-

coated films obtained from the same composition, the XRD spectrum of the films obtained from composition IX are compared in figure 8.7 after calcination at 400 and 600 °C. To reveal, for the film obtained after calcination at 400 °C, only pure wurtzite ZnO phase is obtained. The low intensity of the peaks is a clear sign of reduced crystallinity. Any absence of the TiO_2 peaks also indicates the presence of titania in amorphous state in the film which does not contribute to the XRD signal. For the same film, calcined at 600 °C, no wurtzite or anatase phase is present. Instead, a pure Zn_2TiO_4 crystalline phase is obtain. This highlights the importance of the calcination temperature which results in different crystalline phases for the same film composition. Formation of different crystalline phases essentially depends on the energy required for their formation. The results obtained from the present study are in good agreement with literature where it was shown that the formation of pure Zn_2TiO_4 crystalline phase is preferred at temperatures above 600 °C for most of the compositions of ZnO and TiO_2 in non-sol-gel synthesis routes [41, 246]. Thus for the present sol-gel route similar phase diagrams are valid.

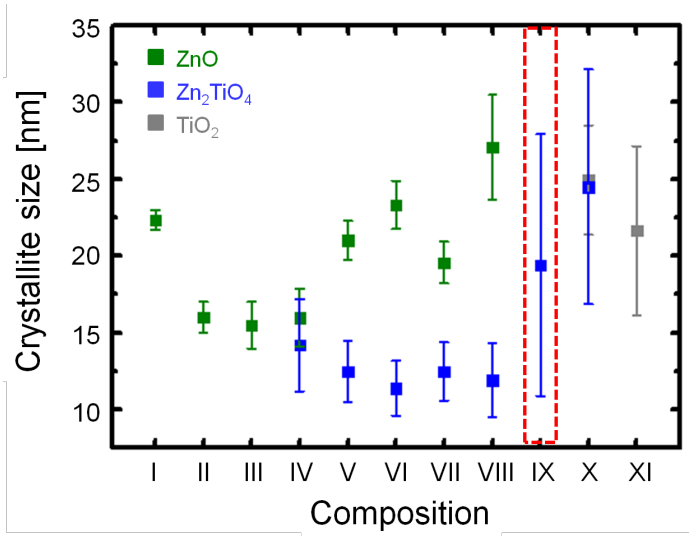

Figure 8.8.: Average crystallite sizes corresponding to ZnO, Zn_2TiO_4 and TiO_2 phases obtained for the spray-deposited films, calcined at 600 °C. The films are obtained from different sol-gel compositions as listed in table 8.1. The error bars are the standard deviation of the sizes obtained from all the diffraction peaks obtained in figure 8.6. The red dashed rectangle highlights the crystallite size corresponding to the film obtained from sol-gel composition IX showing a pure Zn_2TiO_4 crystalline phase.

The crystallite sizes of the films obtained after calcination at 600 °C are shown in figure 8.8. In general, the crystallite sizes for ZnO and Zn_2TiO_4 show an increasing trend for increasing volume ratio of EGMT in the final sol-gel. This is explained by the difference in the weight fractions of the two precursors in their individual sol-gels.

The molar concentration of ZAD in the final sol-gel stays higher than that of EGMT for the compositions I to IX. Hence, a larger crystallite size of ZnO as compared to TiO_2 is justified. Moreover, for the compositions IV to VIII, where mixed phases of ZnO and Zn_2TiO_4 are prominent, it is noticed that the increase in crystallite size for ZnO is accompanied by the decrease of the same for Zn_2TiO_4 and vice versa. This trend is explained by the contribution of a fixed amount of ZnO nanoparticles in the final sol-gel solution towards the formation of pure ZnO or Zn_2TiO_4 phases. Specifically for the Zn_2TiO_4 crystalline phase, the crystallite sizes vary from (11 ± 2) nm to (14 ± 3) nm for the films with composition IV to VIII. For the film with composition IX, a pure Zn_2TiO_4 crystalline phase is obtained with average crystallite size of (19 ± 8) nm. Compared to the SEM image of the pure Zn_2TiO_4 film (figure 8.5IX), a foam-like morphology is observed which is often considered suitable for efficient charge transport [165]. Additionally, large crystallite sizes are favorable in DSSCs as losses are reported to be minimized in large domains [254–256].

Film composition

Spray-coated films obtained from composition IX (table 8.1) and calcined subsequently at 400 and 600 °C are investigated further for their chemical composition. Energy-dispersive x-ray spectroscopy (EDX) is performed on both films with an electron beam of 25 keV. The obtained elemental mapping for both films are shown in figures 8.9(a) and (b).

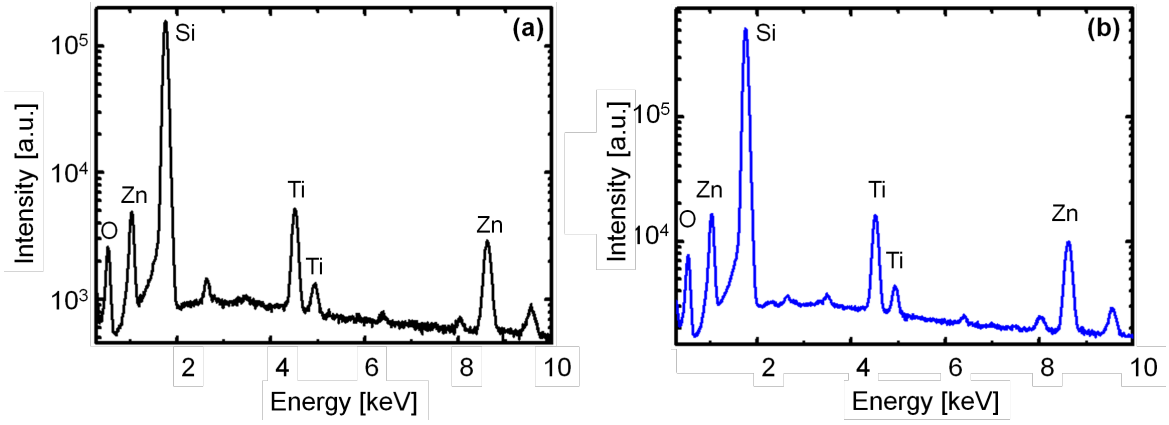

Figure 8.9.: EDX spectra obtained for the spray-coated films obtained from composition IX (table 8.1) after calcination at 400 °C (a) and 600 °C (b).

The strongest signal for both cases are obtained from the silicon substrate. Besides silicon, titanium (Ti), zinc (Zn) and oxygen (O) atoms are detected in both the films confirming the absence of any other impurity in the film which could possibly hamper the

elements	film calcined at 400 °C (atom %)	film calcined at 600 °C (atom %)
Zinc (Zn)	(36.91 ± 0.77)	(40.40 ± 0.44)
Titanium (Ti)	(22.02 ± 0.25)	(20.79 ± 0.14)
Oxygen (O)	(41.07 ± 0.26)	(38.81 ± 0.14)

Table 8.2.: List of atomic compositions derived from EDX analysis for the spray-coated films obtained from composition IX (table 8.1) after calcination at 400 and 600 °C.

formation of pure crystalline phases. The XRD spectrum of the film calcined at 400 °C (figure 8.7) shows no other crystalline phase than wurtzite ZnO in the film. However, the EDX mapping (figure 8.9(a)) confirms the presence of Ti atoms in the system, which points towards the presence of amorphous titania in the film, which does not contribute to the XRD signal. The atom percent of each element extracted from the EDX spectra for both films are listed in table 8.2.

It is clearly noticeable from the elemental analysis, that the atom % of Zn and Ti for the film calcined at 600 °C match the stoichiometric ratio of the compound zinc orthotitanate (Zn_2TiO_4). Whereas, for the film calcined at 400 °C, this is not the case, reconfirming the presence of Zn_2TiO_4 phase only in the former film. As both films are prepared from the same sol-gel composition, the relative ratio between the Zn and Ti atoms present should be equal in theory. However, this is clearly not followed in the present case. This can be attributed to the inconsistency of the film composition and presence of multiple phases when a calcination temperature of 400 °C is used.

8.1.2. Optical properties

UV/Vis spectroscopy (using UV/Vis instrument II, refer to section 3.2.1) is performed on all the films (coated on glass) mentioned in section 8.1.1 and the corresponding band gap of each film is calculated via the Tauc equation, as explained in section 3.2.1. As mentioned before, all the films are essentially composed of zinc oxide and titania in crystalline and amorphous phases. Therefore, for comparison of the band gaps obtained for the films with the theoretical values, the band gaps of anatase titania and wurtzite zinc oxide are taken into consideration. The theoretical band gap reported for wurtzite ZnO is 3.3 eV, whereas, for that of anatase TiO_2 is 3.2 eV [257, 258]. It is also noteworthy that ZnO is reported to have a direct band gap, whereas, for titania, both direct and indirect band gaps are documented. In the present study, our main focus is on zinc orthotitanate phase

(Zn_2TiO_4) which is also reported to have a direct band gap. Hence, the Tauc equation for direct band gap semiconductors is used for calculation of all the band gap energies.

Spray-coated films calcined at 400 °C

The absorbance spectra for the spray-coated films obtained from compositions I to XI (table 8.1) after calcination at 400 °C are shown in figure 8.10(a).

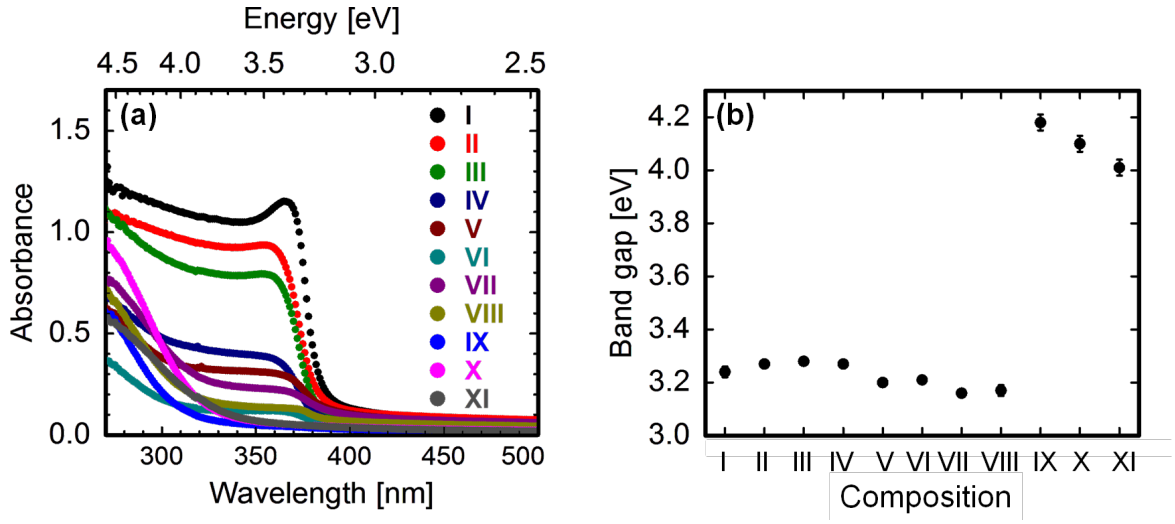

Figure 8.10.: (a) Absorption spectra of all the spray-coated films obtained from different compositions listed in table 8.1 after calcination at 400 °C. (b) The band gaps of the corresponding films, obtained from the linear extrapolation of the absorbance data to the energy axis.

Films obtained from compositions I to III show a higher absorbance than other films, which is explained by the higher thickness of these films as compared to the others. This is determined by the amount of material deposited on the substrate, which for the first three compositions are the highest due to the high molar concentration of ZAD in the final sol-gel (see table 8.1). The most prominent absorption edge for films produced with compositions I to VIII lies in the range of 3.3 to 3.5 eV. This is characteristics of the inorganic metal oxides present in the system which absorbs in the UV region of the optical spectrum. However, for films with compositions III to VIII, an increase in the absorbance is visible in the region larger than 3.8 eV. The presence of this second absorption edge, although not very prominent, is an indication of the presence of mixed phases in the system. It should be noted that the contribution of these mixed phases are not observed in the XRD spectra of the same films. This is a signature of the presence of the mixed phases in their amorphous state which is detected by the absorption measurements, but do not contribute to the crystallinity of the films. For the sake of convenience, the absorption maxima at

energies larger than 3.8 eV are not taken into account for the calculation of the additional band gaps of the films prepared with compositions III to VIII. The films composed of sol-gel solutions IX to XI show a prominent absorption edge at higher energies, larger than 3.8 eV.

In order to obtain quantitative information about the different band gaps for the films, the respective direct band gaps extracted for each film is plotted against the sol-gel composition in figure 8.10(b). The error bars are a result of the uncertainty of the linear fit to derive the band gaps. It is observed from the plot that the band gaps for the films prepared from compositions I to IV lie in the range of 3.24 to 3.27 eV. These band gaps differ from the theoretical band gap reported for wurtzite ZnO by 0.09 to 0.13 eV. However, these altered band gaps agree well with the literature, where it is found that the presence of a second phase, such as titania in the system, affect the band gap in the range of 3.10 to 3.70 eV [259, 260]. Additionally, the co-existence of amorphous phases of TiO_2 and Zn_2TiO_4 cannot be ruled out from the system, which also has an impact on the final band gap of the material. The films with compositions V to VIII show a decrease in the band gap and values between 3.17 and 3.20 eV are obtained. In addition to the presence of different phases in the system, the band gap is also influenced by different crystallite sizes in the film [261]. With increasing molar fraction of EGMT in the final sol-gel, the band gaps show an abrupt increase for the films obtained from compositions IX to XI (figure 8.10(b)). The values range from 4.01 to 4.18 eV. These higher values are also in agreement to the reported values for the band gap of amorphous titania [259] signifying its presence, which is not accessed via the XRD measurements. However, the band for any of the compositions from II to X does not correspond to that of crystalline Zn_2TiO_4, which conveys the absence of this particular crystalline phase in the films calcined at 400 °C.

Spray-coated films calcined at 600 °C

The absorbance spectra for the spray-coated films obtained from compositions I to XI (table 8.1) after calcination at 600 °C are shown in figure 8.11(a). The absorption behavior of the films appear similar to the ones obtained for the films calcined at 400 °C (figure 8.10(a)). The prominent absorption maximum for the films obtained with compositions I to VIII lies in the range of 3.3 and 3.5 eV. The band gap of the films have been derived from this absorption maximum. For the films with higher molar concentration of EGMT in the final sol-gel (compositions IX to XI), a blue shift in the absorption maximum is observed for energies > 3.8 eV. For the films with compositions IV to VIII, double absorption maxima are obtained as in the case for the films calcined at 400 °C. Unlike the film obtained with composition IV after calcination at 400 °C, the same film after

being calcined at 600 °C, shows an increased absorbance, which is related to the onset of formation of crystalline Zn_2TiO_4 phase in the film as probed by the XRD measurements (figure 8.6).

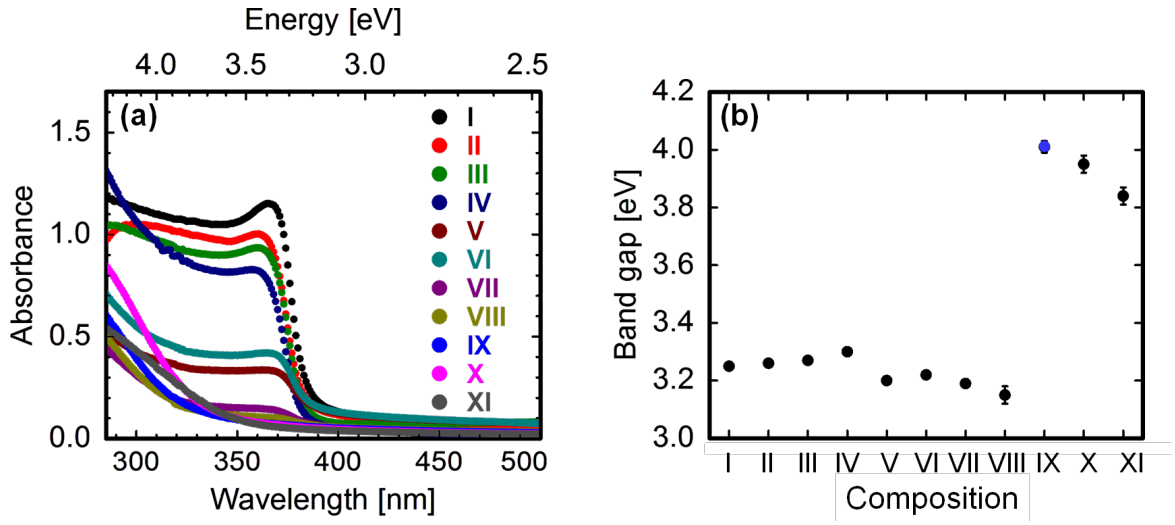

Figure 8.11.: (a) Absorption spectra of all the spray-coated films obtained from different compositions listed in table 8.1 after calcination at 600 °C. (b) The band gaps of the corresponding films, obtained from the linear extrapolation of the absorbance data to the energy axis. The band gap obtained for the film prepared from composition IX is highlighted in blue to represent the pure Zn_2TiO_4 crystalline phase present in the film.

The band gaps obtained for all the films are plotted in figure 8.11(b). Among the films obtained from sol-gel compositions I to VIII, the film with composition IV shows the maximum value of the band gap of (3.3 ± 0.01) eV. This film contains the crystalline wurtzite phase of ZnO with a slight indication of the presence of the crystalline Zn_2TiO_4 phase (figure 8.6). The band gap however corresponds to the wurtzite ZnO. With an increasing amount of EGMT molar concentration in the system, the films calcined at 600 °C show an increasing contribution from the crystalline Zn_2TiO_4 phase in the films (section 8.1.1). However, from the calculation of the band gaps, a decrease in the values are observed for the same films (compositions between V and VIII). This is in good agreement with the literature values for the band gaps in a system containing mixed phases of ZnO and TiO_2 [259]. The decrease in the band gap is also often explained by the increased amounts of defect states and grain boundaries in the system when significant amount of both the phases are present [260]. It is observed that the band gap of the film obtained from composition IX matches very well with the value reported for crystalline Zn_2TiO_4 in literature [46–48]. This is also in a very good accordance with the conclusion drawn from the crystallinity study of the same films performed in section 8.1.1. Hence,

for this particular composition, it can be stated that any other amorphous phase does not coexist with the crystalline Zn_2TiO_4, for this would have affected the band gap of the film. With a further increase in the volume % of EGMT in the final sol-gel solution for composition X and XI, a decrease in the band gaps is observed also with respect to the values obtained for the films with same compositions, but calcined at 400 °C. This indicates an improvement in the crystalline phase of the material as also evident from the XRD studies (figure 8.6). However, the presence of a band gap corresponding to pure crystalline TiO_2 phase is still not observed, even for composition XI. This suggests the presence of a significant amount of amorphous TiO_2 phase in the film in addition to the crystalline phase observed by the XRD measurements (figure 8.6).

8.1.3. Solar cell performance

The main focus of this chapter has been to develop and synthesize a new ternary compound phase using ZnO and TiO_2, namely Zn_2TiO_4, which has been obtained only after calcination of a spray-coated film at 600 °C, prepared using the sol-gel composition IX as described in detail in section 8.1.1. Since, only one of all the films studied in this chapter has shown the presence of a pure Zn_2TiO_4 phase, DSSCs are prepared with two different thicknesses of this film as the active layer and the I/V-curves of the respective DSSCs are shown in figure 8.12. A thin crystalline TiO_2 film is used as the hole-blocking layer for both solar cells. The preparation details regarding the blocking layer and the entire solar cell assembly is explained in section 4.2.3.

Applications of Zn_2TiO_4 films have been confined mainly to the areas of photocatalysis and pigments so far [47,262]. Only a few attempts have been reported where Zn_2TiO_4 has been incorporated as an active layer in a solar cell. However, these studies have remained unsuccessful till date [263]. The main reason for the failure of Zn_2TiO_4 in solar cells is associated to the morphology of the active layer. In the present investigation, the unique copolymer template-assisted route associated with sol-gel chemistry allows for optimizing the film morphology in conjugation with wet chemical deposition. The foam-like network morphology obtained for the film used as the active layer in the DSSCs (see figure 8.5(i), for the SEM surface image) is highly beneficial for the production of working solar cells with this material. Thus, for the first time, to the best of our knowledge, DSSCs with Zn_2TiO_4 are realized.

Different amounts of sol-gel solution are spray-coated. The I/V-curves of both the films appear very similar with the difference of an enhanced open-circuit voltage (V_{OC}) and short-circuit current (I_{SC}) for the film obtained by spraying a higher amount of the

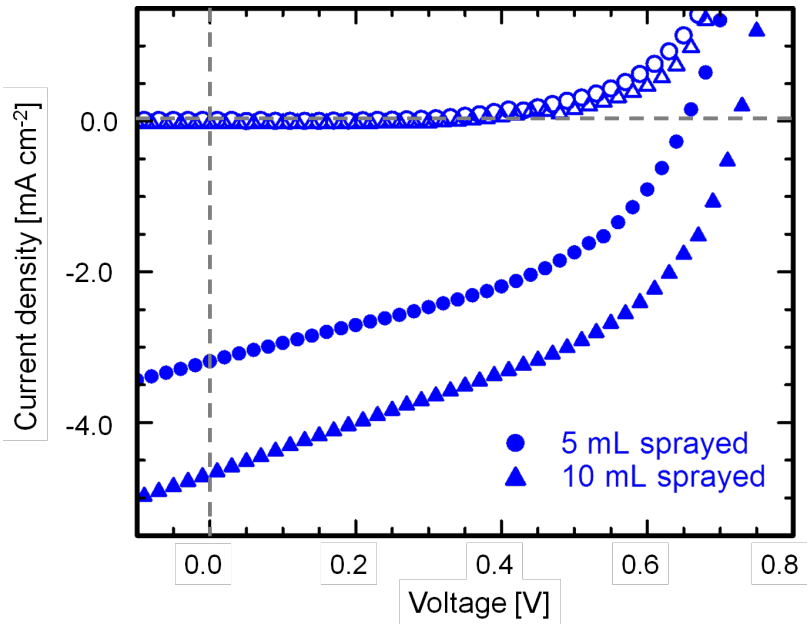

Figure 8.12.: Current density-voltage characteristics of dye-sensitized solar cells in dark (open symbols) and under illumination (closed symbols), prepared from different amounts of spray-deposited zinc orthotitanate films. The films are calcined at 600 °C.

sol-gel (10 mL). The characteristic solar cell parameters for both cells are listed in table 8.3.

amount sprayed	I_{SC} [mA/cm^2]	V_{OC} [V]	FF [%]	η [%]
5 mL	-3.1	0.65	43.1	0.9
10 mL	-4.6	0.72	43.6	1.5

Table 8.3.: I/V characteristics of the DSSCs obtained from spraying different amounts of Zn_2TiO_4 sol-gel (composition IX of table 8.1). The films are calcined at 600 °C. The parameters are obtained from analyzing the I/V-curves shown in figure 8.12.

The clear increase in the I_{SC} and V_{OC} for the cell with higher active layer thickness is attributed to the extra charge carrier pathways generated in the system with increasing amount of material. The improvement in the V_{OC} also indicates a reduction in electron back transfer from Zn_2TiO_4 to the oxidized electrolyte. This results in an improved power conversion efficiency (η) of 1.5 % instead of 0.9 %. In total, the performance of both the cells are very promising considering the first initiative to use the new ternary compound, Zn_2TiO_4 as an active layer in DSSCs.

8.1.4. Results & discussion

The investigation made by varying the concentrations of ZnO and TiO_2 precursors in a sol-gel system, gives rise to the formation of a series of ZnO-TiO_2 nanocomposite structures in the solution. Assisted by the diblock copolymer template in the sol-gel approach, different length scales of these nanostructures are achievable. In order to obtain the nanostructures in the form of thin films for large-scale practical applications, the spray-deposition method is proved to be suitable in order to obtain wide area coverage of morphologies, which can be further tuned according to the requirements. The series of different morphologies obtained after calcination of the films at different temperatures (400 and 600 °C), show an additional control over the structural length scales in the film, however, keeping the morphology intact. Moreover, a pure ternary compound, Zn_2TiO_4 is also successfully synthesized using the temperature treatment at 600 °C.

The formation of different phases in ZnO-TiO_2 nanocomposites has been well-established as a function of composition of ZnO and TiO_2 in the system and reported as a phase diagram by Dulin and Rase using melt mixing method [264]. The authors have shown that for a calcination temperature below 600 °C, the anatase and the ZnO phases coexist in the system without any signature of other phases, over a wide composition range (including pure ZnO and TiO_2 systems). In the present study, the different morphologies also support the fact of the presence of multiple phases at the same time in the film. From the XRD investigations performed on the spray-coated films after calcination at 400 °C, no other crystalline phase than wurtzite ZnO is observed which indicates towards the presence of the TiO_2 phase in amorphous state. The seggregation of these two phases is clearly visible in the SEM images of the calcined films obtained over different compositions of the sol-gel. For films containing high molar concentrations of ZAD or EGMT, uniform foam-like morphologies are obtained throughout the film. For the intermediate compositions, large rod-like clusters along with a foam-like network morphology are observed on the surface of the films which belong to one or the other phase present in the system for the particular film composition. However, the higher molar concentration of ZAD than that of EGMT for most of the compositions suggests that the larger clusters are mainly composed of ZnO. On the other hand, the foam-like nanostructures can be linked with amorphous TiO_2, as this morphology is homogeneously present for the film obtained from pure TiO_2 sol-gel. Also, no anatase phase is observed for the films calcined at 400 °C. For the synthesis of inorganic metal oxides in a solution process, it is often reported that the presence of ZnO in the system hampers the crystallinity of the TiO_2 phases [265, 266]. This is also clearly visible from the band gaps extracted from the absorption measurements performed on the films. The obtained values are in good agreement with those given in the literature for composite systems. A shifting in the

Fermi level is often observed for films with multiple phases contributing to changes in the band gap. For the intermediate compositions, two absorption edges are visible referring to multiple band gaps of the seggregated phases in the film.

As compared to the phase diagram reported for different ZnO and TiO_2 compositions, a mixed phase of ZnO and zinc orthotitanate (Zn_2TiO_4) exist for compositions richer in ZnO for temperatures above 600 °C [264]. For the present investigations, similar results are obtained for spray-coated films calcined at 600 °C. These findings are confirmed by the XRD measurements where combined phases of ZnO and Zn_2TiO_4 are detected for the sol-gel compositions with higher molar concentration of ZAD in the final sol-gel solution. For the sol-gels with a higher molar concentration of EGMT, mixed phases of Zn_2TiO_4 and anatase titania are observed. For the intermediate compositions, the mixed phases of ZnO and Zn_2TiO_4 persists in the system with varied combinations. For ZAD : EGMT molar concentration of 1.05 : 1, a pure phase of crystalline Zn_2TiO_4 is observed in the system. The coexistence of different phases in the system also encompasses the availability of phases which remain amorphous in the films. The band gaps extracted for these films from the absorption measurements prove the presence of amorphous phases in the films. However, the band gap obtained for the film with the composition showing pure Zn_2TiO_4 phase in XRD, matches with the theoretical band gap for Zn_2TiO_4 crystalline phase. In general, an improved crystallinity for the films calcined at 600 °C is observed from both the band gap values and the XRD spectra obtained for the films of different compositions of sol-gel solutions.

Morphologically, the films calcined at 600 °C also show seggregation of the two phases for sol-gels having intermediate compositions of ZAD and EGMT. The final Zn_2TiO_4 phase shows uniform foam-like morphology. This foam-like interconnected network is also present for the films with intermediate concentrations of ZAD and EGMT in the sol-gel solutions. Thereby, the large clusters observed for the same compositions are again associated to the ZnO and the additional foam-like network structures are linked to the Zn_2TiO_4 phase. The conclusions drawn are in accordance with the results obtained from XRD measurements. However, the presence of amorphous component of ZnO or TiO_2 in the morphologies shown by the different sol-gel compositions cannot be neglected completely. The pure crystalline Zn_2TiO_4 phase as established by the XRD and absorption measurements, indeed shows a promising performance as an active layer in dye-sensitized solar cells.

8.2. Summary

A complete morphological investigation is performed on two different series of ZnO-TiO_2 nanocomposite films: one calcined at 400 °C and the other at 600 °C. Eleven different compositions are studied in each series with varied molar concentration of the ZnO precursor (ZAD) and the TiO_2 precursor (EGMT). Different morphologies ranging from spherical granules, to foam-like network structures via rod-like architectures are obtained with different length scales tuned by the structure-directing diblock copolymer template, P(S-*b*-EO). Some of the morphologies, such as the foam-like inter-connected network structures are highly beneficial for charge transport as active layers in solar cells. All the films show homogeneous surface coverage, rendering spray-coating as a suitable method for the deposition of ZnO-TiO_2 nanocomposite films. Along with different ZnO-TiO_2 nanocomposites, a pure compound phase of Zn_2TiO_4 is successfully synthesized via the sol-gel route for the first time. It is demonstrated in the study that the composition of the ZnO and TiO_2 sol-gel as well as the correct calcination temperature are extremely crucial in order to obtain the single pure phase. The different crystalline phases present for the pure as well as the nanocomposite films are studied using XRD. The synthesis of Zn_2TiO_4 is further confirmed by elemental analysis of the films. Optical characterization of all the nanocomposite films reveals that the band gap value depends on the amount of increasing molar concentration of EGMT in the final system. The optical properties of the films containing mixed phases show differences from those of pure phases. The band gap of the film containing the pure crystalline Zn_2TiO_4 phase, corresponds to the literature value which proves the success in synthesizing the compound via sol-gel route. Foremost, DSSCs fabricated from the pure crystalline Zn_2TiO_4 show promising performance with a reasonably high open-circuit voltage, also reported for the first time. An increase in the thickness of the active layer results in upliftment of the power conversion efficiency of the device to 1.5 %. Foam-like morphology of the Zn_2TiO_4 active layer along with the spray deposition route play a significant role behind the success of the DSSCs.

In summary, Zn_2TiO_4 nanostructures have been synthesized in the form of a foam-like morphology for a spray-deposited film using the template-assisted sol-gel approach for the first time. The novel combination of the chosen precursors (EGMT and ZAD) has lead to the success. The performance of the DSSCs using the film, however needs further optimization for the dye and the electrolyte used, additionally to the active layer thickness.

9. Summary and outlook

In the present thesis, two potential inorganic metal oxide semiconductors, zinc oxide (ZnO) and zinc orthotitanate (Zn_2TiO_4) are investigated for being applied as electron-accepting layers in dye-sensitized solar cells (DSSCs). The investigations shown, present answers to the questions introduced in the beginning regarding the functionality of the chosen materials towards suitable applications. The principle focus of this thesis was on novel synthesis and tailoring routines for nanostructured morphologies of these materials in the form of thin films, via solution-based approaches. Along with unique nanomorphologies, thickness, optical properties and crystallinity of the thin films are also studied thoroughly. More precisely, the present thesis covers mainly four major aspects, which are of particular importance to develop new pathways in order to obtain tuneable ZnO and Zn_2TiO_4 nanostructured films with promising properties for applications in DSSCs. These aspects are: (1) Fabrication of ZnO films using a solution of pure precursor deposited via spray deposition, (2) customizing various morphologies and length scales of ZnO nanostructures using sol-gel synthesis route assisted with a suitable diblock copolymer template, (3) providing additional tuneability to the structural length scales evolved in the films obtained from the template-assisted sol-gel solutions, by solvent vapor treatment of the ZnO-polymer hybrid films for different time scales and (4) synthesis and integration of Zn_2TiO_4 films in dye-sensitized solar cells providing decent efficiencies.

The first attempt to produce ZnO nanostructures is successfully accomplished by preparing a solution of the pure ZnO precursor and depositing it by spin-coating, solution-casting and spray-coating. An interconnected nanostructured morphology is observed for all the films fabricated from this simple system. Such a morphology is highly promising for applications in DSSCs. Although the length scales of the nanostructures obtained in the films are difficult to alter, the thickness of the films is efficiently controlled from a few nanometers to tens of micrometers via different deposition methods used, as mentioned above. In-situ evolution of the structures while spraying the ZnO precursor solution is monitored by grazing incidence small angle x-ray scattering (GISAXS) measurements. This kinetic study is documented for the first time using a ZnO system, which gives fruitful insight to the evolution of various structure sizes in the film volume with increasing spraying time.A competent spray protocol is derived from the study taking into account the dif-

ferent parameters such as spraying rate, time, substrate temperature and sample-nozzle distance, needed to obtain homogeneous coverage of the substrate along with interesting film morphologies and desired film thickness. Depending on the developed routine, liquid electrolyte-based DSSCs with a short-circuit current density of 20.8 mA cm^{-2} is reported which yields a reasonable power conversion efficiency of 4.1 %. This short-circuit current density is among the highest reported values so far for ZnO-based liquid electrolyte DSSCs.

In order to promote tuneability to the promising ZnO nanostructures, the novel structuring routine of block copolymer assisted sol-gel is employed. Two different templates, P(S-*b*-EO) and P(S-*b*-4VP) are used with two different molecular weights for each template. Such a synthesis procedure with high degree of control over the dimensions of nanostructures is demonstrated for the first time for the ZnO system. Based on the synthesis of nanostructures using the low molecular weight P(S-*b*-EO) template, a ternary phase diagram is established via the variation of various ingredients of sol-gel solutions. A complex assortment of morphologies is synthesized, consisting of worm-like aggregates, circular vesicles, spherical granules and foam-like morphology. Within the investigated boundaries of the phase diagram, the foam-like morphology is the most frequently occurring and hence, is explored further in details with GISAXS, which reveals the presence of suitable length scales of the nanostructures in the film volume for photovoltaic applications. Additionally, promising opto-electronic properties and crystallinity of the nanostructures are demonstrated. Furthermore, to fine-tune the length scales obtained in the film volume, a high molecular weight derivative of the same diblock copolymer template, P(S-*b*-EO) is employed. This provides longer chains to host an increased number of ZnO molecules, thereby resulting in different length scales to suit the needs, while preserving the desired morphology. The average pore size of the foam-like morphology obtained from the high molecular weight P(S-*b*-EO) is found to be smaller than that obtained from low molecular weight counterpart of the diblock copolymer. Hence, an extended pathway to tailor the length scales of ZnO nanomorphologies is exhibited. The applicability of these films in DSSCs, is however marginalized by the low film thickness. This challenge is overcome by production of ZnO pastes and depositing them via blade-coating, resulting in films up to 7 µm in thickness. Custom-made pastes are prepared from sol-gel solutions with varied compositions, which provide ZnO nanoparticles upon solution-casting with different sizes and surface areas. Upon fabrication of pastes out of these ZnO nanoprticles in identical manner, variations in the film morphology are observed. The impact of these morphologies on the performance of electrolyte-based DSSCs and solid-state DSSCs (ss-DSSCs) is examined. All the ss-DSSCs cease to perform as solar cells even after several attempts due to the high surface roughness of the ZnO blade-coated films because of the

increased probability of short-cuts in the stack architecture of the device. Despite the poor performance of the final devices, a uniform film morphology and successful backfilling of ZnO nanostructures using P3HT as the hole conductor has been achieved. Different temperature treatments are also provided to the blade-coated films obtained from the ZnO paste, showing the most promising surface morphology. Liquid electrolyte-based DSSCs assembled from the blade-coated films treated with different temperatures show the highest power conversion efficiency of 1.72 %, when a calcination temperature of 600 °C is used. Hence, the study enacts a novel strategy to fabricate pastes from custom-synthesized ZnO nanoparticles via the sol-gel process.

As a next step, ZnO nanostructured morphologies in the form of thin films are synthesized with long range order with the aid of P(S-*b*-4VP) as a template coupled with the sol-gel route. Nano grid-like morphology is obtained using this polymer template, showing well-defined pores of the order of 20 nm. The optical properties as well as the crystallinity obtained from the calcined films are promising towards the development of these films for potential applications in nano devices. A better control over the pore sizes of the ZnO nano grid, while preserving the exclusive morphology, is achieved by treating the ZnO-polymer hybrid films with a suitable solvent vapor. This provides a successful workaround to the problem of using diblock copolymer templates with different molecular weights to tune the length scales of a specific morphology, which is not always feasible. The solvent vapor-treated films are subsequently calcined. The structural changes provided by the solvent vapor to the polymer template are transferred to the ZnO particles embedded into the polymer matrix. It is shown that after removal of the polymer template from the solvent-annealed films via calcination, an altered length scale of the ZnO nano grid is achieved depending on the solvent-annealing time. Solvents with or without preferential selectivity towards one of the blocks of P(S-*b*-4VP) are used for vapor treatment. Chloroform is used as the non-selective solvent and hence, the structures show considerable loss in order after solvent-annealing for different time scales. However, for tetrahydrofuran (THF), which is slightly selective to the P4VP block, the pore sizes can be successfully tuned within a range of 37 % for a solvent annealing time of 48 hours. The success of the investigation opens a competent pathway to tune several other nanostrutcured systems templated with a diblock copolymer, by use of a suitable solvent vapor. The ZnO sol-gel solutions prepared using a high molecular weight P(S-*b*-4VP) are spray-deposited for direct applications in DSSCs, acquiring a power conversion efficiency of up to 2.18 %.

Lastly, a step ahead of the conventional inorganic metal oxide semiconductors is taken in order to synthesize a compound of ZnO and TiO_2 (titania). Zn_2TiO_4 is reported to be synthesized from a template-assisted sol-gel approach for the first time as a result of a novel combination of ZnO and TiO_2 sol-gel solutions. Along with Zn_2TiO_4, a series of

different compositions of ZnO-TiO_2 sol-gels are studied as spray-deposited films. A series of film morphologies ranging from spherical granules, to nano rods and finally foam-like nanostructures is synthesized by using the high molecular weight P(S-*b*-EO) template. Zn_2TiO_4 is formed at a calcination temperature of 600 °C and shows opto-electronic properties corresponding to a wide band gap semiconductor. The power conversion efficiency of Zn_2TiO_4 as an active layer in electrolyte-based DSSCs is achieved to be 1.5 %. This is the highest efficiency of a DSSC presented with Zn_2TiO_4 as the electron-accepting layer, reported so far.

As a synopsis, the present thesis established a suitable wet chemical process to synthesize novel tuneable ZnO, ZnO-TiO_2 and Zn_2TiO_4 nanomorphologies. Deposition of these nanostructures via different deposition methods were demonstrated. Additionally, routes to extend the tuneability of length scales of the nanostructures were investigated. Finally, application of ZnO and Zn_2TiO_4 nanostructured films in dye-sensitized solar cells showed promising device efficiencies.

As an outlook, several interesting aspects can be explored in future projects following the present investigations. Since, a successful route to tune ZnO nanostructures in the form of thin films has been already established in the present thesis, further customization of the nanomorphologies is now possible using different templates and different precursors for ZnO. Custom-designed precursors with properties to yield crystalline ZnO at low temperatures would extend the applications of ZnO nanostructures for flexible solar cells. The nano grid-like ZnO morphology synthesized in the present thesis with additional tueability of the average pore size via solvent annealing, is also an attractive choice to be tested in ss-DSSCs with the established backfilling route for the hole-conducting polymer. After the first successful synthesis of Zn_2TiO_4 via a template-based sol-gel route, different morphologies of the compound would be interesting to study using different deposition methods. Further optimization of the film morphology and solar cell fabrication protocol can further improve the ultimate efficiency of the solar cells.

A. Appendix

Among the different weight fraction combinations of the solvents and the precursors used for the sol-gel synthesis of ZnO nanostructures using the low molecular weight P(S-*b*-4VP) template, the compositions listed in table A.1 did not result in clear solutions. Hence, these sol-gel solutions were not transferred into thin films. Possible reason behind the failure is explained in chapter 7.

composition	$w_{\mathrm{DMF}} : w_{\mathrm{H_2O}} : w_{\mathrm{ZAD}}$	composition	$w_{\mathrm{DMF}} : w_{\mathrm{H_2O}} : w_{\mathrm{ZAD}}$
VI	0.98 : 0.01 : 0.01	X	0.955 : 0.025 : 0.02
VII	0.94 : 0.03 : 0.03	XI	0.952 : 0.021 : 0.027
VIII	0.925 : 0.025 : 0.05	XII	0.91 : 0.08 : 0.01
IX	0.925 : 0.01 : 0.065	XIII	0.97 : 0.025 : 0.005

Table A.1.: List of different weight fraction (w) combinations of the solvent pair (DMF, H_2O) and the precursor (ZAD) used for preparing sol-gels using the low molecular weight P(S-*b*-4VP) template.

Bibliography

[1] A. E. Becquerel, "Mémoire sur les effets électriques produits sous l'influence des rayons solaires," *Comptes Rendus Hebdomadaires des Séances de l'Académie des Sciences*, vol. 9, pp. 561–567, 1839.

[2] C. Fritts, "On the fritts selenium cell and batteries," *Van Nostrands Engineering Magazine*, vol. 32, pp. 388–395, 1885.

[3] M. A. Green, "The path to 25 % silicon solar cell efficiency: History of silicon cell evolution," *Prog. Photovoltaics Res. Appl.*, vol. 17, pp. 183–189, May 2009.

[4] K. Cnops, B. P. Rand, D. Cheyns, B. Verreet, M. A. Empl, and P. Heremans, "8.4 % efficient fullerene-free organic solar cells exploiting long-range exciton energy transfer," *Nat. Commun.*, vol. 5, pp. 1–6, 2013.

[5] M. A. Green, K. Emery, Y. Hishikawa, W. Warta, and E. D. Dunlop, "Solar cell efficiency tables (version 39)," *Prog. Photovolt: Res. Appl.*, vol. 20, pp. 12–20, 2012.

[6] N. S. Sariciftci, D. Braun, C. Zhang, V. I. Srdanov, A. J. Heeger, G. Stucky, and F. Wudl, "Semiconducting polymer-buckminsterfullerene heterojunctions: Diodes, photodiodes, and photovoltaic cells," *Appl. Phys. Lett.*, vol. 62, p. 585–587, 1993.

[7] G. Yu, J. Gao, J. C. Hummelen, F. Wudl, and A. J. Heeger, "Polymer photovoltaic cells: enhanced efficiencies via a network of internal donor-acceptor heterojunctions," *Science*, vol. 270, p. 1789–1791, 1995.

[8] J. J. M. Halls, C. A. Walsh, N. Greenham, E. A. Marseglia, R. Friend, S. C. Moratti, and A. Holmes, "Efficient photodiodes from interpenetrating polymer networks," *Nature*, vol. 376, p. 498–500, 1995.

[9] C. Chiang, C. Fincher, Y. Park, A. Heeger, H. Shirakawa, E. Louis, S. Gau, and A. MacDiarmid, "Electrical conductivity in doped polyacetylene," *Phys. Rev. Lett.*, vol. 39, no. 17, pp. 1098–1101, 1977.

[10] B. O'Regan and M. Grätzel, "A low-cost, high-efficiency solar cell based on dye-sensitized colloidal tio_2 films," *Nature*, vol. 353, pp. 737–740, 1991.

[11] S. Ito, T. N. Murakami, P. Comte, P. Liska, C. Grätzel, M. K. Nazeeruddin, and M. Grätzel, "Fabrication of thin film dye sensitized solar cells with solar to elec-

tric power conversion efficiency over 10 %," *Thin Solid Films*, vol. 516, no. 14, p. 4613–4619, 2008.

[12] A. Yella, H. W. Lee, H. N. Tsao, C. Yi, A. K. Chandiran, M. K. Nazeeruddin, E. W. G. Diau, C. Y. Yeh, S. M. Zakeeruddin, and M. Grätzel, "Porphyrin-sensitized solar cells with cobalt (ii/iii)–based redox electrolyte exceed 12 percent efficiency," *Science*, vol. 334, pp. 629–633, 2011.

[13] J. Burschka, N. Pellet, S. J. Moon, R. Humphry-Baker, P. Gao, M. K. Nazeeruddin, and M. Grätzel, "Sequential deposition as a route to high-performance perovskite-sensitized solar cells," *Nature*, vol. 499, p. 316–319, 2013.

[14] N. Memarian, I. Concina, A. Braga, S. M. Rozati, A. Vomiero, and G. Sberveglieri, "Hierarchically assembled zno nanocrystallites for high-efficiency dye-sensitized solar cells," *Angew. Chem. Int. Ed.*, vol. 50, p. 12321 –12325, 2011.

[15] Y. J. Cheng and J. S. Gutmann, "Morphology phase diagram of ultrathin anatase tio2 films templated by a single ps-b-peo block copolymer," *J. Am. Chem. Soc.*, vol. 128, no. 14, p. 4658–4674, 2006.

[16] A. D. Jenkins, P. Kratochvíl, R. F. T. Stepto, and U. W. Suter, "Glossary of basic terms in polymer science," *Pure Appl. Chem.*, vol. 68, p. 2287–2311, 1996.

[17] G. Strobl, *The Physics of Polymers: Concepts for Understanding their Structures and Behavior*. Springer Berlin Heidelberg, 3 ed., 2007.

[18] O. F. Pascui, R. Lohwasser, M. Sommer, M. Thelakkat, T. Thurn-Albrecht, and K. Saalwächter, "High crystallinity and nature of crystal-crystal phase transformations in regioregular poly(3-hexylthiophene)," *Macromolecules*, vol. 43, no. 22, p. 9401–9410, 2010.

[19] C. Fougnies, M. Dosiére, M. H. J. Koch, and J. Roovers, "Morphological study and melting behavior of narrow molecular weight fractions of poly(aryl ether ether ketone) (peek) annealed from the glassy state," *Macromolecules*, vol. 31, no. 18, p. 6266–6274, 1998.

[20] L. Zhu, S. Z. D. Cheng, B. H. Calhoun, Q. Ge, R. P. Quirk, E. L. Thomas, B. S. Hsiao, F. Yeh, and B. Lotz, "Crystallization temperature-dependent crystal orientations within nanoscale confined lamellae of a self-assembled crystalline-amorphous diblock copolymer," *J. Am. Chem. Soc.*, vol. 122, no. 25, p. 5957–5967, 2000.

[21] P. J. Flory, "Thermodynamics of high polymer solutions," *J. Chem. Phys.*, vol. 9, p. 660–661, 1941.

[22] M. L. Huggins, "Thermodynamic properties of solutions of long-chain compounds," *Ann. N. Y. Acad. Sci.*, vol. 43, no. 1, p. 1–32, 1942.

[23] F. S. Bates and G. H. Fredrickson, "Block copolymer thermodynamics: Theory and experiment," *Annu. Rev. Phys. Chem.*, vol. 41, no. 1, p. 525–557, 1990.

[24] T. Johansson, W. Mammo, M. Svensson, M. Andersson, and O. Inganäs, "Electrochemical bandgaps of substituted polythiophenes," *J. Mater. Chem.*, vol. 13, no. 6, pp. 1316–1323, 2003.

[25] M. C. Orilall and U. Wiesner, "Block copolymer based composition and morphology control in nanostructured hybrid materials for energy conversion and storage: solar cells, batteries, and fuel cells," *Chem. Soc. Rev.*, vol. 40, pp. 520–535, 2011.

[26] K. Sarkar, M. Rawolle, E. M. Herzig, W. Wang, A. Buffet, S. V. Roth, and P. Müller-Buschbaum, "Custom-made morphologies of zno nanostructured films templated by a poly(styrene-block-ethylene oxide) diblock copolymer obtained by a sol–gel technique," *ChemSusChem*, vol. 6, p. 1414–1424, 2013.

[27] M. Rawolle, *Structuring and filling of titania films for applications in photovoltaics*. PhD thesis, Technischen Universität München, Munich, Germany, 2013.

[28] M. Rivallin, M. Benmami, A. Gaunand, and A. Kanaev, "Temperature dependence of the titanium oxide sols precipitation kinetics in the sol-gel process," *Chem. Phys. Lett.*, vol. 398, no. 1-3, pp. 157–162, 2004.

[29] P. L. Soo and A. Eisenberg, "Preparation of block copolymer vesicles in solution," *J. Polym. Sci., Part B: Polym. Phys.*, vol. 42, no. 6, p. 923–938, 2004.

[30] M. Rawolle, E. V. Braden, M. A. Niedermeier, D. Magerl, K. Sarkar, T. Fröschl, N. Hüsing, JPerlich, and P. Müller-Buschbaum, "Low temperature route to crystalline titania network-structures in thin films," *ChemPhysChem*, vol. 13, pp. 2412–2417, 2012.

[31] S. Y. Choi, M. Mamak, S. Speakman, N. Chopra, and G. A. Ozin, "Evolution of nanocrystallinity in periodic mesoporous anatase thin films," *Small*, vol. 1, p. 226–232, 2005.

[32] M. A. Niedermeier, *Novel structuring routines of titania films for application in photovoltaics*. PhD thesis, Technische Universität München, Munich, Germany, 2013.

[33] L. L. Hench and J. K. West, "The sol-gel process," *Chem. Rev.*, vol. 90, no. 1, p. 33–72, 1990.

[34] M. Vaseem, A. Umar, and Y. B. Hahn, *Metal Oxide Nanostructures and Their Applications*. American Scientific Publishers, 2010.

[35] R. G. Heideman, P. V. Lambeck, and J. G. E. Gardeniers, "High quality zno layers with adjustable refractive indices for integrated optics applications," *Opt. Mater.*, vol. 4, no. 6, p. 741–755, 1995.

[36] S. Rossbauer, "Organic-metal oxide hybrid phototransistors," Master's thesis, Centre for Plastic Electronics, Imperial College London, Technische Universität München, Munich, Germany, 2011.

[37] A. Janotti and C. G. V. de Walle, "Fundamentals of zinc oxide as a semiconductor," *Rep. Prog. Phys.*, vol. 72, p. 126501 (29pp), 2009.

[38] D. C. Look, D. C. Reynolds, J. R. Sizelove, R. L. Jones, C. W. Litton, G. Cantwe, and W. C. Harsch, "Electricalproperties of bulk zno," *Solid State Commun.*, vol. 105, no. 6, pp. 399–401, 1998.

[39] M. Caglar, S. Ilican, Y. Caglar, and F. Yakuphanoglu, "Electrical conductivity and optical properties of zno nanostructured thin film," *Appl. Surf. Sci.*, vol. 255, p. 4491–4496, 2009.

[40] A. G. Vega-Poot, M. Macías-Montero, J. Idígoras, A. Borrás, A. Barranco, A. R. Gonzalez-Elipe, F. I. Lizama-Tzec, G. Oskam, and J. A. Anta, "Mechanisms of electron transport and recombination in zno nanostructures for dye-sensitized solar cells," *ChemPhysChem*, vol. 15, p. 1088 – 1097, 2014.

[41] H. T. Kim and Y. Kim, "Titanium incorporation in zn_2tio_4 spinel ceramics," *J. Am. Ceram. Soc.*, vol. 84, no. 5, pp. 1081–1086, 2001.

[42] A. C. Chavesa, S. J. G. Limab, R. C. M. U. Araújo, M. Aldeiza, M. A. Maureraa, E. Longoc, P. S. Pizanid, L. G. P. Simoes, L. E. B. Soledadea, A. G. Souzaa, and I. M. G. dos Santos, "Photoluminescence in disordered zn_2tio_4," *J. Solid State Chem.*, vol. 179, p. 985–992, 2006.

[43] R. B. Rankin, A. Campos, H. Tian, R. Siriwardane, A. Roy, J. James, J. Spivey, D. S. Sholl, and J. K. Johnson, "Characterization of bulk structure in zinc orthotitanate: A density functional theory and exafs investigation," *J. Am. Ceram. Soc.*, vol. 91, no. 2, p. 584–590, 2008.

[44] R. L. Millard and R. C. Peterson, "Study of the cubic to tetragonal transition in mg2ti04 and zn2ti04 spinels by ^{17}o mas nmr and rietveld refinement of x-ray diffraction data," *Am. Mineral.*, vol. 80, pp. 885–896, 1995.

[45] Y. Lee, Y. Huang, W. Lee, and F. Shieu, "Formation and transformation of $zntio_3$ prepared by sputtering process," *Thin Solid Films*, vol. 518, p. 7366–7371, 2010.

[46] Z. Ali, S. Ali, I. Ahmad, I. Khan, and H. A. R. Aliabad, "Structural and optoelectronic properties of the zinc titanate perovskite and spinel by modified beckejohnson potential," *Physica B*, vol. 420, p. 54–57, 2013.

[47] J. C. Conesa, "Band structures and nitrogen doping effects in zinc titanate photocatalysts," *Catal. Today*, vol. 208, p. 11–18, 2013.

[48] L. Li, Y. Fan, D. Wang, G. Feng, and D. Xu, "Refractive index dispersion of spinel zn_2tio_4 single crystal," *Crystall Research Technology*, vol. 46, no. 5, p. 475–479, 2011.

[49] K. H. Yoon, J. Cho, and D. H. Kang, "Physical and the photoelectrochemical properties of tio_2-zno system," *Mater. Res. Bull.*, vol. 34, no. 9, p. 1451–1461, 1999.

[50] S. Wenger, *Strategies to Optimizing Dye-Sensitized Solar Cells: Organic Sensitizers, Tandem Device Structures, and Numerical Device Modeling.* PhD thesis, École Polytechnique Fédérale deLaussane, Laussane, Switzerland, 2010.

[51] H. Tsubomura, M. Matsumura, Y. Nomura, and T. Amamiya, "Dye sensitised zinc oxide: aqueous electrolyte: platinum photocell," *Nature*, vol. 261, p. 402–403, 1976.

[52] J. Franck, "Elementary processes of photochemical reactions," *Trans. Faraday Soc.*, vol. 21, p. 536–542, 1926.

[53] E. Condon, "A theory of intensity distribution in band systems," *Phys. Rev.*, vol. 28, p. 1182–1201, 1926.

[54] A. Linsebigler, G. Lu, and J. Yates, "Photocatalysis on tio2 surfaces: Principles, mechanisms, and selected results," *Chem. Rev.*, vol. 95, no. 3, pp. 735–758, 1995.

[55] H. Gerischer and F. Willig, "Reaction of excited dye molecules at electrodes," *Physical and Chemical Applications of Dyestuffs, Topics in Current Chemistry*, vol. 61, p. 31–84, 1976.

[56] H. J. Snaith, "Estimating the maximum attainable efficiency in dye-sensitized solar cells," *Adv. Funct. Mater.*, vol. 20, p. 13–19, 2010.

[57] H. M. Cheng and W. F. Hsieh, "Electron transfer properties of organic dye-sensitized solar cells based on indoline sensitizers with zno nanoparticles," *Nanotechnology*, vol. 21, p. 485202 (8pp), 2010.

[58] G. Boschloo and A. Hagfeldt, "Characteristics of the iodide/triiodide redox mediator in dye-sensitized solar cells," *Acc. Chem. Res.*, vol. 42, no. 11, pp. 1819–1826, 2009.

[59] G. G. G. M. N. Hemamali and G. R. A. Kumara, "Solid state solar cells based on tio2 sensitized with natural pigment extracted from the anthurium," *International Journal of Scientific and Research Publications*, vol. 3, no. 12, pp. 1–5, 2013.

[60] I. Chung, B. Lee, J. He, R. H. Chang, and M. G. Kanatzidis, "All-solid-state dye-sensitized solar cells with high efficiency," *Nature*, vol. 485, p. 486–489, 2012.

[61] M. Rawolle, K. Sarkar, M. A. Niedermeier, M. Schindler, P. Lellig, J. S. Gutmann, J. F. Moulin, M. Haese-Seiller, A. S. Wochnik, C. Scheu, and P. Müller-Buschbaum, "Infiltration of polymer hole-conductor into mesoporous titania structures for solid-state dye-sensitized solar cells," *ACS Appl. Mater. Interfaces*, vol. 5, p. 719–729, December 2013.

[62] S. J. Moon, *Solid-State Sensitized Heterojunction Solar Cells: Effect of Sensitizing Systems on Performance and Stability.* PhD thesis, École Polytechnique Fédérale de Laussane, Laussane, Switzerland, 2011.

[63] H. J. Snaith, R. Humphry-Baker, P. Chen, I. Cesar, S. M. Zakeeruddin, and M. Grätzel, "Charge collection and pore filling in solid-state dye-sensitized solar-cells," *Nanotechnology*, vol. 19, no. 42, pp. 424003–1–12, 2008.

[64] B. E. Hardin, H. J. Snaith, and M. D. McGehee, "The renaissance of dye-sensitized solar cells," *Nat. Photonics*, vol. 6, no. 3, p. 162–169, 2012.

[65] M. Tolan, *X-Ray Scattering from Soft-Matter Thin Films.* Springer Berlin Heidelberg, 1999.

[66] H. Dosch, B. Batterman, and D. Wack, "Depth-controlled grazing-incidence diffraction of synchrotron x-radiation," *Phys. Rev. Lett.*, vol. 56, no. 11, pp. 1144–1147, 1986.

[67] L. Spieß, R. Schwarzer, H. Behnken, and G. Teichert, *Moderne Röntgenbeugung: Röntgendiffraktometrie für Materialwissenschaftler, Physiker und Chemiker.* Teubner, 1 ed., 2005.

[68] A. Guinier, *X-ray diffraction in crystals, imperfect crystals, and amorphous bodies.* Dover Publications, 1994.

[69] U. Holzwarth and N. Gibson, "The scherrer equation versus the 'debye-scherrer equation'," *Nat. Nanotechnol.*, vol. 6, p. 534, 2011.

[70] R. Lazzari, "Isgisaxs: a program for grazing-incidence small-angle x-ray scattering analysis of supported islands," *J. Appl. Crystallogr.*, vol. 35, no. Part 4, pp. 406–421, 2002.

[71] P. Müller-Buschbaum, *Polymer Surfaces and Interfaces: Characterization, Modification and Applications*, ch. Structure Determination in Thin Film Geometry Using Grazing Incidence Small-Angle Scattering, p. 17–46. Springer Berlin Heidelberg, 2008.

[72] P. Müller-Buschbaum, *Applications of Synchrotron Light to Scattering and Diffraction in Materials and Life Sciences*, vol. 776 of *Lecture Notes in Physics*, ch. A Basic Introduction to Grazing Incidence Small-Angle XRay Scattering, p. 61–89. Springer Berlin Heidelberg, 2009.

[73] J. L. Baker, L. H. Jimison, S. Mannsfeld, S. Volkman, S. Yin, V. Subramanian, A. Salleo, A. P. Alivisatos, and M. F. Toney, "Quantification of thin film crystallographic orientation using x-ray diffraction with an area detector," *Langmuir*, vol. 26, no. 11, p. 9146–9151, 2010.

[74] D. M. Smilgies, "Scherrer grain-size analysis adapted to grazing-incidence scattering with area detectors," *J. Appl. Crystallogr.*, vol. 42, p. 1030–1034, 2009.

[75] Y. Yoneda, "Anomalous surface reflection of x rays," *Phys. Rev.*, vol. 131, no. 5, pp. 2010–2013, 1963.

[76] L. Reimer and P. W. Hawkes, "Scanning electron microscopy: Principles of image formation and microanalysis," tech. rep., Springer Berlin Heidelberg, 2nd ed., 1998.

[77] D. Nečas and P. Klapetek, "Gwyddion: an open-source software for spm data analysis," *Cent. Eur. J. Phys.*, vol. 10, no. 1, pp. 181–188, 2012.

[78] B. P. Dinte, G. S. Watson, J. F. Dobson, and S. Myhra, "Artefacts in non-contact mode force microscopy: The role of adsorbed moisture," *Ultramicroscopy*, vol. 63, pp. 115–124, 1996.

[79] R. Meier, *Novel Structuring Routines for Organic Photovoltaics*. PhD thesis, Technische Universität München, Munich, Germany, 2012.

[80] M. Rawolle, V. Körstgens, M. A. Ruderer, E. Metwalli, S. Guo, G. Herzog, G. Benecke, M. Schwartzkopf, A. Buffet, J. Perlich, S. V. Roth, , and P. Müller-Buschbaum, "Comparison of grazing incidence small angle x-ray scattering of a titania sponge structure at the beamlines bw4 (doris iii) and p03 (petra iii)," *Rev. Sci. Instrum.*, vol. 83, no. 10, pp. 106104–1–3, 2012.

[81] J. Tauc, R. Grigorovici, and A. Vancu, "Optical properties and electronic structure of amorphous germanium," *physica status solidi (b)*, vol. 15, no. 2, p. 627–637, 1966.

[82] B. S. Rao, B. R. Kumar, V. R. Reddy, and T. S. Rao, "Preparation ans characterization of cds nanoparticles by chemical co-precipitation technique," *Chalcogenide Letters*, vol. 8, p. 177–185, 2011.

[83] Srikant and D. R. Clarke, "On the optical band gap of zinc oxide," *J. Appl. Phys.*, vol. 83, p. 5447, 1998.

[84] L. Jing, Y. Qu, B. Wang, S. Li, B. Jiang, L. Yang, W. Fu, H. Fu, and J. Sun, "Review of photoluminescence performance of nano-sized semiconductor materials and its relationships with photocatalytic activity," *Solar Energy Materials & Solar Cells*, vol. 90, no. 12, pp. 1773–1787, 2006.

[85] P. Life and A. Sciences, "Ft-ir spectroscopy attenuated total reflectance (atr)," tech. rep., Perkin Elmer, 2005.

[86] J. C. Russ, M. A. Frs, R. Kiessling, and J. Charles, *Fundamentals of Energy Dispersive X-ray Analysis*. Elsevier, 1984.

[87] T. Ishioka, Y. Shibata, M. Takahashi, I. Kanesaka, Y. Kitagawa, and K. T. Nakamura, "Vibrational spectra and structures of zinc carboxylates i - zinc acetate dihydrate," *Spectrochim. Acta, Part A*, vol. 54, p. 1827–1836, 1998.

[88] R. Rossmanith, C. K. Weiss, J. Geserick, N. Hüsing, U. Hörmann, U. Kaiser, and K. Landfester, "Porous anatase nanoparticles with high specific surface area prepared by miniemulsion technique," *Chem. Mater.*, vol. 20, no. 18, p. 5768–5780, 2008.

[89] J. Geserick, *Synthese mesoskopisch organisierter Nanopartikel*. PhD thesis, Universität Ulm, Ulm, Germany, 2009.

[90] Y. Denkwitz, M. Makosch, J. Geserick, U. Hörmann, S. Selve, U. Kaiser, N. Hüsing, and R. J. Behm, "Influence of the crystalline phase and surface area of the tio_2 support on the co oxidation activity of mesoporous au/tio_2 catalysts," *Appl. Catal., B*, vol. 91, no. 1-2, pp. 470–480, 2009.

[91] S. Ito, H. Miura, S. Uchida, M. Takata, K. Sumioka, P. Liska, P. Comte, P. Péchy, and M. Grätzel, "High-conversion-efficiency organic dye-sensitized solar cells with a novel indoline dye," *Chem. Commun.*, p. 5194–5196, 2008.

[92] C. Y. Lin, Y. H. Lai, H. W. Chen, J. G. Chen, C. W. Kung, R. Vittala, and K. C. Ho, "Highly efficient dye-sensitized solar cell with a zno nanosheet-based photoanode," *Energy Environ. Sci.*, vol. 4, pp. 3448–3455, 2011.

[93] Y. Ren, Y. Z. Zheng, J. Zhao, J. F. Chen, W. Zhou, and X. Tao, "A comparative study on indoline dye- and ruthenium complex-sensitized hierarchically structured zno solar cells," *Electrochem. Commun.*, vol. 16, p. 57–60, January 2012.

[94] S. Ito, S. M. Zakeeruddin, R. Humphry-Baker, P. Liska, R. Charvet, P. Comte, M. K. Nazeeruddin, P. Péchy, M. Takata, H. Miura, S. Uchida, and M. Grätzel, "High-efficiency organic-dye-sensitized solar cells controlled by nanocrystalline-tio2 electrode thickness," *Adv. Mater.*, vol. 18, p. 1202–1205, 2006.

[95] G. Li, V. Shrotriya, Y. Yao, J. Huang, and Y. Yang, "Manipulating regioregular poly(3-hexylthiophene): [6,6]-phenyl-c-61-butyric acid methyl ester blends - route towards high efficiency polymer solar cells," *J. Mater. Chem.*, vol. 17, no. 30, pp. 3126–3140, 2007.

[96] K. Coakley and M. McGehee, "Photovoltaic cells made from conjugated polymers infiltrated into mesoporous titania," *Appl. Phys. Lett.*, vol. 83, no. 16, pp. 3380–3382, 2003.

[97] J. A. Chang, J. H. Rhee, S. H. Im, Y. H. Lee, H. J. Kim, S. I. Seok, M. K. Nazeeruddin, and M. Grätzel, "High-performance nanostructured inorganic-organic heterojunction solar cells," *Nano Lett.*, vol. 10, no. 7, pp. 2609–2612, 2010.

[98] A. Nathan, "Tuning conductivity of thin conjugated polymer films and its application," Master's thesis, Technische Universität München, Munich,, Germany, 2010.

[99] S. Ito, P. Chen, P. Comte, M. K. Nazeeruddin, P. Liska, P. Péchy, and M. Grätzel, "Fabrication of screen-printing pastes from tio_2 powders for dye-sensitised solar cells," *Prog. Photovolt: Res. Appl.*, vol. 15, p. 603–612, May 2007.

[100] J. Kim, J. K. Koh, B. Kim, S. H. Ahn, H. Ahn, D. Y. Ryu, J. H. Kim, and E. Kim, "Enhanced performance of i2-free solid-state dye-sensitized solar cells with conductive polymer up to 6.8 pp. 4633–4639, 2011.

[101] L. Schmidt-Mende and M. Grätzel, "Tio2 pore-filling and its effect on the efficiency of solid-state dye-sensitized solar cells," *Thin Solid Films*, vol. 500, no. 1-2, pp. 296–301, 2006.

[102] P. Müller-Buschbaum, "Influence of surface cleaning on dewetting of thin polystyrene films," *The European Physical Journal E*, vol. 12, no. 3, p. 443–448, 2003.

[103] C. J. Lawrence, "The mechanics of spin coating of polymer films," *Phys. Fluids*, vol. 31, p. 2786–2795, 1988.

[104] D. W. Schubert and T. Dunkel, "Spin coating from a molecular point of view: its concentration regimes, influence of molar mass and distribution," *Mater. Res. Innovations*, vol. 7, no. 5, p. 314–321, 2003.

[105] I. Mansoor and B. Stoeber, "Piv measurements of flow in drying polymer solutions during solvent casting," *Exp. Fluids*, vol. 50, no. 5, pp. 1409–1420, 2011.

[106] E. J. Lavernia and Y. Wu, *Spray atomization and deposition*. Wiley, 1996.

[107] D. Perednis and L. J. Gauckler, "Thin film deposition using spray pyrolysis," *J. Electroceram.*, vol. 14, no. 2, p. 103–111, 2005.

[108] J. B. Mooney and S. B. Radding, "Spray pyrolysis processing," *Annu. Rev. Mater. Sci.*, vol. 12, no. 1, p. 81–101, 1982.

[109] J. C. Viguié and J. Spitz, "Chemical vapor deposition at low temperatures," *J. Electrochem. Soc.*, vol. 122, no. 4, p. 585–588, 1975.

[110] P. Müller-Buschbaum, "Surfaces and interfaces, lecture - polymer physics ii - summer term 2014," tech. rep., Technische Universität München, 2014.

[111] H. Yu, S. Zhang, H. Zhao, G. Will, and P. Liu, "An efficient and low-cost tio2 compact layer for performance improvement of dye-sensitized solar cells," *Electrochim. Acta*, vol. 54, no. 4, p. 1319–1324, 2009.

[112] C. Panatarani, W. Lenggoro, and K. Okuyama, "Synthesis of single crystalline zno nanoparticles by salt-assisted spray pyrolysis," *Journal of Nanoparticle Research*, vol. 5, p. 47–53, 2003.

[113] B. Weintraub, Z. Zhou, Y. Libc, and Y. Deng, "Solution synthesis of one-dimensional zno nanomaterials and their applications," *Nanoscale*, vol. 2, p. 1573–1587, May 2010.

[114] P. Yang, H. Yan, S. Mao, R. Russo, J. Johnson, R. Saykally, N. Morris, J. Pham, R. He, and H. J. Choi, "Controlled growth of zno nanowires and their optical properties," *Adv. Funct. Mater.*, vol. 12, pp. 323–331, May 2002.

[115] S. Dilger, C. Lizandara-Pueyo, M. Krumm, and S. Polarz, "Hierarchical zinc oxide materials with multiple porosity prepared by ultrafast temperature gradient chemical gas-phase synthesisnon," *Adv. Mater.*, vol. 24, p. 543–548, 2012.

[116] Z. L. Wang and J. Song, "Piezoelectric nanogenerators based on zinc oxide nanowire arrays," *Science*, vol. 312, no. 5771, pp. 242–246, 2006.

[117] A. Becheri, M. Dürr, P. L. Nostro, and P. Baglioni, "Synthesis and characterization of zinc oxide nanoparticles: application to textiles as uv-absorbers," *J Nanopart Res*, vol. 10, p. 679–689, 2008.

[118] H. Bahadur, A. K. Srivastava, D. haranath, H. Chander, A. Basu, S. B. Samanta, K. N. Sood, R. Kishore, R. K. Sharma, Rashmi, V. Bhatt, P. Pal, and S. Chandra, "Nanostructured zno films by sol-gel process," *Indian J. Pure Appl. Phys.*, vol. 45, pp. 395–399, April 2007.

[119] Z. Fan and J. G. Lu, "Zinc oxide nanostructures: Synthesis and properties," Department of Chemical Engineering and Materials Science & Department of Electrical Engineering and Computer Science University of California, Irvine, CA 92697, USA, April 2005.

[120] J. J. Schneider, R. C. Hoffmann, J. Engstler, O. Soffke, W. Jaegermann, A. Issanin, and A. Klyszcz, "A printed and flexible field-effect transistor device with nanoscale zinc oxide as active semiconductor material," *Adv. Mater.*, vol. 20, p. 3383–3387, July 2008.

[121] C. M. Ghimbeu, J. Schoonman, M. Lumbreras, and M. Siadat, "Electrostatic spray deposited zinc oxide films for gas sensor applications," *Appl. Surf. Sci.*, vol. 253, p. 7483–7489, 2007.

[122] A. Bashir, P. H. Wöbkenberg, J. Smith, J. M. Ball, G. Adamopoulos, D. D. C. Bradley, and T. D. Anthopoulos, "High-performance zinc oxide transistors and circuits fabricated by spray pyrolysis in ambient atmosphere," *Adv. Mater.*, vol. 21, p. 2226–2231, 2009.

[123] K. S. Kim, H. Jeong, M. S. Jeong, and G. Y. Jung, "Polymer-templated hydrothermal growth of vertically aligned single-crystal zno nanorods and morpho-

logical transformations using structural polarity," *Adv. Funct. Mater.*, vol. 20, p. 3055–3063, 2010.

[124] L. Xiao-bo, S. Hong-lie, Z. Hui, and L. Bin-bin, "Optical properties of nanosized zno films prepared by sol-gel process," *Trans. Nonferrous Met. Soc. China*, vol. 17, pp. s814–s817, 2007.

[125] A. M. Peiró, P. Ravirajan, K. Govender, D. S. Boyle, P. O'Brien, D. D. C. Bradley, J. Nelson, and J. R. Durrant, "Hybrid polymer/metal oxide solar cells based on zno columnar structures," *J. Mater. Chem.*, vol. 16, p. 2088–2096, 2006.

[126] J. Wu, Z. Lan, S. Hao, P. Li, J. Lin, M. Huang, L. Fang, and Y. Huang, "Progress on the electrolytes for dye-sensitized solar cells," *Pure Appl. Chem.*, vol. 80, no. 11, p. 2241–2258, 2008.

[127] A. Sacco, A. Lamberti, R. Gazia, S. Bianco, D. Manfredi, N. Shahzad, F. Cappelluti, S. Mac, and E. Tresso, "High efficiency dye-sensitized solar cells exploiting sponge-like zno nanostructures," *Phys. Chem. Chem. Phys.*, vol. 14, pp. 16203–16208, 2012.

[128] L. M. Peter, "The grätzel cell: Where next?," *Jornal of Physical Chemistry Letters*, vol. 2, p. 1861–1867, 2011.

[129] T. W. Hamann, A. B. F. Martinson, J. W. Elam, M. J. Pellin, and J. T. Hupp, "Aerogel templated zno dye-sensitized solar cells," *Adv. Mater.*, vol. 20, p. 1560–1564, 2008.

[130] M. S. Tirumkudulu and W. B. Russel, "Role of capillary stresses in film formation," *Langmuir*, vol. 20, pp. 2947–2961, 2004.

[131] S. Seghaier, N. Kamoun, R. Brini, and A. B. Amara, "Structural and optical properties of pbs thin films deposited by chemical bath deposition," *Mater. Chem. Phys.*, vol. 97, p. 71–80, 2006.

[132] D. Cahen, G. Hodes, M. Grätzel, J. F. Guillemoles, and I. Riess, "Nature of photovoltaic action in dye-sensitized solar cells," *J. Phys. Chem. B*, vol. 104, no. 9, pp. 2053–2059, 2000.

[133] C. M. Sim, Y. J. Hong, and Y. C. Kang, "Electrochemical properties of yolk-shell, hollow, and dense wo_3 particles prepared by using spray pyrolysis," *ChemSusChem*, vol. 6, p. 1320–1325, 2013.

[134] A. Abdellah, K. S. Virdi, R. Meier, M. Döblinger, P. Müller-Buschbaum, C. Scheu, P. Lugli, and G. Scarpa, "Successive spray deposition of p3ht/pcbm organic photoactive layers: Material composition and device characteristics," *Adv. Funct. Mater.*, vol. 22, p. 4078–4086, 2012.

[135] Y. Zhang, Y. H. Wen, J. C. Zheng, and Z. Z. Zhuc, "Direct to indirect band gap transition in ultrathin zno nanowires under uniaxial compression," *Appl. Phys. Lett.*, vol. 94, p. 113114, 2009.

[136] P. S. Hale, L. M. Maddox, J. G. Shapter, and N. H. Voelcker, "Growth kinetics and modeling of zno nanoparticles," *J. Chem. Educ.*, vol. 82, no. 5, pp. 775–778, 2005.

[137] N. L. Tarwal, V. M. Khot, N. S. Harale, S. A. Pawar, S. B. Pawar, V. B. Patil, and P. S. Patil, "Spray deposited superhydrophobic zno coatings via seed assisted growth," *Surface & Coatings Technology*, vol. 206, p. 1336–1341, 2011.

[138] R. Bhattacharjee and I. M. Hung, "A sno_2 and zno nanocomposite photoanodes in dye-sensitized solar cells," *ECS Solid State Letters*, vol. 2, pp. Q101–Q104, 2013.

[139] B. E. Hardin, E. T. Hoke, P. B. Armstrong, J. H. Yum, P. Comte, T. Torres, J. M. J. Fréchet, M. K. Nazeeruddin, M. Grätzel, and M. D. McGehee, "Increased light harvesting in dye-sensitized solar cells with energy relay dyes," *Nat. Photonics*, vol. 3, pp. 406–411, 2009.

[140] L. Schmidt-Mende and J. L. MacManus-Driscoll, "Zno – nanostructures, defects, and devices," *Materials today*, vol. 10, no. 5, pp. 40–48, 2007.

[141] M. Willander, O. Nur, J. R. Sadaf, M. I. Qadir, S. Zaman, A. Zainelabdin, N. Bano, and I. Hussain, "Luminescence from zinc oxide nanostructures and polymers and their hybrid devices," *Materials*, vol. 3, pp. 2643–2667, 2010.

[142] M. D. McCluskey and S. J. Jokela, "Defects in zno," *J. Appl. Phys.*, vol. 106, p. 071101, 2009.

[143] S. S. Kurbanov, G. N. Panin, T. W. Kim, and T. W. Kang, "Strong violet luminescence from zno nanocrystals grown by the low-temperature chemical solution deposition," *J. Lumin.*, vol. 129, pp. 1099–1104, 2009.

[144] T. M. Borsmeth, B. G. Svensson, and A. Y. Kuznetsov, "Indentification of oxygen and zinc vacancy optical signals in zno," *Appl. Phys. Lett.*, vol. 89, p. 262112, 2006.

[145] J. S. Kang, H. S. Kang, S. S. Pang, E. S. Shim, and S. Y. Lee, "Investigation on the origin of green luminescence from laser-ablated zno thin film," *Thin Solid Films*, vol. 443, pp. 5–8, 2003.

[146] R. Katoh, A. Huijser, K. Hara, T. J. Savenije, and L. D. A. Siebbeles, "Effect of the particle size on the electron injection efficiency in dye-sensitized nanocrystalline tio_2 films studied by time-resolved microwave conductivity (trmc) measurements," *J. Phys. Chem. C*, vol. 111, pp. 10741–10746, 2007.

[147] J. Liu, G. Cao, Z. Yang, D. Wang, D. Dubois, X. Zhou, G. L. Graff, L. R. Pederson, and J. G. Zhang, "Oriented nanostructures for energy conversion and storage," *ChemSusChem*, vol. 1, p. 676 – 697, 2008.

[148] X. Li, X. San, Y. Zhang, T. Ichii, M. Meng, Y. Tan, and N. Tsubaki, "Direct synthesis of ethanol from dimethyl ether and syngas over combined h-mordenite and cu/zno catalysts," *ChemSusChem*, vol. 3, p. 1192–1199, 2010.

[149] T. W. Lee, J. Hwang, and S. Y. Min, "Highly efficient hybrid inorganic–organic light-emitting diodes by using air-stable metal oxides and a thick emitting layer," *ChemSusChem*, vol. 3, p. 1021–1023, July 2010.

[150] S. Navalón, A. Dhakshinamoorthy, M. Álvaro, and H. Garcia, "Photocatalytic co2 reduction using non-titanium metal oxides and sulfides," *ChemSusChem*, vol. 6, p. 562–577, March 2013.

[151] J. Bai, X. Xu, L. Xu, J. Cui, D. Huang, W. Chen, Y. Cheng, Y. Shen, and M. Wang, "Potassium-doped zinc oxide as photocathode material in dye-sensitized solar cells," *ChemSusChem*, vol. 6, p. 622–629, March 2013.

[152] J. Bouclé, H. J. Snaith, and N. C. Greenham, "Simple approach to hybrid polymer/porous metal oxide solar cells from solution-processed zno nanocrystals," *J. Phys. Chem. C*, vol. 114, p. 3664–3674, February 2010.

[153] B. O'Regan, D. T. Schwartz, S. M. Zakeeruddin, and M. Grätzel, "Electrodeposited nanocomposite n-p heterojunctions for solid-state dye-sensitized photovoltaics," *Adv. Mater.*, vol. 12, pp. 1263–1267, 2000.

[154] S. Chu, G. Wang, W. Zhou, Y. Lin, L. Chernyak, J. Zhao, J. Kong, L. Li, J. Ren, and J. Liu, "Electrically pumped waveguide lasing from zno nanowires," *Nat. Nanotechnol.*, vol. 6, pp. 506–510, 2011.

[155] A. Tsukazaki, A. Ohtomo, T. Onuma, M. Ohtani, T. Makino, M. Sumiya, K. Ohtani, S. F. Chichibu, S. Fuke, Y. Segawa, H. Ohno, H. Koinuma, and M. Kawasaki, "Repeated temperature modulation epitaxy for p-type doping and light-emitting diode based on zno," *Nat. Mater.*, vol. 4, pp. 42–46, 2005.

[156] F. Sun, C. X. Shan, B. H. Li, Z. Z. Zhang, D. Z. Shen, Z. Y. Zhang, and D. Fan, "A reproducible route to p-zno films and their application in light-emitting devices," *Opt. Lett.*, vol. 36, no. 4, pp. 499–501, 2011.

[157] F. Nunzi, L. Storchi, M. Manca, R. Giannuzzi, G. Gigli, and F. D. Angelis, "Shape and morphology effects on the electronic structure of tio_2 nanostructures: From nanocrystals to nanorods," *ACS Appl. Mater. Interfaces*, vol. 6, p. 2471–2478, February 2014.

[158] H. Yu, Z. Zhang, M. Han, X. Hao, and F. Zhu, "A general low-temperature route for large-scale fabrication of highly oriented zno nanorod/nanotube arrays," *J. Am. Chem. Soc.*, vol. 127, no. 8, p. 2378–2379, 2005.

[159] M. M. Brewster, X. Zhou, M. Y. Lua, and S. Gradečak, "The interplay of structural and optical properties in individual zno nanostructures," *Nanoscale*, vol. 4, pp. 1455–1462, 2012.

[160] H. J. Fan, Y. Yang, and M. Zacharias, "Zno-based ternary compound nanotubes and nanowires," *J. Mater. Chem.*, vol. 19, pp. 885–900, 2009.

[161] M. Ahmad and J. Zhu, "Zno based advanced functional nanostructures: synthesis, properties and applications," *J. Mater. Chem.*, vol. 21, pp. 599–614, 2011.

[162] C. T. Wu and J. J. Wu, "Room-temperature synthesis of hierarchical nanostructures on zno nanowire anodes for dye-sensitized solar cells," *J. Mater. Chem.*, vol. 21, pp. 13605–13610, 2011.

[163] Y. Liu, Z. Chen, Z. Kang, I. Bello, X. Fan, I. Shafiq, W. Zhang, and S. T. Lee, "Self-catalytic synthesis of zno tetrapods, nanotetraspikes, and nanowires in air at atmospheric pressure," *J. Phys. Chem. C*, vol. 112, no. 25, p. 9214–9218, 2008.

[164] X. Gao, X. Li, W. Gao, J. Qiu, X. Gan, C. Wang, and X. Lenga, "Nanocrystalline/nanoporous zno spheres, hexapods and disks transformed from zinc fluorohydroxide, their self-assembly and patterned growth," *CrystEngComm*, vol. 13, pp. 4741–4747, 2011.

[165] J. Perlich, G. Kaune, M. Memesa, J. S. Gutmann, and P. Müller-Buschbaum, "Sponge-like structures for application in photovoltaics," *Philos. Trans. R. Soc. London Ser. A*, vol. 367, p. 1783– 1798, 2009.

[166] G. Kaune, M. Memesa, R. Meier, M. A. Ruderer, A. Diethert, S. V. Roth, M. D'Acunzi, J. S. Gutmann, and P. Müller-Buschbaum, "Hierarchically structured titania films prepared by polymer/colloidal templating," *ACS Appl. Mater. Interfaces*, vol. 12, p. 2862–2869, 2009.

[167] M. Rawolle, M. A. Ruderer, S. M. Prams, Q. Zhong, D. Magerl, J. Perlich, S. V. Roth, P. Lellig, J. S. Gutmann, and P. Müller-Buschbaum, "Nanostructuring of titania thin films by a combination of microfluidics and block-copolymer-based sol–gel templating," *Small*, vol. 7, no. 7, p. 884–891, 2011.

[168] M. Nedelcu, S. Guldin, M. C. Orilall, J. Lee, S. Hüttner, E. J. W. Crossland, S. C. Warren, C. Ducati, P. R. Laity, D. Eder, U. Wiesner, U. Steinerabd, and H. J. Snaith, "Monolithic route to efficient dye-sensitized solar cells employing diblock copolymers for mesoporous tio_2," *J. Mater. Chem.*, vol. 20, pp. 1261–1268, 2010.

[169] P. Docampo, S. Guldin, M. Stefik, P. Tiwana, M. C. Orilall, S. Hüttner, H. Sai, U. Wiesner, U. Steiner, and H. J. Snaith, "Control of solid-state dye-sensitized solar cell performance by block-copolymer-directed tio2 synthesis," *Adv. Funct. Mater.*, vol. 20, p. 1787–1796, 2010.

[170] L. Chuenchom, R. Kraehnert, and B. M. Smarsly, "Recent progress in soft-templating of porous carbon materials," *Soft Matter*, vol. 8, pp. 10801–10812, 2012.

[171] K. Sarkar, M. Rawolle, M. A. Niedermeier, W. Wang, E. M. Herzig, V. Körstgens, A. Buffet, S. V. Roth, and P. Müller-Buschbaum, "A quantitative approach to tune metal oxide network morphology based on grazing-incidence small-angle x-ray scattering investigations," *J. Appl. Cryst.*, vol. 47, p. 76–83, 2014.

[172] H. Shen, L. Zhang, and A. Eisenberg, "Multiple ph-induced morphological changes in aggregates of polystyrene-block-poly(4-vinylpyridine) in dmf/h_2o mixtures," *J. Am. Chem. Soc.*, vol. 121, no. 12, p. 2728–2740, 1999.

[173] K. Yu and A. Eisenberg, "Bilayer morphologies of self-assembled crew-cut aggregates of amphiphilic ps-b-peo diblock copolymers in solution," *Macromolecules*, vol. 31, no. 11, p. 3509–3518, 1998.

[174] Y. Mai and A. Eisenberg, "Controlled incorporation of particles into the central portion of vesicle walls," *J. Am. Chem. Soc.*, vol. 132, no. 29, p. 10078–10084, 2010.

[175] M. D. McGehee, "Nanostructured organic–inorganic hybrid solar cells," *MRS Bulletin*, vol. 34, pp. 95–100, 2009.

[176] Z. R. Khan, M. S. Khan, M. Zulfequar, and M. S. Khan, "Optical and structural properties of zno thin films fabricated by sol-gel method," *Materials Sciences and Applications*, vol. 2, pp. 340–345, 2011.

[177] V. Ischenko, S. Polarz, D. Grote, V. Stavarache, K. Fink, and M. Driess, "Zinc oxide nanoparticles with defects," *Adv. Funct. Mater.*, vol. 15, p. 1945–1954, 2005.

[178] C. Matranga, L. Chen, M. Smith, E. B. J. K. Johnson, and B. Bockrath, "Trapped co2 in carbon nanotube bundles," *J. Phys. Chem. B*, vol. 107, no. 47, p. 12930–12941, 2003.

[179] Y. Wang, Y. Li, Z. Zhou, X. Zu, and Y. Deng, "Evolution of the zinc compound nanostructures in zinc acetate single-source solution," *Journal of Nanoparticle Research*, vol. 13, pp. 5193–5202, 2011.

[180] Y. F. Zhu, D. H. Fan, and W. Z. Shen, "A general chemical conversion route to synthesize various zno-based core/shell structures," *J. Phys. Chem. C*, vol. 112, no. 28, p. 10402–10406, 2008.

[181] N. Krins, J. D. Bass, B. Julián-López, P. Evrar, C. Boissière, L. Nicole, C. Sanchez, H. Amenitsch, and D. Grosso, "Mesoporous sio_2 thin films containing photoluminescent zno nanoparticles and simultaneous saxs/waxs/ellipsometry experiments," *J. Mater. Chem.*, vol. 21, pp. 1139–1146, 2011.

[182] G. Baldinozzi, G. Muller, C. Laberty-Robert, D. Gosse, D. Simeone, and C. Sanchez, "Probing properties, stability, and performances of hierarchical mesoporous materials with nanoscale interfaces," *J. Phys. Chem. C*, vol. 116, no. 14, p. 7658–7663, 2012.

[183] G. Kaune, M. Haese-Seiller, R. Kampmann, J. F. Moulin, Q. Zhong, and P. Müller-Buschbaum, "Tof-gisans investigation of polymer infiltration in mesoporous tio2 films for photovoltaic applications," *J. Polym. Sci., Part B: Polym. Phys.*, vol. 48, no. 14, p. 1628–1635, 2010.

[184] J. Perlich, M. Memesa, A. Diethert, E. Metwalli, W. Wang, S. V. Roth, A. Timmann, J. S. Gutmann, and P. Müller-Buschbaum, "Layer-by-layer fabrication of hierarchical structures in sol–gel templated thin titania films," *physica status solidi (RRL) - Rapid Research Letters*, vol. 3, no. 4, p. 118–120, 2009.

[185] M. Memesa, S. Weber, S. Lenz, J. Perlich, R. Berger, P. Müller-Buschbaum, and J. S. Gutmann, "Integrated blocking layers for hybrid organic solar cells," *Energy Environ. Sci.*, vol. 2, pp. 783–790, 2009.

[186] J. Perlich, M. Memesa, A. Diethert, E. Metwalli, W. Wang, S. V. Roth, A. Timmann, J. S. Gutmann, and P. Müller-Buschbaum, "Preservation of the morphology of a self-encapsulated thin titania film in a functional multilayer stack: An x-ray scattering study," *ChemPhysChem*, vol. 10, p. 799–805, 2009.

[187] S. Lepoutre, B. J.-L. pez, C. Sanchez, H. Amenitsch, M. Linden, and D. Grosso, "Nanocasted mesoporous nanocrystalline zno thin films.," *J. Mater. Chem.*, vol. 20, pp. 537–542, 2010.

[188] J. W. Li, L. W. Yang, Z. F. Zhou, P. K. Chu, X. H. Wang, J. Zhou, L. T. Li, and C. Q. Sun, "Bandgap modulation in zno by size, pressure, and temperature," *J. Phys. Chem. C*, vol. 114, no. 31, p. 13370–13374, 2010.

[189] H. Wang, H. Y. Wang, B. R. Gao, L. Wang, Z. Y. Yang, X. B. Du, Q. D. Chen, J. F. Song, and H. B. Sun, "Exciton diffusion and charge transfer dynamics in nano phase-separated p3ht/pcbm blend films," *Nanoscale*, vol. 3, pp. 2280–2285, 2011.

[190] J. Guo, H. Ohkita, H. Benten, and S. Ito, "Charge generation and recombination dynamics in poly(3-hexylthiophene)/fullerene blend films with different regioregularities and morphologies," *J. Am. Ceram. Soc.*, vol. 132, p. 6154–6164, 2010.

[191] M. Rawolle, M. A. Niedermeier, G. Kaune, J. Perlich, P. Lellig, M. Memesa, Y. J. Cheng, J. S. Gutmann, and P. Müller-Buschbaum, "Fabrication and characterization of nanostructured titania films with integrated function from inorganic–organic hybrid materials," *Chem. Soc. Rev.*, vol. 41, pp. 5131–5142, 2012.

[192] W. C. Chang, C. H. Lee, W. C. Yu, and C. M. Lin, "Optimization of dye adsorption time and film thickness for efficient zno dye-sensitized solar cells with high at-rest stability," *Nanoscale Res Lett.*, vol. 7:688, no. 1, pp. 1–10, 2012.

[193] S. Futemvong, N. Hongsith, D. Wongratanaphisan, A. Gardchareon, and S. Choopun, "Energy conversion efficiency improvement of zno dye-sensitized solar cells by dye re-adsorption and n-p junction technique," *Chiang Mai J. Sci.*, vol. 40, no. 4, pp. 783–788, 2013.

[194] P. Teesetsopon, S. Kumar, and J. Dutta, "Photoelectrode optimization of zinc oxide nanoparticle based dye-sensitized solar cell by thermal treatment," *Int. J. Electrochem. Sci.*, vol. 7, pp. 4988 – 4999, 2012.

[195] T. M. El-Agez, A. A. E. Tayyan, A. Al-Kahlout, S. A. Taya, and M. S. Abdel-Latif, "Dye-sensitized solar cells based on zno films and natural dyes," *International Journal of Materials and Chemistry*, vol. 2, no. 3, pp. 105–110, 2012.

[196] B. Nandan, M. K. Vyas, M. Böhme, and M. Stamm, "Composition-dependent morphological transitions and pathways in switching of fine structure in thin films of block copolymer supramolecular assemblies," *Macromolecules*, vol. 43, pp. 2463–2473, 2010.

[197] S. Miller, G. Fanchini, Y. Y. Lin, C. Li, C. W. Chen, W. F. Sub, and M. Chhowallaa, "Investigation of nanoscale morphological changes in organic photovoltaics during solvent vapor annealing," *J. Mater. Chem.*, vol. 18, p. 306–312, 2008.

[198] F. F. Lupi, T. J. Giammaria, M. Ceresoli, G. Seguini, K. Sparnacci, D. Antonioli, V. Gianotti, M. Laus, and M. Perego, "Rapid thermal processing of self-assembling block copolymer thin films," *Nanotechnology*, vol. 24, p. 315601, 2013.

[199] L. Nicole, C. Boissiere, D. Grosso, A. Quach, and C. Sanchez, "Mesostructured hybrid organic-inorganicthin films," *J. Mater. Chem.*, vol. 15, pp. 3598–3627, 2005.

[200] A. Walther, A. S. Goldmann, R. S. Yelamanchili, M. Drechsler, H. Schmalz, A. Eisenberg, and A. H. E. Müller, "Multiple morphologies, phase transitions, and cross-linking of crew-cut aggregates of polybutadiene-block-poly(2-vinylpyridine) diblock copolymers," *Macromolecules*, vol. 41, pp. 3254–3260, 2008.

[201] Y. Mai and A. Eisenberg, "Self-assembly of block copolymers," *Chem. Soc. Rev.*, vol. 41, p. 5969–5985, 2012.

[202] A. W. Fahmi and M. Stamm, "Spatially correlated metallic nanostructures on self-assembled diblock copolymer templates," *Langmuir*, vol. 21, pp. 1062–1066, 2005.

[203] B. Bharatiya, J. M. Schumers, E. Poggi, and J. F. Gohy, "Supramolecular assemblies from poly(styrene)-block-poly(4-vinylpyridine) diblock copolymers mixed with 6-hydroxy-2-naphthoic acid," *Polymers*, vol. 5, pp. 679–695, 2013.

[204] K. Fukunaga, H. Elbs, R. Magerle, and G. Krausch, "Large-scale alignment of abc block copolymer microdomains via solvent vapor treatment," *Macromolecules*, vol. 33, no. 3, p. 947–953, 2000.

[205] S. Park, B. Kim, J. Xu, T. Hofmann, B. M. Ocko, and T. P. Russell, "Lateral ordering of cylindrical microdomains under solvent vapor," *Macromolecules*, vol. 42, no. 4, pp. 1278–1284, 2009.

[206] C. Y. Chang, Y. C. Lee, P. J. Wu, J. Y. Liou, Y. S. Sun, and B. T. Ko, "Micellar transitions in solvent-annealed thin films of an amphiphilic block copolymer controlled with tunable surface fields," *Langmuir*, vol. 27, no. 23, p. 14545–14553, 2011.

[207] Y. Xuan, J. Peng, L. Cui, H. Wang, B. Li, and Y. Han, "Morphology development of ultrathin symmetric diblock copolymer film via solvent vapor treatment," *Macromolecules*, vol. 37, no. 19, p. 7301–7307, 2004.

[208] S. Kim, M. Misner, and T. Russell, "Solvent-induced ordering in thin film diblock copolymer/homopolymer mixtures," *Adv. Mater.*, vol. 16, no. 23-24, p. 2119–2123, 2004.

[209] K. A. Cavicchi, K. J. Berthiaume, and T. P. Russell, "Solvent annealing thin films of poly(isoprene-b-lactide)," *Polymer*, vol. 46, pp. 11635–11639, 2005.

[210] W. Huang, P. Y. Chen, and S. H. Tung, "Effects of annealing solvents on the morphology of block copolymer-based supramolecular thin films," *Macromolecules*, vol. 45, p. 1562–1569, 2012.

[211] W. V. Zoelen, T. Asumaa, J. Ruokolainen, O. Ikkala, and G. T. Brinke, "Phase behavior of solvent vapor annealed thin films of ps-b-p4vp(pdp) supramolecules," *Macromolecules*, vol. 41, p. 3199–3208, 2008.

[212] W. V. Zoelen, S. Bondzic, T. F. Landaluce, J. Brondijk, K. Loos, A. J. Schouten, P. Rudolph, and G. T. Brinke, "Nanostructured polystyrene-block-poly(4-vinyl pyridine)(pentadecylphenol) thin films as templates for polypyrrole synthesis," *Polymer*, vol. 50, p. 3617–3625, 2009.

[213] A. Sidorenko, I. Tokarev, S. Minko, and M. Stamm, "Ordered reactive nanomembranes/nanotemplates from thin films of block copolymer supramolecular assembly," *J. Am. Chem. Soc.*, vol. 125, p. 12211–12216, 2003.

[214] O. Seifarth, R. Krenek, I. Tokarev, Y. Burkov, A. Sidorenko, S. Minko, M. Stamm, and D. Schmeisser, "Metallic nickel nanorod arrays embedded into ordered block copolymer templates," *Thin Solid Films*, vol. 515, p. 6552–6556, 2007.

[215] P. S. Chinthamanipeta, Q. Lou, and D. A. Shipp, "Periodic titania nanostructures using block copolymer templates," *ACS Nano*, vol. 5, no. 1, p. 450–456, 2011.

[216] K. Müller, "Synthesis of nanostructured zinc oxide morphologies using zinc acetate dihydrate as a precursor for applications in hybrid photovoltaics," Master's thesis, Technische Universität München, Munich, Germany, 2012.

[217] K. Sarkar, C. J. Schaffer, D. M. González, A. Naumann, J. Perlichb, and P. Müller-Buschbaum, "Tuning the pore size of zno nano-grids via time-dependent solvent annealing," *J. Mater. Chem. A*, vol. 2, pp. 6945–6951, 2014.

[218] S. Pogorzalek, "Tailoring zno nanostructures for hybrid solar cells," Master's thesis, Technische Universität München, Munich, Germany, 2013.

[219] J. Allen, R. Campbell, M. Bakker, R. Schad, D. R. Lee, X. Li, and J. Wang, "Grazing incidence small angle x-ray scattering (gisaxs) study of mesoporous silica thin films on metal substrates," *Joshua*, vol. 7, pp. 3–8, 2010.

[220] M. Vaseem, A. Umar, and Y.-B. Hahn, *Metal Oxide Nanostructures and Their Applications*, vol. 5. American Scientific Publishers, 2010.

[221] C. Tian, Q. Zhang, A. Wu, M. Jiang, Z. Liang, B. Jianga, and H. Fu, "Cost-effective large-scale synthesis of zno photocatalyst with excellent performance for dye photodegradation," *Chem. Commun.*, vol. 48, pp. 2858–2860, 2012.

[222] L. Wang, Y. Kang, X. Liu, S. Zhang, W. Huang, and S. Wang, "Zno nanorod gas sensor for ethanol detection," *Sens. Actuators, B*, vol. 162, p. 237–243, 2012.

[223] J. Huang and Z. Y. nd Q Zheng, "Applications of zno in organic and hybrid solar cells," *Energy Environ. Sci.*, vol. 4, pp. 3861–3877, 2011.

[224] J. W. Spalenka, P. Gopalan, H. E. Katz, and P. G. Evans, "Electron mobility enhancement in zno thin films via surface modification by carboxylic acids," *Appl. Phys. Lett.*, vol. 102, p. 041602, 2013.

[225] D. Chen, S. Park, J. T. Chen, E. Redston, and T. P. Russell, "A simple route for the preparation of mesoporous nanostructures using block copolymers," *ACS Nano*, vol. 3, no. 9, p. 2827–2833, 2009.

[226] Z. Chen, H. Cui, K. Hales, Z. Li, K. Qi, D. J. Pochan, and K. L. Wooley, "Unique toroidal morphology from composition and sequence control of triblock copolymers," *J. Am. Chem. Soc.*, vol. 127, no. 24, p. 8592–8593, 2005.

[227] P. Busch, M. Rauscher, J. F. Moulin, and P. Müller-Buschbaum, "Debye–scherrer rings from block copolymer films with powder-like order," *J. Appl. Crystallogr.*, vol. 44, p. 370–379, 2011.

[228] X. Li, J. Peng, Y. Wen, D. H. Kim, and W. Knoll, "Morphology change of asymmetric diblock copolymer micellar films during solvent annealing," *Polymer*, vol. 48, no. 2, p. 434–443, 2007.

[229] S. Benramache, B. Benhaoua, and F. Chabane, "Effect of substrate temperature on the stability of transparent conducting cobalt doped zno thin films," *J. Semicond.*, vol. 33, no. 9, pp. 093001–1–4, 2012.

[230] K. D. Lee, "Effect of substrate temperature on the optical and the electrochromic properties of sputtered tio_2 thin films," *Journal of the Korean Physical Society*, vol. 46, no. 6, pp. 1383–1391, 2005.

[231] M. F. Hossain and T. Takahashi, "The effect of substrate temperature on the spray-deposited tio_2 nanostructured films for dye-sensitized solar cells," *J Nanosci Nanotechnol.*, vol. 11, no. 4, pp. 3222–3228, 2011.

[232] E. Bacaksiz, S. Yılmaz, M. Parlak, A. Varilci, and M. Altunbaş, "Effects of annealing temperature on the structural and optical properties of zno hexagonal pyramids," *J. Alloys Compd.*, vol. 487, no. 1-2, p. 367–370, 2009.

[233] S. W. Xue, X. T. Zu, W. L. Zhou, H. X. Deng, X. Xiang, L. Zhang, and H. Deng, "Effects of post-thermal annealing on the optical constants of zno thin film," *J. Alloys Compd.*, vol. 448, no. 1-2, p. 21–26, 2008.

[234] Z. Xue, W. Zhang, X. Yin, Y. Cheng, L. Wanga, and B. Liu, "Enhanced conversion efficiency of flexible dye-sensitized solar cells by optimization of the nanoparticle size with an electrophoretic deposition technique," *RSC Advances*, vol. 2, p. 7074–7080, 2012.

[235] L. C. Chen, C. C. Chen, and B. S. Tseng, "Improvement of short-circuit current density in dye-sensitized solar cells using sputtered nanocolumnar tio_2 compact layer," *Journal of Nanomaterials*, vol. 2010, pp. 1–4, 2010.

[236] R. Steim, *The impact of interfaces on the performance of organic photovoltaic cells.* PhD thesis, Karlsruhe Institut für Technologie, Karlsruhe, Germany, 2010.

[237] A. Djelloul, K. Bouzid, and F. Guerrab, "Role of substrate temperature on the structural and morphological properties of zno thin films deposited by ultrasonic spray pyrolysis," *Turk J. Phys.*, vol. 32, p. 49 – 58, 2008.

[238] L. Xu, Y. Guo, Q. Liao, and J. Zhang, "Morphological control of zno nanostructures by electrodeposition," *J. Phys. Chem. B*, vol. 109, p. 2813 –2825, June 2005.

[239] M. Niederberger, "Nonaqueous sol–gel routes to metal oxide nanoparticles," *Acc. Chem. Res.*, vol. 40, p. 793–800, April 2007.

[240] W. J. E. Beek, M. M. Wienk, and R. A. J. Janssen, "Hybrid solar cells from regioregular polythiophene and zno nanoparticles," *Adv. Funct. Mater.*, vol. 16, p. 1112–1116, April 2006.

[241] S. A. Kumar and S. M. Chena, "Nanostructured zinc oxide particles in chemically modified electrodes for biosensor applications," *Anal. Lett.*, vol. 41, pp. 141–158, February 2008.

[242] M. Grätzel, "Mesoporous oxide junctions and nanostructured solar cells," *Curr. Opin. Colloid Interface Sci.*, vol. 4, no. 4, pp. 314–321, 1999.

[243] X. Fu, L. A. Clark, Q. Yang, and M. A. Anderson, "Enhanced photocatalytic performance of titania-based binary metal oxides: Tio_2/sio_2 and tio_2/zro_2," *Environ. Sci. Technol.*, vol. 30, no. 2, pp. 647–653, 1996.

[244] J. W. Elam and S. M. George, "Growth of zno/al_2o_3 alloy films using atomic layer deposition techniques," *Chem. Mater.*, vol. 15, no. 4, pp. 1020–1028, 2003.

[245] N. Nolan, M. Seery, and S. Pillai, "Crysrallization and phase-transition characteristics of sol-gel-synthesized zinc titanates," *Chem. Mater.*, vol. 23, p. 1496–1504, 2011.

[246] Q. Xu, M. Järn, M. Lindén, and J.-H. Smatt, "Nanopatterned zinc titanate thin films prepared by the evaporation-induced self-assembly process," *Thin Solid Films*, vol. 531, pp. 222–227, 2013.

[247] Z. X. Chen, J. van der Eyden, W. Koot, R. van den Berg, J. van Mechelen, and A. Derking, "Preparation of zinc titanate thin films by low-pressure metalormetal chemical vapor deposition," *J. Am. Ceram. Soc.*, vol. 78, no. 11, pp. 2993–3001, 1995.

[248] G. Akgül, "Synthesis and structural characterization of zinc titanates," *J. Mol. Struct.*, vol. 1037, p. 35–39, 2013.

[249] S. K. Manik, P. Bose, and S. K. Pradhan, "Microstructure characterization and phase transformation kinetics of ball-milled prepared nanocrystalline zn_2tio_4 by rietveld method," *Mater. Chem. Phys.*, vol. 82, p. 837–847, 2003.

[250] Z. Cai, J. Song, J. Li, F. Zhao, X. Luo, and X. Tang, "Synthesis and characterization of zinc titanate fibers by sol-electrospinning method," *J Sol-Gel Sci Technol*, vol. 61, pp. 49–55, 2012.

[251] Y. Yang, X. W. Sun, B. K. Tay, J. X. Wang, Z. L. Dong, and H. M. Fan, "Twinned zn_2tio_4 spinel nanowires using zno nanowires as a template," *Adv. Mater.*, vol. 19, p. 1839–1844, 2007.

[252] Y. S. Chang, Y. H. Chang, I. G. Chen, G. J. Chen, and Y. L. Chai, "Synthesis and characterization of zinc titanate nano-crystal powders by sol–gel technique," *J. Cryst. Growth*, vol. 243, p. 319–326, 2002.

[253] E. V. Braden, "Sol-gel templated films of different zinc oxide and titania ratios for application in photovoltaics," Master's thesis, Technische Universität München, Munich, Germany, 2014.

[254] H. Guo, X. He, C. Hu, Y. Tian, Y. Xi, J. Chen, and L. Tian, "Effect of particle size in aggregates of zno-aggregate-based dye-sensitized solar cells," *Electrochim. Acta*, vol. 120, pp. 23–29, 2014.

[255] T. P. Chou, Q. Zhang, B. Russo, G. E. Fryxell, and G. Cao, "Titania particle size effect on the overall performance of dye-sensitized solar cells," *J. Phys. Chem. C*, vol. 111, pp. 6296–6302, February 2007.

[256] K. Zhu, N. R. Neale, A. Miedaner, and A. J. Frank, "Enhanced charge-collection efficiencies and light scattering in dye-sensitized solar cells using oriented tio_2 nanotubes arrays," *Nano Lett.*, vol. 7, pp. 69–74, November 2007.

[257] Y. Zhang, G. Li, Y. Wu, Y. Luo, and L. Zhang, "The formation of mesoporous tio_2 spheres via a facile chemical process," *J. Phys. Chem. B*, vol. 109, no. 12, p. 5478–5481, 2005.

[258] J. J. Wu and C. C. Yu, "Aligned tio_2 nanorods and nanowalls," *J. Phys. Chem. B*, vol. 108, no. 11, p. 3377–3379, 2004.

[259] S. Valencia, J. M. Marín, and G. Restrepo, "Study of the bandgap of synthesized titanium dioxide nanoparticules using the sol-gel method and a hydrothermal treatment," *The Open Materials Science Journal*, vol. 4, p. 9–14, 2010.

[260] S. A. Mayén-Hernández, G. Torres-Delgado, R. Castanedo-Pérez, M. G. Villarreal, A. Cruz-Orea, J. G. M. Alvarez, and O. Zelaya-Angel, "Optical and structural properties of zno + zn_2tio_4 thin films prepared by the sol–gel method," *J. Mater. Sci.: Mater. Electron.*, vol. 18, p. 1127–1130, 2007.

[261] L. E. Brus, "Electron-electron and electron-hole interactions in small semiconductor crystallites: The size dependence of the lowest excited electronic state," *J. Chem. Phys.*, vol. 80, pp. 4403–4409, May 1984.

[262] S. C. Souza, I. M. G. Santos, M. R. S. Silva, M. R. Cassia-Santos, L. E. B. Soledade, A. G. Souza, S. J. G. Lima, and E. Longo, "Influence of ph on iron diped zn_2tio_4 pigments," *J. Therm. Anal. Calorim.*, vol. 79, no. 2, pp. 451–454, 2005.

[263] M. H. Habibi, M. Mikhak, M. Zendehdel, and M. Habibi, "Influence of nanostructured zinc titanate, zinc oxide or titanium dioxide thin film coated on fluorine doped tin oxide as working electrodes for dye-sensitized solar cell," *Int. J. Electrochem. Sci.*, vol. 7, pp. 6787 – 6798, August 2012.

[264] F. H. Dulin and D. E. Rase, "Phase equilibria in the system zno-tio_2," *J. Am. Ceram. Soc.*, vol. 43, no. 3, pp. 125–131, 1960.

[265] J. M. G. Amores, V. S. Escribano, and G. Busca, "Anatase crystal growth and phase transformation to rutile in high - area tio_2, moo_3,-tio_2, and other tio_2- supported oxide catalytic systems," *J. Mater. Chem.*, vol. 5, no. 8, p. 1245–1249, 1995.

[266] F. Lonyi and J. Valyon, "Themally effected structural and surface transformation of sulfated tio_2, zro_2 and tio_2-zro_2 catalysts," *J. Therm. Anal.*, vol. 46, p. 211–218, 1996.

List of publications

Publications related to the dissertation

- K. Sarkar, M. Rawolle, E. M. Herzig, W. Wang, A. Buffet, S. V. Roth, P. Müller-Buschbaum, "Custom-made morphologies of ZnO nanostructured films templated by a poly(styrene-block-ethylene oxide) diblock copolymer obtained by a sol–gel technique", *ChemSusChem*, vol. 6, pp. 1414–1424, 2013.
- K. Sarkar, M. Rawolle, M. A. Niedermeier, W. Wang, E. M. Herzig, V. Körstgens, A. Buffet, S. V. Roth, P. Müller-Buschbaum, "A quantitative approach to tune metal oxide network morphology based on grazing-incidence small-angle X-ray scattering investigations", *Journal of Applied Crystallography*, vol. 47, pp. 76–83, 2014.
- K. Sarkar, C. J. Schaffer, D. Moseguí González, A. Naumann, J. Perlichb, P. Müller-Buschbaum, "Tuning the pore size of ZnO nano-grids via time-dependent solvent annealing", *Journal of Materials Chemistry A*, vol. 2, pp. 6945–6951, 2014.
- K. Sarkar, E. V. Braden, S. Pogorzalek, S. Yu, S. V. Roth, P. Müller-Buschbaum, "Monitoring structural dynamics of in-situ spray-deposited zinc oxide films for application in dye-sensitized solar cells", *ChemSusChem*, accepted,
  DOI: 10.1002/cssc.201402049, 2014.
- K. Sarkar, E. V. Braden, T. Fröschl, N. Hüsing, P. Müller-Buschbaum, "Spray-deposited zinc titanate films obtained via sol-gel synthesis for application in dye-sensitized solar cells", *Journal of Materials Chemistry A*, accepted,
  DOI: 10.1039/c4ta02031f, 2014.
- M. Rawolle, K. Sarkar, M. A. Niedermeier, M. Schindler, P. Lellig, J. S. Gutmann, J.-F. Moulin, M. Haese-Seiller, A. Wochnik, C. Scheu, P. Müller-Buschbaum, "Infiltration of polymer hole-conductor into mesoporous titania structures for solid-state dye-sensitized solar cells", *ACS Applied Materials & Interfaces*, vol. 5, pp. 719–729, 2013.
- M. Rawolle, E. V. Braden, M. A. Niedermeier, D. Magerl, K. Sarkar, T. Fröschl, N. Hüsing, J. Perlich, and P. Müller-Buschbaum, "Low-temperature route to crystalline

titania network structures in thin films", *ChemPhysChem*, vol. 13, no. 9, pp. 2412–2417, 2012.

Further publication

- S. Yu, G. Santoro, K. Sarkar, B. Dicke, P. Wessels, S. Bommel, R. Döhrmann, J. Perlich, M. Kuhlmann, E. Metwalli, J. F. H. Risch, M. Schwartzkopf, M. Drescher, P. Müller-Buschbaum, S. V. Roth, "Formation of Al nanostructures on Alq3: An in situ grazing incidence small angle X-ray scattering study during RF sputter deposition", *Journal of Physical Chemistry Letters*, vol. 4, pp. 3170–3175, 2013.

Award

- TUM.ENERGY BEST PRESENTATION AWARD 2012, in recognition of the poster, "Hybrid films based on ZnO network structures for applications in organic photovoltaics", *2nd Colloquium of the Munich School of Engineering*, Garching (Germany), 28.06.2012.

Scientific reports

- K. Sarkar, S. V. Roth, P. Müller-Buschbaum, "Inorganic-organic hybrid materials for applications in photovoltaics : titania, dye and P3HT", *Lehrstuhl für Funktionelle Materialien, Annual Report*, 2010.
- K. Sarkar, M. Rawolle, E. M. Herzig, W. Wang, A. Buffet, S. V. Roth, P. Müller-Buschbaum, "Foam-like ZnO nanostructured morphology synthesized via sol-gel technique for applications in photovoltaics", *Lehrstuhl für Funktionelle Materialien, Annual Report*, 2011.
- K. Sarkar, C. Schaffer, A. Naumann, D. Moseguí González, J. Perlich, P. Müller-Buschbaum, "Morphology evolution of ZnO nanostructures upon solvent vapor treatment", *Lehrstuhl für Funktionelle Materialien, Annual Report*, 2012.
- K. Sarkar, E. V. Braden, S. Pogorzalek, S. Yu, S. V. Roth, P. Müller-Buschbaum, "A kinetic study of structural evolution in spray-deposited ZnO film for application in dye-sensitized solar cells", *Lehrstuhl für Funktionelle Materialien, Annual Report*, 2013.

- K. Sarkar, V. Körstgens, M. A. Niedermeier, W. Hefter, A. Buffet, S. V. Roth, P. Müller-Buschbaum, "P(S-*b*-4VP) templated ordered ZnO nanostructures via sol-gel route", *HASYLAB Annual Report*, 2011.
- K. Sarkar, M. Rawolle, E. M. Herzig, W. Wang, A. Buffet, S. V. Roth, P. Müller-Buschbaum, "Foam-like ZnO nanostructured morphology for applications in photovoltaics", *HASYLAB Annual Report*, 2011.
- K. Sarkar, C. Schaffer, A. Naumann, D. Moseguí González, J. Perlich, S. V. Roth, P. Müller-Buschbaum, "Morphology evolution of ZnO nanostructures upon solvent vapour treatment", *HASYLAB Annual Report*, 2012.
- K. Sarkar, E. V. Braden, S. Pogorzalek, S. Yu, S. V. Roth, P. Müller-Buschbaum, "Monitoring structural evolution of in-situ spray-deposited ZnO nanostructured film via GISAXS", *DESY Annual Report*, 2013.

Conference talks

- K. Sarkar, M. Rawolle, E. M. Herzig, W. Wang, P. Müller-Buschbaum, "Sol-Gel Templated Zinc oxide Films for Solar Cell Application", *DPG Frühjahrstagung*, Berlin (Germany), 25.–30.03.2012.
- K. Sarkar, C. Schaffer, A. Naumann, D. Moseguí González, P. Müller-Buschbaum, "Morphology evolution of diblock copolymer based ZnO nanostructures upon solvent vapor treatment", *DPG Frühjahrstagung*, Regensburg (Germany), 10.–15.03.2013.
- K. Sarkar, E. V. Braden, S. Pogorzalek, S. Yu, S. V. Roth, P. Müller-Buschbaum, "Spray deposition of zinc oxide nanostructured films for applications in dye-sensitized solar cells", *DPG Frühjahrstagung*, Dresden (Germany), 30.03–04.04.2014.
- K. Sarkar, C. Schaffer, A. Naumann, D. Moseguí González, J. Perlich, P. Müller-Buschbaum, "GISAXS study of morphology evolution of diblock copolymer based ZnO nanostructures upon solvent vapor treatment", *2^{nd} International Grazing Incidence Small Angle X-ray Scattering workshop*, Kyoto (Japan), 13.–15.11.2012.
- K. Sarkar, M. Rawolle, E. M. Herzig, W. Wang, M. A. Niedermeier, V. Körstgens, W. Hefter, A. Buffet, S. V. Roth, P. Müller-Buschbaum, "Mesoporous zinc oxide morphologies for applications in hybrid photovoltaics", *15^{th} International Small-Angle Scattering conference*, Sydney (Australia), 18.–23.11.2012.
- M. Rawolle, K. Sarkar, "Hybrid solar cells: inorganic-organic photovoltaics without and with dye", *E13 Summer School*, Rudolfshütte (Austria), 12.–15.06.2012.

- K. Sarkar, M. Rawolle, E. M. Herzig, W. Wang, E. V. Braden, S. Pogorzalek, C. Schaffer, A. Naumann, D. Moseguí González, A. Buffet, J. Perlich, S. V. Roth, P Müller-Buschbaum, "Zinc oxide nanostructures for applications in dye-sensitized solar cells", *Nanosystems for solar energy conversions*, Munich (Germany), 24.–26.07.2013.
- K. Sarkar, M. Rawolle, E. M. Herzig, W Wang, M. A. Niedermeier, C. Schaffer, C. M. Palumbiny, D. Moseguí González, N. Paul, A. Naumann, A. Buffet, J. Perlich, S. V. Roth, P. Müller-Buschbaum, "Hybrid films based on ZnO network structures for applications in organic photovoltaics", *3rd Colloquium TUM-HASYLAB "The polymer metal interface"*, Garching (Germany), 10.–11.09.2012.

Conference poster presentations

- K. Sarkar, M. Rawolle, E. M. Herzig, W. Wang, S. V. Roth, P. Müller-Buschbaum, "ZnO nanostructures templated by a PS-b-PEO diblock copolymer via sol-gel route", *1st Colloquium of the Munich School of Engineering*, Garching (Germany), 18.07.2011.
- K. Sarkar, M. Rawolle, W. Wang, E. M. Herzig, P. Müller-Buschbaum, "Hybrid films based on zinc oxide network structures for applications in organic photovoltaics", *2nd Colloquium of the Munich School of Engineering*, Garching (Germany), 28.06.2012.
- K. Sarkar, M. A. Niedermeier, E. V. Braden, S. Pogorzalek, P. Müller-Buschbaum, "Zinc oxide nanostructured films for applications in organic photovoltaics", *3rd Colloquium of the Munich School of Engineering*, Garching (Germany), 04.07.2013.
- K. Sarkar, M. Rawolle, E. M. Herzig, W. Wang, S. V. Roth, P. Müller-Buschbaum, "ZnO nanostructures templated by a PS-b-PEO diblock copolymer via sol-gel route", *Joint Nanoworkshop*, Garching (Germany), 01.06.2011.
- K. Sarkar, M. Rawolle, E. M. Herzig, W. Wang, S. V. Roth, P. Müller-Buschbaum, "ZnO nanostructures templated by a PS-b-PEO diblock copolymer via sol-gel route", *5th FRM II Science Meeting*, Burg Rothenfels (Germany), 06.–09.06.2011.
- K. Sarkar, M. Rawolle, E. M. Herzig, W. Wang, E. V. Braden, S. Pogorzalek, S. V. Roth, P. Müller-Buschbaum, "ZnO nanostructured films for applications in organic photovoltaics", *6th FRM II Science Meeting*, Grainau (Germany), 10.–13.06.2013.
- K. Sarkar, M. Rawolle, M. A. Niedermeier, P. Müller-Buschbaum, "ZnO nanostructures templated by a PS-b-PEO diblock copolymer via sol-gel route", *DPG Frühjahrstagung*, Dresden (Germany), 13.-18.03.2011.

- K. Sarkar, M. Rawolle, M. A. Niedermeier, P. Müller-Buschbaum, "ZnO nanostructures templated by a PS-b-PEO diblock copolymer via sol-gel route", *1st Tag der Physikerinnen*, Garching (Germany), 10.02.2011.
- K. Sarkar, M. Rawolle, M. A. Niedermeier, P. Müller-Buschbaum, "ZnO nanostructures templated by a PS-b-PEO diblock copolymer via sol-gel route", *2nd Tag der Physikerinnen*, Garching (Germany), 15.02.2012.
- K. Sarkar, M. A. Niedermeier, E. V. Braden, S. Pogorzalek, P. Müller-Buschbaum, "ZnO nanostructured films for applications in organic photovoltaics", *3rd Solar Technologies - International Conference*, Wildbad Kreuth (Germany), 27.–30.04.2014.
- K. Sarkar, M. Rawolle, E. M. Herzig, W. Wang, E. V. Braden, S. Pogorzalek, S. V. Roth, P. Müller-Buschbaum, "ZnO nanostructured films for applications in organic photovoltaics", *NIM Workshop "Young Ideas in Nanoscience"*, Munich (Germany), 19.–20.11.2013.

Acknowledgments

To begin with, I want to thank Prof. Dr. Peter Müller-Buschbaum to allow me to continue my PhD in his group. This gave me a wide range of possibilities to enrich and develop my knowledge in the interesting field of photovoltaics. Additionally, I want to thank him for his continuous support, despite the busy schedule. All his advice and discussion have always guided me throughout my PhD studies. I highly appreciate the excellent opportunities that he offered me to participate in the international conferences in Kyoto and Sydney. Furthermore, all the chances that he presented for me to join beamtimes in Germany as well as abroad have helped me to gain technical knowledge as well as to acquire organizational experience.

The beamtimes have become successful with the support and expertise of a lot of experienced beamline scientists and technicians. Moreover, I want to thank all the colleagues who had participated enthusiastically during the measurement times. I want to thank the people who were involved in no specific order: Dr. Jan Perlich, Dr. Gonzalo Santoro, Dr. Adeline Buffet, Dr. Shun Yu, Dr. Matthias Schwartzkopf, Dr. Stephan V. Roth, Dr. André Rothkirch, Ralf Röhlsberger, Gerd Herzog, Gunthard Benecke from DESY, Dr. Alessandro Sepe, Dr. Jonathan Rawle, Dr. Tom Arnold and Shu-Hao Liu from Diamond Light Source, Dr. Monika Rawolle, Dr. Eva M. Herzig, Weijia Wang, Dr. Volker Körstgens, Dr. Martin Niedermeier (BBTFF), William Hefter, Erik Braden, Anna Naumann, Christoph Schaffer, Neelima Paul, Claudia Palumbiny, Markus Schindler, David Magerl and Daniel Moseguí González from TUM. My special thanks to Markus Schindler, Claudia Palumbiny and Dr. Ezzeldin Metwalli for giving me the chances to join them for neutron beamtimes at PSI and ILL. The short trips that were possible due to the long measurement times with the neutrons, will always remain memorable for me, specially the ones to the Grottes-de-choranche and Rhine falls. My particular thanks go to Markus and Claudia (my first driving teachers) who practically risked their lives in order to teach me driving in the parking area of PSI!

Furthermore, the results presented in the thesis would not be complete without the measurements performed using several instruments at other chairs at the Technishe Universität München. For this, I want to thank Prof. Dr. Alexander W. Holleitner and Peter Weiser from WSI to provide the possibility to measure SEM, Peter weiser for the access

to the clean room of ZNN for DEKTAK measurements, Prof. Dr. Klaus Köhler and Jian Zheng for the FTIR measurements in the Chemistry-Department, Dr. Karen Helm-Knapp and Dr. Stephan Geprägs from WMI for the EDX measurements. Additionally, I also want to thank Prof. Dr. Wolfgang Schmahl for the XRD measurements, Prof. Dr. Bettina V. Lotsch, Ida Pavlichenko and Stephan Werner for providing the possibility of measuring DLS at Ludwig-Maximilians-Universtität.

I am grateful for the financial support of my thesis by TUM. solar in the frame of the Bavarian Collaborative Research Project "Solar Technologies go Hybrid" (SolTech). Parts of the project were also supported by Knut och Alice Wallenberg foundation, BMBF (project 05K10WOA) and EMH the Munich School of Engineering.

I am also thankful to some of the fruitful collaborations that developed throughout the past few years. My thanks go to Prof. Dr. Nicola Hüsing and Thomas Fröschl from Universität Salzburg, Austria for synthesizing EGMT and Prof. Dr. Thomas F. Fässler and Manuel Bentlohner from Chemistry-Department, TUM for bringing the interesting samples for scattering measurements.

I am indeed grateful to my bachelor and master students Kai Müller, Chen Lin, Stefan Pogorzalek, Rui Wang and Erik Braden for all their good work . Their hard work and inputs really contributed to the completeness of the present thesis. Working in the lab would not be even half the fun without them. I wish them all a very successful future ahead. My acknowledgements will be rather incomplete if I do not thank Kai and Stefan for their beautiful flowers and cakes. My special thanks to Erik for his exceptional ideas to set up the spray coater and innumerous help to prepare for the beamtimes, which made them some of the best measurement times I had. Apart from this, he has always been there as a good friend whenever I needed him and has also made it possible to have one of the nicest post-beamtime vacations in England!

I am thankful to our technicians from the workshop for their help, most of all Raffael Jahrstorfer and Reinhold Funer for their help with the designing of several parts of the semi-automatized pray coater. I also want to thank Josef Kaplonski for help with the tube furnaces.

For proof reading and improving my thesis, I am sincerely grateful to Daniel Moseguí González, Stephan Pröller, Dr. Monika Rawolle, Dr. Martin Niedermeier, Claudia Palumbiny, Christoph Schaffer, Nitin Saxena, Lin Song, Weijia Wang, Dr. Eva Herzig, Dr. Volker Körstgens, Christian Jendrzejewski, Dr. Martine Philipp and Konstantinos Kyriakos. I want to thank especially, Stephan to invest his time and effort to write the German part of my thesis abstract and Gregory Tainter with the English corrections.

All the former and present members of Lehrstuhl für Funktionelle Materialien have really provided a friendly and pleasant atmosphere to work. I want to thank Prof. Dr.

Christine M. Papadakis, Dr. Robert Meier, Dr. Alexander Diethert, Dr. Semih Ener, Yuan Yao, Shuai Guo, Dr. Qi Zhong, Su Bo (meme), Johannes Schlipf, Nuri Hohn, Felipe Martinez, Christoph Mayr, Rosa Maria Torrademé, Tobias Widmann, Christina Psylla and Natalya Vishnevetskaya. I especially want to thank Margarita Dyakonova for helping me to earn the teaching points by DSC praktikum. I am grateful to Dr. Matthias Ruderer, Dr. Martin Niedermeier, Dr. Monika Rawolle, Markus schindler and David Magerl (dada - the macro man) for all the intensive scientific discussions and the fun work time that we shared. I am extremely thankful to Dr. Monika Rawolle (one of the most calm and patient human being I have ever met!) and Dr. Martin Niedermeier, who introduced me to the whole group and almost to all the measurement techniques and have also taken care of me as real good friends. I thank Dr. Volker Körstgens for sharing the small office and having all the funny discussions with me. I want to thank Daniel for providing spiritual guidance from time to time and being a strong support, which I will definitely miss. I am specially grateful to Dr. Sebastian Jaksch for spending the awesome post-conference time with me in Australia and saving my life in the Pacific ocean! I want to thank them all for the nice time that I cherished being with them at and besides work. I especially liked and enjoyed the group activities, like the summer and winter hikes, the summer BBQs, the karaoke evenings, Christmas parties, beer festivals, joint conferences and workshops, small shoe shopping events (thanks to Claudia and Monika) and Go-Kart racing, where I held the last position. Literally! In the course of these three and a half years, some of you have really become good friends.

My special thanks to the core operating unit of E13, the beautiful and smart secretaries Petra Douglas, Susanna Fink and Marion Waletzki. I thank them from the bottom of my heart for kindly and patiently dealing with all the administrative problems that I had caused being a foreigner, especially those related to my visa. Also, I especially thank Susanna to arrange heaps of travel documents and reimbursement forms for me. You all have been an unending source of mental support for me and beyond that! I also thank Dieter Müller for his technical support.

I am very grateful to Hsin-Yin, Shuai, Nindiya and David, who have always provided the atmosphere of being home away from home. I thank especially Hsin-Yin, Shuai and Sofía for sharing all the good and bad times with grace and honor. I also want to apologize to all the friends, whom I could not give enough time in the recent past when I was busy writing my thesis. I thank my host mother in Munich, Mrs. Gudula Opolony for her intensive care and support in every possible way, which has made my stay in Munich very extraordinary. She never made me realize that I am living far from my family and have always provided more than enough love and moral support.

Last but not least, I want to thank my friends and family in India for believing in

me and constantly supporting me in my decisions and hard work. All the motivation provided by you have made it possible for me to come this far. I thank Ruchi for visiting me here in Munich, which was definitely one of the best presents she has ever given me. My biggest thank you goes to my brother and parents on whom I can always rely. I want to dedicate my thesis to them and daktar dadu, who have made it possible for me to be where I am.